# Functional Genomics of Nocturnal Carboxylation in Crassulacean Acid Metabolism

Thesis submitted in accordance with the requirements of the

University of Liverpool for the degree of Doctor in Philosophy

by Jack Davies

July 2017

## Abstract

Crassulacean acid metabolism (CAM) is an evolutionary adaptation of photosynthesis by which plant photosynthetic organs carry out phosphoenolpyruvate carboxylase (PPC)-catalysed $CO_2$ fixation during the night, store nocturnally-fixed carbon in the form of malate, break down the stored malate during the day, and re-fix the $CO_2$ thus internally generated. The internal supply of $CO_2$ as substrate for Rubisco-catalysed fixation during the day has the potential to greatly reduce the demand for $CO_2$ from the atmosphere. This allows CAM species growing in arid or water-limited niches to mitigate water loss from transpiration by closing their stomatal pores during the hotter and drier day. This adaptive trait has motivated efforts to genetically engineer CAM into economically-important $C_3$ species in order to increase their resistance to drought in the hotter and drier climates that it is anticipated will result from anthropogenic climate change.

Efforts to characterise CAM at the molecular genetic level through reverse genetics, guided by genomic and transcriptomic analysis, are ongoing by the Hartwell group, University of Liverpool, using *Kalanchoë* species as CAM model species. Two membrane-bound metabolite transporter proteins, a vacuolar aluminium-activated malate transporter (ALMT) family protein and a tonoplast dicarboxylate transporter (TDT), have been suggested to play a role in mediating cytosol-to-vacuolar lumen malate transport in CAM, during nocturnal malate accumulation and diurnal malate breakdown, respectively. Prior to the start of this PhD project, *Kalanchoë fedtschenkoi* lines were generated in which *KfALMT* or *KfTDT* was targeted for transcriptional silencing by a transgenic hairpin RNA in conjunction with endogenous RNA interference (RNAi) pathways. Phenotypic characterisation of *KfALMT* RNAi lines showed that CAM was suppressed at the level of nocturnal $CO_2$ fixation and diel malate turnover in these lines, with downstream effects on diel patterns of carbohydrate metabolism. Vacuolar membranes were extracted from two *KfALMT* RNAi lines for *in vitro* functional characterisation of ALMT. This showed that suppression of *KfALMT* transcript greatly reduced the $H^+$-malate coupled transport activity of the tonoplasts, providing a protein function correlate to CAM suppression *in vivo*. CAM suppression via *KfALMT* RNAi was also found to perturb the entrainment of the core circadian clock, which is thought to regulate the diel CAM cycle, and the clock-controlled, CAM-regulatory phosphoenolpyruvate kinase (PPCK). Multi-level CAM suppression was not found in *KfTDT* RNAi lines, but preliminary phenotyping suggested that TDT could act as vacuolar citrate transporter.

Malate dehydrogenase (MDH) is required to catalyse the conversion of oxaloacetate (OAA), the product of PPC-catalysed nocturnal $CO_2$ fixation, into malate in order to accumulate the latter at night in CAM. However, it is unknown which of the plant cell's multiple MDH isoforms mediates this metabolic flux. Isogene-specific silencing of MDH via RNAi in transgenic *Kalanchoë laxiflora* was attempted. Preliminary phenotypic characterisation of *MDH* RNAi lines found some evidence of a small degree of CAM suppression in cytosolic NAD-MDH (*KlCMDH*)

RNAi and plastidic NAD-MDH (*KlPdMDH*) RNAi lines. It was suggested that the two enzymes could act synergistically in partially independent and parallel pathways to mediate nocturnal accumulation of malate in CAM.

# Table of Contents

## List of figures and tables

### Chapter 1



### Chapter 2



### Chapter 3

**Chapter 4**

**Chapter 5**

**Chapter 6**

## Glossary of abbreviations

| | |
|---|---|
| 12:12 LD | Conditions of cycles of 12 h light and 12 h darkness |
| 3PGA | 3-phosphoglycerate |
| ADP | adenosine diphosphate |
| ATP | adenosine triphosphate |
| *CCA1* | *CIRCADIAN CLOCK ASSOCIATED 1* |
| GOGAT | glutamine-oxaloacetate aminotransferase |
| HPR | hydroxypyruvate reductase |
| IRGA | infra-red gas analyser |
| LL | Conditions of constant light |
| NAD | nicotinamide adenine dinucleotide, oxidised |
| NADH | nicotinamide adenine dinucleotide, reduced |
| NADP | nicotinamide adenine dinucleotide phosphate, oxidised |
| NADPH | nicotinamide adenine dinucleotide phosphate, reduced |
| NAD-ME | NAD-malic enzyme |
| NADP-ME | NADP-malic enzyme |
| OAA | oxaloacetate |
| PEP | phosphoenolpyruvate |
| PEPCK | phosphoenolpyruvate carboxykinase |
| PETC | photosynthetic electron transport chain |
| $P_i$ | inorganic phosphate |
| PPC | phosphoenolpyruvate carboxylase |
| PPCK | phosphoenolpyruvate carboxylase kinase |
| PPDK | pyruvate, phosphate dikinase |
| PPi | inorganic pyrophosphate |
| Rubisco | ribulose 1,5-bisphosphate carboxylase/oxygenase |

| | |
|---|---|
| TCA | tricarboxylic acid (cycle) |
| *TOC1* | *TIMING OF CAB EXPRESSION 1* |

**Acknowledgments**

First and foremost, thanks must go to my PhD supervisor, James Hartwell, who not only gave me the opportunity to pursue this project, but has offered patient support, guidance and positivity from the first to the last. Over the last five years, I have benefited from Dr Hartwell's knowledge of and insights into Crassulacean acid metabolism and the broader field of plant science on many more occasions than I can recall, and his readiness to offer them at a moment's notice.

This thesis would also not have been possible without Professor Andrew Smith of the Department of Plant Sciences, Oxford University. I spent several weeks in Professor Smith's lab developing tonoplast function assays, and the subcellular fractionation method on which they depend. He has also given over ample portions of his time to discussions of vacuolar malate transport in CAM and associated topics, and my data. For this I am immensely thankful. Thanks also to Dr Paulinha Pereira, who, as a visiting student to Professor Smith's laboratory, provided hands-on training in tonoplast vesicle extraction and quinacrine $H^+$ transport assays.

Thank you to the staff and students in the Hartwell group, past and present - Dr Susanna Boxall, Dr Louisa Dever, Dr Jade Waller, Dr Phaitun Bupphada, Ms Nirja Kadu and Mr Richard Heaton – who have taught me vital technical skills, passed on their experience and expertise, appraised my data, and given freely of their time, knowledge and friendship. Thank you all.

I also need to thank Ms Jean Wood, senior technician, for her continual and unflappable support for my lab work. Without her help, I would have been stuck on scores of logistical and administrative problems.

Thank you to Professor Rob Beynon and Mrs Lynn McLean for kindly permitting and facilitating access to their spectrofluorometer.

Thank you to my parents, who may have thought their parenting days were over before their son took up a PhD project! I couldn't have done it without you.

Thanks to everyone who has persisted in being a good friend to a bad friend while I worked through this project. You all know who you are.

# Chapter 1 – Introduction

## 1.1 A functional overview of the CAM cycle

Crassulacean acid metabolism (CAM) is an evolutionary adaptation of photosynthesis that allows plants to supply some or all of the $CO_2$ fixed by ribulose 1,5-bisphosphate carboxylase/oxygenase (Rubisco) during the day from decarboxylation of malate accumulated during the previous night (Osmond, 1978). This internal supply of $CO_2$ permits simultaneous stomatal closure and photosynthesis for part or all of the day (Winter, 1980; Kluge *et al.*, 1981; Rascher and Lüttge, 2002; von Caemmerer and Griffiths, 2009). Nocturnal synthesis and accumulation of malate is supplied by phosphoenolpyruvate carboxylase (PPC)-catalysed fixation of $CO_2$. The basic unit of the CAM night-to-day carbon shuttle is most commonly a single leaf or stem mesophyll cell, without any requirement for extracellular transport of metabolic intermediates (Cushman and Bohnert, 1997). This distinguishes CAM from $C_4$ photosynthesis, which is also dependent on PPC activity for primary $CO_2$ assimilation, but in which PPC and Rubisco are usually simultaneously active in morphologically differentiated and spatially distinct neighbouring cell types, namely the leaf mesophyll and bundle sheath cells (von Caemmerer and Furbank, 2003).

In CAM, conversely, Rubisco and PPC are active for largely separate periods of the diel cycle (Fig. 1.1; Borland and Griffiths, 1997; Maxwell *et al.*, 1999). PPC converts phosphoenolpyruvate (PEP) and bicarbonate ($HCO_3^-$) into oxaloacetate (OAA) and inorganic phosphate ($P_i$, $HPO_4^{2-}$). The conversion of $CO_2$ into $HCO_3^-$ is catalysed by carbonic anhydrase (CA; Holtum *et al.*, 1984). PEP is synthesised for nocturnal PPC-catalysed $CO_2$ fixation through the glycolysis pathway, downstream of breakdown of storage carbohydrates (Holtum *et al.*, 2005; Borland *et al.*, 2016). OAA is subsequently reduced by one or more malate dehydrogenases (MDH) to malate, which is a feed-back inhibitor of PPC (Osmond, 1978;

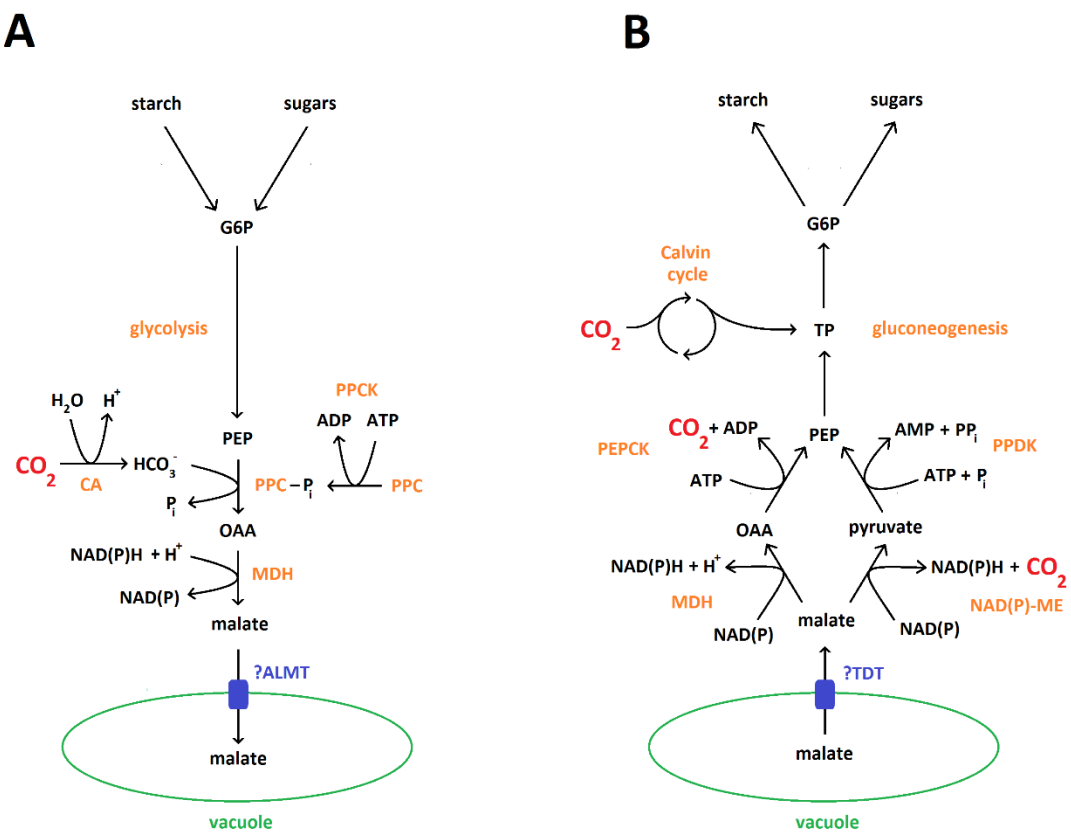


Figure 1.1 - Simplified representation of nocturnal (A) and diurnal (B) CAM pathways. Additional abbreviations: G6P, glucose 6-phosphate; TP, triose phosphate.

Nimmo *et al.*, 1984). Phosphorylation of PPC at night by a circadian clock-controlled protein kinase (phosphoenolpyruvate carboxylase kinase, PPCK) decreases the sensitivity of the enzyme to inhibition by malate and permits the accumulation of malate to higher concentrations (Nimmo *et al.*, 1984; Hartwell *et al.*, 1999; Nimmo, 2000). PPC phosphorylation is largely restricted to the night by transcriptional repression of PPCK during the day (Hartwell *et al.*, 1996; Borland *et al.*, 1999).

Malate is transported into the cell vacuole during the night, which prevents the cytosol from becoming acidified or hyperosmotic (Hafke *et al.*, 2001). Vacuolar malate import is thought to proceed by facilitated diffusion through a tonoplast (i.e. vacuolar membrane) anion channel

protein (Hafke *et al.*, 2003), possibly an aluminium-activated malate transporter (ALMT, Fig. 1.1A; Holtum *et al.*, 2005). Cytosol-to-vacuolar lumen transport of malate against its concentration gradient is driven by an $H^+$ concentration gradient between the vacuolar lumen and the cytosol, which is in turn established by active $H^+$ transport, catalysed by $H^+$-translocating vacuolar ATPase (V-ATPase) and/or pyrophosphatase (PPase; Smith *et al.*, 1996).

Release of malate from the vacuole begins after dawn and is thought to entail symport of malate with nocturnally-accumulated $H^+$, or alternatively uniport of undissociated malic acid (Lüttge and Smith, 1984; Holtum *et al.*, 2005). Tonoplast dicarboxylate transporter (TDT; Emmerlich *et al.*, 2003) has been suggested as a candidate vacuolar malate exporter in CAM (Holtum *et al.*, 2005). Two distinct pathways for breaking down malate and releasing $CO_2$ within photosynthetic tissues have been reported in CAM species (Fig. 1.1B). In the first pathway, malate is broken down to pyruvate and $CO_2$ by a decarboxylating malate dehydrogenase (malic enzyme), either of the NAD- or the NADP-binding types (NAD-ME and NADP-ME, respectively), and pyruvate is converted to PEP by pyruvate, phosphate dikinase (PPDK). In the second pathway, MDH re-oxidises malate to OAA, which is then broken down to PEP and $CO_2$ by phosphoenolpyruvate carboxykinase (PEPCK). PEP regenerated from malate breakdown is subsequently converted to carbohydrate by gluconeogenesis (Fig. 1.1B; Christopher and Holtum, 1996; Holtum *et al.*, 2005; Dever *et al.*, 2015).

Stomatal closure functions as a $CO_2$ concentrating mechanism during malate breakdown by the CAM decarboxylases, but in many species stomata are not closed throughout the day, allowing substantial assimilation of $CO_2$ diffusing directly from the atmosphere (Dodd *et al.*, 2002). Three distinct diurnal phases (II, III and IV) were defined by C. B. Osmond (1978) in a widely-used nomenclature for the diel rhythm of $CO_2$ uptake in CAM, in addition to Phase I,

which describes the entire period of nocturnal carboxylation by PPC. In Phase II, at the beginning of the day, external $CO_2$ may be directly assimilated by concurrent PPC and Rubisco activity as the former is deactivated by dephosphorylation and the latter activated by carbamylation (Winter and Tenhunen, 1982; Borland and Griffiths, 1997; Maxwell *et al.*, 1999). Phase II ends with stomatal closure and the onset of Phase III, when $CO_2$ is primarily supplied to Rubisco by decarboxylation of malate. PEP resulting from the breakdown of malate may be converted by gluconeogenesis to hexose, and subsequently to starch and/or sugars for storage until the next Phase I (Holtum and Osmond, 1981). Phase IV arises when stomata open in the latter part of the day to permit direct fixation by Rubisco. PPC activity may also begin to increase during Phase IV (Griffiths *et al.*, 1990; Borland and Griffiths, 1997).

## 1.2 Evolutionary and ecological aspects of CAM

CAM species are found in at least 36 plant families and approximately 6-7% of vascular plant species (Winter and Smith, 1996; Borland *et al.*, 2009). The diversity and widespread phylogenetic distribution of CAM photosynthesis reveals that CAM has arisen many times independently by convergent evolution from multiple $C_3$ ancestors (Silvera *et al.*, 2010). For example, CAM is thought to have independently evolved ≥3 times in the Bromeliaceae (Crayn *et al.*, 2004) and ≥10 times in the Orchidaceae (Silvera *et al.*, 2009). Based on current understanding of CAM biochemistry, higher plant genomes encode all of the enzymes and many of the membrane-bound transport proteins necessary for CAM photosynthesis, and the evolution of CAM is thought to entail, at the level of individual genes, up-regulation of expression to accommodate increased metabolic flux and/or altered temporal control of expression to coordinate the phases of CAM (Cushman and Bohnert, 1997; Silvera *et al.*, 2010; Ming *et al.*,

2015; Brilhaus *et al.*, 2016; Abraham *et al.*, 2016). A study by Silvera *et al.* (2014) of the PPC isogenes of CAM and $C_3$ orchids has provided insight into the process of gene recruitment to CAM. Phylogenetic analysis of PPC transcript sequences showed that gene duplication of PPC may lead to neofunctionalisation of one paralog as the nocturnal carboxylase in the course of CAM evolution, while the other paralog remains a relatively low activity 'housekeeping' enzyme (Silvera *et al.*, 2014). Further examples of expanded enzyme gene families have been found from which 1-2 isoforms were recruited to CAM (e.g. NADP-ME, phosphoglucomutase); conversely, some genes participate in CAM but do not have additional non-CAM isoforms (e.g. PPDK; Cushman and Bohnert, 1997).

The most commonly identified adaptive benefit of CAM is resistance to drought stress by enhancement of water use efficiency (WUE), the molar ratio of photosynthetic $CO_2$ fixation to $H_2O$ transpired over a given period. Higher ambient temperature during the day increases the rate of transpiration from open stomata, and therefore partial or full stomatal closure during CAM Phase III reduces transpirational water loss and enhances WUE (Black, 1973; Smith and Lüttge, 1985; Lüttge, 2004). CAM commonly occurs in epiphytes, which may inhabit tropical forests with high annual rainfall, but which are vulnerable to short-term or seasonal water limitation (Griffiths and Smith, 1983; Winter *et al.*, 1983; Lüttge, 2004). CAM species are thought to comprise more than 50% of epiphytic species globally (Lüttge, 2004), and although $C_3$ species are far from excluded from epiphytic niches, a phylogenetic study of the Orchidaceae has suggested that evolution from $C_3$ to CAM photosynthesis aided terrestrial ancestors of CAM epiphytes in invading them (Silvera *et al.*, 2009). CAM has also been associated with evolutionary radiation into more arid habitats in terrestrial species (Lüttge, 2004). In the mainly terrestrial genus *Kalanchoë*, for example, it has been concluded that radiation from humid to arid

regions of Madagascar was associated with an increased contribution of nocturnal $CO_2$ assimilation to total photosynthesis (Kluge *et al.*, 1991*a*; Gehrig *et al.*, 2001; Lüttge, 2004). CAM evolution has been linked to adaptation to arid environments on geological time-scales. Horn *et al.* (2014) used a molecular phylogenetic analysis of the genus *Euphorbia* to deduce the most probable photosynthetic mode of the ancestral species of its current mixture of $C_3$, $C_4$ and CAM species. By adding molecular dating to their phylogeny, it was possible to approximate the dates of multiple evolutionary origins of CAM photosynthesis and rapid species diversification. Based on these results, convergent evolution of CAM, during a period of climate change when arid habitats were increasing in area, may have enabled dramatic evolutionary "bursts" of speciation in order to exploit recently-available niches (Horn *et al.*, 2014).

In stark contrast, CAM has also evolved to improve the photosynthetic efficiency of aquatic plants in habitats with low $CO_2$ availability, either because of competition from other photosynthetic organisms or low ambient $HCO_3^-$ concentrations due to low pH, and because in both cases $CO_2$ diffuses more slowly in water than air (Klavsen *et al.*, 2011). CAM permits aquatic plants to assimilate $CO_2$ at night when $C_3$ species cannot compete for it, and raise their internal $CO_2$ concentration so that Rubisco oxygenation and photorespiration are suppressed (Klavsen *et al.*, 2011; Pedersen *et al.*, 2011). While freshwater aquatic CAM species lack stomata (Klavsen *et al.*, 2011), stomatal closure during Phase III leads to accumulation of $O_2$ evolved from Photosystem II activity in internal air spaces, which may eliminate the possibility of suppression of photorespiration by elevated $CO_2$ concentration or limit the efficacy of such a mechanism in land CAM species (Lüttge, 2010).

In CAM, the stoichiometric ratios of both ATP and reducing equivalents consumed to $CO_2$ molecules assimilated is higher than in $C_3$ photosynthesis (Winter and Smith, 1996). A

number of $C_3$-CAM intermediate species and taxa have been identified that only switch from $C_3$ to CAM under certain environmental conditions, when the higher energetic cost of CAM may be compensated by an increased rate of survival and/or reproduction (Cushman and Borland, 2002; Herrera, 2009; Winter and Holtum, 2014). Induction of facultative CAM by drought has been identified in many species, and although it consistently coincided with decreased photosynthesis over the whole 24 h period (Winter *et al.*, 2008; Winter and Holtum, 2014), the adaptive benefit of the $C_3$-to-CAM transition may be to maintain low-level photosynthetic activity while stomata close to conserve water (Cushman and Borland, 2002; Herrera, 2009). The extent of facultative CAM can be limited to CAM-cycling or CAM-idling. In both of these modes of CAM, respiratory $CO_2$ is the only substrate available for nocturnal malate synthesis, but in the latter stomata are closed continuously and $CO_2$ is shuttled by CAM between malate and storage carbohydrates (Cushman and Borland, 2002; Borland *et al.*, 2011). While nocturnal malate synthesis cannot contribute to net $CO_2$ uptake in these species, scavenging of respiratory $CO_2$ may limit wastage of biomass, and mitigate oxidative damage by supplying $CO_2$ to Rubisco when stomata are closed during the day, and thus maintain the Calvin cycle as a sink for reducing equivalents from the photosynthetic electron transport chain (Griffiths *et al.*, 1989; Herrera, 2009). In many species studied, drought stress-induced facultative CAM was readily reversed by re-watering, and may provide relatively short-term or seasonal resistance to water stress (Winter *et al.*, 2008; Herrera, 2009; Winter and Holtum, 2014).

Plasticity of Phases I-IV and their respective contributions to total $CO_2$ assimilation has also been found in almost all species with non-facultative, developmentally-determined CAM, known as ‘constitutive’ or ‘obligate’ CAM (Dodd *et al.*, 2002; Lüttge, 2004). Some constitutive CAM species that are restricted to CAM cycling under well-watered conditions transition to full

CAM with net uptake of $CO_2$ at night when subjected to drought stress (Cushman and Borland, 2002). Short-term plasticity in the duration and rate of atmospheric $CO_2$ assimilation during Phases II-IV has been suggested as a means to ensure that the accumulation of storage carbohydrates during the day is sufficient to supply optimal rates of nocturnal carboxylation during the following night (Dodd *et al.*, 2002). Under experimental conditions that suppressed nocturnal PPC activity, Phase II and/or Phase IV were expanded during the following day and permitted CAM plants to rapidly recover the same total $CO_2$ assimilation over 24 h as control plants (Borland and Griffiths, 1997; Roberts *et al.*, 1997). Over longer periods, drought stress can accelerate the developmental induction of CAM (Winter *et al.*, 2008; Borland *et al.*, 2011). Some constitutive CAM plants have been found to transition to CAM idling under prolonged drought stress (Sipes and Ting, 1985; Lüttge, 2004).

Succulence is a morphological trait that is frequently associated with CAM. Typically, in succulent leaves mesophyll cells are large and uniformly sized, their vacuoles are large and occupy a very high proportion of the cell volume, and intercellular air spaces are narrow (Maxwell *et al.*, 1997; Lüttge, 2004). Large vacuolar volumes are adapted to store malate in CAM and to store water to increase tolerance to drought stress (Borland *et al.*, 2011). However, diffusion pathways from the atmosphere to the active sites of Rubisco and PPC in succulent tissues are tortuous, and the rate of conductance of $CO_2$ and $O_2$ is low (Maxwell *et al.*, 1997). Relatively low partial pressure ratios of $CO_2$ to $O_2$ in Phase IV are thought to limit the efficiency of direct uptake of atmospheric $CO_2$ by Rubisco, while retaining respiratory $CO_2$ in the mesophyll for re-fixation by PPC during Phase I (Cote *et al.*, 1989; Maxwell *et al.*, 1997; Rascher and Lüttge, 2002; Borland *et al.*, 2011). Surveys of CAM species have shown that "strong CAM", where the contribution of Phase I to the total 24 h $CO_2$ uptake is large relative to

Phases II-IV, is associated with succulence (Silvera *et al.*, 2005; Nelson and Sage, 2008). Succulence may therefore be incompatible with "weak CAM", in which only a small proportion of the total $CO_2$ fixed by Rubisco is derived from nocturnally-synthesised malate (Griffiths *et al.*, 2008; Borland *et al.*, 2011).

## 1.3 Prospects for genetic engineering of CAM and its applications to agriculture and biofuels

*Agave sisalana* (sisal), *Ananas comosus* (pineapple) and *Opuntia ficus-indica* (prickly pear) are examples of CAM species that are grown agriculturally, and CAM crops have been found to attain high biomass productivity in relatively dry climates (Borland *et al.*, 2009). Anthropogenic climate change has been projected to decrease water availability over a large proportion of the earth's surface by the end of the 21$^{st}$ century through a combination of decreased precipitation, increased soil evaporation and increased transpiration (Cook *et al.*, 2014). CAM species are therefore considered to be increasingly attractive for cultivation on so-called marginal and seasonally drought-prone lands that are unsuitable for $C_3$ or $C_4$ crops (Borland *et al.*, 2009). *Opuntia* have already been used on marginal lands around the Mediterranean basin as a drought-resistant emergency source of fodder for dairy herds and for erosion control, in addition to being an agricultural crop (Le Houérou, 1996).

CAM engineering, the genetic engineering of CAM photosynthesis into $C_3$ species, has been proposed as way to more fully exploit marginal lands for agricultural and biofuels production than the available CAM crops allow (Borland *et al.*, 2014; Yang *et al.*, 2015). In order to engineer CAM into target $C_3$ crop species, the minimal set of genes required for CAM photosynthesis and the transcriptional, translational and/or post-translational regulatory networks

that coordinate Phases I-IV must be established in existing CAM species. The underlying leaf and stem developmental mechanisms of mesophyll succulence, and the signalling mechanisms responsible for diurnal stomatal closure/nocturnal stomatal opening (von Caemmerer and Griffiths, 2009) must also be characterised (Borland *et al.*, 2014; Yang *et al.*, 2015). Species of the genus *Populus* are considered to be promising targets for genetic engineering as a CAM biofuel crop because they are relatively fast-growing, their leaf morphology has displayed variation between species and plasticity between individuals, and genomes of a number of species have already been sequenced and annotated (Borland *et al.*, 2014). An international project to explore the possibility of engineering CAM into *Populus* is currently in progress (http://cambiodesign.org/), with participation from the research group where this thesis was completed, the Hartwell group at the University of Liverpool (Hartwell et al., 2016).

Tractable model CAM species are required to achieve the detailed molecular-genetic, biochemical and physiological comprehension of CAM needed for its forward engineering into $C_3$ species (Borland *et al.*, 2009; Yang *et al.*, 2015; Hartwell *et al.*, 2016). Model CAM species have recently been developed within the genus *Kalanchoë*. *K. fedtschenkoi* and *K. laxiflora* are two closely-related, constitutive CAM species that have been used extensively by the Hartwell group as model species. The genomes of both species have been sequenced, assembled and annotated (Hartwell *et al.*, 2016), and made publicly available:

https://phytozome.jgi.doe.gov/pz/portal.html#

A broad range of enzyme, transporter and regulatory protein genes have been targeted by RNA interference (RNAi) in transgenic *K. fedtschenkoi* and *K. laxiflora* in order to deduce the minimal set of genes required to drive CAM in these species (Dever *et al.* 2015; Hartwell, Boxall, Dever, Kneřova & Kadu, unpublished results). The chief advantages of both species for CAM research

are the ease with which they can be clonally propagated via the adventitious plantlets that grow on their leaf margins, and the predictable developmental progression of their young leaves from $C_3$ to CAM, which has allowed comparative transcriptomics of *K. fedtschenkoi* in both photosynthetic modes (Hartwell *et al.*, 2016). Both species have proven amenable to *Agrobacterium*-mediated transformation with vectors for both target gene overexpression and RNAi gene silencing (Dever *et al.*, 2015; Hartwell *et al.*, 2016). However, *K. laxiflora* sets seed, whereas developing seed in *K. fedtschenkoi* fails to achieve dehydration tolerance in the final stages of seed maturation (Hartwell *et al.*, 2016). Thus, *K. laxiflora* is superior model species as it allows for genetic crossing and/or selfing of transgenic lines (Hartwell *et al.*, 2016).

## 1.4 Thesis overview by chapter

The protein transporters that mediate and control the diel flux of malate between the cytosol and vacuolar lumen, and vice versa, in CAM have not been identified at the molecular level. However, as stated above, it has been suggested previously that one or more ALMT family protein mediates the nocturnal import of malate to vacuoles, and that TDT mediates its diurnal export. This was based on reported functional data on both in $C_3$ species (Holtum *et al.*, 2005; Borland *et al.*, 2009), and Chapter 3 presents a detailed review of this data. Current molecular physiological models of vacuolar malate import/export in CAM-performing tissues are also reviewed, and the functional properties of vacuolar ALMTs and TDT that could have led them to be recruited to CAM during its evolution from $C_3$ photosynthesis are considered. Molecular phylogenetics of the *K. fedtschenkoi* ALMT (*KfALMT*) family and *ALMT*s of $C_3$ species was used to predict which of the former are targeted to the vacuolar membrane. Quantitative RNA sequencing (RNA-seq) datasets were used to associate individual *KfALMT*s with CAM photosynthesis by identifying genes that were highly expressed at the steady-state transcript level

in CAM-performing leaves relative to $C_3$-performing leaves, and in CAM leaf mesophyll relative to CAM leaf epidermis. Transgenic *K. fedtschenkoi* lines expressing an RNA interference (RNAi) construct designed to silence predicted CAM-associated vacuolar *KfALMT*s (*KfALMT* RNAi lines) were screened for suppression of CAM, and three independent lines were selected for further study. Multiple transgenic RNAi lines in which *KfTDT* was targeted for silencing were also screened for a CAM-suppressed phenotype, but none was identified. Phenotypic characterisation of a single *KfTDT* RNAi line confirmed that *KfTDT* transcript levels were markedly suppressed, and that CAM function was largely retained. However, increased citrate accumulation in CAM leaves of this line, relative to wild type, hints at a role for KfTDT in vacuolar citrate transport.

In Chapter 4, detailed phenotypic characterisation of the three independent *KfALMT* RNAi lines is reported. Transcriptional silencing of *KfALMT* was confirmed in each line, which displayed suppression of CAM photosynthesis at the levels of nocturnal $CO_2$ assimilation and malate accumulation. An *in vitro* assay of coupled $H^+$-malate transport activity was used on extracted tonoplast membranes of two of the *KfALMT* RNAi lines to show that the loss of KfALMT-mediated tonoplast malate permeability could plausibly have directly caused impairment of nocturnal vacuolar malate import in these lines. *KfALMT* loss-of-function also altered diurnal patterns of $CO_2$ gas exchange and carbohydrate metabolism. These results are discussed in the context of the existing understanding of the differential control of PPC- and Rubisco-mediated atmospheric $CO_2$ fixation over the diel CAM cycle, and of partitioning of fixed carbon between CAM and non-CAM pathways, both topics introduced above (Section 1.1). Differences were observed between a single *KfALMT* RNAi line and wild type in terms of *PPCK*

transcription and activity over the diel CAM cycle, and their possible implications for feedback control of PPCK and PPC activity are discussed.

PPCK activity and $CO_2$ gas exchange are controlled in CAM species by one or more circadian oscillators, and these mechanisms of control have previously been isolated from those responding to environmental factors by placing *Kalanchoë* in constant conditions, also known as free-running conditions, for extended periods (Nimmo *et al.*, 1987; Wilkins, 1992; Dever *et al.*, 2015). In Chapter 5, the current understanding of CAM-specific circadian rhythms and the non-CAM specific circadian oscillator, also known as the core circadian clock, is reviewed. Previously reported evidence that CAM circadian rhythms have evolved from the core circadian clock of $C_3$ ancestors as part of the overall process of CAM evolution is also discussed. Circadian rhythms of $CO_2$ gas exchange and *KfPPCK* expression that occurred in wild type *K. fedtschenkoi* were found to be altered in a severely CAM-suppressed *KfALMT* RNAi line, 23A. Free-running rhythms in steady-state transcript levels of two core circadian clock genes were also altered in *KfALMT* RNAi 23A, suggesting retrograde signalling from CAM to the core circadian clock, which would be consistent with previous observations (Dever *et al.*, 2015). Possible inferences about the interface between the CAM pathway and the core circadian clock, based on the phenotypic data on the *KfALMT* RNAi lines presented in Chapters 4 and 5, are discussed.

Nocturnal MDH activity is required in all CAM species to convert OAA formed by PPC-catalysed $CO_2$ fixation to malate for subsequent vacuolar storage. However, plants possess several MDH isoforms with distinct sub-cellular localisation and/or cofactor (NAD/NADP) specificity (Gietl, 1992; Scheibe, 2004), and their individual roles in CAM has yet to be comprehensively determined. In Chapter 6, four *K. fedtschenkoi* MDH isogenes were suggested to be CAM-associated due to their increased transcript levels in CAM-performing tissues,

according to the aforementioned quantitative RNA-seq data. Phylogenetic analysis of predicted *KfMDH*s revealed that this subset comprised a cytosolic NAD-MDH (CMDH), a plastidic NAD-MDH (PdMDH), a chloroplastic NADP-MDH (NADP-MDH) and a peroxisomal NAD-MDH (PxMDH). Hairpin RNA constructs were designed to specifically target the *K. laxiflora* orthologs of each of these isogenes for silencing by RNAi, and stable transgenic lines expressing each construct were generated. For each of these genes, at least one line was identified with marked suppression of transcript levels relative to wild type controls. Some indication of CAM suppression was found in both *KlPdMDH* RNAi and *KlCMDH* RNAi lines, and the possibility of synergy between PdMDH and CMDH during CAM Phase I is discussed.

# Chapter 2 - Materials and methods

## 2.1 Plant material

### 2.1.1 Propagation of plant material

Both *Kalanchoë fedtschenkoi* and *Kalanchoë laxiflora* were propagated clonally from adventitious plantlets. *K. fedtschenkoi* plantlets were grown in Sinclair Potting Growth Medium (William Sinclair Horticulture) with added Perlite (William Sinclair Horticulture), for improved aeration, and Osmocote Exact slow-release fertiliser applied at the manufacturer's recommended dose rate for long-lived perennials. *K. laxiflora* plantlets were grown in this mixture combined with John Innes No.2 compost (J. Arthur Bowers) in a 2:1 ratio to improve drainage. Plantlets were grown in a small volume of compost mix in the plug pots of Aracon trays (Arasystem) for approximately 6 weeks before being re-potted in groups of 3 individual plants into 13 x 13 x 13 cm square black plastic pots. Cuttings were grown in the same growth medium as plantlets of the same species. For tonoplast extraction experiments, three individual plants were grown in round pots 18 cm in height and 20 cm in diameter.

Plants were grown in a roof-top greenhouse in Liverpool, UK. A 16 h light period was maintained by supplementary lighting from computer-controlled high-pressure sodium lamps that provided high-intensity artificial light and that switched on below a certain external light level in order to maintain a light-period minimum light intensity of approximately 250 $\mu mol\ m^2\ s^{-1}$. Day-length in Liverpool varies over the year from 7 h 30 mins of daylight on the shortest day of the year (December 21$^{st}$) to 17 h of daylight on the longest day of the year (June 21$^{st}$). Therefore, in winter, at least half of the daily 16 h light period was supplied by the supplementary lamps. On dull winter days, the supplementary lights were kept on throughout the 16 h light period. Conversely, on bright, sunny summer days when the natural day length

exceeded the 16 h photoperiod setting of the greenhouse, the supplementary lights could have potentially never switched on.

### 2.1.2 Time course experiments under light/dark cycles (12:12 LD); and constant light, constant temperature, constant humidity, circadian free-running (LL) conditions

Snijders Microclima MC-1000 plant growth cabinets (Snijders Labs) were used to standardise photoperiod, light intensity and quality, temperature, and humidity for time course experiments, gas exchange measurements using the infra-red gas analyser (IRGA) system, and tonoplast extraction experiments. Plants that had been previously grown in a rooftop glasshouse were transferred to 12:12 light-dark (12:12 LD) conditions. These comprised 12 h light at ~500 µmol $m^{-2}$ $s^{-1}$, 25 ˚C, 60% humidity; and 12 h dark, 15 ˚C, 70% humidity. Plants were entrained under 12:12 LD for 7-8 cycles before the start of measurements or sample collection. For constant light (LL) time course experiments, conditions were subsequently switched at the end of the dark period to constant conditions of ~100 µmol $m^{-2}$ $s^{-1}$ light, 15 ˚C, 70% humidity.

### 2.1.3 Collection, preparation and storage of frozen leaf tissue for assays

Leaves were picked and immediately snap-frozen in liquid nitrogen. Leaf tissue was stored at -80 ˚C until use. Leaves were ground in liquid nitrogen to a homogenous powder the approximate consistency of icing sugar using a pestle and mortar pre-chilled in liquid nitrogen. The ground leaf tissue was stored at -80 ˚C.

### 2.1.4 Plant growth and productivity experiments

7-10 replicates of each genotype were grown side-by-side from adventitious plantlets in individual 11 x 11 x 12 cm pots. Growth conditions were otherwise identical to those of plants used for other experiments. Plants were grown for 91 d between 22.4.2016 and 23.7.2016. The positions of the plants on the bench were randomised at two- to three-week intervals to reduce positional or edge effects on growth.

Plants were cut down to the roots to harvest above-ground biomass. Plant material was placed in lightweight paper bags, stapled shut and weighed. Plant material was oven dried for three weeks with monitoring of sample weight every 2-4 days. Plant material was considered dry when the weight remained consistent across measurements on 3 consecutive days. Staples were removed and the dried material and paper bag were weighed together to account for seepage of sap into the bag in some replicates. Dry mass was calculated by subtracting the mean weight of the paper bags.

## 2.2 RNA interference (RNAi) in transgenic *K. laxiflora* and *K. fedtschenkoi*

### 2.2.1 Design and cloning of the RNAi binary constructs for the family of candidate CAM malate dehydrogenase (MDH) genes from tetraploid *K. laxiflora*

The available genomic and transcriptomic resources (described in full below, Section 2.9.1) were used to predict the sequences of mature transcripts encoding various *K. laxiflora* malate dehydrogenase (MDH) isogenes. These predicted cDNA sequences were used to design primers for amplification of DNA gene-specific fragments for cloning into the binary RNAi vector pK7GWIWG2(I) (Karimi *et al.*, 2002).

An EST of the *K. fedtschenkoi* ortholog of the desired *K. laxiflora* MDH isogene was used as a query sequence for a BLASTN search of the *K. laxiflora* genomic sequence scaffolds.

The highest-scoring match of this search was used for gene-specific primer design. This match consisted of at least one high-scoring pair (HSP) representing high-identity sequence alignments between exons in the *K. fedtschenkoi* gene and exons in sequences of the orthologous *K. laxiflora* genes. The HSPs typically covered the full *K. fedtschenkoi* sequence (except the far 5' and 3' ends). Exons of the *K. laxiflora* ortholog that were predicted based on the mature transcript sequence from *K. fedtschenkoi* were merged *in silico* to generate a predicted open reading frame (ORF) for each *K. laxiflora* MDH ortholog. As *K. laxiflora* is likely to be an allotetraploid, its genome possesses two copies of every gene identified in the *K. fedtschenkoi* diploid genome. In all cloning work, the *K. laxiflora* gene with the highest pairwise identity, relative to its *K. fedtschenkoi* ortholog, was selected for primer design and cloning. The second gene copy had such high pairwise identity that it was predicted that a single RNAi construct designed specifically to target one gene copy would in fact silence both copies of that particular gene family member.

An online interface for Primer3Plus (http://www.bioinformatics.nl/cgi-bin/primer3plus/primer3plus.cgi/; Untergasser *et al.*, 2007) was used to design primers for PCR amplification of a gene-specific fragment for insertion into a binary RNAi vector suitable for *Agrobacterium tumefaciens*-mediated transformation of *K. laxiflora*. Primer pairs were designed to amplify a gene-specific fragment with its length in the 250-400 bp range (Table 2.1). A CACC sequence was added to the 5' end of each forward primer in order to facilitate directional TOPO-cloning with the p-ENTR/D blunt-end TOPO cloning system (Thermo Fisher).

Table 2.1 – Primers used for cloning of MDH genes

| Gene | Cytosolic NAD-MDH 1 (*KlCMDH1*) | Peroxisomal NAD-MDH 1 (*KlPxMDH1*) | Chloroplastic NADP-MDH (*KlNADP-MDH*) | Plastidic NAD-MDH 1 (*KlPdMDH1*) |
|---|---|---|---|---|
| *A. thaliana* ortholog | AT1G04410 | AT5G09660 | AT5G58330 | AT3G47520 |
| *K. laxiflora* predicted transcript number | Kalax.0075s0049.1/ Kalax.0094s0014.1 | Kalax.0405s0018.1/ Kalax.0061s.0014.1 | Kalax.0100s0048.1/ Kalax.0131s0010.1 | Kalax.0520s0005.1/ Kalax.0326s0011.1 |
| Forward primer | 5′CACCTATCAT GCTAGGCCCTGA CC3′ | 5′CACCCAGAAGTGT GACATACAAC3′ | 5′CACCACCAGG TCCCAGACTTTC T3′ | 5′CACCTGCAAC TGGAGAGCTGAC TG3′ |
| Reverse primer | 5′TTCTTAGCAGGGA TCGATGG3′ | 5′ACAGAACTCCCAT ACTTC3′ | 5′TAGACCTGCACGG CATACTG3′ | 5′CTCTCTCCATGGC GTATGGT3′ |
| Base pairs in fragment | 372 | 316 | 298 | 381 |
| Topology of fragment with respect to ORF | exon-to-exon | exon-to-3’ UTR | exon-to-exon | exon-to-3’ UTR |

### 2.2.2 Agarose gel electrophoresis for visualisation of PCR products

1% (w/v) agarose was mixed with 1X TAE buffer (40 mM Tris-acetic acid, pH 8.5; 1 mM ethylenediaminetetraacetic acid (EDTA)), and dissolved by heating the mixture in a microwave. The molten gel was mixed with 0.1 mg/L ethidium bromide and poured into a horizontal gel tray with a suitable comb to create the loading wells and allowed to set by cooling to room temperature. Samples were loaded alongside a pre-stained DNA ladder (Hyperladder 1 kb or Hyperladder 100 bp, Bioline) to allow estimation of the approximate DNA length of the amplified PCR products. Horizontal agarose gel electrophoresis was run at 100 mV in 1X TAE buffer with 0.1 mg/mL ethidium bromide. Following DNA migration, ethidium bromide-stained PCR products and DNA ladder standards were visualised and photographed using a UV light box fitted with a digital camera (Syngene UGenius gel documentation system).

### 2.2.3 PCR amplification of gene-specific fragments

Gene-specific fragments for *K. laxiflora* MDH genes were amplified from a *K. laxiflora* cDNA pool (see below, Section 2.4.4) by polymerase chain reaction (PCR) using a high-fidelity, hot-start DNA polymerase (KOD, Merck Millipore) and the gene-specific primers (Table 2.1) under the following PCR thermal cycling conditions:

| Step | Time (seconds) | Temp (°C) | Repetitions |
|---|---|---|---|
| KOD activation/Denaturation | 120 | 95 | 1 |
| Denaturation | 20 | 95 | 33 |
| Primer annealing | 10 | 55-56 | |
| Elongation | 40 | 72 | |
| Final Elongation | 300 | 72 | 1 |

Primer oligonucleotides were synthesised by Integrated DNA Technologies (Leuven, Belgium) and used at a final concentration of 1 µM. PCR products were purified using a QIAquick PCR Purification Kit (Qiagen) to final concentrations of 10-22 ng/µL. 1 µL of PCR product was analysed by agarose gel electrophoresis. Primers for *KlPdMDH1*, *KlPxMDH1* and *KlNADP-MDH* yielded a single gel band of the appropriate size using an annealing temperature of 55 ˚C. Directly-isolated PCR product, generated with the Qiagen PCR clean-up kit used according to the manufacturer's instructions, was therefore used directly for cloning. Primers for *KlCMDH1* yielded an additional PCR product that was longer than predicted from the genome sequence. The band intensity, and therefore the desired PCR product yield, for the expected smaller PCR product was increased by increasing the PCR primer annealing temperature to 56 ˚C and increasing the $MgCl_2$ concentration in the PCR mixture from 1.5 mM to 2 mM. The lower molecular weight band was excised from the horizontal agarose gel, and the amplified gene

fragment for *KlCMDH1* was purified using a QIAquick Gel Extraction Kit (Qiagen) according to the manufacturer's instructions.

### 2.2.4 Entry vector cloning

PCR amplified gene fragments were cloned into the pENTR/D Gateway-compatible entry vector plasmid using a pENTR/D Directional TOPO Cloning Kit (Thermo Fisher). In the cloning reaction, the quantities of reagents used were half those specified in the protocol. 10 ng of each cleaned-up PCR product was used in the cloning reaction. Competent *Escherichia coli* TOP10 cells provided with the pENTR/D TOPO Cloning Kit were transformed by heat shock-mediated transformation with the completed pENTR/D TOPO cloning reactions, and incubated in nutrient rich SOC medium for 1 h at 37˚C. The suspension of transformed cells was then spread onto LB agar plates containing 50 mg/L Kanamycin to select for the Kanamycin resistance gene present in the pENTR/D plasmid. LB-agar plates were incubated overnight at 37˚C to allow colonies to grow and develop.

Colonies were analysed by a diagnostic "colony PCR" reaction using a 10 µl reaction volume with BioMix Red ready-mixed DNA polymerase and dNTPs (Bioline), 1 µM M13F vector backbone-specific primer (5' CACGACGTTGTAAAACGACGGCCAG 3') and 1 µM gene-specific reverse primer (see Table 2.1). The following PCR conditions were used:

| Step | Time (seconds) | Temp (°C) | Repetitions |
|---|---|---|---|
| Denaturation | 60 | 90 | 35 |
| Primer annealing | 30 | 55 | |
| Elongation | 60 | 72 | |
| Final Elongation | 360 | 72 | 1 |

The completed reactions were loaded onto 1% agarose gels in 1X TAE and analysed by electrophoresis as described above. Colonies corresponding to bands of appropriate size (the expected gene fragment length plus 159 bp due to the position of the M13F primer site in the pENTR/D vector) were picked into 10 mL sterile liquid LB medium with 50 mg/L Kanamycin, and grown overnight at 37 °C on a shaker. Plasmids were purified from the cultures using a plasmid miniprep kit according to the manufacturer's instructions (Qiaprep Spin Miniprep kit, Qiagen), and quantified using a NanoDrop spectrophotometer (Thermo Scientific). Diagnostic PCR was repeated using 1 µL of prepared plasmid DNA with the number of PCR cycles reduced to 27. Where diagnostic PCR revealed bands of the correct size, plasmids were sequenced commercially using Sanger dideoxy sequencing in order to confirm correct insertion of the desired gene fragment (LIGHTRUN, GATC Biotech).

### 2.2.5 Cloning of RNAi destination vectors

Gene-specific fragments for *K. laxiflora* MDH genes were sub-cloned into pK7GWIWG2(I), a binary GATEWAY RNAi destination vector that contains two pairs of *attR* sequences providing a pair of acceptor sites complimentary to *attL* sequences in the entry vector, and Streptomycin- and Spectinomycin-resistance genes for selection in *E. coli* and *A. tumefaciens* (Karimi *et al.*, 2002). Half reactions of an LR clonase kit (GATEWAY LR Clonase II enzyme mix, Thermo Fisher Scientific) were mixed (50 ng of entry vector and 75 ng binary destination vector, plus 1.9 U Topoisomerase II (Thermo Fisher) to relax supercoiling in the vectors) and left at room temperature for 1 h. The reaction was stopped by incubation for 10 minutes at 37 °C with 0.5 µL Proteinase K (included with the LR Clonase kit).

Competent *E. coli* (SoloPack Gold, Agilent) were transformed by heat shock treatment following mixing of the ice-defrosted competent cells with 2.4 µL of each LR clonase reaction

volume. The transformed cells were then incubated in SOC medium at 37 °C, spread on LB Agar plates containing 300 mg/L Streptomycin and 100 mg/L Spectinomycin, and incubated overnight at 37 °C. Colonies were screened by quadruple diagnostic PCR (Table 2.2), where the correct subcloning of the gene-specific fragment into the two acceptor sites in pK7GWIWG2(I) was diagnosed by single bands in each reaction of approximately equal size. The same PCR programme as in diagnostic PCR of entry vector transformants was used.

Table 2.2 – Primers used in quadruple diagnostic PCR to confirm/refute correct binary destination vector assembly

| | Primer 1 | Primer 1 sequence | Primer 2 |
|---|---|---|---|
| 1 | T35S | 5′TCTGGGAACTACTCACACATTCTG3′ | Gene-specific reverse |
| 2 | DV intron, -ve | 5′GAGTATGAAACCTTACCTCATCATTTC3′ | Gene-specific forward |
| 3 | DV intron, +ve | 5′TTTAACGTGTTTGCAGGTCAGCTTG3′ | Gene-specific forward |
| 4 | P35S | 5′CTGCAGGACGATCCGTATTTTTACA3′ | Gene-specific reverse |

When the diagnostic PCR predicted correct sub-cloning of the destination vector, colonies were picked into 10 mL LB medium containing 300 mg/L Streptomycin and 100 mg/L Spectinomycin, and grown overnight at 37°C. Destination vector plasmids were isolated from the 10 mL overnight liquid cultures using the Qiagen plasmid miniprep kit, and the isolated plasmids were re-checked by the aforementioned diagnostic PCR reactions. As in entry vector cloning, destination vector plasmids were sequenced to confirm correctly-oriented sub-cloning of the gene-specific fragment in both acceptor sites, allowing confirmation that the desired gene specific fragment was correctly cloned into the binary vector in both the sense and antisense orientations, with the intron in between.

### 2.2.6 Transformation of *Agrobacterium tumefaciens*

Competent cells of *Agrobacterium tumefaciens* (strain GV3101) were transformed with 1 µg of each assembled binary destination vector (pK7GWIWG2(I)) by freeze-thaw shock (as described in Dever *et al*., 2015). The destination vector and 100 µL GV3101 competent cells suspension ($OD_{600}$ = 0.1) were mixed and incubated on ice for 15 minutes, snap-frozen in liquid nitrogen and thawed in a water bath at 37 °C for 5 mins. The suspension of transformed GV3101 cells was then mixed with 1 mL sterile SOC medium (New England Biolabs) and incubated at 28 °C for 2-4 h to allow expression of antibiotic resistance genes. Cells were pelleted by centrifugation at maximum speed in a benchtop microcentrifuge for 30 s, re-suspended in 100 µL fresh SOC, and spread on LB agar plates containing 10 mg/L Rifampicin, 25 mg/L Gentamycin, 300 mg/L Streptomycin and 100 mg/L Spectinomycin. GV3101 is resistant to Rifampicin and Gentamycin due to chromosomal and helper plasmid resistance genes present in the untransformed strain. Plates were incubated for 2 d at 28 ˚C. Colonies were analysed using the same diagnostic colony PCR reactions described in Section 2.2.5.

### 2.2.7 Preparation of sterile *K. laxiflora* explants for stable transformation

*K. laxiflora* seed was sterilised by immersion in 70% ethanol for 3 mins. The seed was washed 5 times in sterile deionised water and suspended in sterile 0.2 % Phytoagar. The seed was pipetted onto sterile half-strength MS30 growth medium (Murashige and Skoog medium with Gamborg B5 vitamins, plus 3% added sucrose at full strength, pH 5.8), solidified by addition of 8% (w/v) Phytoagar. Seedlings were germinated and grown under long-day conditions (16 h at 100 µmol $m^{-2}$ $s^{-1}$ light and 8 h dark, constant 20 ˚C temperature) for 4-6 weeks prior to use for the generation of explants for stable transformation with *A. tumefaciens*.

### 2.2.8 Transformation of tissue culture-grown *K. laxiflora* seedling explants

Successfully-transformed colonies produced as described in Section 2.2.6 were picked into 10 mL of LB with 10 mg/L Rifampicin, 25 mg/L Gentamycin, 300 mg/L Streptomycin and 100 mg/L Spectinomycin, and incubated overnight at 28 °C. The LB liquid culture was then centrifuged at 3,600 *g* for 10 mins, and the *Agrobacterium* cell pellet was re-suspended in 10 mL sterile MS30. The culture was further diluted in the same medium to give a final optical absorbance at 600 nm of 0.1 over a 1 cm path length. Acetosyringone was added to the cultures to a final concentration of 0.1 mM, and the cultures were then incubated at room temperature for ~3 h to allow for acetosyringone to activate the *vir* genes required for T-DNA transfer.

Leaves of the sterile *in vitro* propagated K. laxiflora seedlings were sliced with a sterile scalpel into ~2 mm explants under sterile conditions in a pre-sterilised laminar flow bench. The GV3101 culture carrying the specific, desired RNAi construct was poured over the explants in a sterile petri dish, and incubated for 1 h at room temperature with regular gentle agitation to mix the seedling tissue explants with the GV3101 culture. The explants were blotted dry on filter paper and transferred to sterile MS30 with 1 mg/L thidiazuron (TDZ), 0.2 mg/L indole-3-acetic acid (IAA) and 0.1 mM acetosyringone, solidified by addition of 8% (w/v) Phytoagar without any antibiotic selection. The explants were then kept in a growth room for 3 days (growth conditions as described in Section 2.2.7).

### 2.2.9 Generation of stable transgenic plants by tissue culture

Explants were transferred to sterile callus induction medium (CIM: MS30 with 1 mg/L TDZ, 0.2 mg/L IAA, 100 mg/L Kanamycin and 200 mg/L Carbenicillin, solidified with 8% (w/v) Phytoagar) and kept in this growth medium until explants had either grown prominent calluses or died off. Explants were then transferred to sterile shoot induction medium (SIM: MS30 with 1

mg/L 6-benzylaminopurine (BAP), 0.2 mg/L IAA, 100 mg/L Kanamycin and 200 mg/L Carbenicillin, solidified with 8% (w/v) Phytoagar) until the calluses developed shoot primordia. During the CIM and SIM stages, explants were kept in a growth room (conditions as described in Section 2.2.7), and transferred to fresh media every 3-4 weeks to prevent drying-out or over-growth by the *Agrobacterium*.

Explants were subsequently transferred to sterile root induction medium (RIM: MS30 with 100 mg/L Kanamycin and 200 mg/L Carbenicillin, solidified with 8% (w/v) Phytoagar), and shoots were left in a growth room to develop viable roots. The newly formed plantlets were removed from the Phytoagar, washed and planted out as described in Section 2.1.1.

### 2.2.10 Generation of *K. fedtschenkoi KfALMT* RNAi and *KfTDT* RNAi transgenics

*KfALMT* RNAi and *KfTDT* RNAi mutants were produced in the Hartwell lab by J. Kneřova prior to the beginning of this PhD project. A broadly similar method was used for transformation of wild-type *K. fedtschenkoi* as that described above for transformation of *K. laxiflora* and this method has been published previously (Dever *et al.*, 2015). An earlier assembly of the *K. fedtschenkoi* RNA-seq data set (described below, Section 2.9.1) was used to design primers to amplify gene-specific fragments of *KfALMT* and *KfTDT* (Table 2.3). Gene-specific fragments were amplified by PCR from a *K. fedtschenkoi* cDNA pool, and cloned and subcloned into entry and destination vectors as described above.

Table 2.3 – Primers used for amplifying gene-specific fragments

| Gene | Aluminium-activated malate transporter | Tonoplast malate transporter |
|---|---|---|
| Symbol | *KfALMT* | *KfTDT* |
| Closest *A. thaliana* ortholog | AT1G68600 | AT5G47560 |
| *K. laxiflora* annotation reference | Kaladp0024s0194.1, Kaladp0073s0021.1 | Kaladp0042s0251.1 |
| Primers | 5′TGGAAACTCTGAGCATGTGGTGGAG3′<br><br>5′GCCCCAGCTCTGAATACCCTTTCCTT3′ | 5′ACCGCGTTCGTCAGCATGTGGATG3′<br><br>5′TGGCAGTGCCATCACCAACTCGACCGTC3′ |
| Base pairs in fragment | 225 | 662 |
| Topology of fragment with respect to ORF | 5’ UTR-to-exon | exon-to-exon |

## 2.3 Leaf metabolite measurement

In all of the colorimetric metabolite measurements, assay volumes were mixed in flat-bottomed, 96-well plates with a well volume of 382 µL (Greiner Bio One). Assays were conducted using a plate reader (Multiskan GO, Thermo Scientific) to mix, incubate and measure the absorbance of samples. The plate reader had a ‘shake’ function that, unless otherwise indicated, was used to mix the assay components (buffer, sample and activating enzyme), and its temperature control was set to 30 °C. Absorbance measurements were corrected to a pathlength of 1 cm using a built-in pathlength correction function. For each sample, three replicate assays were conducted in adjacent wells, with a fourth blank well to which no activating enzyme was added, and of which absorbance measurements were taken and subtracted from concurrent absorbance measurements of the other three wells. The mean of the three replicates was taken as the final result.

### 2.3.1 Extraction of soluble metabolites from leaf tissue

Pre-ground, frozen leaf tissue (450-600 mg) was weighed into a 15 mL Falcon tube that had been pre-chilled in liquid nitrogen. 4 mL of 80% (v/v) methanol was added and agitated with a bench-top vortex to fully suspend the ground tissue. Samples were incubated at 80 °C for 1 h in a water bath, with frequent inversion of tubes to keep insoluble material in suspension. Samples were centrifuged at 3,600 *g* for 10 mins and the methanol extract removed with a Pasteur pipette. The suspension, heating and centrifugation steps were repeated using 2 mL and then 1 mL of 80% methanol. Insoluble material pelleted in the final centrifugation was retained for starch assay (see below, Section 2.3.4). The pooled extracts were dried down in a vacuum concentrator at 45 °C to a minimal liquid volume before dilution in 0.5 mL of 0.2 M Bicine-HCl, pH 7.8. Alternatively, for the results reported in Chapter 3, 1 mL Bicine-HCl was used. Extracts were stored at -20 °C.

### 2.3.2 Malate

Malate was measured by a colorimetric assay based on the absorption at 340 nm ($A_{340}$) of reduced nicotinamide adenine dinucleotide (NADH) produced by oxidation of malate, catalysed by malate dehydrogenase (MDH), coupled with transamination of the resultant oxaloacetate, catalysed by glutamate-oxaloacetate transaminase (GOT) (Möllering, 1974).

Metabolite extracts were diluted with deionised water by a factor of 20-100, with the factor of dilution chosen to give a measurable absorption at 340 nm without saturation of the assay. 10 µL of diluted extract was added to 190 µL of malate assay medium (77 mM 3-amino-1-propanol buffered with HCl to pH 10.0; 50 mM L-glutamate-NaOH, pH 10.0; 2 mM β-nicotinamide adenine dinucleotide (β-NAD); 2.5 U GOT (ammonium sulphate solution, Megazyme)).

Extract and buffer were mixed by shaking for 20 s and initial $A_{340}$ was measured. 1 µL ammonium sulphate solution containing 15 U MDH (Megazyme) was added to each well and mixed by shaking for 20 s. The reaction was left to reach equilibrium, where $A_{340}$ was constant, before measuring final $A_{340}$.

The final malate concentration (M) in moles per gram fresh weight was calculated by the formula:

$$M = (A_{340,final} - A_{340,initial}) \cdot \frac{1}{\varepsilon} \cdot w \cdot d \cdot \frac{t}{a} \cdot \frac{1}{m}$$

where $\varepsilon$ = 6,220 $mol^{-1}$ $cm^{-1}$, the extinction coefficient of NADH at 340 nm; $w$ = 2 x $10^{-4}$, the volume in each well in $dm^3$; $d$ is the factor by which the original extract was diluted; $t$ is the total volume of extract in µL; $a$ = 10, the volume of diluted sample added to each well in µL; and $m$ is the mass of powdered tissue extracted in grams.

### 2.3.3 Citrate

Citrate was measured using citrate lyase (CL) to catalyse conversion of citrate to oxaloacetate, coupled with reduction of oxaloacetate and oxidation of NADH, catalysed by MDH, decreasing $A_{340}$ of NADH. Lactate dehydrogenase (LDH) was also added to account for oxaloacetate converted to pyruvate by spontaneous decarboxylation (Möllering, 1985).

Samples of soluble metabolite extract were diluted with deionised water by factors of 2-5 to give a measurable change in $A_{340}$ without saturating the assay. 10 µL of diluted sample was added to 190 µL citric acid assay medium (160 mM Tricine-NaOH, pH 7.8; 0.19 mM $ZnCl_2$; 0.32 mM NADH; 3.8 U/mL MDH, as in Section 2.3.2; 8.8 U/mL LDH (Sigma-Aldritch)) and

mixed by shaking for 20 s. $A_{340}$ was monitored for 2 mins to ensure any pyruvate or oxaloacetate in the sample had reacted and $A_{340}$ was then measured as an initial value. 0.05 U CL (lyophilised powder, Sigma) dissolved in 1 µL assay medium was added. The reaction was allowed to incubate to reach equilibrium before final $A_{340}$ was measured.

Citric acid concentration (C) in moles per gram fresh weight was determined by the following formula:

$$C = -(A_{340,final} - A_{340,initial}) \cdot \frac{1}{\varepsilon} \cdot w \cdot d \cdot \frac{t}{s} \cdot \frac{1}{m}$$

where $\varepsilon$ = 6,220 $mol^{-1}$ $cm^{-1}$, the extinction coefficient of NADH; $w$ is 2 x $10^{-4}$, the volume of assay medium in $dm^3$; $d$ is the dilution factor; $t$ is the total volume of extract in µL; $s$ is the volume of sample used, 10 µL; and $m$ is the original mass of tissue extracted in grams.

### 2.3.4 Leaf starch content determination

The level of insoluble starch was assayed indirectly by converting it to soluble glucose through enzymatic digestion (Smith and Zeeman, 2006). Starch-derived glucose was measured by a colorimetric assay in which phosphorylation and oxidation of glucose catalysed by, respectively, hexokinase (HK) and glucose-6-phosphate dehydrogenase (G6PDH) was coupled to reduction of nicotinamide adenine dinucleotide phosphate (NADP) to NADPH by the latter enzyme (Smith and Zeeman, 2006). Like NADH (Section 2.3.2), NADPH concentration can be quantified by $A_{340}$ (Smith and Zeeman, 2006).

Insoluble material pelleted during soluble metabolite extraction was heated at 80 °C for 5-10 mins to evaporate any remaining methanol. The insoluble material was re-ground to a

smooth homogenate in de-ionised water using a pestle and mortar. The homogenate was made up to a total volume of 5 mL with de-ionised water in a 15 mL Falcon tube. Tubes were agitated for >10 s with a bench-top vortex to completely suspend solid material before 0.5 mL aliquots were pipetted into two 1.5 mL screw-capped tubes. The aliquots were heated to 100 °C for 10 mins to gelatinise starch granules, then left to cool on the bench. 0.5 mL 0.2M sodium acetate-acetic acid (pH 5.5) buffer was added to each aliquot. >2U α-amylase (Sigma), as a lyophilised powder dissolved in sodium acetate-acetic acid buffer, and 6U amyloglucosidase in ammonium sulphate solution (Megazyme) were added to one tube, with the second retained as a control. Aliquots were incubated overnight at 37 °C on a shaker in order to digest the starch into free glucose units. Tubes were centrifuged at maximum speed in a bench-top microcentrifuge for 5 mins to pellet insoluble material, and the supernatant was then removed for assay.

10 µL of starch digest was added to 190 µL starch assay medium (9.6 mM imidazole-NaOH, pH 6.9; 4.8 mM $MgCl_2$; 1 mM ATP; 2 mM NADP). Supernatant and medium were mixed by shaking for 20 s and an initial measurement of $A_{340}$ was taken. 1 µL ammonium sulphate solution containing 0.42U HK and 0.21U G6PDH (Megazyme) was added, and mixed by shaking for 20 s. $A_{340}$ was monitored as the reaction proceeded to equilibrium and a final reading of $A_{340}$ was taken.

Glucose concentration (G) in moles per gram fresh tissue was determined using the following formula:

$$G = (A_{340,final} - A_{340,initial}) \cdot \frac{1}{\varepsilon} \cdot W \cdot \frac{t \cdot d}{s \cdot a} \cdot \frac{1}{m}$$

where $\varepsilon$ = 6,220 $mol^{-1}$ $cm^{-1}$, the extinction coefficient of NADPH at 340 nm; $w = 2 \times 10^{-4}$, the volume of assay medium each well in $dm^3$; $t$ = 5000, the total volume of re-ground homogenate in µL; $d$ = 1000, the total volume of each digestion reaction in µL; $s$ = 10, the volume of starch digest added to the well in µL; $a$ = 500, the volume of homogenate added to each digestion reaction in µL; $m$ is the mass of ground leaf tissue used originally for soluble metabolite extraction in grams.

### 2.3.5 Glucose, fructose and sucrose

Leaf glucose, fructose and sucrose were assayed sequentially by adding enzymes to convert them one-by-one into substrates for G6PDH, producing a change in absorbance signal at $A_{340}$, as in the starch assays (Section 2.3.4).

5-25 µL soluble metabolite extract was added to sugar assay medium (96 mM imidazole-NaOH, pH 7.8; 4.8 mM $MgCl_2$; 1mM ATP; 2 mM NADP) to give a total volume of 1 mL, mixed, and four 200 µL aliquots were used for the assay. Glucose was assayed as for the determination of starch-derived glucose (Section 2.3.4) and the final measurement of $A_{340}$ was taken as the initial value for assaying fructose. Fructose was assayed by measuring the increase in $A_{340}$ following addition of 1 µL of 4.5 U/µL phosphoglucoisomerase (PGI) in ammonium sulphate solution (Sigma) diluted 2:3 with assay medium. PGI catalyses conversion of fructose 6-phosphate produced by hexokinase into glucose 6-phosphate, which can then be oxidised by G6PDH. Sucrose was assayed by measuring the further increase of $A_{340}$ following the addition of >5 U invertase (Sigma) dissolved in 1 µL sugar assay medium to catalyse hydrolysis of sucrose to fructose and glucose.

Glucose and fructose concentration (N) in moles per gram fresh tissue were determined using the following formula:

$$N = (A_{340,final} - A_{340,baseline}) \cdot \frac{1}{\varepsilon} \cdot w \cdot \frac{1}{a} \cdot t \cdot \frac{1}{m}$$

where ε is 6,220 $mol^{-1}$ $cm^{-1}$, the extinction coefficient of NADPH at 340 nm; *w* is the volume of assay medium in each well in $dm^3$; *a* is the volume of soluble metabolite extract in each well in µL (i.e. the total volume of extract added, divided by 5); *t* is the total volume of extract produced by the original metabolite extraction in µL; *m* is the mass of ground leaf tissue extracted in grams.

Sucrose concentration was determined using the same formula with the final result halved to account for the particular stoichiometry of the sucrose assay.

## 2.4 Measurement of the steady state abundance of target gene transcripts by reverse transcriptase coupled to quantitative PCR (RT-qPCR)

### 2.4.1 RNA extraction

Total leaf RNA was extracted from 100 mg liquid nitrogen-ground tissue (Section 2.1.3) using the Spectrum Plant Total RNA kit (Sigma-Aldritch). The initial Cell Lysis Solution provided with the kit was supplemented with 0.15 % (w/v) polyethylene glycol 20,000 to bind polyphenols which would otherwise interfere with efficient extraction (Dever et al. 2015). The concentration and purity of isolated RNA was measured using a NanoDrop ND-1000 (Thermo Scientific). Extracted RNA was stored at -80 °C.

### 2.4.2 Total RNA quality control

The quality and integrity of the extracted RNA was analysed by formaldehyde-MOPS horizontal agarose gel electrophoresis. To prepare RNA samples for electrophoresis, 5 μg RNA extract was diluted with molecular grade water to a total volume of 6 μL and mixed with 8 μL sample buffer (70% (v/v) formamide; 2.3 % (v/v) formaldehyde; 46 mM MOPS-NaOH, pH 8.0; 12 mM sodium acetate; 2.3 mM EDTA; 0.1 mg/L ethidium bromide). Samples were heated to 65 °C for 150 s to denature RNA secondary structure and bind ethidium bromide, and snap-cooled on ice before gel loading. Gel electrophoresis was carried out at 100 mV for 30-45 mins on formaldehyde-MOPS agarose gels (1.3% (w/v) agarose; 3.7 % (v/v) formaldehyde; 1X MOPS, pH 8.0) in 1X MOPS pH 7.0 buffer. MOPS buffers were prepared as 10X stocks containing 0.2 M MOPS-NaOH (pH 7.0 or pH 8.0), 50 mM sodium acetate and 10 mM EDTA.

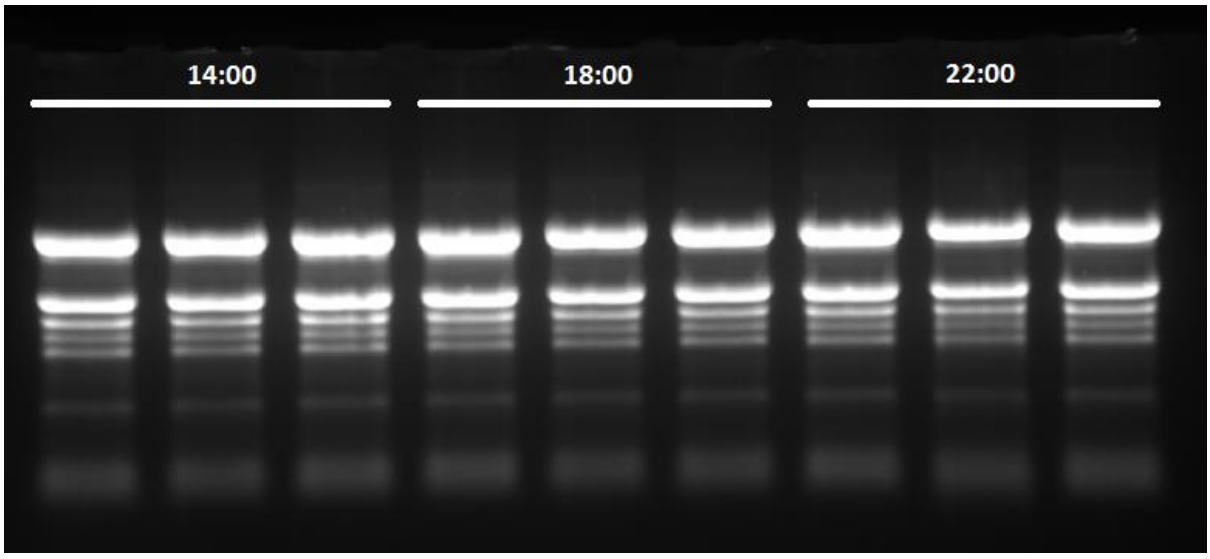


Figure 2.1 – An example of quality control using formaldehyde gel electrophoresis. The RNA samples shown were taken from WT CAM leaf samples that that were taken in the dark period of a 12:12 LD cycle, with the time-point in 24 h time format displayed above the bands (see Section 4.2.1). The direction of band migration was from the top to the bottom of the figure. RNA extracts with 4 discernible ribosomal RNA bands with little inter-band blurring were considered to be of sufficiently high quality for cDNA synthesis.

Gels were visualised and photographed using a UV light box housed in a gel-documentation system with a digital camera (Syngene UGenius). RNA quality was considered to be adequate for further use when ribosomal RNA could be visualised as sharp bands with little or no inter-band blurring to indicate degradation (Fig 2.1)

### 2.4.3 Reverse transcription of RNA into first strand cDNA

QuantiTect reverse transcription kits (Qiagen) were used for synthesis of complementary DNA (cDNA) from leaf total RNA extracts. Quantities of all reagents were halved from the recommended quantities, and 0.5 μg of each total RNA sample was used rather than the recommended input of 1 μg. After the addition of reverse transcriptase, primers and buffer, samples were incubated at 42 °C for 45 mins, rather than the manufacturer's recommended 15

mins, in order to optimise cDNA synthesis (S. Boxall, personal communication). cDNA samples were diluted 1:4 with deionised water that had been autoclaved and kept at -20 °C.

### 2.4.4 cDNA pools for cloning gene fragments for RNAi binary construct generation and for usage as RT-qPCR standards

Pooled cDNA libraries were synthesised from a mixture of RNA extracted from leaf samples taken at 4 h intervals over a 12:12 LD cycle (see Section 2.1.2). Samples from different time points were used to avoid large abundance or deficiency in the concentration of cDNAs of genes which show large diel variations in mRNA levels in *Kalanchoë* species (e.g. *KfPPCK1*, Hartwell *et al.*, 1999).

cDNA pools were made for *K. laxiflora* and *K. fedtschenkoi*. For both species, 0.17 μg RNA was taken per full QuantiTect reaction from each of six 12:12 LD time points: 2, 6 and 10 h into the dark period and 2, 6 and 10 h into the light period. The resulting cDNA was diluted 1:4 as described in Section 2.4.3. RNA for the *K. fedtschenkoi* library was taken from wild type plants sampled in the 12:12 LD timecourse reported in Chapter 4 of this thesis. RNA for the *K. laxiflora* cDNA library was taken from wild type plants sampled in a 12:12 LD timecourse collected in the course of this PhD project, but not otherwise reported in it.

### 2.4.5 RT-qPCR using SYBR green Taq polymerase mastermix

SensiFast SYBR No-ROX (Bioline) was used as the reagent for RT-qPCR. For initial screening of *KlCMDH* RNAi, *KlPxMDH* RNAi and *KlNADP-MDH* RNAi lines (Chapter 6), full-volume reactions were used (20 μL). Subsequently, for all other experiments, half-sized (10 μL) reactions were used. In all experiments, 1 μL of diluted cDNA was used. Primer concentration was 0.4 μM. RT-qPCR experiments were run in 96-well plates (Star Labs) sealed with a clear

plastic film (CyclerSeal, Axygen). An Agilent Mx3005P thermal cycler (Agilent Technologies) was used to run the RT-qPCR assays.

The following PCR thermal cycling parameters were used in initial screening of the various *MDH* RNAi lines (Chapter 6 only):

| Step | Time (s) | Temp (°C) | Cycles |
|---|---|---|---|
| Reagent activation/Denaturation | 600 | 95 | 1 |
| Denaturation | 20 | 95 | 40 |
| Primer annelation/Measurement | 20 | various | |
| Elongation | 20 | 72 | |

The following PCR cycling parameters were used for *K. fedtschenkoi* time courses and other *K. laxiflora MDH* transcript abundance measurements:

| Step | Time (s) | Temp (°C) | Cycles |
|---|---|---|---|
| Reagent activation/Denaturation | 120 | 95 | 1 |
| Denaturation | 5 | 95 | 40 |
| Primer annelation/Measurement | 10 | various | |
| Elongation | 10 | 72 | |

All protocols included a dissociation curve as a final stage to confirm that the RT-qPCR protocol had produced a single PCR product.

The amplification efficiency for each primer pair was determined using a standard curve (Rodríguez *et al.*, 2015). The threshold cycle number ($C_t$) for serial dilutions of cDNA pool (1, 0.25, 0.1, 0.01 and 0.001) was measured using an otherwise identical assay mixture and the primer pair-specific PCR cycling parameters. The results were graphed in Microsoft Excel with the base-10 logarithm of the ratio of the undiluted to diluted transcript abundance on the x-axis

and $C_t$ on the y-axis. The gradient of the linear regression, m, was used to calculate the amplification efficiency, E, where 1 is complete efficiency:

$$E = \left(10^{-\frac{1}{m}}\right) - 1$$

The transcript abundance-$C_t$ graphs used to determine amplification efficiency of primer pairs have been collected in Appendix 1.

### 2.4.6 Primer design

A Primer3Plus interface (http://www.bioinformatics.nl/cgi-bin/primer3plus/primer3plus.cgi, Untergasser *et al.*, 2007) was used to design RT-qPCR primers. The 454 RNA-seq *K. fedtschenkoi* transcriptome assembly (described below, Section 2.9.1) was used to design primers for *K. fedtschenkoi* cDNA samples. Additional primers were designed and provided by Dr. Susanna Boxall, a post-doctoral researcher in the Hartwell group (Table 2.4). *In silico* predictions of *K. laxiflora* transcript cDNA sequences (as described above, Section 2.2.1) were used to design primers for *K. laxiflora* cDNA sequences (Table 2.5). Subsequently, the predicted transcriptomes of *K. fedtschenkoi* and *K. laxiflora* (see below, Section 2.9.1) were used to check the specificity of each primer pair with respect to amplifying the desired isogene in multiple gene families (Appendix 2).

Table 2.4 – Primers used for RT-qPCR of *K. fedtschenkoi* cDNA

| Gene | *K. fedtschenkoi* annotation reference | GenBank Accession No. | Primer sequences | Topology of amplicon relative to ORF |
|---|---|---|---|---|
| Aluminium-activated malate transporter (*KfALMT1*) | Kaladp0073s0021.1 | - | 5′CCCGAACTGCCTAAAGACAA3′<br>5′CACGATGAAGGGCAAATAGG3′ | ORF to 3’ UTR |
| Circadian clock associated 1 (*KfCCA1*) | Kaladp0066s0115.1/ Kaladp0496s0018.1 | KM078717.1 / KM078718.1 | 5′TCAGTCCACCTCTCCCTCTG3′<br>5′GGGAGGTTCAGCGATTTGA3′ | 5’ UTR to ORF |
| NAD-malic enzyme, β subunit 1 (*KfNAD_MEb1*) [1] | Kaladp0472s0027.1 | KM078712.1 | 5′TTGAGGGAGGAGGATCTCTTC3′<br>5′TAATCAGGCAAAAGCAGGGAG3′ | 3’ UTR to 3’ UTR |
| Phosphoenolpyruvate carboxylase kinase 1 (*KfPPCK1*) | Kaladp0037s0517.1 | KM078720.1 | 5′GCAGAGATGTGTCCAGGAGATT3′<br>5′CTTGCTGGATTGGGTGATG3′ | ORF to 3’ UTR |
| Phosphoenolpyruvate carboxylase, CAM isoform (*KfPPC_CAM*) [1] | Kaladp0095s0055.1 | KM078709.1 | 5′CACAGCAGCTCCTTCCTCGC3′<br>5′ATGCGGAGGAAATTGCTGGGG3′ | 3’ UTR to 3’ UTR |
| Timing of *CAB1* expression 1-2 (*KfTOC1-2*) | Kaladp0040s0446.1 | KM078726.1 | 5′CTCGCCTGTCACACTTTGG3′<br>5′AAACTCGTTCCTCGCCATC3′ | 5’ UTR to ORF |
| Tonoplast dicarboxylate transporter (*KfTDT*) | Kaladp0042s0251.1 | - | 5′GCCACCCCATCTTCATCTTG3′<br>5′GCCGCATTGTCACTTCTCAT3′ | ORF to 3’ UTR |
| Vacuolar $H^+$-translocating ATPase subunit H (*KfVHA_H*) [1] | Kaladp0032s0079.1 | - | 5′CCTCGGAGCCAAGTATGCAAG3′<br>5′ACCTTCACAAACTCTCGGCG3′ | ORF to 3’UTR |

[1] Primers that were designed and provided by Dr. Susanna Boxall, post-doctoral researcher in the Hartwell group.

Table 2.5 – Primers used for RT-qPCR of *K. laxiflora* cDNA

| Gene | *K. laxiflora* predicted transcript | Primer sequences | Topology of amplicon relative to ORF |
|---|---|---|---|
| Cytosolic NAD malate dehydrogenase 1 (*KlCMDH1*) | Kalax.0075s0049.1/ Kalax.0094s0014.1 | 5′CTACTCATGCCTC ACATAG3′<br>5′CTACTTCTCTTAC ATGGACA3′ | ORF to 3' UTR |
| Peroxisomal NAD malate dehydrogenase 1 (*KlPxMDH1*) | Kalax.0405s0018.1/ Kalax.0061s.0014.1 | 5′AACCAGTACAAGA GTTGG3′<br>5′TCATCAGGAAGTA AGACAG3′ | ORF to 3' UTR |
| Plastidic NAD malate dehydrogenase 1 (*KlPdMDH1*) | Kalax.0520s0005.1/ Kalax.0326s0011.1 | 5′GCGGAGGTGAGTA AGATA3′<br>5′AGTCGCTCAGAGT TCAAG3′ | 5' UTR to ORF |
| Chloroplastic NADP malate dehydrogenase (*KlNADP-MDH*) | Kalax.0100s0048.1/ Kalax.0131s0010.1 | 5′TAAGAGTGAGGCA GAGTT3′<br>5′GATGGTGCTTGTG TTAGT3′ | ORF to 3' UTR |
| Mitochondrial NAD malate dehydrogenase 1 (*KlMMDH1*) | Kalax.0092s0056.1/ Kalax.0610s0029.1/ Kalax.0018s0053.1/ Kalax.0021s0058.1 | 5′CAGACAAGTAAAC AACTCATC3′<br>5′GATTCTTCTCCTT TCTCAC3′ | Both primers in 3' UTR |

### 2.4.7 Selection of appropriate reference genes for RT-qPCR in *K. fedtschenkoi* and *K. laxiflora*

For some initial screening experiments on the *MDH* RNAi lines generated in *K. laxiflora* (Chapter 6), *POLYUBIQUITIN10* (*KfUBQ10;* GenBank KM114222) was used as the reference/loading control gene required to normalise for minor variations in RNA input amount and/or reverse transcription efficiency between RNA samples. *KfUBQ10* had been used previously in gel-based, semi-quantitative RT-qPCR experiments due to its relatively stable transcript levels over 12:12 LD and LL timecourse experiments (Dever *et al.* 2015).

For 12:12 LD and LL timecourses, in which a reference gene whose transcript level was relatively consistent across time-points was required, SOLiD quantitative RNA-seq data (described below, Section 2.9.1) was filtered for an abundant transcript with low variation in steady-state abundance over a 12:12 LD cycle. A predicted *K. fedtschenkoi* ortholog of a predicted *A. thaliana* thioesterase/thiol ester dehydrase-isomerase superfamily protein (TFP, AT2G30720) was identified as having these features (Fig 2.2). Primers amplifying *K. fedtschenkoi TFP* (*KfTFP*) were used as a reference gene in RT-qPCR assays of samples taken in the time courses reported in Chapters 4 and 5, and displayed relatively consistent threshold cycle numbers ($C_t$) across these samples. *KfTFP* was also used as a reference gene in measurements of relative transcript levels at single time-points as reported in Chapter 3, and its *K. laxiflora* ortholog was used as a reference gene for some of the single-time-point measurements in Chapter 6.

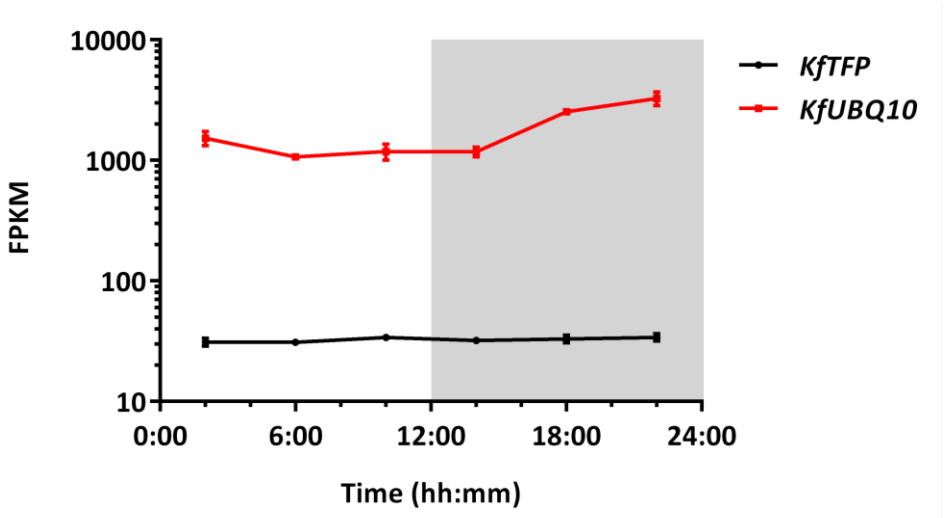


Figure 2.2 - Quantitative RNA-seq (SOLiD) measurements of the steady-state transcript levels of reference genes in *K. fedtschenkoi* CAM leaves. Points represent mean ± S.E.M of 3 replicate samples. Transcript levels are expressed as the number of SOLiD reads (see below, Section 2.9.1) normalised to the length of the sequence to which they were aligned, in kilobases, and the total number of SOLiD reads in millions (FPKM).

Primers were designed for the reference genes (Table 2.6) as described in Section 2.4.6. The same primer pair was used successfully for RT-qPCR of *TFP* in both *K. fedtschenkoi* and *K. laxiflora*.

Table 2.6 – Primers for RT-qPCR standard genes

| Gene | *K. fedtschenkoi* predicted transcript | *K. laxiflora* predicted transcript | Primer sequences | Topology of amplicon relative to ORF |
|---|---|---|---|---|
| *KlUBQ10* | | Kalax.0069s0095.1<br>Kalax.0168s0006.1 | 5′ATGGGAGGACTC TGGCTGAC3′<br>5′CACACCCAACAC ACAACAACC3′ | ORF to 3' UTR |
| *KfTFP* / *KlTFP* | Kaladp0068s0118.1 | Kalax.0134s0055.1<br>Kalax.1110s0007.1 | 5′TGTTGTTCCTGC CACAGAAG3′<br>5′TAGAGGGTGAAG GTCCCAGA3′ | ORF to 3' UTR |

## 2.4.8 Quantification of gene relative transcript abundance

For some screening experiments (Chapter 6), the $2^{-\Delta\Delta Ct}$ method (Livak and Schmittgen, 2001) was used to determine the relative transcript levels of a gene in the *MDH* RNAi lines relative to the same gene in wild type. Either *KlUBQ10* or *KlTFP* was used as the reference gene.

For the remaining RT-qPCR experiments, relative gene expression was calculated using the software interface for the real-time PCR cycler (MxPro, Agilent Technologies) in the 'Comparative quantitation' mode. Threshold fluorescence was set at 10 standard deviations of the baseline fluorescence and threshold cycle number ($C_t$) was taken as the number of cycles needed to reach this threshold. In each 96-well qPCR plate, a calibrating RT-qPCR reaction was run, using the cDNA pool (Section 2.4.4) as template, in order to facilitate inter-plate comparison

of results. *TFP* was used as the reference gene for the relative quantification of transcript levels across different RNA samples from the various experimental treatments.

## 2.5 Immunoblotting

### 2.5.1 Protein extraction

Protein was extracted from liquid nitrogen-ground leaf tissue (Section 2.1.3) by re-grinding with a pestle and mortar in 1.5 mL extraction buffer (1M Tris-HCl, pH 6.8; 20% (v/v) glycerol; 4% (v/v) β-mercaptoethanol; 3% (w/v) sodium dodecyl sulphate (SDS)) and a small quantity of acid-washed sand. Liquid extract was transferred to a screw-capped 1.5 mL tube and immediately boiled at 100 °C for 5 mins. Extracts were centrifuged at maximum speed in a bench-top microcentrifuge for 5 mins to pellet solid material. Protein extracts were stored at -20 °C. On thawing, samples were re-boiled for 2 mins and centrifuged for 5 minutes. Protein concentration was determined by the Bradford assay using Bradford Ultra reagent (Expedion) and a Bovine Serum Albumin (Sigma-Aldritch) standard curve.

### 2.5.2 SDS-PAGE electrophoresis

SDS-PAGE gels were cast in 0.75 mm- or 1.0 mm-deep moulds (BioRad), depending on availability; for direct comparisons of protein expression, moulds of the same depth were used. Initially, resolving gel (375 mM Tris-HCl, pH 8.8; 12.5% (v/v) acrylamide/bis-acrylamide; 0.1% (w/v) SDS; 0.1% (v/v) tetramethylethylenediamine (TEMED); 0.1% (w/v) ammonium persulphate (APS)) was mixed and poured into the mould. Once the resolving gel was set, stacking gel (50 mM Tris-HCl, pH 6.8; 4% (v/v) acrylamide/bis-acrylamide; 0.1 % (w/v) SDS; 0.2 % (v/v) TEMED; 0.1 % (w/v) APS) was poured onto the resolving gel and a comb inserted to form wells. For gel-loading, 20 μg and 5 μg of total protein was loaded onto SDS-PAGE gels for

immunoblotting with PEPC and phospho-PEPC antisera, respectively. PageRule standard marker protein mixture (Thermo Scientific) was used as a molecular weight standard on each gel. Electrophoresis was allowed to proceed for approximately 90 mins at 150 mV in SDS-PAGE running buffer (25 mM Tris, 192 mM glycine, 0.1% (w/v) SDS).

### 2.5.3 Antisera

Antiserum that had been raised against PPC purified from *K. fedtschenkoi* (anti-PPC; Nimmo *et al.*, 1986) was provided by Prof. Hugh G. Nimmo, University of Glasgow, United Kingdom. Antiserum that had been raised against a phosphorylated PPC peptide sequence of *Hordeum vulgare* (anti-phospho-PPC; Feria *et al.*, 2008) was provided by Prof. Cristina Echevarría, Universidad de Sevilla, Spain. Both antisera were used as described previously (Dever *et al.*, 2015).

### 2.5.4 Immunoblotting

After protein separation by electrophoresis, SDS-PAGE gels were assembled into an electro-blotting cassette (BioRad) in transfer buffer (25 mM Tris base; 192 mM glycine; 0.1% SDS; 20% (v/v) methanol). Protein was electro-blotted from the SDS-PAGE gels onto nitrocellulose membranes (Amersham Protran 0.45 μm nitrocellulose, GE Healthcare Life Sciences) at 100 mV for 1 h at 4 °C. Non-specific protein binding to membranes was blocked by overnight incubation with 5% (w/v) powdered milk (Marvel) in TBS-Tween (50mM Tris-HCl, pH 7.5; 150 mM NaCl; 0.1% Tween 20) at 4 °C.

Membranes were washed briefly in TBS-Tween, before incubation with the primary antibody for 2 h at room temperature. Anti-PPC and anti-phospho-PPC stocks were diluted 1:5000 and 1:1000 in TBS-Tween, respectively. Membranes were then washed three times in

TBS-Tween and incubated for 1 h with anti-rabbit IgG, horseradish peroxidase-conjugated horse antibody (Amersham ECL, GE Healthcare) as a secondary antibody. Secondary antibody stocks were diluted 1:20000 and 1:10000 in TBS-Tween for detecting anti-PPC and anti-phospho-PPC, respectively. Membranes were re-washed three times in TBS-Tween. Bands were detected using a peroxidase-based luminescent assay (Pierce ECL, Thermo Scientific) exposed onto chemiluminescent film (Lumifilm, Roche).

## 2.6 Tonoplast function assays

### 2.6.1 Tonoplast membrane isolations from whole leaves

Tonoplast membranes were isolated from fresh *K. fedtschenkoi* leaf tissue in the form of sealed microsomal vesicles, following methods that have been described previously (Bennett and Spanswick, 1983; White and Smith, 1989; Bettey and Smith, 1993) with modifications to suit the current experimental design.

Immediately prior to leaf sampling, plants were moved to a cold room at 4 °C. Illumination was restricted to a lamp screened with translucent green acetate in order to minimise photosynthetically-active radiation. For each extraction, CAM leaves (leaf pairs 6-8) were picked from three *K. fedtschenkoi* clones, either wild type or one of the studied *KfALMT* RNAi lines, and weighed. Petioles were removed with a scalpel blade and the lamina cut into 2-3 mm slices. Cut ends were soaked in cold tonoplast extraction buffer (450 mM mannitol; 100 mM Tricine-BTP, pH 8.0; 10 mM EDTA; 6 mM $MgSO_4$; 25 mM $K_2S_2O_5$; 10 mM dithiothreitol (DTT); 1 mM benzamidine; 0.5% (w/v) polyvinylpyrrolidone (PVP)) for 10 mins.

The extraction buffer was exchanged for 4 mL fresh, ice-cold tonoplast extraction buffer per gram leaf tissue. The mixture was homogenised with a kitchen food processor, using 15 one-second bursts. Homogenate was filtered through four layers of pre-washed muslin and the filtrate

was centrifuged in a Sorval Evolution centrifuge fitted with an angled rotor (FIBERLite F14-6x250y, Thermo Scientific) at 13,000 *g* for 15 mins. 70 mL supernatant was re-centrifuged at 80,000 *g* for 40 mins in an ultracentrifuge (Sorvall Combi) fitted with a tilt rotor (AH-629, Sorvall) in order to pellet the vacuolar fraction; the remainder of the supernatant from the first centrifugation step was discarded in order to standardise the remaining purification steps.

Pellets were resuspended in 8 mL cold glycerol buffer (1.1 M glycerol; 10 mM Tricine-BTP, pH 8.0; 1 mM EDTA; 1 mM DTT) with a nylon paintbrush. The re-suspended pellet was layered onto 8 mL 23% (w/v) sucrose solution in glycerol buffer. The layered solutions were centrifuged at 100,000 *g* for 70 mins. After this high-speed ultra-centrifugation run, tonoplasts could be visualised as cloudiness at the interface between the layers, and removed with a soft disposable plastic Pasteur pipette. Tonoplast membranes isolated in this manner were diluted 1:1 with glycerol buffer and re-pelleted at 100,000 *g* for 50 mins. The supernatant was removed and the pelleted tonoplast membranes were re-suspended in 130 µL glycerol buffer and snap frozen in liquid nitrogen. Prepared tonoplasts were stored at -80 °C. Protein concentration in the tonoplast preparations was measured using Bradford reagent (Sigma) and a Bovine Serum Albumin (Sigma-Aldritch) standard curve.

### 2.6.2 $H^+$ transport activity assays

*In vitro* $H^+$ transport activity of tonoplast vesicles was measured using 6-chloro-9-{[4-(diethylamino)-1-methylbutyl]amino}-2-methoxyacridine (quinacrine) following the method of White and Smith (1989). Quinacrine fluorescence quenching measures the formation of positive-outside pH gradients in membrane vesicles, (Lee and Forte, 1978). The medium used for the transport assays contained: 150 mM mannitol; 25 mM BTP-MES, pH 8.0; 6 mM $MgSO_4$; 0.3 mM EDTA; and 3 µM quinacrine dihydrochloride. 500 mM malate stock solution was made up

from free malic acid and buffered to pH 8.0 with BTP. 30 mM ATP stock solutions were buffered to pH 8.0 with Tris base.

An initial reaction mixture comprising 20 μg tonoplast protein, 50 μL malate stock solution and sufficient transport assay medium for a total volume of 450 μL were mixed in quartz microcuvettes. Fluorescence was tracked in a spectrofluorometer (Fluoromax 4, Horiba Scientific) at 21 °C using an excitation wavelength of 427 nm and an emission wavelength of 495 nm. Reactions were initiated by addition of 50 μL ATP stock solution and left for the fluorescence signal to reach a steady plateau. Fluorescence measurements were converted to a percentage of the initial reading after addition of ATP, and the $H^+$ transport rate taken as the gradient of the linear part of the fluorescence plot immediately following addition of ATP.

### 2.6.3 Vacuolar tonoplast vesicle ATPase assays

Tonoplast ATPase activity was measured by assaying for inorganic phosphate released by the hydrolysis of ATP (Smith *et al.*, 1984*b*).

0.5 or 1 μg of tonoplast protein, or a range of standard quantities of $K_2HPO_4$ (0, 5, 10, 20, 30 or 40 ng) were added to a final reaction volume of 100 μL in glass test tubes. The V-ATPase assay medium contained: 50 mM Tris-Tricine, pH 8.0; 50 mM KCl; 3 mM $MgSO_4$; 0.1 mM EDTA; 0.15 % (w/v) Brij-58; 0.1 mM $NaMoO_4$ (McRae *et al.*, 2002). Nitrate ($KNO_3$) was used at a final concentration of 50 mM as a vacuolar $H^+$-translocating ATPase inhibitor (Warren *et al.*, 1992; McRae *et al.*, 2002). Reactions were initiated by adding ATP to a final concentration of 1 mM (Warren *et al.*, 1992) followed by incubation in a water bath for 30 mins at 37 °C.

Reactions were stopped by the addition of 1.4 mL cold molybdate reagent (340 mM HCl, 115 mM ascorbic acid, 2.9 mM $(NH_4)_6Mo_7O_{24}$, 2% (w/v) sodium dodecyl sulphate) and placed on ice for 10 minutes. 1.5 mL bismuth reagent (1M HCl, 119 mM trisodium citrate, 88 mM

bismuth citrate) was added and reactions were incubated at 37 °C for 10 mins. Absorbance at 710 nm was measured with a spectrophotometer (Cariani *et al.*, 2004). Baseline phosphate measurements were made by pre-mixing ATP with molybdate reagent, and these measurements were subtracted from final phosphate measurements to give the ATPase activity.

## 2.7 NAD-malate dehydrogenase activity assays

The protocol for protein extraction was based on Wang *et al.* (2010) and Dever *et al.* (2015). Soluble protein was extracted from 300 mg pre-ground, frozen leaf tissue by grinding with a pestle and mortar in 1.5 mL extraction buffer (100 mM Tris-HCl, pH 7.8; 5 mM $MgCl_2$; 1 mM EDTA; 1 mM dithiothreitol (DTT); 1 mM Benzamidine-HCl; 2% (w/v) polyethylene glycol 20,000 (PEG-20K)). 60 mg of insoluble polyvinylpolypyrrolidone (PVPP), and a small quantity of acid-washed sand, to improve grinding, was added to the extraction buffer immediately before use. The homogenate was filtered through a single layer of Miracloth (Merck) and centrifuged for 1 min at maximum speed in a bench-top microcentrifuge. The supernatant was diluted 5-fold with extraction buffer for the assay.

The protocol for malate dehydrogenase activity assay was based on Jenner *et al.* (2001). 5 µL extract was added to 195 µL assay buffer in a 96-well plate (100 mM Tris-HCl, pH 7.8; 5 mM $MgCl_2$; 1 mM oxaloacetate (OAA); 0.3 mM NADH). The pathlength-corrected decrease in $A_{340}$ ($\Delta A_{340}$) during the following 2 minutes was measured using a plate reader, with measurements at 5 s intervals made to confirm that the rate of decrease of $A_{340}$ remained linear throughout. Total protein concentration in soluble protein extracts was determined using Bradford reagent (Sigma) with a Bovine Serum Albumin (Sigma-Aldritch) standard curve. NAD-MDH activity (A) in units (µmol $min^{-1}$) per mg total protein was calculated using the following formula:

$$A = -\Delta A_{340} \cdot \frac{1}{\varepsilon} \cdot \frac{1}{t} \cdot w \cdot \frac{1}{p} \cdot 10^6$$

where ε = 6220 $mol^{-1}$ $cm^{-1}$, the extinction coefficient of NADH; t = 2 mins, the time interval; w = 2 x $10^{-4}$ $dm^3$, the volume of the reaction; and p is the mass of total protein added to the reaction in mg.

## 2.8 Real time $CO_2$ gas exchange measurements using detached leaves or whole plants

### 2.8.1 Specimen preparation

Plants that were to be assayed in $CO_2$ gas exchange experiments were first entrained to 12:12 LD for 7-8 days (Section 2.1.2). $CO_2$ gas exchange measurements were performed as described by Dever *et al.* (2015).

For measurements of a detached pair of leaves, two layers of Parafilm (Pechiney Plastic Packaging) were stretched over the rim of a 150 $cm^3$ plastic beaker to form a seal. Two small holes were made in the Parafilm to enable the beaker to be completely filled with deionised water. Leaves were picked at the base of the petiole and the petioles were inserted immediately in the holes in the Parafilm.

For measurements of whole plants, plants were grown initially in small plugs of compost mix in Aracon trays (Arasystem), and then re-potted with additional compost mix in the aforementioned 150 $cm^3$ beakers, modified with holes drilled in the base for drainage. The whole plants were then entrained to 12:12 LD as normal. Immediately before the start of $CO_2$ gas exchange monitoring, the mouth of each beaker was sealed with Parafilm, leaving minimal open space around the plant's stem, in order to minimise the contribution of respiratory $CO_2$ from roots or microbes in the compost to measurements. A tight fit between the beakers and their

receptacle in the IRGA chamber limited gas diffusion between the drainage holes and the air stream flowing through the chamber (see below).

### 2.8.2 Infra-red gas analyser configuration and usage

A custom-built multi-cuvette infra-red gas analyser (IRGA) gas switching system designed by Dr Keith Parkinson (PP Systems, Hitchin, Herts, UK) was used to measure rates of $CO_2$ uptake from detached leaves and whole plants. The IRGA system used a CIRAS-DC gas analyser (PP Systems) controlled by SC-DC software (PP Systems) to measure $CO_2$ concentration in an air stream before and after it flowed through each of 12 ~1000 $cm^3$ clear plastic cuvettes containing plant specimens. Net $CO_2$ uptake or output was calculated from the difference between the two measurements. Each cuvette contained a miniature electric axial fan to ensure efficient mixing of the air inside the cuvette.

Air entering the CIRAS-DC was switched between air outflows from the cuvettes by a 12-channel gas stream switching unit (GSS, PP Systems) so that the 12 cuvettes were monitored consecutively in a repeating cycle. In measuring each cuvette, 60 seconds was permitted for air from the previous cuvette to be displaced from the GSS and CIRAS-DC, followed by 5 repeat measurements of $CO_2$ concentration. The time between two measurements of $CO_2$ exchange in the same cuvette was ~18 mins due to the time required for cycling through each of the 12 cuvettes.

Pressurised air supplied to the gas exchange cuvettes was generated by a compressor (DenComp4) and passed through a medical $CO_2/H_2O$ scrubber (K-MT 3, Parker Zander) to remove atmospheric $CO_2$ and water vapour. Pressurised air was mixed with bottled pure $CO_2$

(BOC Gases) to a controlled $CO_2$ concentration (~390 ppm) in an air supply unit (ASU, PP Systems) before being channelled to the cuvettes.

The IRGA apparatus, including the cuvettes and ASU, was contained within a Snijders plant growth cabinet (see Section 2.1.2) for control of photoperiod, photosynthetically-active radiation (PAR) and temperature. CIRAS-DC recorded PAR via an in-chamber photometer.

### 2.8.3 Data analysis

Measurements of $CO_2$ gas exchange were normalised to leaf area using a built-in function of the SC-DC software. Leaf areas were measured from scans of the leaves taken with a desktop scanner (Epson Stylus DX4400) using open-source image processing software (ImageJ).

Total $CO_2$ uptake over a given time period was estimated by calculating the area under the $CO_2$ assimilation rate ($J_{CO2}$)-time curve. Assuming linear interpolation, the area under the curve between two consecutive $J_{CO2}$ measurements was treated as a right trapezoid, and the total area calculated as a sum of the area of the trapezoids bounded by a given time interval (Fig. 2.3, Eqn. 1). This approach remained valid when estimating the total $CO_2$ uptake in an interval between one positive and one negative $J_{CO2}$ measurement because applying the trapezoid area formula returns the estimate for net $CO_2$ exchange, i.e. $CO_2$ uptake, less $CO_2$ output (Fig. 2.3, Eqn. 2). A second equation was derived for linear interpolation of $J_{CO2}$ at the time of a light/dark or dark/light transition when the two closest $J_{CO2}$ measurements were before and after the transition, respectively (Fig. 2.3, Eqn. 3). A Perl script was used to implement these equations on $J_{CO2}$ timecourse data.

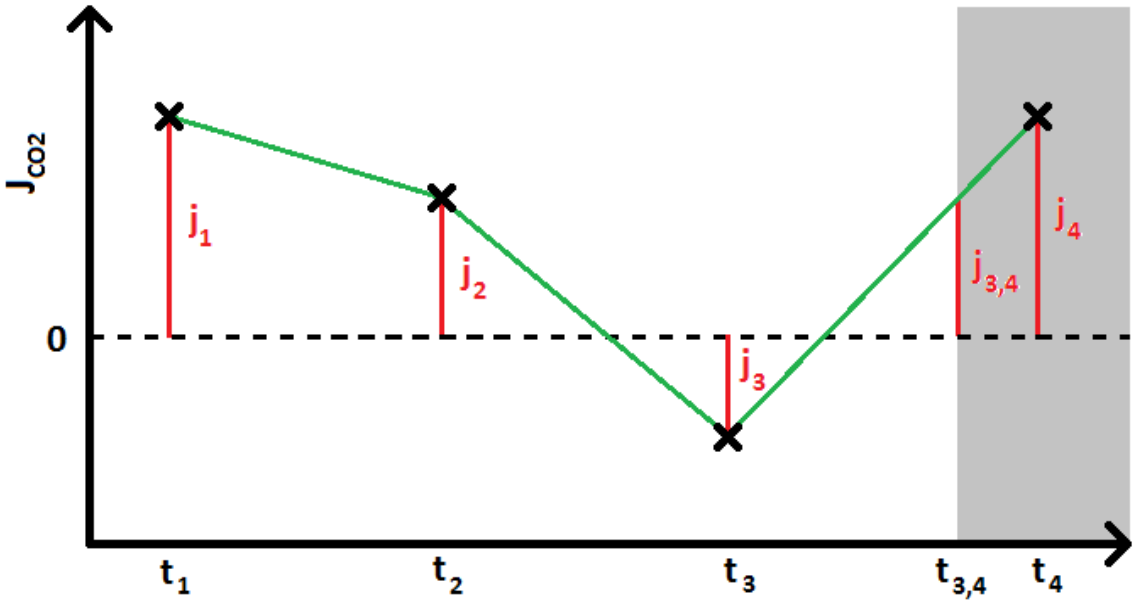


$$\text{(Equation 1)} \quad \int_{t_1}^{t_2} J_{CO2} = 0.5 \,.\, (t_2 - t_1) \,.\, (j_1 + j_2)$$

$$\text{(Eqn. 2)} \quad \int_{t_2}^{t_3} J_{CO2} = 0.5 \,.\, (t_3 - t_2) \,.\, (j_2 + j_3)$$

$$\text{(Eqn. 3)} \quad j_{3,4} = \frac{(t_{3,4} - t_3) \,.\, j_4 + (t_4 - t_{3,4}) \,.\, j_3}{t_4 - t_3}$$

$$\text{(Eqn. 4)} \quad \int_{t_3}^{t_{3,4}} J_{CO2} = 0.5 \,.\, (t_{3,4} - t_3) \,.\, (j_3 + j_{3,4})$$

Figure 2.3 - A total $CO_2$ uptake calculation method. The method for calculating total $CO_2$ uptake is represented with a simplified example of a $J_{CO2}$-time graph. Grey shading represents the duration of the dark period.

## 2.9 Sequence analysis

### 2.9.1 Sequence resources

Before the start of this PhD project, the Hartwell group and collaborating researchers had conducted *de novo* shotgun sequencing (454 Life Sciences) and assembly of the *K. fedtschenkoi* transcriptome. Approximately 21,000 expressed sequence tags (ESTs) were assembled that gave partial coverage of the *K. fedtschenkoi* transcriptome. In addition, samples of $C_3$ (leaf pair 1) and CAM (leaf pair 6) leaves were collected from *K. fedtschenkoi* at 4 h intervals over a single 12:12 LD cycle and subjected to short-read RNA-seq (SOLiD, Thermo Fisher Scientific). 50 bp sequence reads generated by this process were aligned with the 454 sequencing-generated transcriptome in order to quantify the steady-state abundance of the transcript represented by each EST in the $C_3$ and CAM leaves over the 12:12 LD cycle. The number of SOLiD reads that aligned to each EST were normalised to the length of the EST in kb and the total number of SOLiD sequence reads (in millions) to give FPKM (fragments/reads per kilobase per million reads) as a parameter of relative transcript abundance.

Also prior to the start of this PhD project, the Hartwell group and collaborating researchers decoded, assembled and annotated a draft genome sequence for *K. fedtschenkoi*, providing near-comprehensive coverage of the ~31,000 protein coding genes in the ~246 Mb genome (Brenchley *et al*., in preparation). Assembled and annotated genome scaffolds have been made publicly available via the Centre for Genomic Research, University of Liverpool (http://www.cgr.liv.ac.uk/gview/kalanchoe/). The quantity of short reads from the SOLiD dataset that aligned with the spliced transcript of each predicted gene in the draft genome annotation was used to calculate FPKM for that gene in $C_3$ and CAM leaf samples at each timepoint in the 12:12 LD timecourse.

Concurrently with this PhD project, but without any participation from the author, an additional time course of epidermal peel (EP) samples were collected at 2 h intervals for the duration of a single 12:12 LD cycle. EPs are enriched for guard cells, whereas the remainder of the leaf tissue, which was also collected and analysed, was comprised mostly of leaf mesophyll cells (MC). RNA-seq (Illumina) of the EP and MC samples generated a dataset of short (100 bp) sequence reads. The short reads were also aligned with the draft *K. fedtschenkoi* genome annotation in order to quantify differential transcript abundance in guard cells and CAM-performing leaf mesophyll and throughout the 12:12 LD cycle. The number of reads that aligned with each predicted gene were again normalised as FPKM.

*K. laxiflora* genomic sequence data was available from partial *de novo* sequencing and assembly of the genome conducted before the beginning of this PhD project.

Concurrently with this PhD project, but without the involvement of the author, the decoding, assembly and annotation of the *K. laxiflora* and *K. fedtschenkoi* genomes has been completed (Hartwell *et al.*, 2016). Both genomes have now been made publicly available from the US-Department of Energy's Joint Genomics Institute's Phytozome database of plant genome resources (https://phytozome.jgi.doe.gov/pz/portal.html#). These resources were not used to design hairpin RNA constructs for transgenic RNAi or primers for RT-qPCR, but were used subsequently used to validate these sequences (see Sections 3.2.3 and 6.2.2, and Appendix 2).

*A. thaliana* peptide sequences and gene ontology information were downloaded from The Arabidopsis Information Resource (http://www.arabidopsis.org/). Peptide sequences from other species were obtained from the National Center for Biotechnology Information (https://www.ncbi.nlm.nih.gov/).

### 2.9.2 Pair-wise sequence alignments

Pairwise sequence alignments were carried out using the BLAST software package (version 2.2.6, ftp://ftp.ncbi.nlm.nih.gov/blast/executables/legacy/2.2.26/). BLASTN, BLASTP, BLASTX and TBLASTN searches (Altschul *et al.*, 1997) were carried out using blastall.exe on databases formatted using formatdb.exe. Two-sequence BLASTN alignments were carried out using bl2seq.exe.

### 2.9.3 Multiple sequence alignments

Web interfaces for T-Coffee (Notredame *et al.*, 2000; Li *et al.*, 2015) and Clustal Omega (Sievers *et al.*, 2011; Li *et al.*, 2015) were used for multiple sequence alignments.

| Method | Web interface | Last accessed |
|---|---|---|
| T-Coffee | http://www.ebi.ac.uk/Tools/msa/tcoffee/ | 30/4/17 |
| Clustal Omega | http://www.ebi.ac.uk/Tools/msa/clustalo/ | 30/4/17 |

### 2.9.4 Phylogenetic analysis

Sequences were aligned using T-Coffee and the alignments trimmed using Gblocks (Castresana, 2000). Maximum-likelihood phylogenetic trees were constructed with RaxML (Stamatakis, 2006) using a gamma substitution model and the Whelan and Goldman substitution matrix (WAG, Whelan and Goldman, 2001). Bootstrap analysis was conducted with 1000 iterations per tree.

Phylogenetic tools were accessed using the following web interfaces:

| Method | Web interface | Last accessed |
|---|---|---|
| Gblocks | http://molevol.cmima.csic.es/castresana/Gblocks_server.html | 2/10/16 |
| RaXML | http://www.trex.uqam.ca/index.php?action=raxml&project=trex | 2/10/16 |

## 2.10 Data analysis

Statistical analysis was conducted using R (https://www.r-project.org/). For the purposes of statistical tests, the maximum probability of the null hypothesis that was accepted for statistically significant results (α) was 0.05. Data and statistics were presented graphically using GraphPad Prism (http://www.graphpad.com/scientific-software/prism/).

## Chapter 3 - Preliminary screening and phenotypic characterisation of *KfALMT* RNAi and *KfTDT* RNAi lines

### 3.1 Introduction

Malate synthesised from nocturnal $CO_2$ fixation as part of the diel CAM cycle is stored in vacuoles overnight and released gradually to the cytosol during the day. The molecular mechanism of malate import and export through the vacuolar tonoplast membrane is a longstanding area of interest and intensive research in CAM (Lüttge and Ball, 1979; Smith *et al.*, 1996; Holtum *et al.*, 2005).

Malate can accumulate overnight to high-millimolar concentrations in the mesophyll vacuoles of CAM photosynthetic tissue (Lüttge and Smith, 1984; Borland *et al.*, 1992), but inhibits PPC in the low-millimolar range (Nimmo *et al.*, 1984). PPC activity during the night is therefore dependent upon partitioning of malate in the vacuolar lumen. Furthermore, generation of 2 moles of protons ($H^+$) is concomitant with synthesis of each mole of malate (Lüttge and Ball, 1980; Arata *et al.*, 1992), and partitioning of $H^+$ from the cytosol is required to prevent its overwhelming acidification during the night. Active co-transport of malate and $2H^+$ by the tonoplast into the vacuolar lumen is implicit in high concentration gradients between the vacuolar lumen and the cytosol (Lüttge and Ball, 1979; Smith *et al.*, 1996). Passive co-transport in the reverse direction, down the accumulated concentration gradient, has been suggested as the mechanism for vacuolar malate export during the day (Lüttge and Smith, 1984; Smith *et al.*, 1996). The present challenge is to understand, at both the molecular-genetic level and the associated biochemical level, which membrane transport proteins were recruited in the course of evolution from $C_3$ to CAM to mediate controlled vacuolar malate import and export (Borland *et al.*, 2009).

### 3.1.1 Mechanisms of coupled vacuolar import of $H^+$ and malate

In both $C_3$ and CAM species, vacuoles maintain a negative membrane electrical potential ($\Delta\psi$) by active transport of $H^+$ from the cytosol into the vacuole. By convention, a negative potential indicates that the charge of the cytosol is lower than that of the vacuolar lumen (Bertl *et al.*, 1992). Vacuoles use the energy stored in this membrane potential to import a wide range of solutes to the vacuolar lumen against concentration gradients (Etxeberria *et al.*, 2012).

$H^+$ translocation to the vacuole is catalysed by vacuolar ATPase (V-ATPase) and vacuolar pyrophosphatase (V-PPase), concomitant with the hydrolysis of ATP and inorganic pyrophosphate ($PP_i$) respectively. V-ATPase is a multisubunit protein complex with homology to the F-type ATP synthase of the mitochondrial inner membrane in most of its subunits, and likewise comprises one membrane-bound and one cytosolic domain which rotate with respect to one another (Ratajczak, 2000; Cipriano *et al.*, 2008). Rotational catalysis by V-ATPase provides the molecular basis for the coupling of ATP hydrolysis to translocation of $H^+$ from the cytosol to the vacuolar lumen (Cipriano *et al.*, 2008). By contrast, V-PPase is an α-helical integral membrane protein comprising a single polypeptide chain (Maeshima, 2000).

V-ATPase activity increases during the transition from $C_3$ to CAM in the facultative CAM species *Kalanchoë blossfeldiana* (Mariaux *et al.*, 1997) and *Mesembryanthemum crystallinum* (Bremberger and Lüttge, 1992). In *Kalanchoë daigremontiana* and *Kalanchoë pinnata*, both constitutive CAM species that are closely related to *K. fedtschenkoi* (Gehrig *et al.*, 2001), higher extractable activities of V-PPase, relative to the V-ATPase, have been found (White and Smith, 1989; Chen and Nose, 2000). Both enzymes may be important for maintaining the negative vacuolar membrane potential (Smith *et al.*, 1996; Holtum *et al.*, 2005). The respective substrates of V-ATPase and PPase are found in similar concentrations in the dark

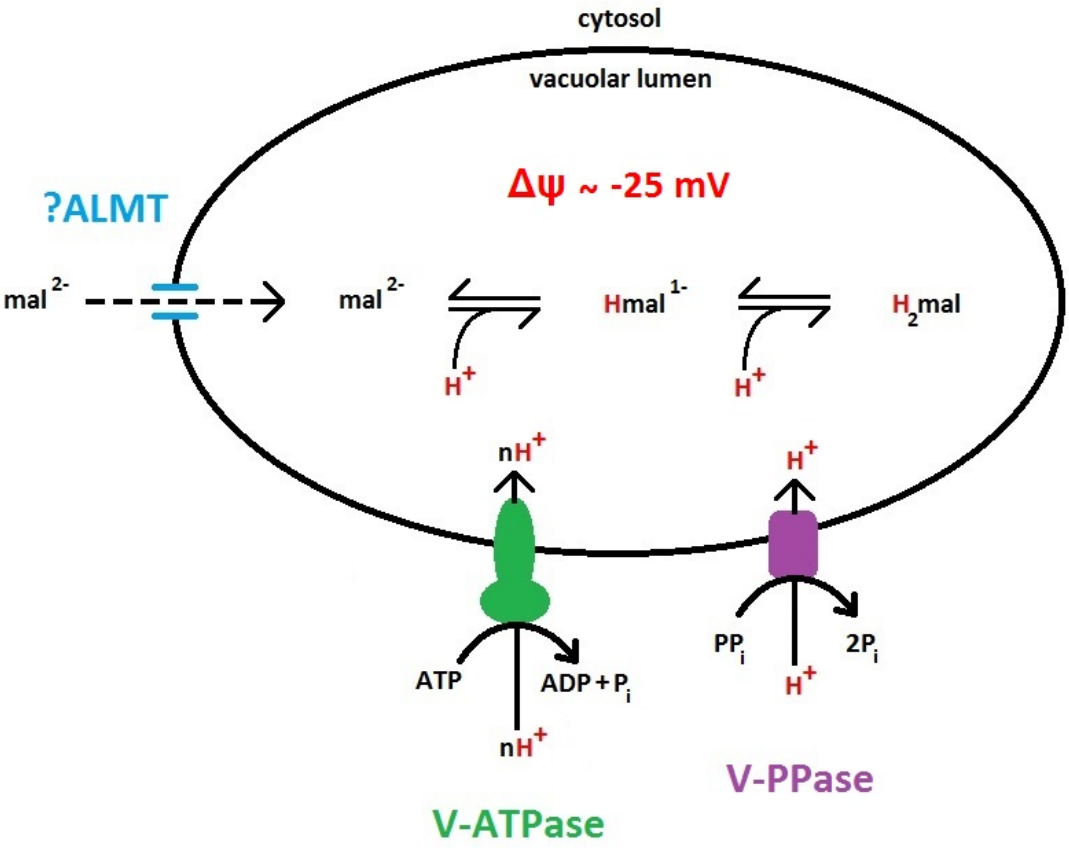


Figure 3.1 - A proposed model for the mediation of vacuolar malate import in CAM. V-PPase and/or V-ATPase catalysed $H^+$-translocation is coupled to selective conductance of $mal^{2-}$ through an anion channel, possibly an ALMT. Value for $\Delta\psi$ taken from Rona *et al.* (1980)

period in *K. daigremontiana* and *K. pinnata* (Chen and Nose, 2004), but ATP competes to bind free magnesium ions ($Mg^{2+}$), which are required for allosteric activation of V-PPase (White *et al.*, 1990). It has therefore been suggested that V-PPase compensates for V-ATPase when ATP concentrations decline, liberating intracellular $Mg^{2+}$ (White *et al.*, 1990).

The coupling of vacuolar malate and $H^+$ import has been proposed to rely on a tonoplast malate channel (Smith *et al.*, 1996; Hafke *et al.*, 2003; Holtum *et al.*, 2005). In this model (Fig. 3.1), inward diffusion of the divalent anion of malate ($mal^{2-}$) through protein anion channels, driven by the negative membrane electrical potential across the tonoplast (Rona *et al.*, 1980),

dissipates the positive charge of $H^+$ translocated by V-ATPase and PPase, and energetically enables protracted acidification of the vacuolar lumen by further $H^+$ import (Smith *et al.*, 1996; Cheffings *et al.*, 1997). Decreasing pH in the vacuolar lumen causes mono-protonation of $mal^{2-}$ to the monovalent anion ($Hmal^{1-}$) or di-protonation to neutral malic acid ($H_2mal$) (Lüttge and Smith, 1984; Arata *et al.*, 1992), to which the malate channel is impermeant, and thereby traps malate to high concentration relative to the cytosol (Lüttge and Ball, 1979; Smith *et al.*, 1996) (Fig. 3.1). The constitutive presence of $Ca^{2+}$-$isocitrate^{2-}$, with a carboxylate group $pK_a$ value intermediate to those of $mal^{2-}$ and $Hmal^-$, in the vacuolar lumen may absorb $H^+$ and limit the formation of $H_2mal$ in *K. daigremontiana* and other CAM species (Arata *et al.*, 1992). However, accumulation of $Hmal^-$ but not $H_2mal$ would not invalidate this model.

Evidence for cooperation between vacuolar anion transport and V-ATPase/V-PPase-driven $H^+$ translocation has been gathered in various physiological measurements on CAM species. Weakly-basic fluorescent dyes, such as quinacrine, have proven to be useful *in vitro* biochemical assays for anion co-transport-dependent $H^+$ transport activity in purified tonoplast membranes of CAM species, which form vesicles in solution (White and Smith, 1989). In addition, V-ATPase- and pH gradient-dependent import of radiolabelled [$^{14}$C]malate has been measured in isolated vacuoles of *K. daigremontiana* (Nishida and Tominaga, 1987).

Increased $mal^{2-}$-dependent $H^+$ transport activity was found in purified tonoplast vesicles from *M. crystallinum* in its induced CAM state relative to its constitutive $C_3$ state (Struve and Lüttge, 1987), and in tonoplast vesicles from a CAM orchid species relative to those from a $C_3$ orchid species (White and Smith, 1992). Similar anion co-transport specificity of $H^+$ transport activity has been found in purified tonoplasts of phylogenetically disparate CAM species, which suggests recruitment of the same transporter in convergent evolution of CAM (White and Smith,

1989, 1992). In purified *K. daigremontiana* tonoplast vesicles, a $K^+$-ionophore, valinomycin, has been used to generate an artificial, $H^+$-independent negative $\Delta\psi$ in order to demonstrate that this alone is sufficient to drive vacuolar malate import (Ratajczak *et al.*, 1994). The vesicles were rapidly mixed with a high concentration of K-gluconate, a $K^+$ salt with a membrane-impermeable counter-anion. The large $K^+$ concentration drove valinomycin-mediated diffusion of $K^+$ into the vesicle, which decreased the membrane electrical potential and in turn drove inward movement of [$^{14}$C]$mal^{2-}$. This elegantly demonstrated that vacuolar $mal^{2-}$ import could be driven by $\Delta\psi$ alone, independently of the trans-tonoplast chemical potential difference of $H^+$ (Ratajczak *et al.*, 1994).

More recently, patch clamp electrophysiology has been used to characterise the vacuolar malate transport activity of isolated *K. daigremontiana* vacuoles (Cheffings *et al.*, 1997; Pantoja and Smith, 2002; Hafke *et al.*, 2003). Malate currents were found to be mediated by a $mal^{2-}$-specific, inward-rectifying malate channel (Hafke *et al.*, 2003), which is consistent with the model described above (Fig. 3.1). Extrapolation from whole-vacuole $mal^{2-}$ currents has shown that the observed malate transport activity is sufficient for complete vacuolar import of malate synthesised during the dark period in *K. daigremontiana* (Hafke *et al.*, 2003). As an inward-rectifying channel, the *K. daigremontiana* vacuolar malate channel is voltage-gated so that diffusion of malate is restricted to inward movements under low/negative membrane potentials (Pantoja and Smith, 2002; Hafke *et al.*, 2003). Patch clamp measurements of stochastic transitions between open and closed conformations of a single vacuolar malate channel have shown that the probability of an open, conductive conformation increases as membrane potential decreases, and the net effect over the whole vacuole is higher rates of inward conductance of malate (Hafke *et al.*, 2003). Intriguingly, inward-rectification was found to be stronger in the

vacuolar malate channel of *K. daigremontiana* in mature leaves, following CAM induction, relative to younger, $C_3$ leaves (Pantoja and Smith, 2002).

Plausible candidates for a CAM vacuolar membrane channel were identified by the discovery of the aluminium-activated malate transporter (ALMT) family (Holtum *et al.*, 2005). Transcriptional up-regulation of two ALMT genes has been found to accompany CAM induction by drought in the facultative CAM species *Talinum triangulare*, and down-regulation occurred as plants were re-watered and reverted to $C_3$ photosynthesis (Brilhaus *et al.*, 2016).

The prototypical ALMT, TaALMT1, was identified in the root apices of aluminium-tolerant varieties of *Triticum aestivum* (wheat). TaALMT1 exports malate across the plasma membrane in order to chelate, and thereby mitigate, toxic $Al^{3+}$ in the soil around roots (Sasaki *et al.*, 2004), as does an *Arabidopsis thaliana* homolog, AtALMT1 (Yamaguchi, 2005; Hoekenga *et al.*, 2006). There are as many as 14 genes in the *A. thaliana* ALMT gene family (Hoekenga *et al.*, 2006), including at least three encoding vacuolar anion channels: *AtALMT4* (Zhang, 2013), *AtALMT6* (Meyer *et al.*, 2011) and *AtALMT9* (Kovermann *et al.*, 2007). These ALMTs are part of a clade that is phylogenetically distinct from that containing *AtALMT1*, signifying that the vacuolar tonoplast membrane ALMTs have evolved their own unique amino acid signatures that likely associate with their specific targeting to the tonoplast membrane and their associated transport specificity for particular anions (Kovermann *et al.*, 2007; De Angeli *et al.*, 2013*a*; Palmer *et al.*, 2016).

AtALMT9 is perhaps the vacuolar ALMT that has been most fully characterised at the functional level. AtALMT9 has been reported to be permeable to malate, fumarate and chloride ($Cl^-$) (Kovermann *et al.*, 2007). The AtALMT9 homolog of *Vitis vinifera* was also characterised as a tonoplast-localised malate channel, and is thought to mediate malate accumulation in the

vacuoles of grape mesocarp (De Angeli *et al.*, 2013*a*). Although AtALMT9 assayed *in vitro* was found to conduct malate more rapidly than $Cl^-$ when the solutes were applied independently (Kovermann *et al.*, 2007), malate was later reported to be an allosteric activator of AtALMT9, leading to much more rapid conductance of $Cl^-$ (De Angeli *et al.*, 2013*b*). It was therefore concluded that AtALMT9 was most likely to mediate $Cl^-$ influx into the vacuole as part of the mechanism of light-induced stomatal opening in *A. thaliana* (De Angeli *et al.*, 2013*b*; Palmer *et al.*, 2016). There is, however, no indication of increasing $Cl^-$ conductance by the *K. daigremontiana* channel due to allosteric activation by malate (Lüttge *et al.*, 2000). Molecular modelling and site-directed mutagenesis studies have indicated that AtALMT9 is an α-helical integral membrane protein, and that multimerisation of AtALMT9 polypeptides forms the transmembrane anion pore via quaternary-structure interactions (Zhang *et al.*, 2013). AtALMT9 is an inward-rectifying anion channel, and, like the CAM vacuolar malate channel, single channel measurements have shown it undergoes stochastic conformational changes to an open conformation at increasing frequency as the vacuolar membrane electrical potential decreases (De Angeli *et al.*, 2013*b*).

AtALMT6 has been characterised as an inward-rectifying malate channel in guard cell vacuoles (Meyer *et al.*, 2011), and vacuolar malate import by AtALMT6 is thought to complement the aforementioned AtALMT9-mediated $Cl^-$ import in lowering the vacuolar osmotic potential during stomatal opening (Palmer *et al.*, 2016). As a vacuolar malate-specific channel, it is apparent that a homolog of AtALMT6 could be well-adapted for recruitment to CAM. Interestingly, AtALMT6 displayed anion selectivity for fumarate > malate > citrate ~ $Cl^-$ (Meyer *et al.*, 2011), which was consistent with findings reported for the *K. daigremontiana* vacuolar anion channel (Hafke *et al.*, 2003). Furthermore, AtALMT6 has been shown to

selectively exclude $Hmal^-$ from its channel pore (Meyer *et al.*, 2011), which, in CAM, would allow malate to be trapped by protonation after import into a low-pH vacuole, as discussed above (Fig. 3.1). However, some functional properties of AtALMT6 are not shared with the *K. daigremontiana* vacuolar anion channel. AtALMT6 requires activation by $Ca^{2+}$ (Meyer *et al.*, 2011), while the *K. daigremontiana* channel is $Ca^{2+}$-insensitive (Pantoja and Smith, 2002). AtALMT6 is activated by low pH in the vacuolar lumen (Meyer *et al.*, 2011), while the *K. daigremontiana* channel is not (Pantoja and Smith, 2002). Conversely, the *K. daigremontiana* channel is sensitive to inhibition by small decreases in cytoplasmic pH (Pantoja and Smith, 2002), while AtALMT6 is apparently insensitive to cytosolic pH (Meyer *et al.*, 2011).

Modulation of ALMT activity by post-translational modification could be an important factor in its putative role in CAM, as inhibition of tonoplast malate channels during Phase III would prevent futile re-import of malate into the vacuole. The molecular basis of kinase activation of malate channels has been probed using TaALMT1 and AtALMT12, expression of the latter being localised to guard cell plasma membranes (Meyer *et al.*, 2010). In a *Xenopus laevis* oocyte heterologous expression system for TaALMT1, malate channel activity was increased in the presence of protein kinase activators and reduced in the presence of a protein kinase inhibitors (Ligaba *et al.*, 2009). Under similar experimental conditions, channel opening of AtALMT12 (renamed as QUAC1) at negative membrane potentials was increased in the presence of the serine/threonine kinase Open Stomata 1, with which QUAC1 interacted (Mustilli *et al.*, 2002; Imes *et al.*, 2013).

### 3.1.2 Regulation of diurnal deacidification by the tonoplast

Vacuolar malate efflux in *Kalanchoë* CAM species occurs in response to increasing temperature (Friemert *et al.*, 1988; Kluge *et al.*, 1991*b*) and intensifying light (Barrow and Cockburn, 1982), and may be a direct output of circadian regulation (Carter *et al.*, 1995*a*). In earlier and more parsimonious models of the CAM system, it was held that $H_2$mal could diffuse through the lipid bilayer rather than through a specialised transport protein. In this model, permeability of the tonoplast to $H_2$mal would be increased by reconfiguration of lipid packing in the bilayer in response to increasing temperature at dawn. Expansion of the tonoplast due to rising turgor pressure resulting from increased malate concentration would increase the readiness of this response (Lüttge and Smith, 1984; Lüttge, 1986; Rygol *et al.*, 1987; Kliemchen *et al.*, 1993; Neff *et al.*, 1998). However, it has been suggested more recently that the rate of vacuolar malate efflux that could be attained by diffusion of $H_2$mal across the lipid bilayer alone is unlikely to suffice for malate breakdown *in vivo* (Holtum *et al.*, 2005).

Import and export of malate by $mal^{2-}$-specific channels in the CAM species *Graptopetalum paraguayense* has been proposed (Iwasaki *et al.*, 1992), more recently via bidirectional conductance of $mal^{2-}$ by vacuolar ALMTs (Palmer *et al.*, 2016). AtALMT6 does in fact display a degree of outward-rectifying malate channel activity at low or negative $\Delta\psi$ under *in vitro* conditions of low lumenal pH and high ratio of lumenal and cytosolic malate concentrations (Meyer *et al.*, 2011), and under such conditions outward conductance of malate from the vacuolar lumen would be possible. However, any model of vacuolar malate export must account for simultaneous breakdown of malate and deacidification by CAM photosynthetic tissues in the light (Lüttge and Ball, 1980; Iwasaki *et al.*, 1988; Hafke *et al.*, 2001). Measurement of a transient decrease in cytosolic pH in *K. daigremontiana* during diurnal breakdown of

nocturnally-accumulated malate has shown that malate and $H^+$ are exported simultaneously (Hafke *et al.*, 2001). Vacuolar malate export by a bidirectional $mal^{2-}$ channel cannot explain these observations without an additional $H^+$ exporter, working in the opposite direction to V-ATPase and/or PPase active transport of $H^+$ (Holtum *et al.*, 2005).

The simplest model for transporter-mediated vacuolar malate export in CAM is symport of 2 $H^+$ and $mal^{2-}$, whether the $mal^{2-}$ and $H^+$ are dissociated or with protonation of one or both of the carboxylate groups of malate (Smith *et al.*, 1996). This model would explain how the tonoplast could export both malate and $H^+$ by passive diffusion driven by concentration gradients of both solutes, with minimal transmembrane charge imbalance. The discovery of a plant $H^+$-organic acid symporter, known as the tonoplast dicarboxylate transporter (TDT), in *A. thaliana* (Emmerlich *et al.*, 2003) has raised the possibility that its orthologs act as a vacuolar malate exporter in CAM (Holtum *et al.*, 2005; Borland *et al.*, 2009).

AtTDT is a homolog of NaDC-1 (Emmerlich *et al.*, 2003), a mammalian $Na^+$-dicarboxylate transporter and member of the SLC13 family of $Na^+$ co-transporters (Pajor, 2014). NaDC-1 is thought to be an integral membrane protein comprising a single polypeptide chain with α-helical secondary structure. Carboxylate-specific members of the SLC13 family mediate transmembrane diffusion of a range of dicarboxylates, including malate and citrate, and are known to co-transport each mole of these substrates with 3-4 $Na^+$. As a result they are electrogenic by at least one positive charge (Pajor, 2014).

AtTDT is targeted for tonoplast localisation *in vivo*, and, unlike NaDC-1, selectively symports malate but not citrate, and $H^+$ but not $Na^+$ (Emmerlich *et al.*, 2003). When the cytosol is acidified, AtTDT is thought to mediate pH homeostasis by transporting malate to the cytosol, where its decarboxylation and oxidation by malic enzyme traps $H^+$ (Smith and Raven, 1979;

Hurth *et al.*, 2005; Martinoia *et al.*, 2007). Observations of increased *AtTDT* transcript in response to cellular acidification support this role (Hurth *et al.*, 2005).

The question of whether the transport mechanism of AtTDT is the $2H^+$:1 $mal^{2-}$ symport that could be adapted for CAM malate export, under the model given above, has yet to be unambiguously resolved. V-ATPase-dependent $H^+$ translocation was found to stimulate $^{14}C$-labelled malate uptake in isolated wild-type vacuoles to a far greater degree than those of an *AtTDT* knock-out mutant (Emmerlich *et al.*, 2003; Hurth *et al.*, 2005). This suggests that malate import by AtTDT is driven by a proton gradient, which would be uncharacteristic of an electroneutral $H^+$-malate symporter. However, there was no evidence in patch clamp studies that inward- or outward-rectifying malate transport was lost from an *AtTDT* knock-out mutation, or that AtTDT was anything other than an electroneutral transporter (Hurth *et al.*, 2005).

TDT has also been characterised in *Citrus x sinensis* as a citrate transporter (CsCit1) expressed in tonoplasts of the juice sac cells of orange fruit. $H^+$ efflux from purified tonoplast vesicles of *Saccharomyces cerevisiae* expressing *CsCit1* has been shown to depend on internal-external pH and citrate gradients, demonstrating $H^+$-citrate symport (Shimada *et al.*, 2006).

Although mechanistic data on plant $H^+$-malate symporters is relatively scarce, other data on mammalian homologs raise the possibility of gated malate efflux in CAM. Transport activity of the rabbit NaDC-1 homolog in a *X. laevis* oocyte heterologous expression system can be suppressed by a serine/threonine protein kinase activity (Pajor and Sun, 1999). If this function were conserved between the mammalian and *Kalanchoë* TDT, vacuolar malate efflux could be controlled by post-translational modification.

## 3.2 Results

### 3.2.1 Phylogenetic analysis of ALMT sequence data

A database of putative polypeptide sequences from an annotated draft genome sequence of *K. fedtschenkoi* (Hartwell *et al.*, unpublished data) was searched for prospective ALMT genes (*KfALMT*s) for phylogenetic analysis. BLASTP was used to align 13 of the 14 putative *A. thaliana* ALMT genes that have previously been described (Hoekenga *et al.*, 2006) with the *K. fedtschenkoi* database. *AtALMT11* was excluded from the phylogenetic analysis. The *AtALMT11* sequence is exceptionally short (152 amino acids), and therefore would reduce the power of the phylogenetic analysis by limiting the length of the TCoffee sequence alignment (see Section 2.9.3). No published functional information is available for *AtALMT11* that would have justified its inclusion by making the phylogenetic analysis more informative about uncharacterised *KfALMT*s.

12 predicted *KfALMT* amino acid sequences were retrieved from the BLASTP search results. Each of the sequences aligned with each of the *A. thaliana* sequences with an expected frequency (E) statistic of $<1 \times 10^{-20}$. Previous phylogenetic analyses have grouped ALMT genes into three clades (Clades I-III; Kovermann *et al.*, 2007; De Angeli *et al.*, 2013*a*; Palmer *et al.*, 2016). ALMTs in Clade II – including *AtALMT4*, *AtALMT6*, *AtALMT9* and *VvALMT9* – have mostly been functionally characterised as vacuolar anion channels (Table 3.1 and Section 3.1.1). A maximum-likelihood phylogeny was constructed from sequences of predicted *KfALMT*s, predicted and functionally-characterised *AtALMT*s, *TaALMT1* and *VvALMT9* (Table 3.1) using RaxML (Fig. 3.2).

Table 3.1 – Functional information on non-*K. fedtschenkoi* polypeptide sequences used in phylogenetic analysis

| Gene | Organ | Subcellular location | UniProtKB accession | Reference |
|---|---|---|---|---|
| *TaALMT1* | Root | Plasma membrane | Q76LB1 | Sasaki *et al.*, 2004; Yamaguchi *et al.*, 2005 |
| *AtALMT1* | Root | Plasma membrane (presumed) | Q9SJE9 | Hoekenga *et al.*, 2006 |
| *AtALMT4* | Leaf mesophyll, root | Vacuolar membrane | Q9C6L8 | Zhang, 2013 |
| *AtALMT6* | Guard cell, flower, mesophyll to a lesser extent | Vacuolar membrane | Q9SHM1 | Meyer *et al.*, 2011 |
| *AtALMT9* | Leaf mesophyll, guard cell, hypocotyl and root at some stages | Vacuolar membrane | Q9LS46 | Kovermann *et al.*, 2007; de Angeli *et al.*, 2013*b* |
| *VvALMT9* | Berry mesocarp | Vacuolar membrane (targeted) | D7SIX9 | de Angeli *et al.*, 2013*a* |
| *AtALMT12* | Guard cell, pollen, root stele | Plasma membrane | O49696 | Meyer *et al.*, 2010 |

Using this method, Clades II and III have been replicated with a mixture of *A. thaliana*, *K. fedtschenkoi* and *V. vinifera* sequences (Fig. 3.2). Bootstrap support for these clades was high (>70%), with the exception of some of the more distal internal ones (*AtALMT9*-*AtALMT3*-KF85525 and *AtALMT5*-*AtALMT6*). Five predicted *KfALMT*s were clustered in Clade II with the known vacuolar ALMT genes *AtALMT4*, *AtALMT6*, *AtALMT9* and *VvALMT9*. Conversely, Clade I was not replicated around a single node (Fig. 3.2), although this was arguably found in other analyses also (Kovermann *et al.*, 2007; Palmer *et al.*, 2016).

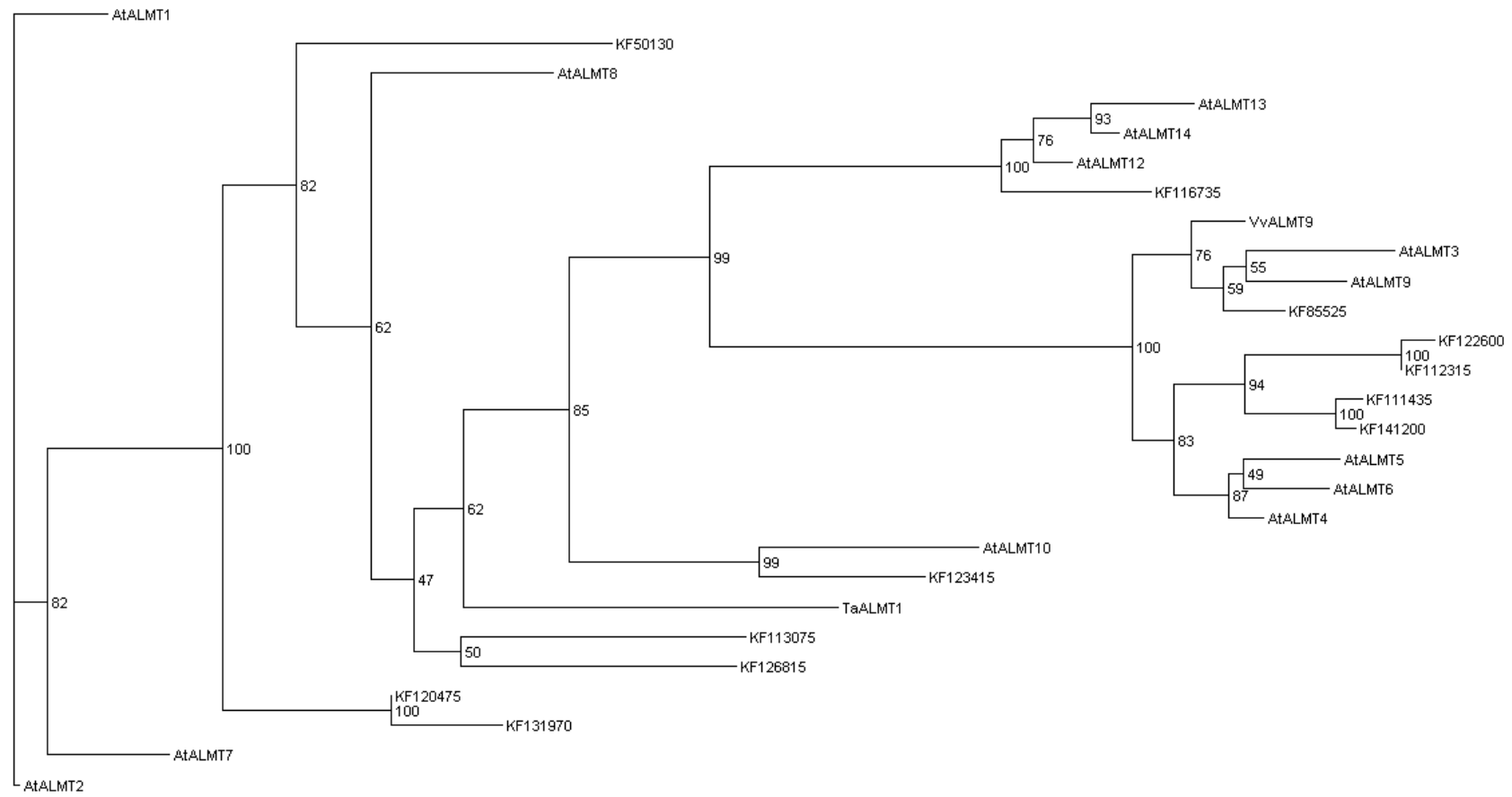


Figure 3.2 – Molecular phylogeny of peptide sequences of predicted and functionally-characterised ALMT genes. Comprehensive sets of *K. fedtschenkoi* (KF) and *A. thaliana* (*At*) *ALMT*s were included in the analysis, in addition to functionally-characterised *ALMT*s of *V. vinifera* (*Vv*) and *T. aestivum* (*Ta*). The phylogenetic tree topology was calculated by RaxML (Stamatakis, 2006). Branch length is proportional to the degree of evolutionary change inferred from aligned peptide sequences. Numbers at each branch give the support for that branch from 1000 iterations of bootstrap analysis.

### 3.2.2 Analysis of differential transcriptional regulation of *KfALMT*s using *K. fedtschenkoi* quantitative RNA-seq data

Quantitative RNA sequencing (RNA-seq) datasets were generated for 12:12 LD timecourse samples of *K. fedtschenkoi* $C_3$ (leaf pair 1, LP1) and CAM (leaf pair 6, LP6) tissues by the Hartwell group and collaborators, separately from this PhD project (see above, section 2.9.1). This has provided a comprehensive dataset revealing the steady-state abundance of individual gene transcripts over a 12:12 LD cycle in $C_3$ and CAM leaves, which can be used to predict gene family members that may be involved in the biology of CAM tissues, as differentiated from that of $C_3$ tissues (Hartwell *et al.*, 2016). This dataset was mined for functional and gene-level regulatory information on the *K. fedtschenkoi* ALMT family.

Steady-state transcript levels varied considerably amongst the *KfALMT*s that were identified in the genome, with several displaying only the nominal presence of detectable transcript (Fig. 3.3). KF122600 was detected at higher levels than any other *KfALMT* gene in both LP1 and LP6. More importantly, KF122600 transcript levels were up-regulated following CAM induction. Transcript levels of KF112315 were also higher following CAM induction in LP6, and higher in both LP1 and LP6 than the remaining putative *KfALMT*s. Transcript levels of other putative *KfALMT*s were either lower in LP6 than in LP1, or very low relative to KF122600 and KF112315, or both (Fig. 3.3).

As previously mentioned in this chapter, some vacuolar ALMTs are involved in the control of guard cell turgor and thus stomatal aperture (De Angeli *et al.*, 2013*b*; Palmer *et al.*, 2016). In a second quantitative RNA-seq experiment, also separate to this PhD project, LP6 were collected from WT *K. fedtschenkoi* at 2 h intervals over a 12:12 LD cycle and epidermal peels were removed to be sampled separately to the remainder of the leaf tissue (see above, Section

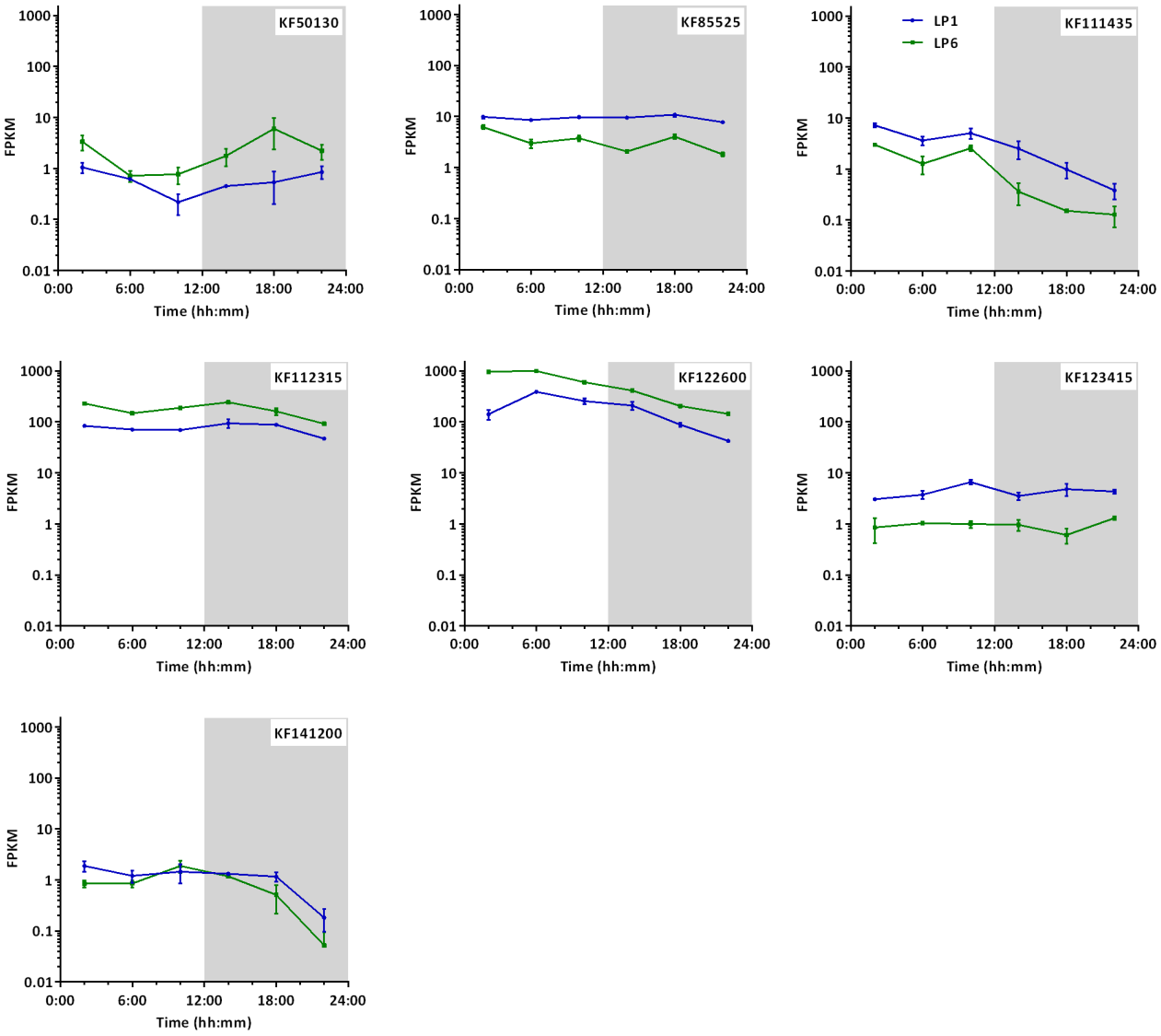


Figure 3.3 – Relative transcript levels of *K. fedtschenkoi* predicted ALMT genes in whole $C_3$ (leaf pair 1, LP1) and CAM (leaf pair 6, LP6) leaves over a 12:12 LD cycle. Relative transcript levels were determined by SOLiD RNA-seq (see Section 2.9.1). Relative transcript levels are expressed as the number of SOLiD sequence fragments aligned per kilobase CDS per million total reads (FPKM). Each point represents the mean ± S.E.M. of 3 independent samples. Grey shading represents the dark period. Transcript time-courses are not shown where sequenced transcript in total over the LD cycle was <5 FPKM.

2.9.1). Epidermal peels are enriched for guard cells, and the dataset generated from this RNA-seq experiment has provided information on differential transcript-level regulation between guard

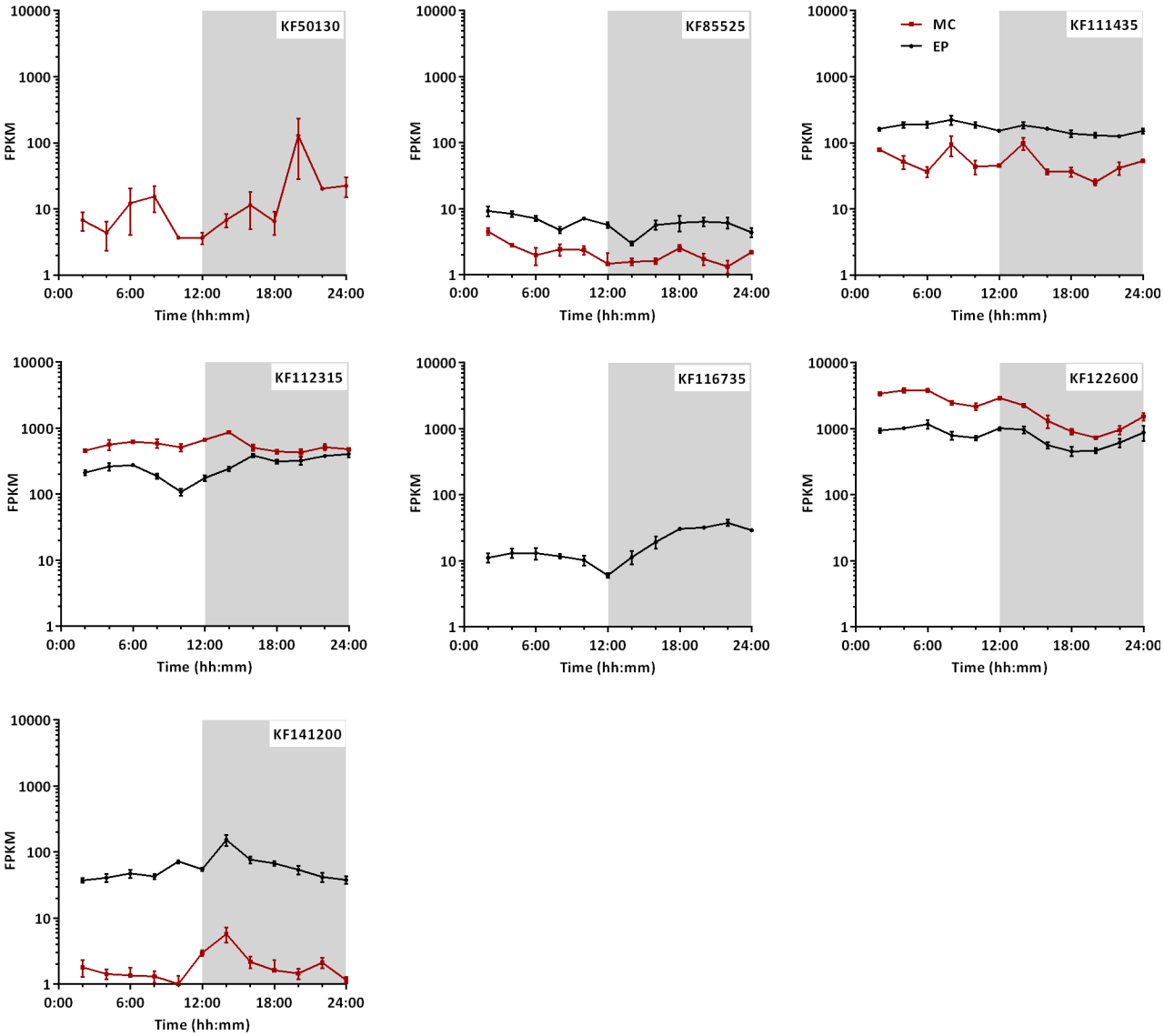


Figure 3.4 – Relative transcript levels of *K. fedtschenkoi* predicted ALMT genes in leaf mesophyll (MC) and epidermal peels (EP) of WT CAM leaves (LP6) over a 12:12 LD cycle. Relative transcript abundance was determined by SOLiD RNA-seq (see Section 2.9.1). Relative transcript levels are expressed as the number of SOLiD sequence fragments aligned per kilobase CDS per million total reads (FPKM). Each point represents the mean ± S.E.M. of 3 independent samples. Grey shading represents the dark period. Transcript time-courses are not shown where sequenced transcript in total over the LD cycle was < 20 FPKM.

cells and leaf mesophyll cells, which may be used to infer a functional role for individual genes in stomatal control (Hartwell *et al.*, unpublished results).

Several predicted *KfALMT* transcripts were differentially abundant in the epidermal peels relative to the mesophyll (Fig. 3.4). However, the *KfALMT*s with the first- and second-highest transcript levels in both epidermal peels and leaf mesophyll were, again, KF122600 and KF112315, respectively. For both of these candidate CAM-associated *KfALMT* genes, transcript levels were higher in the leaf mesophyll compared to the epidermal peels. While other predicted *KfALMT*s (KF85525, KF111435, KF116735, KF141200) displayed differential up-regulation of steady-state transcript level in epidermal peels, their transcript levels in both epidermal peels and leaf mesophyll were low relative to the levels of KF112315 or KF122600 transcript in the same samples (Fig. 3.4).

### 3.2.3 Transgenic RNA interference of *KfALMT* and *KfTDT*

Prior to the start of this PhD project, transcriptomics of WT *K. fedtschenkoi* $C_3$ and CAM tissues was used to identify an *AtALMT* ortholog that displayed enhanced transcript abundance in CAM leaves. An assembled EST of this transcript was used to design a hairpin double-stranded RNA (dsRNA) that would target the transcript of the CAM-associated *KfALMT* for RNAi-mediated silencing. The hairpin dsRNA was designed to degrade a section of the transcript located partially in the 5' UTR in order to increase the likelihood of specifically targeting the CAM-associated transcript to the exclusion of other *KfALMT* family genes. The chosen sequence was PCR amplified and cloned into an RNAi binary vector. WT *K. fedtschenkoi* were then transformed with the vector by *Agrobacterium* transformation (see above, Section 2.2.10). The stable transgenic lines generated are hereafter referred to as *KfALMT* RNAi lines.

Subsequently to the generation of *KfALMT* RNAi lines, whole genome sequencing, assembly and annotation of the 246 Mb *K. fedtschenkoi* was completed (see above, Section

# A

```
Kaladp0024s0194.1:   83 TGGAAACTCTGAGCATGTGGTGGAGTGAAATCACTGTCCAAACCTGAGAT 132
                         ||||||||||||||||||||||||||||||||||||||||||||||||||
dsRNA:                1 TGGAAACTCTGAGCATGTGGTGGAGTGAAATCACTGTCCAAACCTGAGAT 50

Kaladp0024s0194.1:  133 TGGATCCATTTCTTAATTTCACTCTTTTTCAAG 165
                         |||||||||||||||||||||||||||||||||
dsRNA:                61 TGGATCCATTTCTTAATTTCACTCTTTTTCAAG 83


Kaladp0024s0194.1:  267 CCTGAAACTTATATTGATGCAACATTTGCGGGCATCAGGAAA 309
                         |||||||||||||||||||||||||||||||||||||||||||
dsRNA:                83 CCTGAAACTTATATTGATGCAACATTTGCGGGCATCAGGAAA 125


Kaladp0024s0194.1:  428 AAGCAAAGATGGCACCTCGAACAGGATCCTTCAGG-CACAGTTTCTTGGA 476
                         |||||||||||||||||||||||||||||||||| ||||||||||||||
dsRNA:              126 AAGCAAAGATGGCACCTCGAACAGGATCCTTCAGGGCACAGTTTCTTGGA 175

Kaladp0024s0194.1:  477 AAAGAGCAAGGAAAGACTCCTATCAAGGAAAGGGTATTCAGAGCTGGGGC 526
                         |||||||||||||||||| ||||||||||||||||||||||||||||||
dsRNA:              176 AAAGAGCAAGGAAAGACTTCTATCAAGGAAAGGGTATTCAGAGCTGGGGC 225
```

# B

```
Kaladp0073s0021.1:   49 TGGAAACTGTAAACATGGGGAGCAGTGAACTCACTCTCTGGAACTGAGGC 98
                         |||||||| | | |||| || | |||||| ||||| ||   | |||||
dsRNA:                1 TGGAAACTCTGAGCATGTGGTGGAGTGAAATCACTGTCCAAACCTGAGAT 60

Kaladp0073s0021.1:  109 TGGATCCATTTCTTATCCTCACTCTTCCTCAA 130
                         ||||||||||||||   ||||||||  ||||
dsRNA:                61 TGGATCCATTTCTTAATTTCACTCTTTTTCAA 82


Kaladp0073s0021.1:  129 AAAATCAAAGATGGGACCTCGACCAGGTTCATTCAGG-CACAGTTTCTTG 177
                         |||| ||||||||| ||||||| |||| || |||||| ||||||||||||
dsRNA:              124 AAAAGCAAAGATGGCACCTCGAACAGGATCCTTCAGGGCACAGTTTCTTG 173

Kaladp0073s0021.1:  178 GAAAAGAGCAAGGAAAGACTTCTATCAAGGAAAGGGTATTCAGAGCTGGG 227
                         |||||||||||||||||||||||||||||||||||||||||||||||||
dsRNA:              174 GAAAAGAGCAAGGAAAGACTTCTATCAAGGAAAGGGTATTCAGAGCTGGG 223

Kaladp0073s0021.1:  228 GC 229
                         ||
dsRNA:              224 GC 225
```

# C

```
Kaladp0062s0038.1:  224 AGCCACAATGGCGGCGCGAATCGGATCGTACCGGCCG-AGTTTCACAGAC 272
                         ||| |  ||||  | ||||  |||| | | || |  ||||||   ||
dsRNA:              127 AGCAAAGATGGCACCTCGAACAGGATCCTTCAGGGCACAGTTTCTTGGAA 176

Kaladp0062s0038.1:  273 AAGAGCAAGGAGAG 286
                         ||||||||||| ||
dsRNA:              177 AAGAGCAAGGAAAG 190
```

2.9.1). A BLAST database of predicted transcript sequences from this genome annotation was used to determine which of the predicted *KfALMT*s would likely be silenced in *KfALMT* RNAi lines. The database was searched using BLASTN with the RNA hairpin-encoding sequence as a key. The parameters of the BLASTN algorithm were adjusted to maximise its sensitivity to low-identity alignments: The minimum exact sequence match ('word') required to begin an alignment was reduced to its lowest permitted length (4 bp), the mismatch penalty was increased to its maximum (i.e. least negative) permitted value (-1), and the low-complexity filter was deactivated. Paired alignments of >30 bp were found between three of the predicted *KfALMT* transcripts and the *KfALMT*-targeting sequence (Fig. 3.5). Kaladp0024s0194.1 aligned with the hairpin sequence over the complete length of the latter with >99% sequence identity, although the three portions of the transcript that aligned with the *KfALMT*-targeting sequence were interspersed with non-matching portions (Fig. 3.5A). 5' and 3' portions of the *KfALMT*-targeting sequence were found to align with Kaladp0073s0021.1 with 76% and 94% identity, respectively, with 100% identity along the 3' 66 bp of the alignment. This alignment covered the entire 5' UTR of the predicted transcript (Fig. 3.5B). A 64 bp section of Kaladp0062s0038.1 aligned with the *KfALMT*-targeting sequence with 70% sequence identity (Fig. 3.5C). Each of the alignments traversed the predicted start codon, as intended in the original design of the hairpin RNA.

---

Figure 3.5 – Pair-wise BLASTN alignments of the double-stranded RNA (dsRNA) used to generate *KfALMT* RNAi transgenics with predicted *K. fedtschenkoi* transcripts. The published *K. fedtschenkoi* transcriptome (Section 2.9.1) was used as the database for the BLASTN search. Black-on-white highlighting indicates the primer sequences. Blue lettering represents the predicted Start/Met codon.
A - Kaladp0024s0194.1 (KF112315)
B - Kaladp0073s0021.1 (KF122600)
C - Kaladp0062s0038.1 (KF111435)

Table 3.2 - Summary of BLASTP alignments of predicted *KfALMT* peptide sequences from two *de novo* assemblies of the *K. fedtschenkoi* genome.

| Predicted peptide, draft genome annotation | | | | Predicted peptide, completed genome (Phytozome) annotation | | | | Length of ungapped alignment (aa) | ID (%) | Gaps (± aa) |
|---|---|---|---|---|---|---|---|---|---|---|
| # | TL | S | E | # | TL | S | E | | | |
| KF50130 | 388 | 6 | 388 | Kaladp0011s0027.1 | 483 | 101 | 483 | 383 | 100 | - |
| KF85525 | 581 | 1 | 581 | Kaladp0048s0850.1 | 585 | 5 | 585 | 581 | 100 | - |
| | | 144 | 581 | Kaladp0048s0850.2 | 438 | 1 | 438 | 438 | 100 | - |
| KF111435 | 588 | 1 | 588 | Kaladp0062s0038.1 | 571 | 1 | 571 | 571 | 100 | -17 |
| KF112315 | 575 | 1 | 559 | Kaladp0024s0194.1 | 574 | 1 | 559 | 559 | 99 | - |
| KF113075 | 432 | 36 | 418 | Kaladp0011s0304.1 | 434 | 5 | 420 | 383 | 99 | +33 |
| KF116735 | 542 | 1 | 542 | Kaladp0091s0013.1 | 542 | 1 | 542 | 542 | 99 | - |
| KF120475 | 445 | 1 | 444 | Kaladp0093s0149.1 | 511 | 1 | 444 | 444 | 99 | - |
| KF122600 | 569 | 1 | 569 | Kaladp0073s0021.1 | 569 | 1 | 569 | 569 | 99 | - |
| KF123415 | 500 | 1 | 500 | Kaladp0007s0011.1 | 500 | 1 | 500 | 500 | 99 | - |
| KF126815 | 481 | 1 | 355 | Kaladp0696s0001.1 | 372 | 1 | 353 | 353 | 99 | -2 |
| KF131970 | 485 | 1 | 485 | Kaladp0011s0028.1 | 512 | 1 | 512 | 485 | 95 | +19, +8 |
| KF141200 | 569 | 78 | 569 | Kaladp0050s0298.1 | 492 | 1 | 492 | 492 | 99 | - |
| | | 170 | 569 | Kaladp0050s0298.2 | 400 | 1 | 400 | 400 | 99 | - |
| | | 170 | 569 | Kaladp0050s0298.3 | 400 | 1 | 400 | 400 | 99 | - |
| KF148075 | 559 | 1 | 548 | Kaladp0042s0251.1 | 541 | 1 | 530 | 530 | 99 | -18 |

Abbreviations: TL, total length of peptide sequence; S and E, number of amino acid residue at the N-terminal and C-terminal ends of the alignment, respectively; ID, sequence identity of ungapped alignment. Each gap is listed as an insertion in (+ sign) or deletion (- sign) from the KaladpXXXXsXXXX.X sequence.

A BLAST library of peptide sequences that were predicted by the completed *K. fedtschenkoi* genome annotation was searched using BLASTP with the low-complexity filter deactivated, and with each of the 12 *KfALMT* peptide sequences included in the phylogenetic analysis as a search key. This matched predicted peptide sequences of the draft genome annotation (Figs. 3.2-3.4) and those of the completed annotation (Fig. 3.5). The highest-identity match(es) returned for each sequence are displayed in Table 3.2. The sequence identity of most of these alignments was 99-100%, although discreet gaps in the alignments suggested that the pairs of predicted peptide sequences differed in the inclusion or exclusion of certain exons. Despite these minor differences, these pairs of sequences are considered to represent the same gene.

In order to compare the amino acid sequences of Kaladp0024s0194.1/KF112315 and Kaladp0073s0021.1/KF122600, the predicted *KfALMT*s that were likely to be targeted for RNAi-mediated silencing in *KfALMT* RNAi lines, the predicted peptide sequences from the completed *K. fedtschenkoi* genome were aligned with the peptide sequence for the functionally-characterised vacuolar malate transporter *AtALMT6* (Table 3.1) using TCoffee (Fig. 3.6). Based on this alignment, the two *K. fedtschenkoi* sequences were 91.4% identical, excluding a 5 a.a. insertion in Kaladp0024s0194.1. By contrast, several indels were present in the alignments of Kaladp0024s0194.1 and Kaladp0073s0021.1 with *AtALMT6*, and the ungapped alignments were 59.6% and 60.6% identical, respectively (Fig. 3.6).

Generation of stable transgenic lines with RNAi-mediated silencing of *K. fedtschenkoi TDT* (*KfTDT* RNAi lines) was also completed prior to the start of this PhD project. An EST with high sequence similarity to *AtTDT* (AT5G47560.1) was selected to design a *KfTDT*-specific dsRNA sequence of 562 bp, complementary to part of the *KfTDT* coding sequence, to be cloned

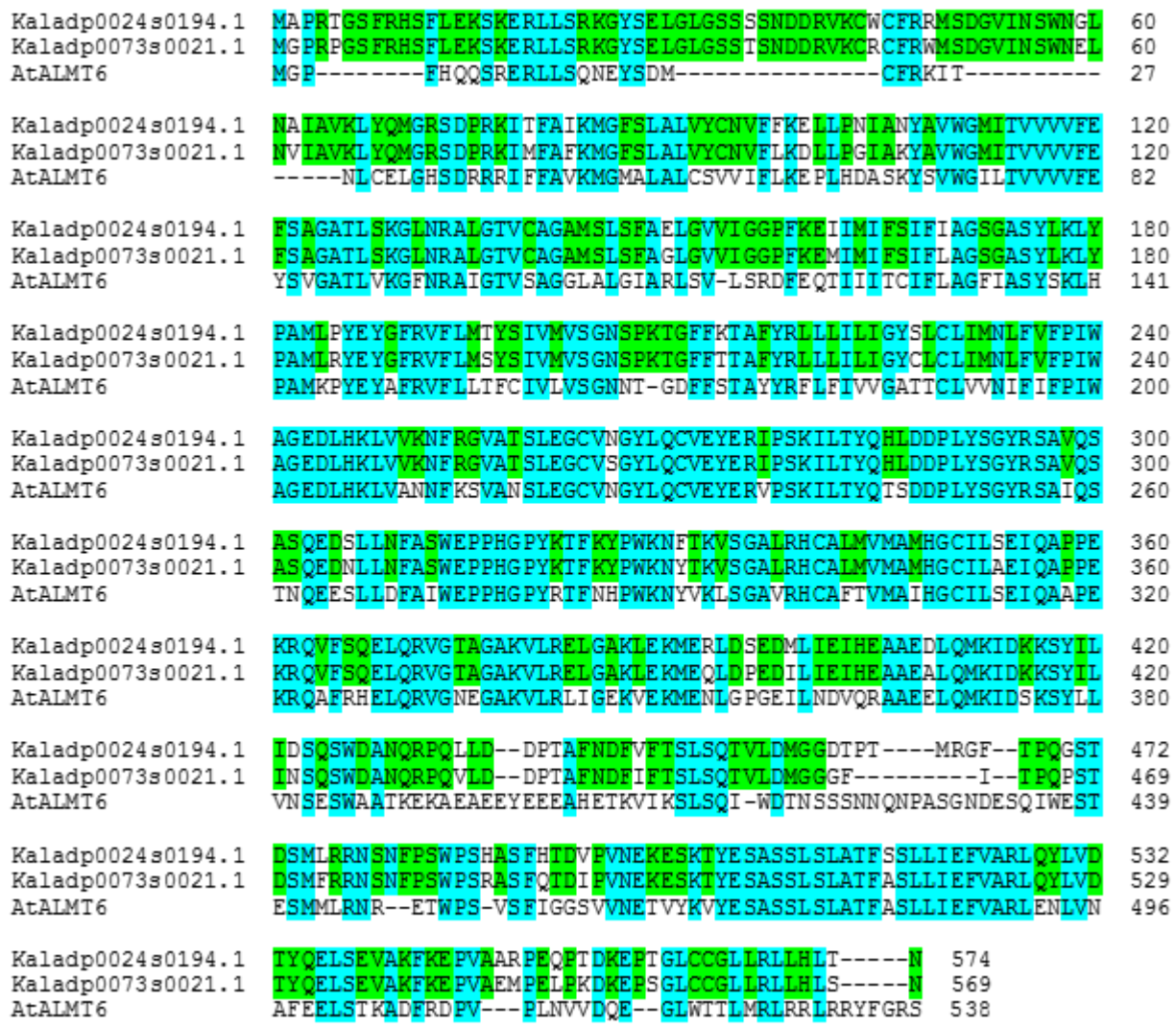


Figure 3.6 – Multiple sequence alignment of the predicted peptide sequences of the two *KfALMT*s that were thought to have been targeted for silencing in *KfALMT* RNAi transgenic lines, and *AtALMT6*. Sequences were aligned using TCoffee. Reference sequences for the *KfALMT*s were taken from the most recent *K. fedtschenkoi* genome annotation (see Section 2.9.1). Blue highlighting identifies residues that are conserved between the sequences; green highlighting identifies residues that are conserved between KF112315 and KF122600 only.

into the RNAi binary vector. This vector construct was, again, transformed into WT *K. fedtschenkoi* using *Agrobacterium*.

A BLASTN search of *K. fedtschenkoi* predicted transcript sequences found that the hairpin dsRNA sequence aligned with the predicted *KfTDT* transcript (Kaladp0042s0251.1/

KF148075) over the entire length of the former and with 99% sequence identity. The next highest-scoring alignment was only 60 bp long and 70% identical. BLASTP alignment of the peptide sequence of Kaladp0042s0251.1 with the TAIR10 library of *A. thaliana* protein sequences found the two sequences to be 72% identical.

### 3.2.4 Preliminary screening of *KfALMT* RNAi and *KfTDT* RNAi lines

Decreased pH during the night is tightly coupled to malate accumulation in CAM photosynthetic tissues. The pH indicator chlorophenol red was used to screen for differences in leaf cell sap acidity between *KfALMT* RNAi and *KfTDT* RNAi lines and WT controls, as described previously (Cushman *et al.*, 2008*a*; Dever *et al.*, 2015). A selection of developmentally-synchronised stem cuttings of independent candidate lines were entrained to 12:12 LD. At 2 h before dusk (10:00) and 2 h before dawn (22:00), leaf discs were punched from CAM leaves (LP6) for chlorophenol red-based screening of cell sap acidity. Two cohorts of *KfALMT* RNAi and *KfTDT* RNAi lines were screened, each with their own wild type controls for comparison (Fig. 3.7).

No change was detected in the diel acidity fluctuations between any of the *KfTDT* RNAi lines and wild type controls (Fig. 3.7A and B). An observation of increased acidity at 10:00 in one line, *KfTDT* RNAi 52A (Fig. 3.7A), was not replicated in a second screen (Fig. 3.7B). Leaf discs from independent *KfALMT* RNAi lines were consistently less acidic at 22:00 than wild type controls were, indicating that less malate had been synthesised during the dark period (Fig. 3.7B). Acidity of *KfALMT* RNAi leaf discs at 10:00 was consistently in the range of wild type controls.

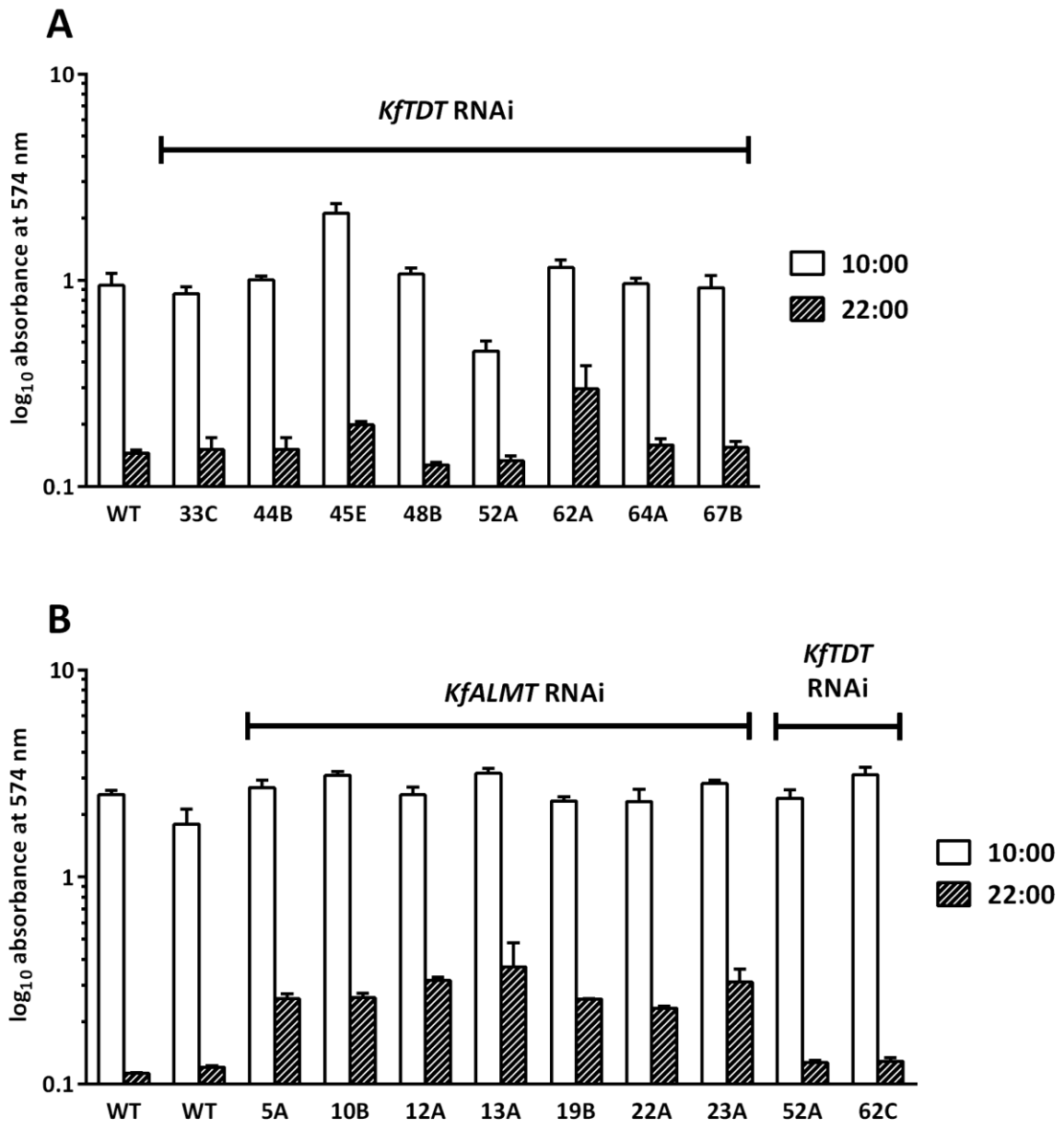


Figure 3.7 – Screening of leaf discs of *KfALMT* RNAi and *KfTDT* RNAi mutant lines with the pH indicator chlorophenol red. Protonation of the indicator at low pH decreases absorbance at 574 nm. A and B show the results of screening of two cohorts of plants entrained to 12:12 LD, with samples taken as punched leaf discs at 2 h before the start of the dark period (10:00) and 2 hours before the start of the light period (22:00). Bars show $\log_{10}$ of the mean ± S.E.M. of 3 leaf discs punched from the same leaf.

### 3.2.5 Preliminary phenotyping of a single *KfTDT* RNAi line

As for *KfALMT*s (Figs. 3.3 and 3.4), quantitative RNA-seq datasets were informative about differential regulation of *KfTDT* steady-state transcript levels in CAM leaves and CAM leaf mesophyll, relative to $C_3$ leaves and CAM leaf epidermal peels, respectively, over a 12:12 LD cycle. There was a large diel oscillation in the steady-state transcript abundance of *KfTDT* in each of the sampled leaf tissues (Fig. 3.8). Some minor differences were found in the diel patterns of transcript oscillation in CAM leaf mesophyll and whole CAM leaves in the separate RNA-seq experiments, but in general, transcript levels reached their daily trough late in the light period and increased throughout the dark period to a broad peak spanning the dark-light transition (Fig. 3.8). *KfTDT* transcript levels were consistently higher in CAM leaf mesophyll samples than in epidermal peels over the 12:12 LD cycle (Fig. 3.8A). *KfTDT* steady-state transcript abundance was up-regulated by more than two-fold in CAM leaves sampled in the light period at 02:00 and 06:00, relative to $C_3$ leaves, but was detected at similar or higher levels in $C_3$ leaves compared to CAM leaves in the dark period (Fig. 3.8B).

*KfTDT* RNAi line 80A was selected on the basis of previous screening done in the Hartwell lab (Kneřova, Boxall, Dever and Hartwell, personal communication). *KfTDT* RNAi 80A and WT were grown side-by-side under greenhouse conditions for 11 weeks, beginning with adventitious plantlets, and then entrained to 12:12 LD. CAM leaf (LP6) samples were collected at 4 h intervals beginning in the light period at 02:00 and ending at 22:00 in the dark period. Relative *KfTDT* transcript levels were measured by RT-qPCR in LP6 samples taken in the middle of the light period (06:00), on the basis that the reduction of transcript level by RNAi should be measured at a time when it would be expected to be at its daily peak, according to

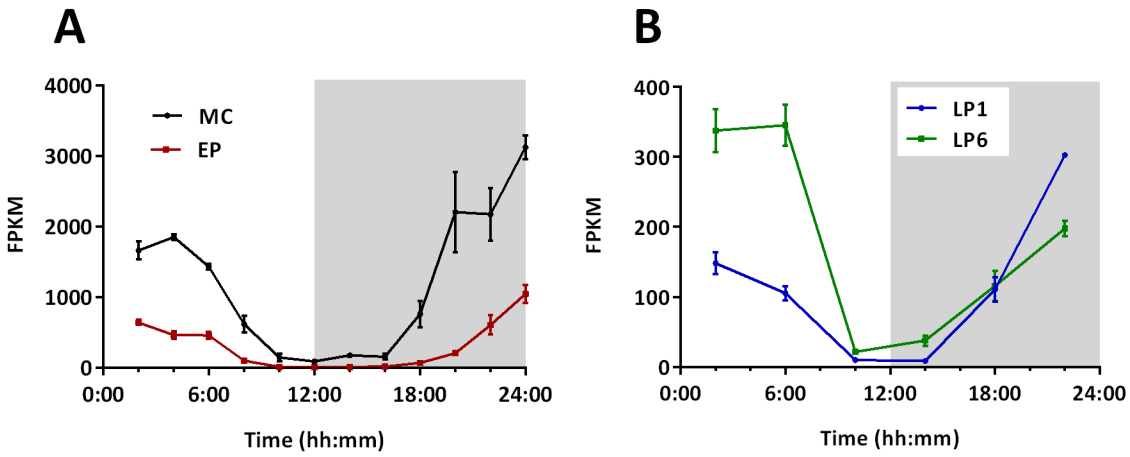


Figure 3.8 – Variation of relative steady-state transcript abundance of *KfTDT* over a 12:12 LD cycle in different *K. fedtschenkoi* tissues. Relative transcript level is presented as the number of SOLiD RNA-seq sequence fragments aligned to *KfTDT* predicted transcript per kilobase CDS per million total reads (FPKM). Each point is the mean ± S.E.M. of 3 independent samples. Grey shading represents the duration of the dark period.
A – *KfTDT* transcript in mesophyll (MC) and epidermal peels (EP) of leaf pair 6.
B – *KfTDT* transcript in $C_3$ (leaf pair 1/LP1) and CAM (leaf pair 6/LP6) leaves.

RNA-seq data (Fig. 3.8). *KfTDT* transcript abundance was markedly and significantly reduced in *KfTDT* RNAi 80A compared to the WT control (Fig. 3.9A).

Soluble metabolites were extracted from LP6 samples collected 2 h before the end of the light period (10:00) and 2 h before the end of the dark period (22:00). A minor, but statistically significant, reduction in leaf malate concentration at 22:00 was found in *KfTDT* RNAi 80A relative to wild type (Fig. 3.9B). Conversely, a significant relative increase was found in citrate concentration at both 10:00 and 22:00 in *KfTDT* RNAi 80A (Fig. 3.9C). Consequently, the difference between mean LP6 citrate concentration at 10:00 and 22:00 was somewhat reduced in *KfTDT* RNAi 80A.

Wild type and *KfTDT* RNAi 80A stem cuttings were grown under greenhouse conditions for 7 weeks, then entrained to 12:12 LD, and CAM leaves (LP6) were detached for measurement

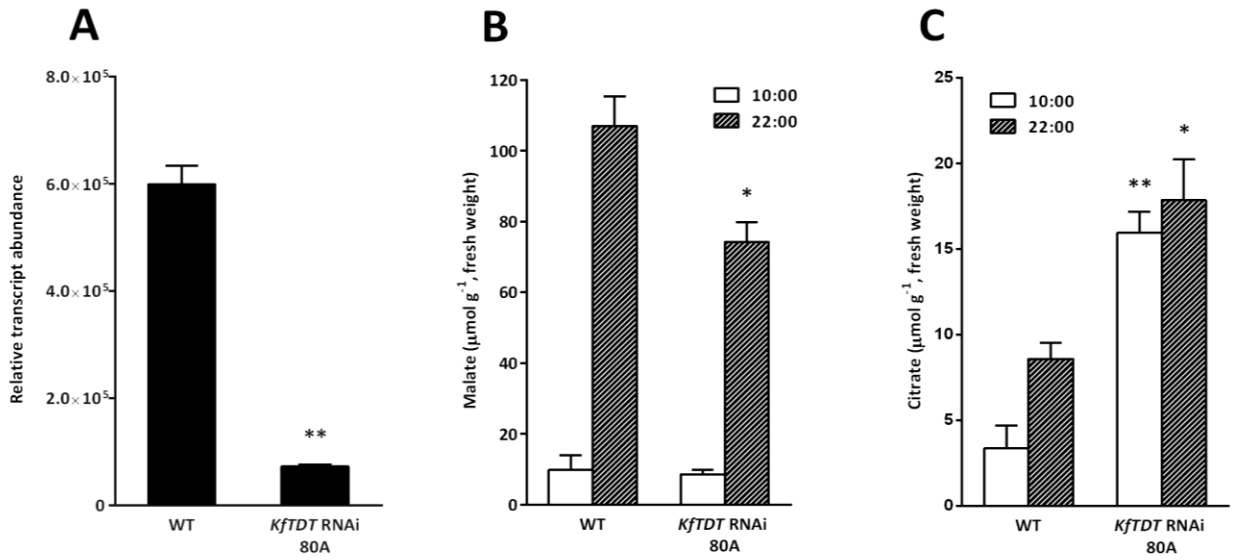


Figure 3.9 – Phenotyping of a *KfTDT* RNAi line, 80A. CAM leaves (leaf pair 6, LP6) were sampled for the analyses at various point in a 12:12 LD cycle. Bars represent mean ± S.E.M., n = 3. The results of Welch's t-test of difference between simultaneous measurements are displayed above the columns: $P > 0.05$, not shown; $P \leq 0.05$, *; $P \leq 0.01$, **.
A – *KfTDT* relative transcript abundance measured using RT-qPCR. cDNA to be analysed by RT-qPCR was synthesised from total RNA extracts of LP6 sampled in the middle of the light period (06:00).
B – Malate concentration in LP6 sampled at 2 h before the end of the light period (10:00) and 2 h before the end of the dark period (22:00).
C – Citrate concentration in LP6 at 10:00 and 22:00.

of $CO_2$ gas exchange using an IRGA system. No consistent differences were apparent in the dark-period rate of $CO_2$ uptake ($J_{CO2}$), or its temporal control, in the comparison between *KfTDT* RNAi 80A and WT leaves (Fig. 3.10). There was a rapid increase in $J_{CO2}$ following the beginning of the dark period, peaking 4-6 h into the dark period, followed by a more gradual decrease in $J_{CO2}$ through to the beginning of the light period, when it fell off rapidly (Fig. 3.10). In both WT LP6 sampled, there was marked Phase II and Phase IV $CO_2$ uptake in the first full light period, but $CO_2$ gas exchange in all CAM leaves was almost completely suppressed in the second light period.

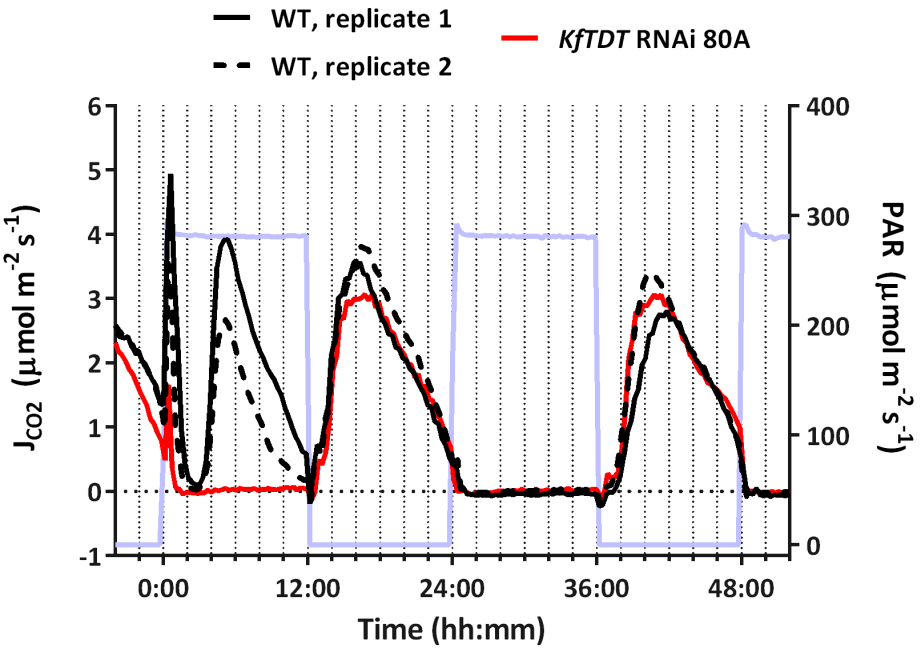


Figure 3.10 – Timecourse of $CO_2$ gas exchange measured in detached CAM leaves of *KfTDT* RNAi 80A and WT under 12:12 LD. Leaf pairs were detached from the stem and placed in the IRGA cuvette at ~12 h before the beginning of the first light period (0:00). Net $CO_2$ uptake occurred when $J_{CO2} > 0$, and is normalised to leaf area. Photosynthetically active radiation (PAR) is also displayed (blue).

## 3.3 Discussion

### 3.3.1 Two relatively abundant *K. fedtschenkoi* vacuolar ALMT transcripts are predicted to have been silenced in *KfALMT* RNAi lines

The *KfALMT* RNAi and *KfTDT* RNAi lines studied here were generated in the Hartwell lab as part of a previous BBSRC-funded grant. RNAi binary vector constructs were cloned and stable lines expressing transgenic hairpin RNA were produced prior to the beginning of this PhD project. *K. fedtschenkoi* quantitative RNA-seq data was used for the initial identification of the candidate *KfALMT* genes, and it is important to note that this was done prior to the availability of the annotated whole-genome sequence for *K. fedtschenkoi*. The *KfALMT* RNAi binary vector produced can now be predicted, on the basis of BLASTN alignments with the annotated *K. fedtschenkoi* genome (Fig. 3.5), to target two of the putative *KfALMT*s identified in the whole genome sequence, namely KF112315 and KF122600. KF112315 and KF122600 are very closely-related *KfALMT*s that belong to the well-characterised ALMT4/5/6 clade of tonoplast-localised anion channels in *A. thaliana* (Fig. 3.2). There was a low level of sequence divergence between the predicted amino acid sequences of KF112315 and KF122600 (Fig. 3.6). Less than half of the RNAi fragment's hairpin dsRNA product aligns with KF122600 (Fig. 3.5B). However, because the basic determinant of RNAi sequence specificity is the cleavage of dsRNA into 21 to 24 bp small interfering RNAs (siRNAs) by Dicer-like enzymes (Fusaro *et al.*, 2006; Small, 2007), it appears likely that KF122600 transcripts would be silenced by this construct along with those of KF112315, which is a near-perfect match for the RNAi fragment (Fig. 3.5A). BLASTN aligned 63 bp of the predicted transcript of a third *KfALMT*, KF111435, with the

*KfALMT* RNAi dsRNA sequence, but with relatively low sequence identity (73%, Fig. 3.5C), and therefore this transcript is not predicted to be silenced in *KfALMT* RNAi lines.

Sub-cellular localisation of KF112315 and KF122600 to the vacuolar membrane may be inferred from the phylogeny of the *KfALMT* gene family relative to the functionally-characterised *AtALMT*s that have been demonstrated experimentally to localise to the tonoplast membrane (Fig. 3.2). Of the *AtALMT*s, KF112315 and KF122600 were closest related to a clade containing *AtALMT4* and *AtALMT6*, both known to be tonoplast-localised malate channels (Meyer *et al.*, 2011; Zhang, 2013). Expression of fusion constructs of these *K. fedtschenkoi* genes with green fluorescent protein (GFP), in combination with fluorescence microscopy, could now be used to confirm their localisation to the tonoplast *in vivo* (Kovermann *et al.*, 2007; Meyer *et al.*, 2011; Zhang, 2013).

The available *K. fedtschenkoi* quantitative RNA-seq data revealed that transcript levels of KF112315 and KF122600 both increased coincident with the development of CAM in LP6 (Fig. 3.3), supporting a potential role for both of these KfALMTs in the CAM pathway. The steady-state transcript levels of both genes in epidermal peels of CAM leaves were high relative to other *KfALMT* family transcripts in the same samples, but low relative to their respective levels in leaf mesophyll (Fig. 3.4). It is important to consider the possibility that KF112315 and KF122600, the two *KfALMT*s that are predicted to be targeted for silencing by RNAi in the *KfALMT* RNAi lines, may have roles in mediating both nocturnal vacuolar malate import in CAM mesophyll and anion movements in guard cells associated with stomatal control. *AtALMT6* itself is expressed primarily in guard cells and is thought to participate in stomatal opening (Meyer *et al.*, 2011). However, *AtALMT6* knockout mutants retain normal stomatal control, presumably due to redundancy among the vacuolar AtALMTs (Meyer *et al.*, 2011). Likewise, the KF112315-

KF122600 clade contains two additional putative *KfALMT*s, KF111435 and KF141200, and both of their transcripts were more abundant in epidermal peels than leaf mesophyll (Fig. 3.4). Transcript of these genes showed decreased steady-state abundance following CAM induction in intact LP6, but as guard cells comprised a small proportion of the tissue sampled in such samples, this need not indicate their transcriptional repression in guard cells of CAM leaves.

The phylogenetic analysis presented above, combined with the quantitative RNA-seq data, may be used provisionally to assign functions to other members of the *KfALMT* gene family. KF85525 is the predicted *KfALMT* most closely-related to *AtALMT9* (Fig. 3.2). This gene displayed higher transcript abundance in CAM leaf epidermal peels relative to the leaf mesophyll (Fig. 3.4). KF85525 may therefore be the ortholog of the Arabidopsis vacuolar $Cl^-$ channel AtALMT9 (De Angeli *et al.*, 2013*b*), leading to the prediction that this *KfALMT* gene encodes a channel that functions in the tonoplast membrane of the guard cells. KF116735 transcript levels were also higher in epidermal peels (Fig. 3.4). This gene was the only predicted *KfALMT* to cluster in Clade III (Fig. 3.2). This therefore suggests that it is the *K. fedtschenkoi* ortholog of *AtALMT12*, the guard cell plasma membrane anion channel (Meyer *et al.*, 2010).

Clade I (*AtALMT1*, *-2*, *-7* and *-8*; Kovermann *et al.*, 2007) was not coherently replicated by this phylogenetic analysis (Fig. 3.2). However, the capacity of *K. fedtschenkoi* for $Al^{3+}$ tolerance through malate exudation into the rhizosphere from its roots, as mediated by AtALMT1 (Hoekenga *et al.*, 2006) and TaALMT1 (Sasaki *et al.*, 2004), remains at present uncharacterised, and therefore the significance of the topology of Clade I for this function is unclear.

### 3.3.2 Preliminary screening suggests disruption of CAM in *KfALMT* RNAi lines

Results from the chlorophenol red screening of various independent *KfALMT* RNAi mutant lines suggested that nocturnal malate accumulation was impaired in the mutants relative to wild type (Fig. 3.7). Two of the *KfALMT* RNAi lines, 12A and 23A, were selected for further phenotypic analysis (see below, Chapter 4). A third independent line, *KfALMT* RNAi 8B, was also selected for detailed phenotypic characterisation on the basis of previous screening done in the Hartwell lab (Kneřova, Boxall, Dever and Hartwell, personal communication).

### 3.3.3 Preliminary phenotyping of a *KfTDT* RNAi line suggests that TDT functions as a vacuolar citrate transporter

No consistent disruptive effect on CAM-related diel fluctuation of leaf acidity was found by chlorophenol red screening of 9 independent *KfTDT* RNAi lines (Fig. 3.7). Despite this, excessive accumulation of citrate and apparent impairment of citrate turnover during the light period was found in the *KfTDT* RNAi line 80A (Fig. 3.9C). Replication of this result using additional independent *KfTDT* RNAi lines and direct measurement of tonoplast anion permeability in the context of *KfTDT* silencing is now needed to enable firm conclusions about the likely function(s) of KfTDT. However, some speculation on KfTDT function based on these limited results and previous characterisation of plant tonoplast transporters yields testable hypotheses that could be applied to future work.

Citrate accumulates during the dark period and is broken down in the light period in many CAM species, including *Kalanchoë* CAM species (Lüttge, 1988; Chen and Nose, 2004; Holtum *et al.*, 2005). Impairment of vacuolar citrate export is implied in *KfTDT* RNAi 80A by elevated citrate concentrations in both the light and dark periods, and apparent failure to break

citrate down during the light period (Fig. 3.9C). This suggests that KfTDT is a vacuolar citrate exporter, possibly a $H^+$-citrate symporter like CsCit1, the AtTDT ortholog of *C. x sinensis* (Shimada *et al.*, 2006). *A. thaliana* and *C. x sinensis* are both part of an evolutionary clade to which *K. fedtschenkoi* is basal (Chase *et al.*, 2016), so no inference can be made from these phylogenetic relationships about the likelihood that KfTDT has inherited the malate specificity of AtTDT or the citrate specificity of CsCit1. However, knockout mutations of other tonoplast $H^+$-symporters have been shown to result in accumulation of their substrates in vacuoles, and a similar phenotypic effect could explain the constitutive retention of citrate by CAM leaves of *KfTDT* RNAi 80A. For example, INOSITOL TRANSPORTER 1 (INT1) is localised in the vacuoles and mediates symport of $H^+$ and *myo*-inositol (Schneider *et al.*, 2008). *A. thaliana* INT1 knockout mutants accumulated higher concentrations of *myo*-inositol than wild type, and their root growth was impaired when grown in low concentrations of *myo*-inositol, probably due to constitutive sequestration of *myo*-inositol in the vacuole where it is unavailable for biosynthetic processes in the cytosol (Schneider *et al.*, 2008).

Apparent transcriptional repression of *KfTDT* in CAM leaves during the early part of the dark period (Fig. 3.8) would support a role for KfTDT as a transcriptionally-controlled citrate transporter for diurnal citrate efflux. In this scenario, *KfTDT* transcriptional repression from the middle of the light period would prevent futile cycling of citrate back to the cytosol following vacuolar import. *K. fedtschenkoi* mutants overexpressing *KfTDT* may therefore have lower concentrations of citrate relative to the wild type. The Hartwell lab has previously generated *K. fedtschenkoi* transgenic lines expressing a 35S promoter-driven *KfTDT* overexpression construct. These lines could be used to confirm or refute this hypothesis.

There was a small reduction in malate concentration in *KfTDT* RNAi 80A at the end of the dark period (Fig. 3.9B), which implies some impairment of CAM photosynthesis. Dark-period $CO_2$ assimilation in detached *KfTDT* RNAi 80A CAM leaves was not reduced relative to wild type controls (Fig. 3.10), however, so evidence for suppression of CAM due to knock-down of *KfTDT* was, at most, equivocal. It will be important to determine whether dark-period malate accumulation and $CO_2$ uptake are also uncorrelated as indices of CAM activity in other, independent *KfTDT* RNAi lines with severely reduced *KfTDT* transcript relative to WT. In the first full light period of this $CO_2$ gas exchange timecourse, both WT controls displayed greater $CO_2$ uptake than the single *KfTDT* RNAi 80A CAM leaf pair monitored (Fig. 3.10), but, as discussed below, measurements of detached leaves are a poor proxy for CAM leaves attached to intact *K. fedtschenkoi* when measuring light-period $CO_2$ gas exchange (Section 4.3.3).

Suppression of nocturnal malate accumulation in *KfTDT* RNAi 80A might have simply resulted from loss of function of a KfTDT that transports both citrate and malate. *In vitro* transport studies could confirm this. However, the fact that the citrate was over-accumulated but malate was not suggests that this hypothesis is not correct. Alternatively, constitutive over-accumulation of citrate might raise the baseline acidity of the vacuolar lumen, causing the mass-action ratio of vacuolar $H^+$ import to be higher at the onset of nocturnal malate accumulation than in the wild type, and decreasing the quantity of malate and $H^+$ that could be co-transported into the vacuole before further V-ATPase-catalysed $H^+$ translocation would become thermodynamically limited (Smith *et al.*, 1982; Lüttge, 1987). Direct measurements of CAM leaf sap titratable acidity in multiple *KfTDT* RNAi lines would be needed as a first step to determine whether their CAM leaves are constitutively acidified, and to causally link increased citrate accumulation to decreased malate accumulation.

## 3.4 Summary

In the *KfALMT* RNAi transgenic lines studied in this PhD project, two predicted *KfALMT* genes of a larger *KfALMT* family were found to be likely to be targeted for silencing. On the basis of transcriptomic and phylogenetic data, the two KfALMTs are closely-related vacuolar membrane proteins that are preferentially transcribed in CAM leaf mesophyll relative to $C_3$ leaves and the guard cells of CAM leaves. Promising *KfALMT* RNAi lines were selected for further study via a CAM mutant screen based on measurements of leaf cell sap acidity at dawn and dusk using chlorophenol red indicator

*K. fedtschenkoi* has a single *KfTDT* gene, an ortholog of the single copy of this gene found in Arabidopsis. Sequence comparison with orthologous *TDT*s did not provide any conclusive insights into the likely function(s) of KfTDT. No consistent disruption of CAM was found by screening *KfTDT* RNAi lines. However, a single *KfTDT* RNAi mutant line that accumulated high concentrations of citrate was identified, suggesting that KfTDT may mediate vacuolar citrate export in *K. fedtschenkoi*.

# Chapter 4 – Dosage-dependent effects on CAM-associated phenotypes resulting from differential transgenic hairpin dsRNA-mediated silencing of the putative vacuolar inward-rectifying malate channel KfALMT

## 4.1 Introduction

The results presented in this chapter are an attempt to characterise the function of vacuolar ALMTs in CAM, and are part of an ongoing project to determine the genomic requirements of CAM through a functional genomic approach (Yang *et al.*, 2015). Genomics and transcriptomics of the obligate model CAM species *Kalanchoë fedtschenkoi* have revealed a complement of genes putatively involved in enzymatic, membrane transport and regulatory functions of CAM (Hartwell *et. al.*, unpublished results). Systematic silencing of these genes by RNA interference (RNAi) and analysis of the effect on CAM function is currently in progress, as exemplified by a recent study of *KfNAD-MEb1* RNAi and *KfPPDK* RNAi lines (Dever *et al.*, 2015). As in that study, for this chapter suppression of *KfALMT* transcript in *KfALMT* RNAi lines was confirmed, an *in vitro* assay was used to demonstrate loss of *KfALMT* function at the protein level, and its metabolic and regulatory effects on CAM were surveyed.

## 4.2 Results

### 4.2.1 Quantification of the degree of *KfALMT* silencing in transgenic lines of *K. fedtschenkoi* using RT-qPCR

As described in Chapter 3, three independent *KfALMT* RNAi lines were identified as likely to be impaired in CAM function due to decreased leaf acidity at the end of the dark period: 8B, 12A and 23A. *KfALMT* relative transcript abundance in these *KfALMT* RNAi lines was determined

A

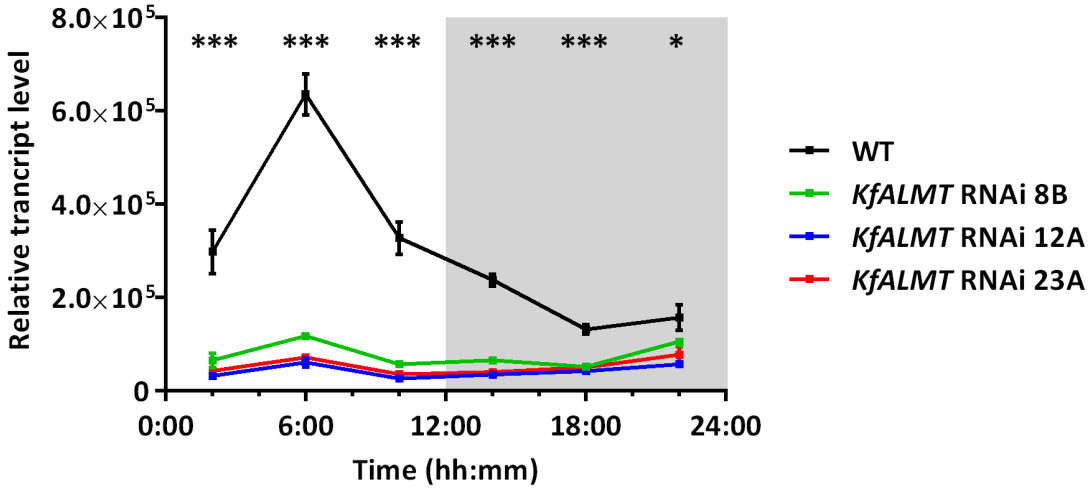


B

| | Time (hh:mm) | | | | | |
|---|---|---|---|---|---|---|
| | 02:00 | 06:00 | 10:00 | 14:00 | 18:00 | 22:00 |
| WT | a | a | a | a | a | a |
| 8B | b | b | b | b | b | a |
| 12A | b | b | b | b | b | b |
| 23A | b | b | b | b | b | b |

Figure 4.1 – Relative transcript level of *KfALMT1* over a 12:12 LD cycle
A – Relative transcript abundance was determined using RT-qPCR, and normalised to a non-oscillating reference gene, *KfTFP*. Points represent mean relative transcript level ± S.E.M, n = 3. Grey shading represents the dark period. The result of one-way ANOVA between *KfALMT1* transcript abundance and genotype at each time-point is displayed above that time point: $P \leq 0.05$, *; $P \leq 0.001$, ***.
B – The results of Tukey HSD tests between mean relative transcript level at each time-point, where letters show groups of genotypes for which $P > 0.05$ for any pair of means.

using RT-qPCR in order to confirm that the intended target of their hairpin dsRNA transgene had been transcriptionally silenced.

*KfALMT* RNAi lines 8B, 12A and 23A were grown alongside WT controls from adventitious plantlets for 9 weeks under greenhouse conditions and entrained to 12:12 LD.

Samples of CAM-expressing leaves (leaf pair 6, LP6) were collected in biological triplicate every 4 h, beginning at 2 h into the light period (02:00; see materials and methods for full details of experimental sampling regimes). Total RNA was extracted from frozen leaf tissue and cDNA was synthesised from RNA extracts by reverse transcription. The primer pair used for RT-qPCR is selective for KF122600/Kaladp0073s0021.1 (Appendix 2), the more abundant of the two predicted *KfALMT* transcripts that are likely to be targeted for RNAi-mediated silencing by the hairpin dsRNA transgene (see above, Section 3.3.1). KF122600/Kaladp0073s0021.1 will be referred to as *KfALMT1* below.

*KfALMT1* steady-state transcript levels were lower in each of the *KfALMT* RNAi lines than in WT controls (Fig. 4.1A). This suppression of transcript abundance was particularly pronounced at the mid-point of the light period (06:00), when relative transcript levels peaked in WT. At 06:00, mean transcript levels were ~6-fold lower in *KfALMT* RNAi 8B, ~8-fold lower in *KfALMT* RNAi 23A and ~10-fold lower in *KfALMT* RNAi 12A, although significant differences were not found between mean relative transcript levels of any of the *KfALMT* RNAi lines at this time-point, or any except 22:00 (Fig. 4.1B).

### 4.2.2 *In vitro* determination of decreased $H^+$ transport activity in *KfALMT* RNAi lines

In order to measure the effect of silencing of *KfALMT*s on malate channel activity, an *in vitro* assay of ATP-driven $H^+$ transport activity in extracted tonoplast vesicles was used. Rapid and protracted vesicular acidification resulting from inward $H^+$ translocation by vacuolar ATPase (V-ATPase) is enabled energetically by inward anion transport (Pantoja and Smith, 2002; Hafke *et al.*, 2003), such as malate transport mediated by ALMTs (Kovermann *et al.*, 2007; Meyer *et al.*, 2011), and accumulation of the vesicle-to-bulk solution pH gradient can be quantified by

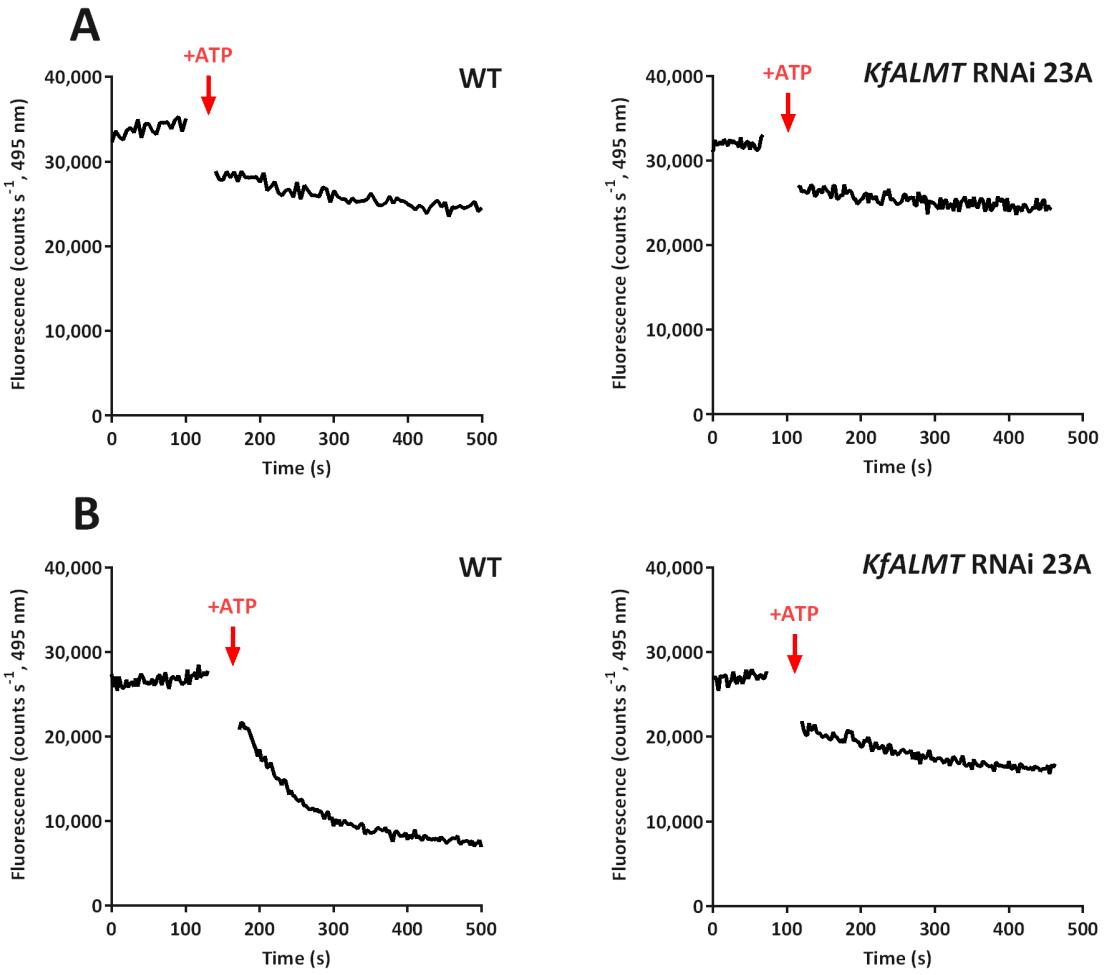


Figure 4.2 – Coupling of malate and $H^+$ transport by tonoplast extracts in the presence of ATP. Representative fluorescence-time traces of tonoplast extracts without (A) or with (B) 50 mM BTP-malate pH 8.0, before and after the addition of 3 mM ATP-Tris pH 8.0. 20 µg of extracted tonoplast protein was used for each assay. Fluorescence of quinacrine probe was measured by excitation at 427 nm and emission at 495 nm. Fluorescence measurements were made at 2.5 s intervals, other than the assay of WT tonoplast extract $H^+$ transport activity in the absence of malate, during which measurements were made at 5 s intervals. Spectrofluorometer readings that were made when its chamber was opened to add ATP have been excluded and leave gaps in the trace.

measuring fluorescence quenching of the dye quinacrine (Bennett and Spanswick, 1983; White and Smith, 1989).

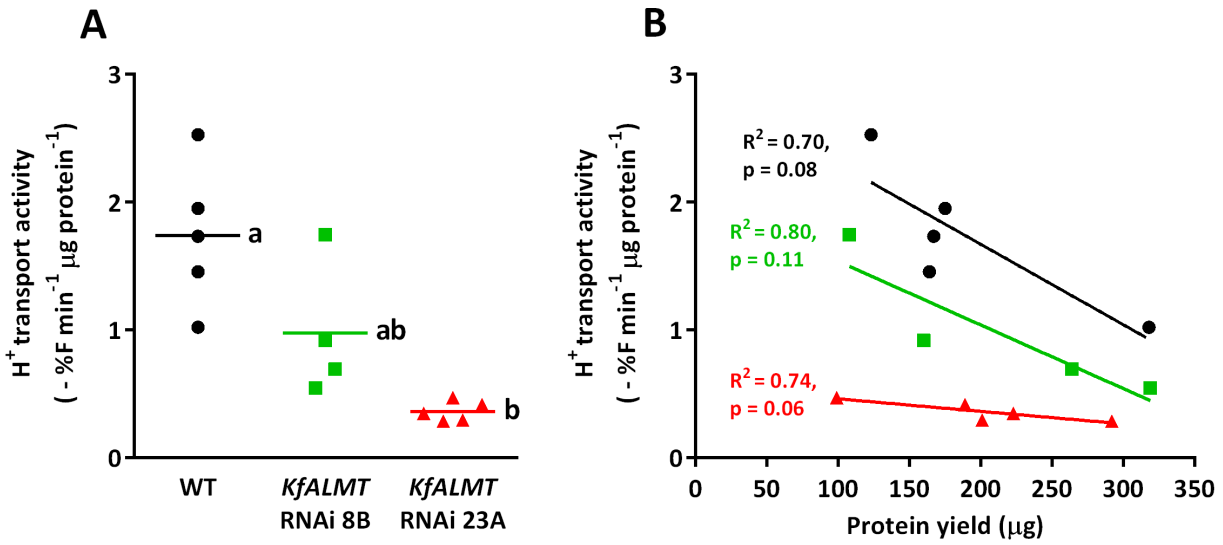


Figure 4.3A – $H^+$ transport activity of tonoplast extracts. Points each represent one tonoplast extract; horizontal lines indicate mean $H^+$ transport activity. The result of one-way ANOVA between $H^+$ transport activity and genotype was $P < 0.01$ (2 and 11 D.F.). The result of a Tukey HSD test between means is displayed; letters denote groups of genotypes where $P > 0.05$ (non-significant) for the difference between any pair of means. B – The correlation between total protein yield of tonoplast extraction and $H^+$ transport activity. Linear regression calculations are displayed for each genotype with their $R^2$, (coefficient of determination) and P (probability of zero gradient, F-test, 1 and 2-3 D.F.).

WT, *KfALMT* RNAi 8B and *KfALMT* RNAi 23A were grown from adventitious plantlets for 13 weeks under greenhouse conditions and then entrained to 12:12 LD. CAM leaf tissue (leaf pairs 6-8) was harvested for tonoplast extraction at 2 h after the beginning of the dark period (14:00). $H^+$ transport activity of 20 µg tonoplast protein in the presence of 50 mM malate and 3 mM ATP was tracked by the rate of quinacrine fluorescence quenching. $H^+$ transport activity was measured as the negative of the initial slope of the decreasing fluorescence-time curve, immediately after addition of ATP (Bennett and Spanswick, 1983; Fig. 4.2), normalised as a percentage of the fluorescence intensity immediately after addition of ATP and to the mass of extracted tonoplast protein used ( - %F $min^{-1}$ µg $protein^{-1}$).

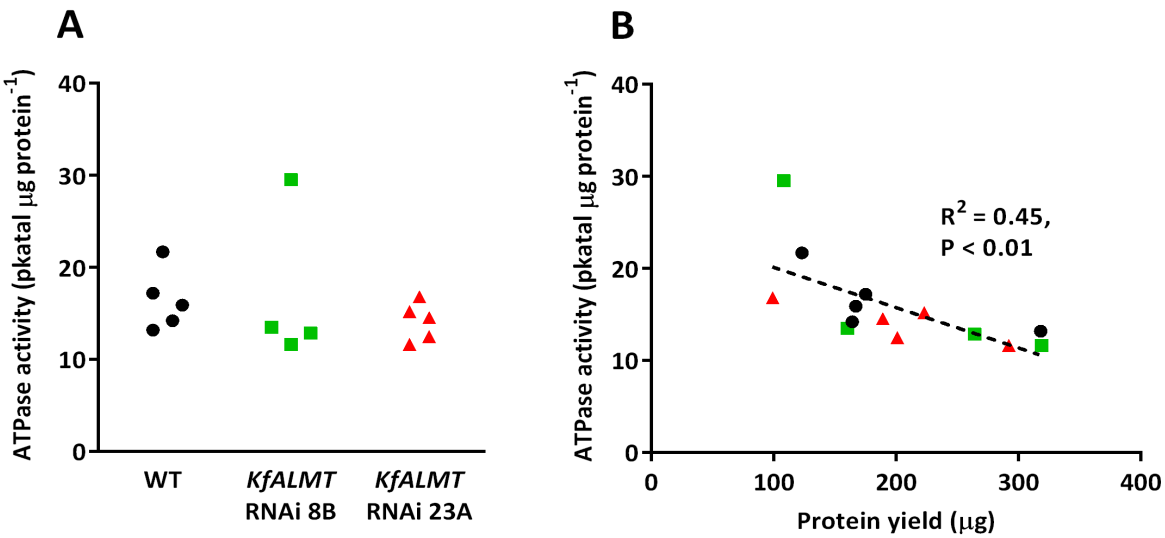


C

| | WT | 8B | 23A |
|---|---|---|---|
| $R^2$ | 0.51 | 0.61 | 0.69 |
| P | 0.18 | 0.22 | 0.01 |

Figure 4.4A - ATPase activity of tonoplast extracts.
B - Correlation between ATPase activity of tonoplast extracts and total protein yield. The broken line shows linear regression calculated for all extracts, with $R^2$ (the correlation coefficient), and P (probability of a zero gradient, F-test, 1 and 12 D.F.).
C - Statistics of linear regression analysis of the correlation between ATPase activity and yield within repeated tonoplast extractions of single genotypes.

$H^+$ transport activity was significantly lower in tonoplast extracts from *KfALMT* RNAi 23A than in WT (Fig. 4.3A). The mean $H^+$ transport rate for *KfALMT* RNAi 8B tonoplast extracts was also lower than that of WT, but there was considerable variation between replicate extracts of both genotypes, and no significant difference between their respective mean transport rates (Fig. 4.3A). The protein yield of the tonoplast extraction also varied more than 3-fold between replicate tonoplast extractions of the same genotype, and across the full cohort of tonoplast extracts. Negative correlation between yield and $H^+$ transport activity within each

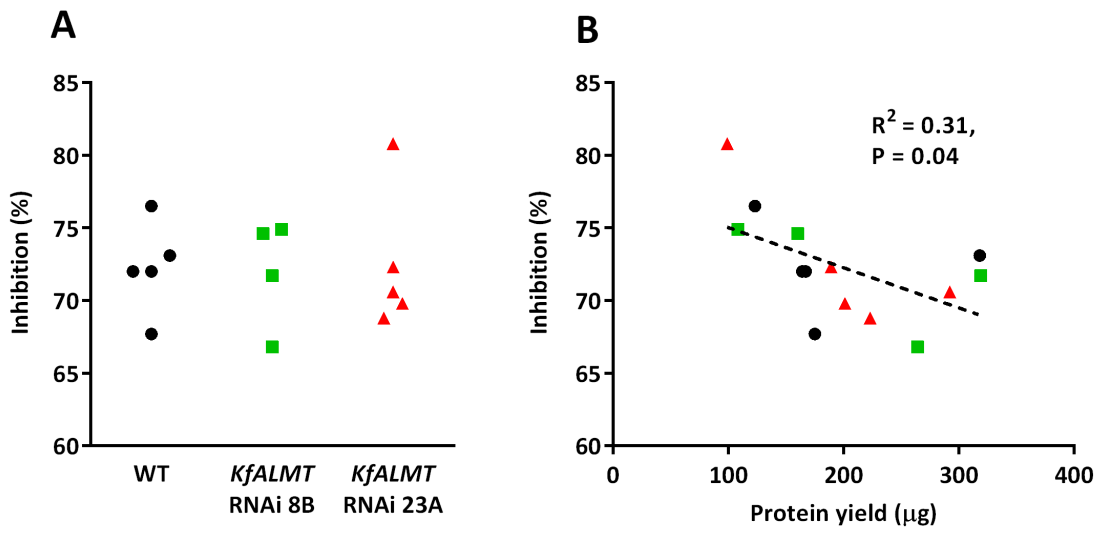


C

| | WT | 8B | 23A |
|---|---|---|---|
| $R^2$ | 0.01 | 0.47 | 0.67 |
| P | 0.87 | 0.32 | 0.09 |

Figure 4.5A - Inhibition of tonoplast extract ATPase activity by 50 mM $KNO_3$.
B - Correlation between protein yield of tonoplast extraction and the rate of inhibition. The broken line shows linear regression calculated for all extracts, with $R^2$ (the correlation coefficient), and P (probability of a zero gradient, F-test, 1 and 12 D.F.).
C - Statistics of linear regression analysis of the correlation between ATPase activity and yield within repeated tonoplast extractions of single genotypes.

genotype suggested that contamination by non-tonoplast-specific protein was a confounding variable (Fig. 4.3B).

V-ATPase is a protein complex that couples ATP hydrolysis to $H^+$ translocation, and as a tonoplast integral membrane protein it should co-purify with vacuolar ALMT (Kluge *et al.*, 2003). In order to normalise purity of tonoplast extracts, ATPase activity was assayed by quantifying inorganic phosphate ($P_i$) released in the presence of 10 mM ATP and 0.5 or 1 µg extracted tonoplast protein, and expressed in units of picomoles $P_i$ generated per second per µg tonoplast protein (pkatal $\mu g^{-1}$).

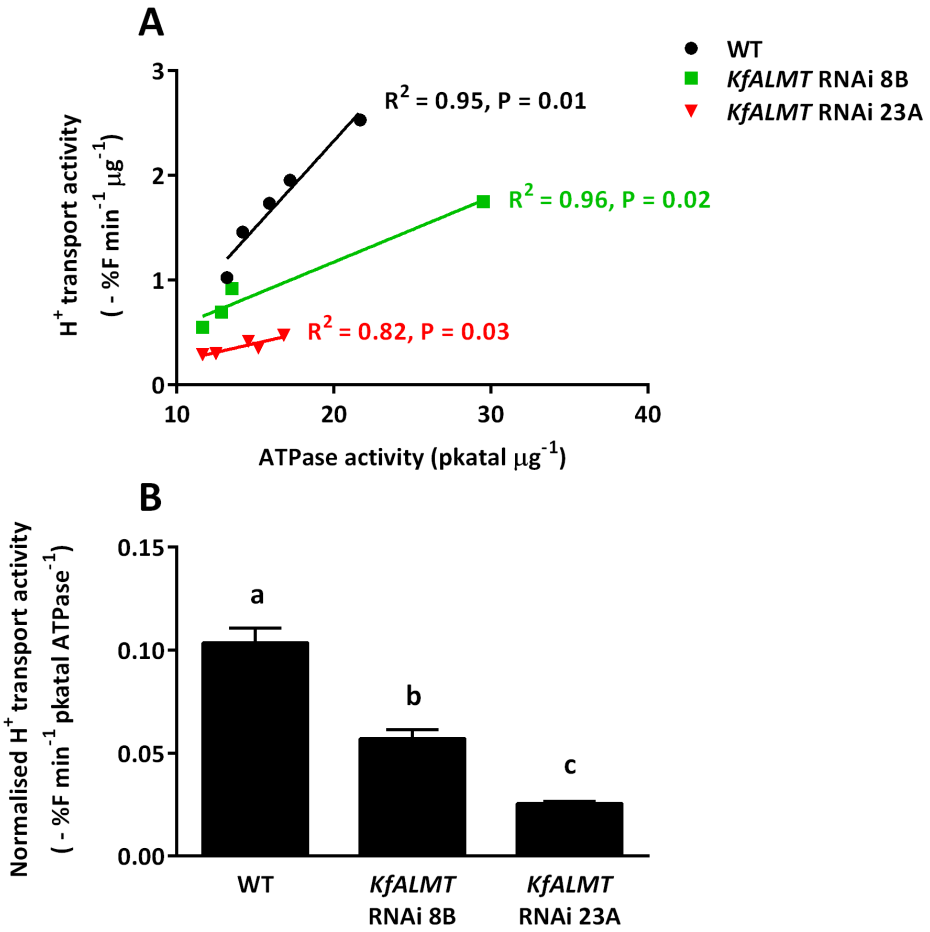


Figure 4.6 – Normalisation of $H^+$ transport activity of tonoplast extracts to ATPase activity.
A – Correlation between $H^+$ transport activity and ATPase activity. Lines represent linear regression of the correlation between $H^+$ transport rate and ATPase activity for each genotype, with $R^2$ (correlation coefficient) and P (probability of a zero gradient, F-test, 1 and 2-3 D.F.).
B – Normalised $H^+$ transport activity for WT and two *KfALMT* RNAi lines. Bars represent mean ± S.E.M, n = 5 for WT and *KfALMT* RNAi 23A and n = 4 for *KfALMT* RNAi 8B. The result of one-way ANOVA (2 and 11 D.F.) between $H^+$ transport activity and genotype was $P < 0.001$. The results of Tukey HSD test are displayed above the bars, with letters representing groups of genotypes within which $P > 0.01$ for the difference between any pair of means.

Large differences in ATPase activity were found between repeated tonoplast extractions of all three genotypes (Fig. 4.4A). ATPase activity varied 1.6-fold in WT, 2.5-fold in *KfALMT*

RNAi 8B and 1.4-fold in *KfALMT* RNAi 23A. However, ATPase activity was broadly consistent across all tonoplast extracts and there were no significant differences in activity between genotypes (One-way ANOVA, P = 0.67, 2 and 11 D.F.). There was a significant negative correlation between tonoplast extraction protein yield and ATPase activity across all samples (Fig. 4.4B), and non-statistically-significant, negative correlations among samples from each of the genotypes alone (Fig. 4.4C). This indicates that, like $H^+$ transport activity, ATPase activity is dependent on the purity of tonoplast extraction.

ATPase activity was also assayed in the presence of 50 mM $KNO_3$, an inhibitor of V-ATPases (Warren *et al.*, 1992; McRae *et al.*, 2002). Rates of inhibition by 50 mM $KNO_3$ ranged between 66.8% and 80.8% (Fig. 4.5A). There was a weak negative linear correlation between protein yield of the tonoplast extraction and the rate of inhibition across all extracts (Fig. 4.5B). There were non-statistically-significant negative correlations within samples from *KfALMT* RNAi 8B and *KfALMT* RNAi 23A, respectively (Fig. 4.5C).

The quotient of $H^+$ transport activity and ATPase activity for each tonoplast extract was used as a normalised measure of $H^+$ transport activity. There was a strong positive correlation between ATPase activity and $H^+$ transport activity within repeated tonoplast extractions of the same genotype (Fig. 4.6A). Consequently, the precision of $H^+$ transport activity normalised to ATPase activity was greatly improved over $H^+$ transport activity normalised to mass of extracted protein (Fig. 4.6B). The mean normalised $H^+$ transport activity in WT tonoplast extracts was significantly greater than those of *KfALMT* RNAi lines 8B and 23A tonoplast extracts, and the mean for line 8B was significantly greater than that of line 23A (Fig. 4.6B).

### 4.2.3 Suppression of nocturnal $CO_2$ uptake

Nocturnal $CO_2$ fixation is a definitive feature of CAM photosynthesis. Diel $CO_2$ gas exchange was measured in order to determine whether nocturnal $CO_2$ uptake was impaired in *KfALMT* RNAi lines.

Stem cuttings of *KfALMT* RNAi lines 8B, 12A and 23A and WT controls were grown for 7 weeks under greenhouse conditions and entrained to 12:12 LD. The leaf area-normalised rate of $CO_2$ gas exchange ($J_{CO2}$) by detached LP6 was measured over two full 12:12 LD cycles (48 h) using a 12-channel infra-red gas analyser (IRGA) (Fig. 4.7). Total $CO_2$ uptake for entire 12 h light or dark periods was determined by calculating the area between the $J_{CO2}$ time-course and the x-axis, assuming linear interpolation between measurements (Fig. 4.8).

A single peak of $J_{CO2}$ was observed in WT and each of the *KfALMT* RNAi lines during both dark periods (Fig. 4.7), representing nocturnal $CO_2$ fixation catalysed by PPC in CAM Phase I (Osmond, 1978). $J_{CO2}$ peaked 3-5 h into the dark period, with a more gradual decline towards the end of the dark period. The *KfALMT* RNAi lines each reached peak $J_{CO2}$ slightly earlier than WT did. There were relatively small differences between $J_{CO2}$ readings from WT and the *KfALMT* RNAi lines in the first 2-3 h of the dark period. $J_{CO2}$ then diverged rapidly between genotypes and was differentiated for the remainder of the dark period. At the end of the dark period, $CO_2$ uptake by WT remained elevated, whereas $J_{CO2}$ of *KfALMT* RNAi line 8B approached zero and $J_{CO2}$ of lines 12A and 23A declined below zero (Fig. 4.7). Total 12 h dark-period $CO_2$ uptake by each of the *KfALMT* RNAi lines was significantly lower than that of WT during both dark periods, while total $CO_2$ uptake by *KfALMT* RNAi line 8B was significantly higher than that of lines 12A and 23A (Fig. 4.8). Prolonged periods of net $CO_2$ output in lines 12A and 23A at the beginning and end of dark periods contributed to their lower totals (Fig. 4.7).

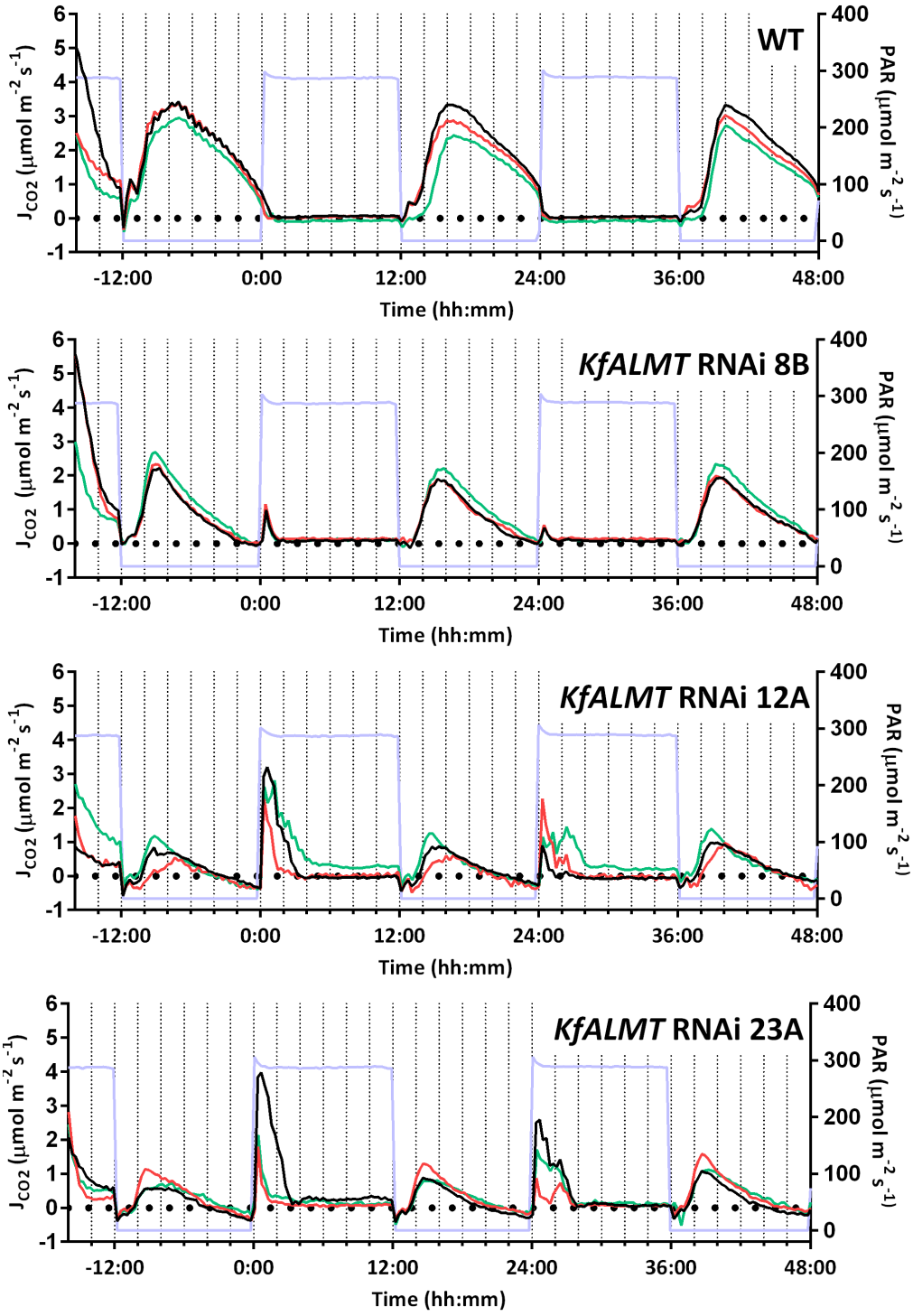


Figure 4.7 – Timecourse of the rate of $CO_2$ gas exchange ($J_{CO2}$) by detached CAM leaves under 12:12 LD. Net $CO_2$ uptake occurred when $J_{CO2} > 0$; $J_{CO2}$ was normalised to leaf area. Three detached LP6 (black, green and red) from independent replicate specimens of each genotype were monitored concurrently, except for a single leaf 6 of *KfALMT* RNAi 12A (red). LP6 were detached and placed in IRGA cuvettes approximately 20 h before the beginning of the first full light period (0:00). Photosynthetically active radiation (PAR) is also shown (light blue).

Phase II was almost totally absent in detached LP6 from WT over the time-course of $CO_2$ gas exchange measurement (Fig. 4.7). In one WT replicate, there was a small peak in $J_{CO2}$ at the beginning of the first light period, but otherwise any positive value of $J_{CO2}$ was a continuation of decline observed during the latter part of the dark period, or an acceleration of the same trend. In two of the three WT replicates, there was a gradual increase during the middle of light period to ~0.05 μmol $m^2$ $s^{-1}$, which is characteristic of Phase IV (Osmond, 1978). Nevertheless, this contributed minimally to total $CO_2$ uptake, and was completely absent in one of the three replicate LP6 measured. Phase II was dramatically expanded in *KfALMT* RNAi lines 12A and 23A, and expanded to a lesser extent in *KfALMT* RNAi 8B (Fig. 4.7). Suppression of $CO_2$ uptake following Phase II was also inconsistent in replicate leaf pairs from *KfALMT* RNAi lines, but in the most extreme example $J_{CO2}$ reached only ~0.3 μmol $m^{-2}$ $s^{-1}$ during Phase III (line 12A, green line), and there was no upward trend in $J_{CO2}$ later in the light period that would have been typical of Phase IV (Fig. 4.7). In spite of the qualitative differences between the patterns of $CO_2$ gas exchange by the *KfALMT* RNAi lines and WT, there was no significant difference between them in terms of light-period mean total $CO_2$ uptake (Fig. 4.8).

As young *K. fedtschenkoi* leaves mature, their capacity for $CO_2$ uptake via the CAM photosynthetic pathway develops progressively and the quantity of atmospheric $CO_2$ fixed directly via the $C_3$ pathway diminishes (Jones, 1975). In order to determine how this process was affected in *KfALMT* RNAi lines, line 23A and WT were grown from adventitious plantlets under glasshouse conditions for 16 weeks and entrained to 12:12 LD. Even-numbered leaf pairs from LP2 to LP12 were detached and $CO_2$ gas exchange by these leaf developmental gradients was measured for 72 h using the 12-channel IRGA. Total 12 h $CO_2$ uptake for each light or dark period was determined as in the previous experiment. The results that are described below were

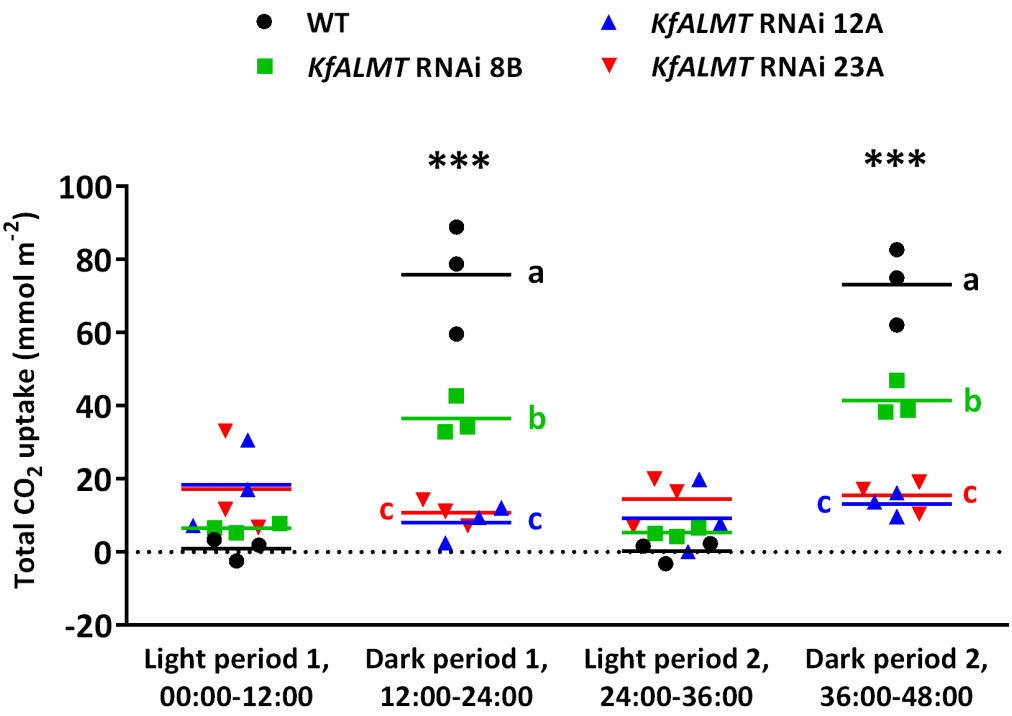


Figure 4.8 – Total $CO_2$ uptake by detached CAM leaf pairs during 12 h light/dark periods over two consecutive 12:12 LD cycles. Points represent the total $CO_2$ uptake in a single LP6 sample, and mean $CO_2$ uptake for each genotype is represented by a colour-coded horizontal line. The result of one-way ANOVA (3 and 8 D.F.) between total $CO_2$ uptake and genotype is displayed above the data for that period: $P > 0.05$, not shown; $P \leq 0.001$, ***. When $P \leq 0.05$ for one-way ANOVA, a Tukey HSD test was performed; colour-coded letters denote groups of genotypes within which the difference between any pair of means is non-significant ($P > 0.05$).

consistent with a repeat developmental series covering even-numbered leaves from LP2 to LP10 of WT and *KfALMT* RNAi 23A stem cuttings (Appendix 3).

The patterns of $J_{CO2}$ during the dark periods in LP4-12 of both *KfALMT* RNAi 23A and WT were similar to those previously observed in LP6. While there were no intervals of $CO_2$ output by *KfALMT* RNAi 23A LP4-10 like those previously observed in LP6 of this line at the end of the dark period, differentiation between $J_{CO2}$ readings from these leaves and their WT opposite numbers was, again, skewed towards the end of the dark period (Fig. 4.9). $J_{CO2}$

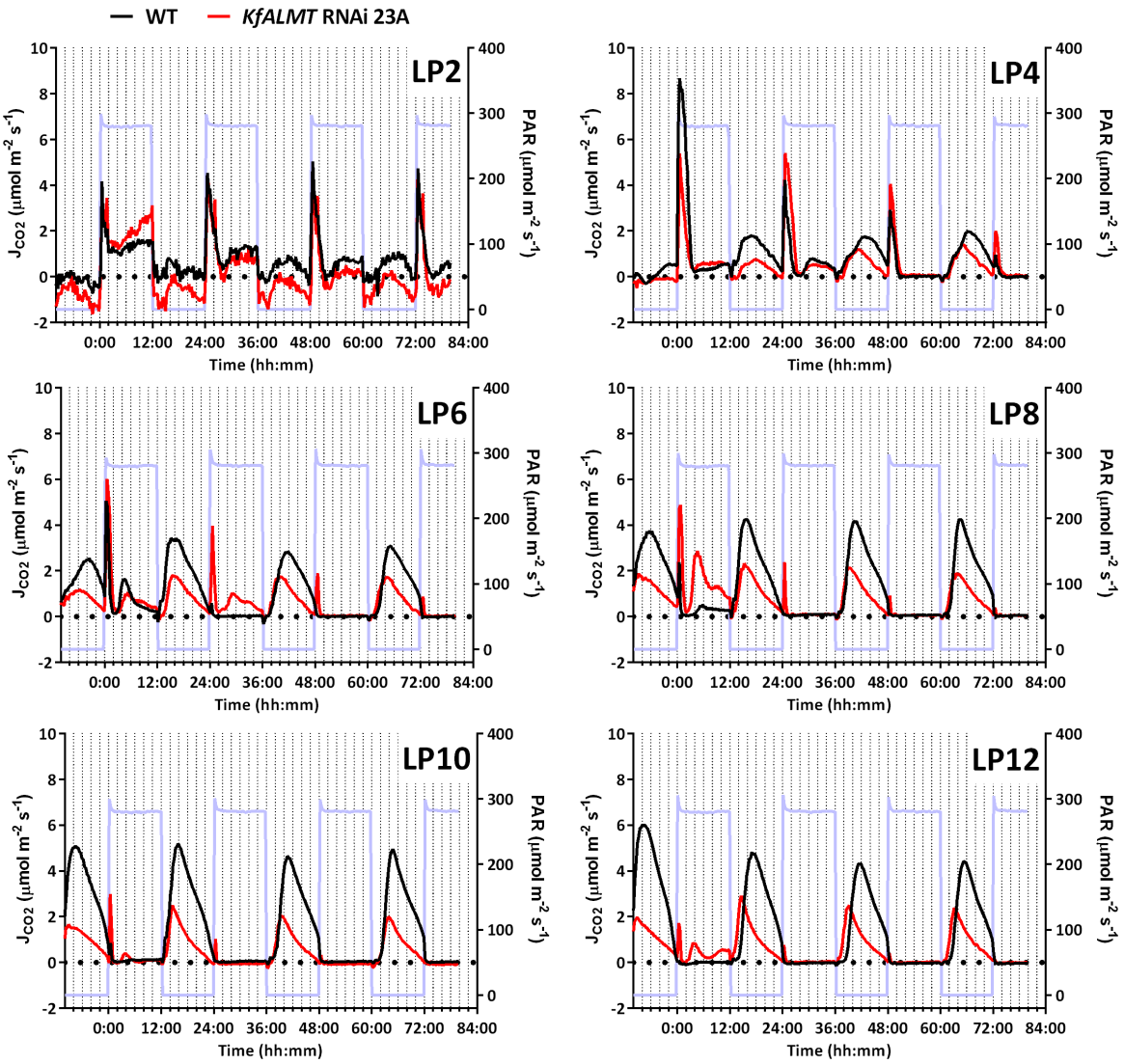


Figure 4.9 – Timecourse of the rate of $CO_2$ gas exchange ($J_{CO2}$) by detached leaf pairs of a leaf developmental gradient under 12:12 LD. Net $CO_2$ uptake occurred when $J_{CO2} > 0$; $J_{CO2}$ was normalised to leaf area. Even-numbered pairs of leaves from LP2-12 were detached from the stem and placed in the 12-channel IRGA at ~12 h before the beginning of first full light period (0:00). Photosynthetically active radiation (PAR) is also displayed (blue).

remained negative or very low throughout each dark period in LP2 of *KfALMT* RNAi 23A, with net total output of $CO_2$, but increased in the middle of the dark period, as in more mature leaves from this line. Conversely, there was a small quantity (~15 mmol $m^{-2}$) of net $CO_2$ uptake by WT

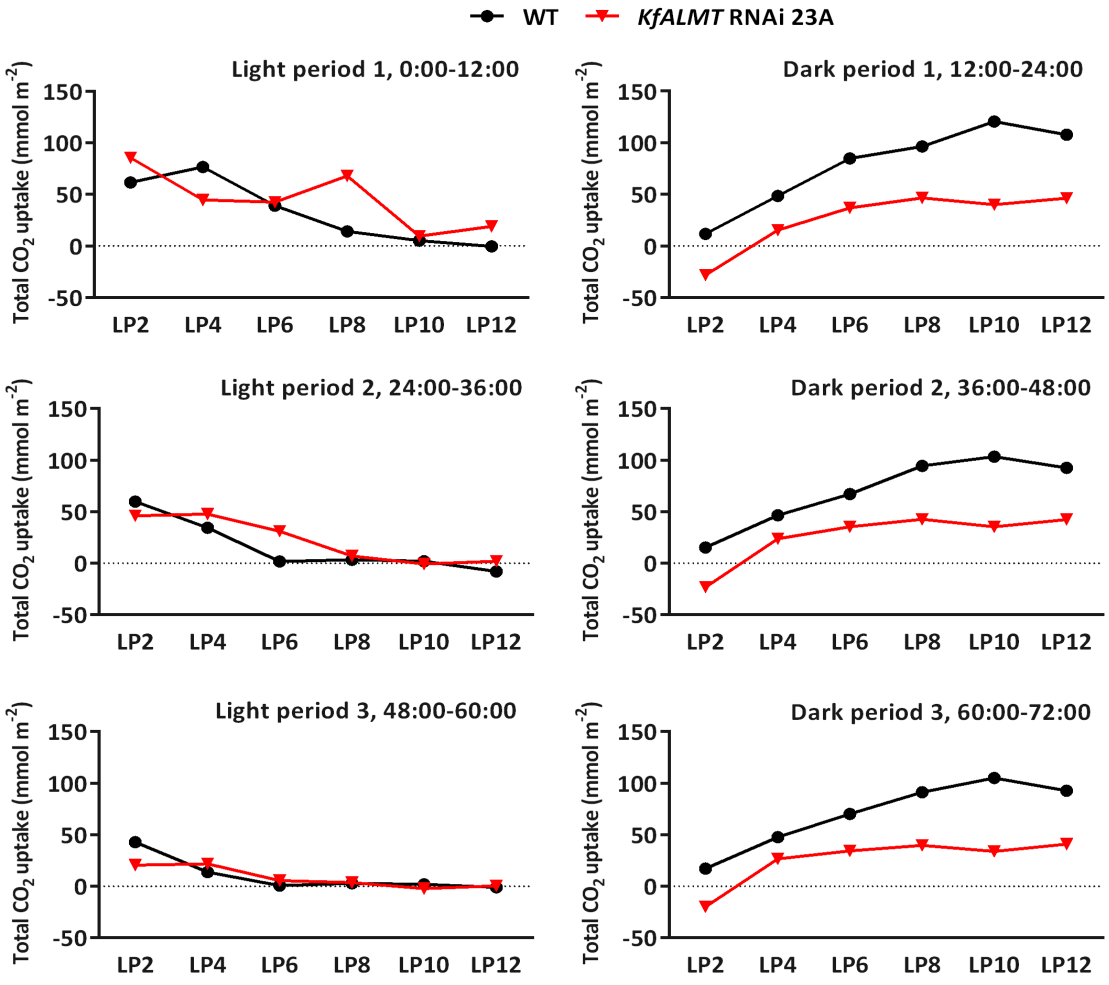


Figure 4.10 – Total $CO_2$ uptake by detached leaf pairs of a leaf developmental gradient during 12 h light/dark periods over three consecutive 12:12 LD cycles.

LP2 during each dark period, with patterns of $J_{CO2}$ that resembled those of more mature leaves during dark periods 2 and 3 (Figs. 4.9 and 4.10). Dark-period $CO_2$ uptake in WT leaves increased along the developmental gradient between LP2 and LP10; it was slightly lower in LP12 than in LP10 (Fig. 4.10). Dark-period $CO_2$ uptake also increased in conjunction with leaf maturity in LP4-8 of *KfALMT* RNAi 23A, but was not increased in LP10 or LP12 relative to LP8, with the

exception of dark period 3, when total $CO_2$ uptake by LP12 was slightly higher than that of LP8 (0.29 mmol $m^{-2}$ difference, Fig. 4.10).

While total 12 h $CO_2$ uptake remained relatively consistent over the three dark periods, total light-period $CO_2$ uptake generally decreased with time (Figs. 4.9 and 4.10). During light period 1, only WT LP12, of the 12 leaf pairs monitored, did not assimilate any $CO_2$. Some degree of Phase II or Phase IV $CO_2$ assimilation, or both, was observed during light period 1 in all other leaf pairs, and the cessation of net $CO_2$ uptake by WT LP2-6 and *KfALMT* RNAi 23A LP2-8 during Phase III was incomplete. In *KfALMT* RNAi 23A LP6-10 and WT LP6-8, $J_{CO2}$ increased rapidly at the end of Phase III, peaked a short time later, and then declined until the end of the light period. In LP10 of *KfALMT* RNAi 23A, net $CO_2$ uptake ceased after a very brief Phase IV, followed by, in effect, a second Phase III (Fig. 4.9). Regardless of genotype or position on the stem, light-period $CO_2$ uptake in the detached leaves decreased after light period 1, in particular by expansion of Phase III and elimination of Phase IV (Figs. 4.9 and 4.10). By light period 3, Phase IV had been eliminated in all leaves except LP2 of WT and *KfALMT* RNAi 23A. Phase II was absent in WT LP8-12 by light period 3, but remained present to some extent in $J_{CO2}$ traces of their opposite numbers, and younger leaves, from the *KfALMT* RNAi 23A specimen (Fig. 4.9).

As the changes that were observed in light-period $CO_2$ gas exchange appeared to be dependent on the time elapsed since the leaves were detached, $CO_2$ gas exchange measurements were made on whole-plant specimens of *KfALMT* RNAi lines 8B, 12A and 23A, and WT *K. fedtschenkoi* in order to eliminate this variable. Specimens with 8-9 leaf pairs were grown from adventitious plantlets in 6 weeks under greenhouse conditions, entrained to 12:12 LD, and three replicates of each genotype were transferred intact to cuvettes of the 12-channel IRGA. After

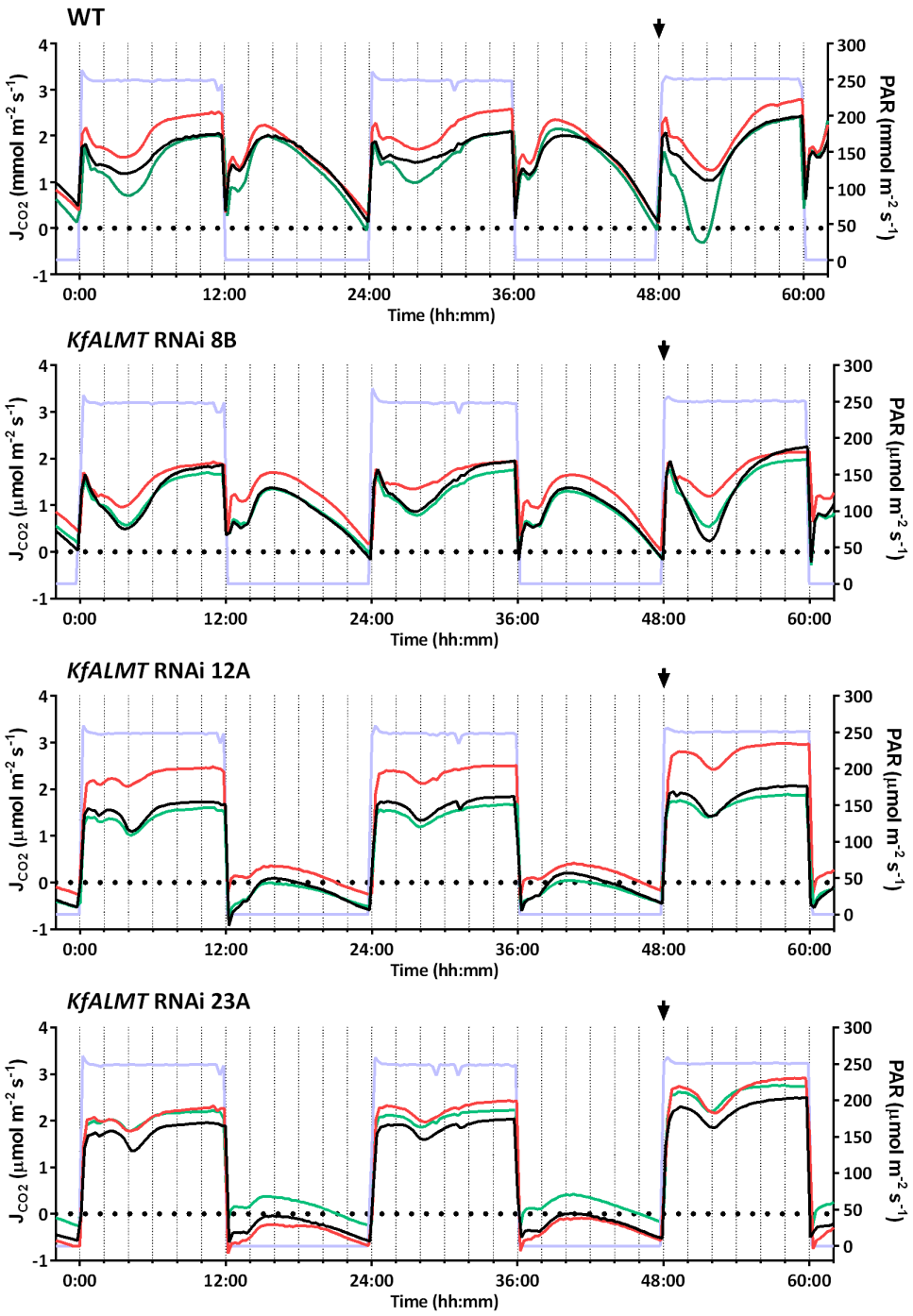


Figure 4.11 – Timecourse of the rate of $CO_2$ gas exchange ($J_{CO2}$) by whole plants under 12:12 LD. Three replicate plants of each genotype (black, red and green lines) were measured in a 12-channel IRGA. Net $CO_2$ uptake occurred when $J_{CO2} > 0$; $J_{CO2}$ was normalised to the total area of leaves and stems. Photosynthetically active radiation (PAR) is also displayed (light blue line). Plants were placed in the cuvettes at ~16 h before the beginning of the first complete light period (0:00). The stem was severed between LP4 and LP5 and the upper part removed from the IRGA at the beginning of the third light period (black arrow).

two full 12:12 LD cycles (48:00), the stem of each plant was severed with a scalpel between LP4 and LP5, the upper part was removed from the IRGA cuvette, and $CO_2$ gas exchange was measured during the subsequent 12 h light period. $J_{CO2}$ was normalised to the total area of the leaves and stem at the time each measurement was made. Total $CO_2$ uptake during each light and dark period was determined as it had been in the previous $CO_2$ gas exchange experiments.

Marked differences were apparent between the $J_{CO2}$ timecourses of WT plants and those of *KfALMT* RNAi lines 12A and 23A (Fig. 4.11). In both 12:12 LD cycles, WT assimilated 40-50% of its total $CO_2$ uptake during the dark period. Conversely, in two replicates each of *KfALMT* RNAi 12A and *KfALMT* RNAi 23A, net $CO_2$ output was observed during dark periods 1 and 2; in one of these *KfALMT* RNAi 23A replicates $J_{CO2}$ was negative throughout both dark periods (Fig. 4.11). Although a third replicate of either line maintained a positive $CO_2$ balance in the dark, this contributed <10% of the 24 h totals. As in detached LP6 (Fig. 4.8), mean total dark-period $CO_2$ uptake in *KfALMT* RNAi 8B was intermediate between that of WT and those of *KfALMT* RNAi lines 12A and 23A (Fig. 4.11). However, the difference between the mean totals of WT and *KfALMT* RNAi 8B for dark period 2 was not statistically significant, although none of the *KfALMT* RNAi 8B replicates assimilated more $CO_2$ than any of the WT replicates during either dark period (Fig. 4.12A). Despite the large differences in near-simultaneous $J_{CO2}$ readings, the distribution of $J_{CO2}$ was remarkably similar in each of the genotypes during the dark periods. Maxima in each genotype occurred 3-5.5 h after the beginning of the dark period. In the early part of both dark periods there was a brief and unexplained interruption in the upward trajectory of $J_{CO2}$ in each cuvette, which produced a minor peak in the $J_{CO2}$ timecourses of WT and *KfALMT* RNAi 8B (Fig. 4.11).

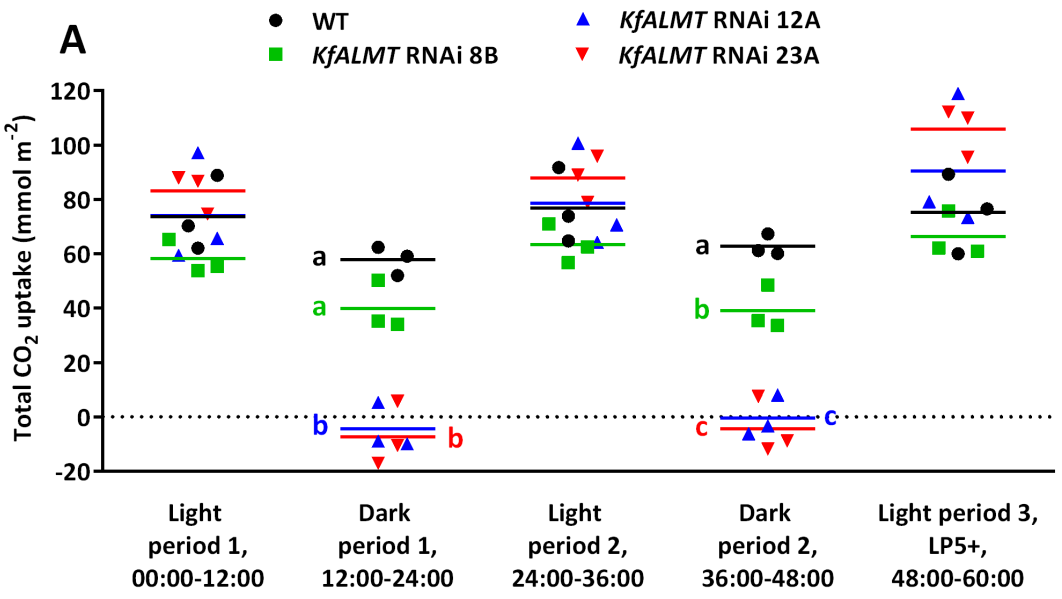


B

| | WT | *KfALMT* RNAi 8B | *KfALMT* RNAi 12A | *KfALMT* RNAi 23A |
|---|---|---|---|---|
| Mean difference ± S.E.M. (mmol $m^{-2}$) | -1.54±2.18 | 2.87±1.65 | 11.91±3.15 | 17.96±1.49 |
| P (paired t-test, 2 D.F.) | 0.553 | 0.224 | 0.065 | 0.007 |

Figure 4.12 – Total $CO_2$ uptake by whole plants during 12 h light/dark periods.
A – Each point represents the total $CO_2$ uptake by a single plant. The results of one-way ANOVA (2 and 8 D.F.) between total $CO_2$ uptake and genotype during each light/dark period are displayed above the data points: $P > 0.05$, not shown; $P \leq 0.001$, ***. Where $P < 0.05$ in one-way ANOVA, the results of a Tukey HSD test are shown. Colour-coded letters represent groups of genotypes within which the difference between any pair of means is non-significant ($P > 0.05$).
B – The results of paired t-tests between mean total $CO_2$ uptake in light period 2 and the 12 h light period following the detachment of the stem between LP4 and LP5 (light period 3).

WT and all three *KfALMT* RNAi lines assimilated almost equal total quantities of $CO_2$ during light periods 1 and 2, with no statistically significant difference between genotypes (Fig. 4.12A). No specimen of any genotype ceased net $CO_2$ uptake at any point during light period 1 or 2, and Phase III was manifested as decline and recovery of $J_{CO2}$ between a relatively brief Phase II and a prolonged Phase IV (Fig. 4.11). Phase III of *KfALMT* RNAi 12A and *KfALMT* RNAi

23A was generally shorter in duration and shallower, in terms of the Phase II-Phase III range of $J_{CO2}$, than WT or *KfALMT* RNAi 8B. The two latter genotypes displayed similar patterns of $J_{CO2}$ in the light (Fig. 4.11).

During light period 3, following the removal of the stem above LP5, there was a significant increase in total $CO_2$ uptake in *KfALMT* RNAi 23A relative to light period 2 (Fig. 4.12B). The increase observed in *KfALMT* RNAi 12A was also larger than that of WT and *KfALMT* RNAi 8B, but was not statistically significant (Fig. 4.12B). Suppression of $J_{CO2}$ during Phase III, relative to Phase II, was slightly intensified in *KfALMT* RNAi 12A and *KfALMT* RNAi 23A. $J_{CO2}$ was suppressed during Phase III to a greater extent in WT and *KfALMT* RNAi 8B; and $J_{CO2}$ from a single replicate specimen of WT declined below zero (Fig. 4.11).

### 4.2.4 Suppression of nocturnal organic acid accumulation

The effect of lower nocturnal $CO_2$ uptake in *KfALMT* RNAi lines on nocturnal malate accumulation was quantified by extracting soluble metabolites from the same timecourse of LP6 samples used for RNA extraction, as described in Section 4.2.1.

The characteristic diel fluctuation of malate concentration of CAM (Osmond, 1978) was found in both the WT control and each of the *KfALMT* RNAi lines (Fig. 4.13A). Accumulated malate present at 02:00 was rapidly turned over thereafter. Malate concentration remained stable or increased slightly between 10:00 and 14:00, and then increased more rapidly during the mid-dark period. Malate accumulated more slowly, relative to WT, in the *KfALMT* RNAi lines, and reached lower concentrations at 2 h before the end of the dark period (22:00). Accumulation of malate at 22:00 was reduced relative to WT to different degrees in the three *KfALMT* RNAi lines, with line 8B somewhat intermediate between WT and lines 12A and 23A (Fig. 4.13).

A

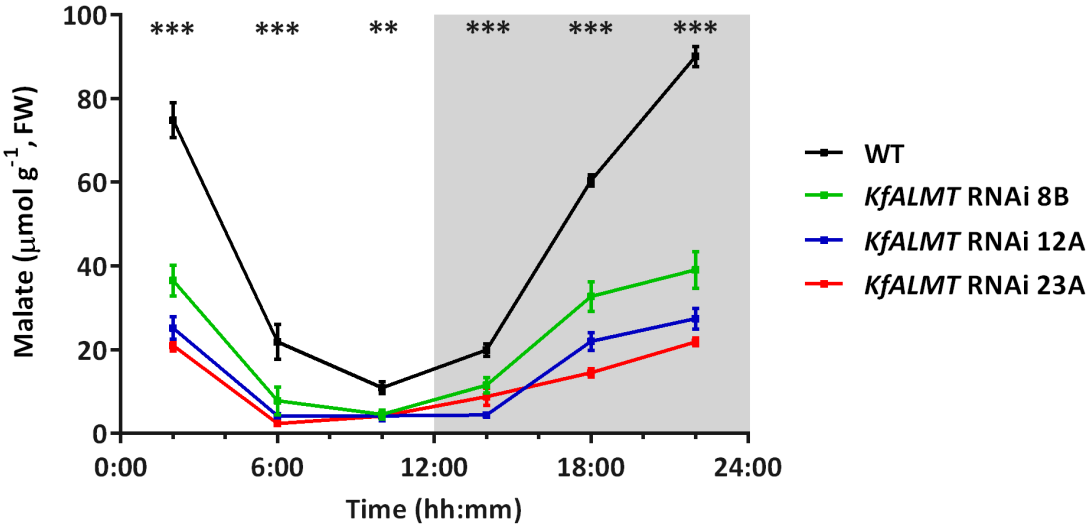


B

| | Time (hh:mm) | | | | | |
|---|---|---|---|---|---|---|
| | 02:00 | 06:00 | 10:00 | 14:00 | 18:00 | 22:00 |
| WT | a | a | a | a | a | a |
| 8B | b | b | b | b | b | b |
| 12A | bc | b | b | b | c | c |
| 23A | c | b | b | b | c | c |

Figure 4.13 – Malate concentration in CAM leaves (leaf pair 6) over a 12:12 LD cycle.
A – Points display mean ± S.E.M for replicate samples; n = 5 for WT and *KfALMT* RNAi 23A, n = 4 for *KfALMT* RNAi 8B and *KfALMT* RNAi 12A. Shading indicates the duration of the dark period. The results of one-way ANOVA (F-test, 3 and 14 D.F.) between mean malate concentration and genotype are displayed above each time-point: **, $P \leq 0.01$; ***, $P \leq 0.001$.
B – Tukey HSD test of significant difference between concurrent mean malate concentrations. Letters indicate groups of genotypes within which the difference between any pair of means is non-significant ($P > 0.05$).

Citrate also accumulates during the night in CAM species such as *Clusia minor* and *K. daigremontiana* (Borland *et al.*, 1992; Chen and Nose, 2004). Citrate concentration was measured in soluble metabolite extracts from samples taken at 2 h before the end of the light period (10:00) and 2 h before the end of the dark period (22:00) in each *KfALMT* RNAi line and

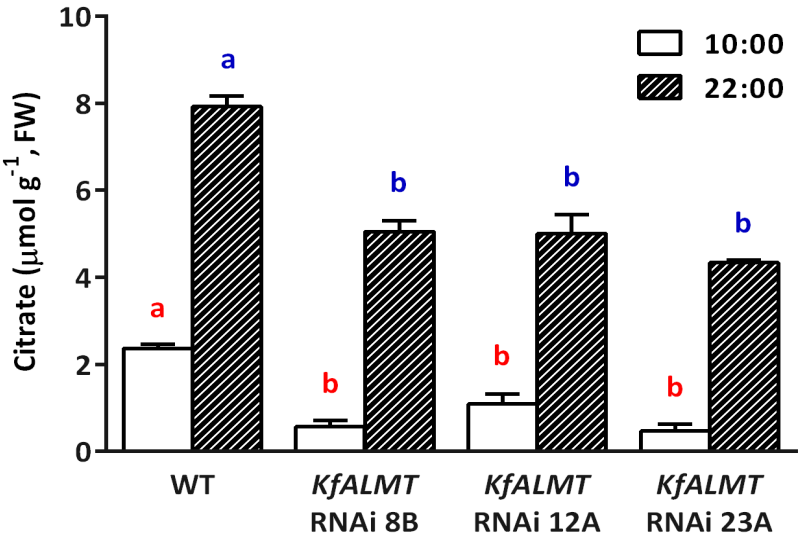


Figure 4.14 - Diel citrate turnover in CAM leaves over a 12:12 LD cycle. Bars represent mean ± S.E.M. of n replicate CAM leaf (LP6) samples; n = 5 for WT and *KfALMT* RNAi 23A, n = 4 for *KfALMT* RNAi lines 8B and 12A. The result of one-way ANOVA (3 and 14 D.F.) between citrate concentration and genotype at both 10:00 and 22:00 was $P < 0.001$. The letters above the bars show the results of Tukey HSD tests, where letters represent groups of genotypes within which the difference between any pair of means is non-significant ($P > 0.05$).

the WT. Citrate concentrations in each of the *KfALMT* RNAi lines were significantly lower than in the WT at both time-points (Fig. 4.14). Citrate accumulation between 10:00 and 22:00 by *KfALMT* RNAi lines 8B, 12A and 23A was 4.48 ± 0.29, 3.91 ± 0.49 and 3.88 ± 0.17 µmol $g^{-1}$, respectively, and was reduced relative to turnover in WT (5.55 ± 0.26 µmol $g^{-1}$). Assuming that citrate concentration at 22:00 was equal to the concentration at the same point in the previous 12:12 LD cycle (i.e. -02:00), the proportion of accumulated citrate that was turned over by 10:00 in each *KfALMT* RNAi line (8B, 89%; 12A, 78%; 23A, 89%) was also greater than in WT (70%).

### 4.2.5 Reciprocal suppression of diurnal carbohydrate synthesis

In order to determine the disruptive effect of apparent CAM suppression on the reciprocal fluctuations of storage carbohydrates with malate (Christopher and Holtum, 1996; Holtum *et al.*, 2005; Cushman *et al.*, 2008; Borland *et al.*, 2016) in the *KfALMT* RNAi lines, starch levels were measured by enzymatic digestion of insoluble material remaining after metabolite extraction using α-amylase and α-amyloglucosidase, followed by a colorimetric assay of the starch-derived glucose. Samples taken from WT and *KfALMT* RNAi 23A at the six time-points in the 12:12 LD time course were assayed, in addition to samples taken from *KfALMT* RNAi 8B and *KfALMT* RNAi 12A at 10:00 and 22:00.

Starch levels fluctuated reciprocally with malate concentration in WT and *KfALMT* RNAi lines, as previously reported for *Kalanchoë* species (Christopher and Holtum, 1996; Dever *et al.*, 2015). Starch levels at 2 h before the end of the light period (10:00) were significantly lower in each *KfALMT* RNAi line than in WT, but differences between mean starch levels in the *KfALMT* RNAi lines were not found to be statistically significant. In each genotype, starch synthesised during the light period was largely degraded by 2 h before the end of the dark period (22:00; Fig 4.15).

Photosynthetically-fixed C is chiefly exported from leaves to sink tissues as sugars in *Kalanchoë*, particularly the disaccharide sucrose (Mayoral and Medina, 1985; Wild *et al.*, 2010). Molar concentrations of glucose, fructose and sucrose were measured in the three *KfALMT* RNAi lines and WT using the same soluble metabolite extracts that were used to determine their leaf malate concentrations (Fig. 4.13).

Glucose concentrations in WT *K. fedtschenkoi* were low during the dark period, but moderately elevated above this baseline concentration during the light period at 02:00 and 06:00.

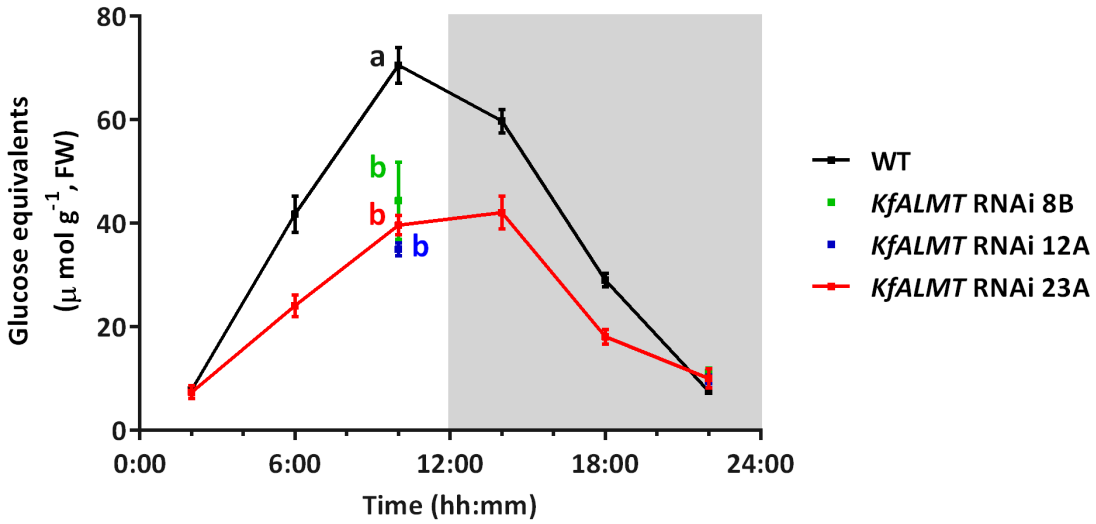


Figure 4.15 – Starch levels in CAM leaves over a 12:12 LD cycle. Points represent mean ± S.E.M; n = 5 for WT and *KfALMT* RNAi 23A, n = 4 for *KfALMT* RNAi 8B and *KfALMT* RNAi 12A. Grey shading represents the duration of the dark period. The result of one-way ANOVA (3 and 14 D.F.) between starch level and genotype at 10:00 was $P < 0.001$.The colour-coded letters next to points at 10:00 display the result of a Tukey HSD test; letters represent groups of genotypes for which the difference between any pair of means is non-significant ($P > 0.05$).

In two of the three *KfALMT* RNAi lines, 8B and 12A, mean glucose concentration was significantly higher than in WT at 02:00 (Fig. 4.16A). Fructose concentration in WT peaked at 06:00, and, again, was reduced to a low baseline concentration between 10:00 and 22:00. Fructose concentration was significantly higher in each *KfALMT* RNAi line relative to WT at 02:00, but lower at 06:00. Peak fructose concentration was therefore shifted to earlier in the light period in the *KfALMT* RNAi lines relative to WT (Fig. 4.16B).

Mean sucrose concentration in WT and *KfALMT* RNAi 8B displayed a prominent peak at 02:00, and then declined to a minimal level at approximately the end of the light period, although the lower sucrose concentrations that were observed at 10:00 and during the dark period remained higher than the simultaneous glucose and fructose concentrations (Fig. 4.16). In *KfALMT* RNAi lines 12A and 23A, the sucrose peak at 02:00 was eliminated, but sucrose

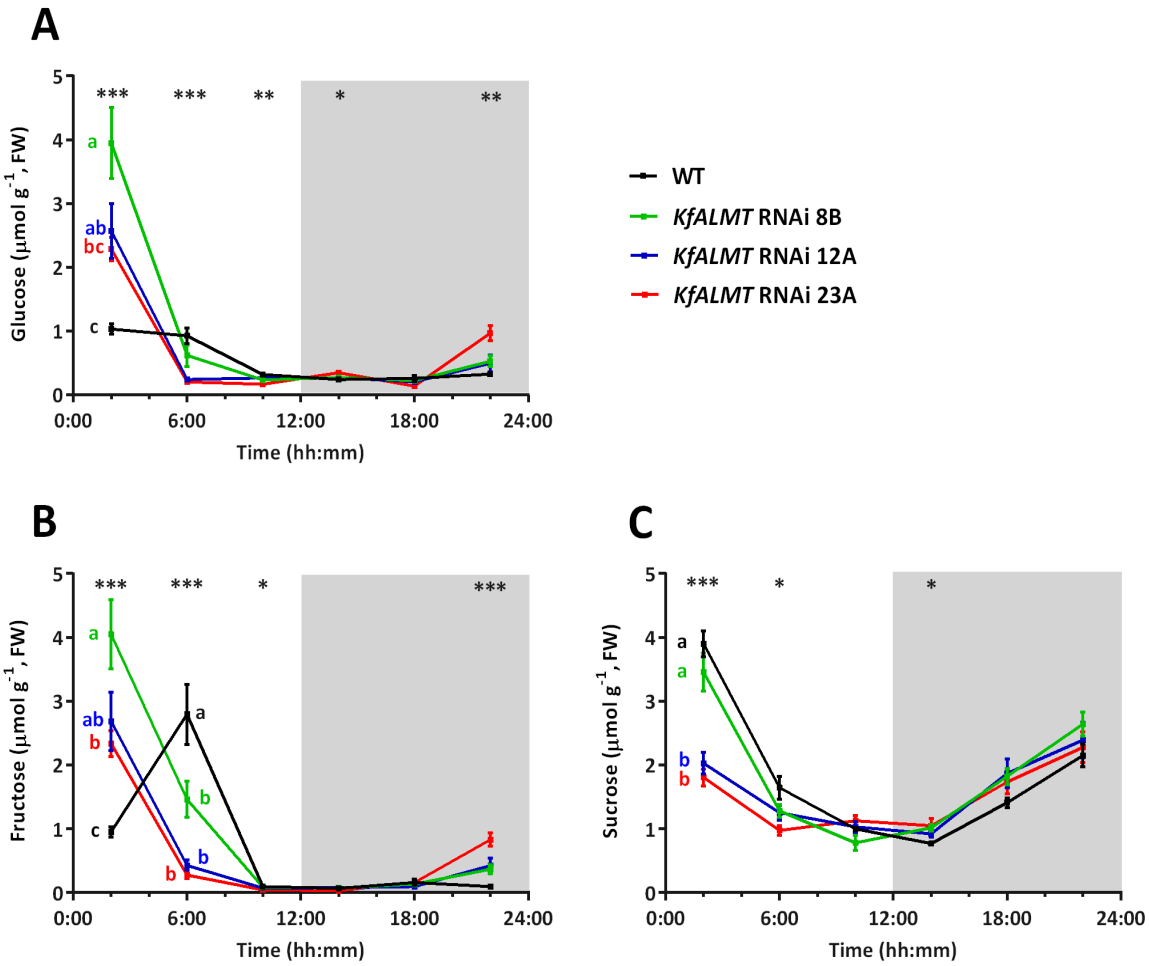


Figure 4.16 – Concentrations of glucose (A), fructose (B) and sucrose (C) in CAM leaves during a 12:12 LD cycle. Points represent mean ± S.E.M sugar concentration; n = 4 for *KfALMT* RNAi 8B and *KfALMT* RNAi 12A, n = 5 for WT and *KfALMT* RNAi 23A. The results of one-way ANOVA (3 and 14 D.F.) between sugar concentration and genotype at each time-point are displayed above that time-point: $P > 0.05$, not shown; $P \leq 0.05$, *; $P \leq 0.01$, **; $P \leq 0.001$, ***. The results of Tukey HSD tests are represented by colour-coded letters next to points at selected times. Letters show groups of genotypes where the difference between any pair of means is non-significant ($P > 0.05$).

concentration in these lines followed WT and *KfALMT* RNAi 8B closely during the latter part of the light period, and throughout the dark period. The range of fluctuation of CAM leaf sucrose concentration over the 12:12 LD cycle was therefore reduced in *KfALMT* RNAi lines 12A and 23A (Fig. 4.16C).

### 4.2.6 Perturbations in the light/dark regulation of CAM-associated genes

Relative transcript levels of some key *K. fedtschenkoi* CAM-associated genes were measured by RT-qPCR using the same WT and *KfALMT* RNAi 23A cDNA samples that had been previously used to measure *KfALMT1* transcript levels (Fig. 4.1).

*PHOSPHOENOLPYRUVATE CARBOXYLASE 1* (*KfPPC1_CAM*; GenBank KM078709) is the principal CAM nocturnal carboxylase (J. Hartwell *et. al.*, unpublished results). *KfPPC1_CAM* relative transcript levels peaked around the end of the light period in both WT and *KfALMT* RNAi 23A. *KfPPC1_CAM* transcript levels were similar during the light period and the early part of the dark period in *KfALMT* RNAi 23A and WT, but were lower at 22:00 in *KfALMT* RNAi 23A, although the difference was not statistically significant (Fig. 4.17).

*β-NAD-MALIC ENZYME1* (*KfNAD_MEb1;* GenBank KM078712) encodes the β subunit of the principal diurnal decarboxylase involved in CAM in *K. fedtschenkoi* (Dever *et al.*, 2015). Relative transcript levels of *KfNAD_MEb1* in both *KfALMT* RNAi 23A and WT peaked at 22:00. While the mean relative transcript level of *KfNAD_MEb1* in WT increased slightly during the light period to peak at 10:00, in *KfALMT* RNAi 23A it was stationary over the light period (Fig. 4.17).

*KfVHA_H* is an ortholog of subunit H of the *A. thaliana* V-ATPase (Kluge *et al.*, 2003). As previously discussed (Section 3.1.1), V-ATPase is thought to contribute to the $H^+$ gradient between the cytosol and vacuolar lumen, which is required for nocturnal vacuolar accumulation of malate in CAM. *KfVHA_H* relative transcript levels in WT and *KfALMT* RNAi 23A were similar across the 12:12 LD timecourse (Fig. 4.17).

*KfPHOSPHOENOLPYRUVATE CARBOXYLASE KINASE1 (KfPPCK1*; GenBank AF162662) is the specific protein kinase responsible for phosphorylating PPC and attenuating its

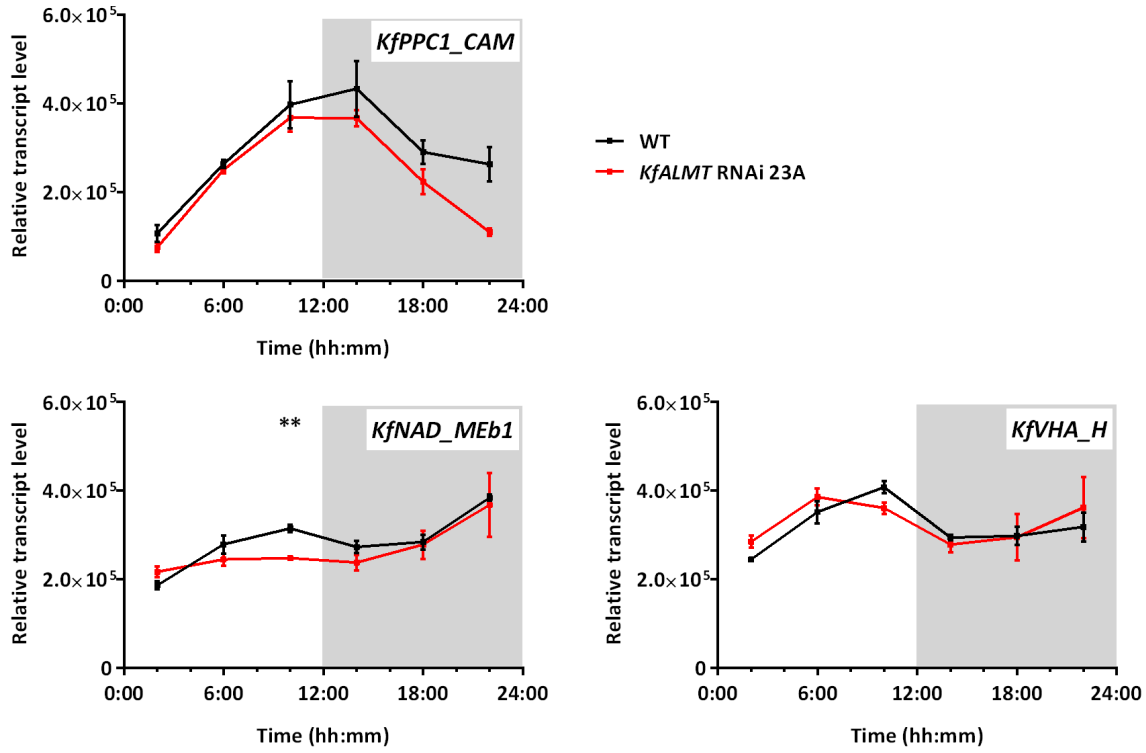


Figure 4.17 – Relative transcript abundance of CAM-associated genes over a 12:12 LD cycle. Relative transcript abundance was determined using RT-qPCR, and normalised to a non-oscillating reference gene, *KfTFP*. Grey shading represents the dark period. Points represent mean ± S.E.M., n = 3. Results of Welch t-tests between mean relative transcript levels are displayed above each point: $P > 0.05$, not shown; $P \leq 0.01$, **.

feed-back inhibition by malate during the night in *K. fedtschenkoi* CAM leaves (Hartwell *et al.*, 1996, 1999). In WT, *KfPPCK1* relative transcript levels were strongly suppressed during the light period, as observed previously in *K. fedtschenkoi* (Hartwell *et al.*, 1996, 1999; Dever *et al.*, 2015), increased slightly from 10:00 to 14:00, and then dramatically increased during the mid-dark period, peaking at 22:00. An altered pattern of *KfPPCK1* transcript abundance was observed in *KfALMT* RNAi 23A (Fig. 4.18). To confirm that this was a consistent effect of hairpin dsRNA-mediated *KfALMT* silencing, cDNA samples from *KfALMT* RNAi lines 8B and 12A (Section 4.2.1) were also used to determine *KfPPCK1* relative transcript abundance over the 12:12 LD timecourse. In the *KfALMT* RNAi lines, *KfPPCK1* relative transcript levels remained

A

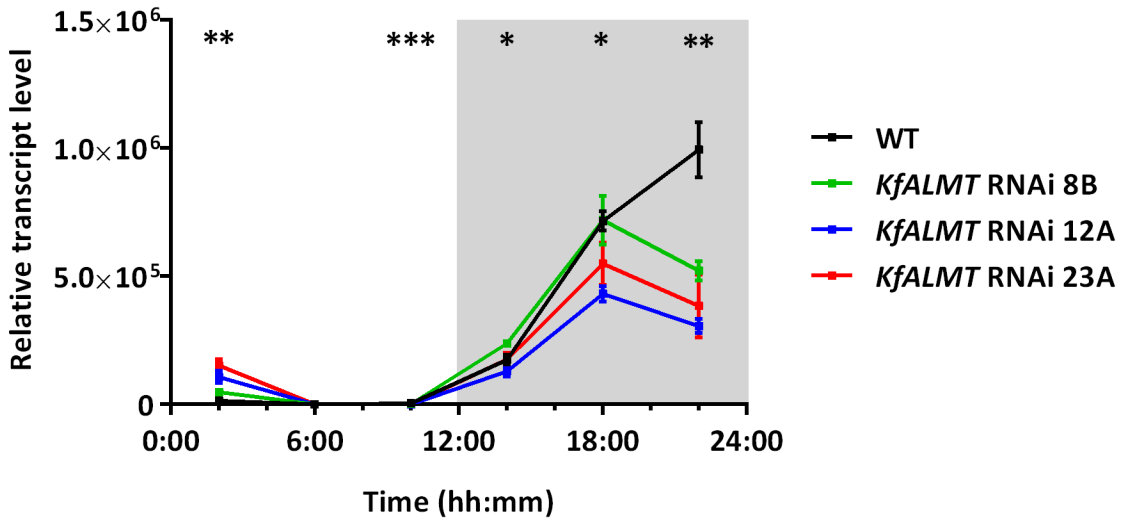


B

| | Time (hh:mm) | | | | |
|---|---|---|---|---|---|
| | 02:00 | 10:00 | 14:00 | 18:00 | 22:00 |
| WT | a | a | ab | a | a |
| 8B | ab | b | a | a | b |
| 12A | bc | b | b | a | b |
| 23A | c | b | ab | a | b |

Figure 4.18 – Relative transcript abundance of *KfPPCK1* over a 12:12 LD cycle.
A – Relative transcript abundance was determined using RT-qPCR, and normalised to a non-oscillating reference gene, *KfTFP*. Points represent mean ± S.E.M., n = 3. Grey shading represents the dark period. Results of one-way ANOVA (3 and 8 D.F.) between relative transcript level and genotype at each time-point are displayed above that time-point: $P > 0.05$, not shown; $P \leq 0.05$, *; $P \leq 0.01$, **; $P \leq 0.001$, ***.
B – Results of Tukey HSD test of mean relative transcript levels when $P \leq 0.05$ for one-way ANOVA. Letters represent groups of genotypes where the difference between any pair of mean relative transcript levels was non-significant ($P > 0.05$).

low at 10:00, and peaked in the middle of the dark period (18:00). *KfPPCK1* transcript abundance declined between 18:00 and 22:00, but remained somewhat higher than in WT at 02:00 in the light period. Therefore, the effect was of a broadening and flattening of the nocturnal peak of *KfPPCK1* transcript abundance (Fig. 4.18).

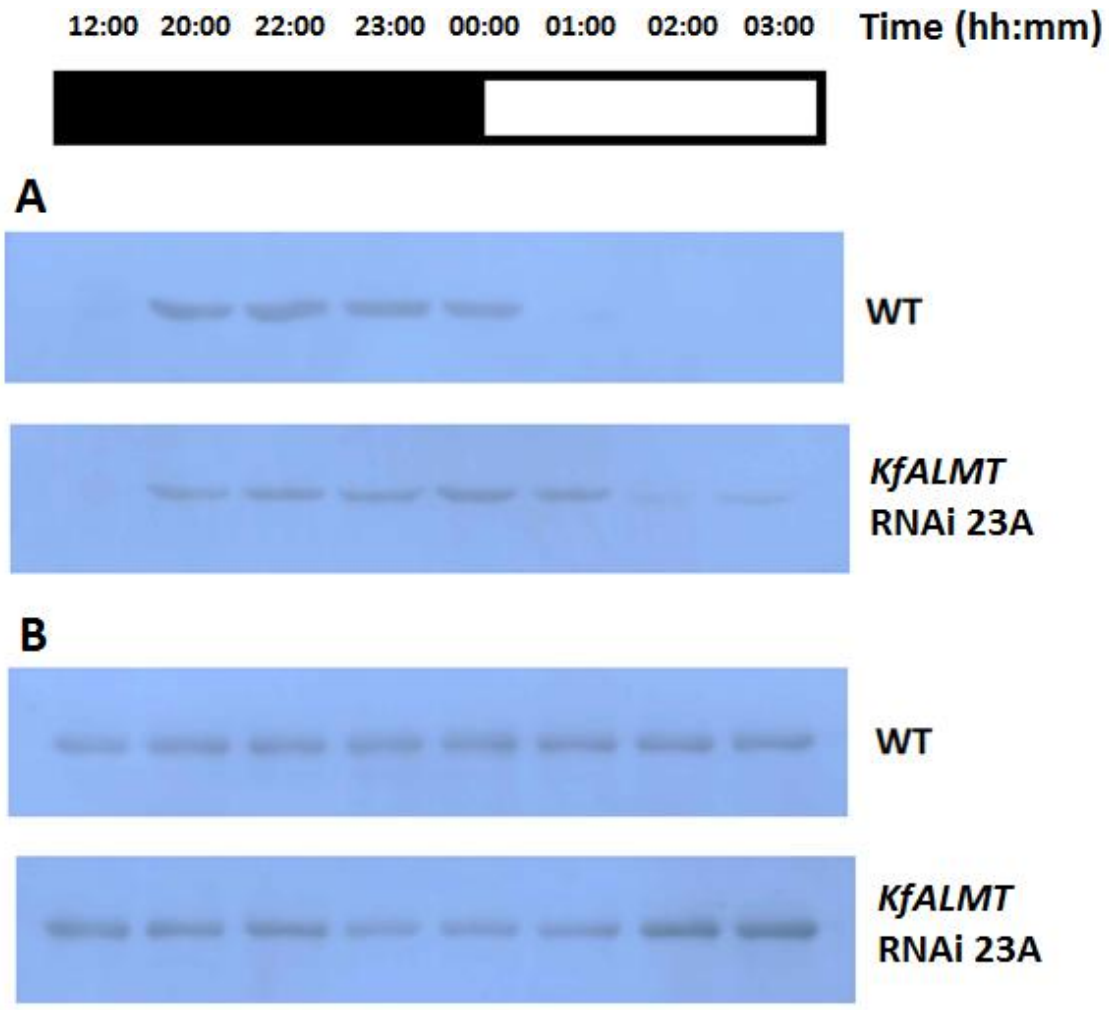


Figure 4.19 – Changes in *in vivo* PPC phosphorylation in CAM leaves (LP6) over the dark-light transition under 12:12 LD. PPC/phosphorylated PPC was detected using immunoblots of total protein extracts of the LP6 samples.
A – Immunoblotting of protein extracts with anti-phospho-PPC antiserum to detect PPC *in vivo* phosphorylation state.
B – Immunoblotting of protein extracts with anti-PPC antiserum as a loading control.

In order to further investigate this effect, a second time-course of LP6 samples was collected from WT and *KfALMT* RNAi 23A in order to measure PPC phosphorylation, as a proxy for *in vivo* PPCK activity, using immunoblotting. Plants were grown for 11 weeks under glasshouse conditions before entrainment to 12:12 LD. LP6 were sampled at the beginning of the

dark period (12:00), and hourly between 20:00 and 03:00 in order to monitor the period around the dark-light transition (00:00) with higher temporal resolution. Total protein was extracted from LP6 samples, separated by SDS-PAGE, and blotted onto nitrocellulose membranes. PPC phosphorylation was detected using an antibody that specifically binds the phosphorylated form of PPC (anti-phospho-PPC; Fig. 4.19A). An anti-PPC antibody without specificity to the phosphorylated form was used as a loading control (Fig. 4.19B).

In both WT and *KfALMT* RNAi 23A LP6 samples, phospho-PPC was not detected at 12:00, but was detected between 20:00 and 00:00 (Fig. 4.19A). 1 h after the beginning of the light period (01:00), the phospho-PPC band of WT was almost completely absent, whereas that of *KfALMT* RNAi 23A was approximately as intense at 01:00 as it was between 20:00 and 00:00. Faint phospho-PPC bands were also observed in *KfALMT* RNAi 23A at 02:00 and 03:00, but were absent in WT. Based on PPC phosphorylation, down-regulation of KfPPCK1 was delayed in the light period in *KfALMT* RNAi 23A relative to WT (Fig. 4.19A).

### 4.2.7 Similarity of growth phenotypes between WT and *KfALMT* RNAi lines

In order to determine whether there was any effect of *KfALMT* silencing on growth, *KfALMT* RNAi lines 8B, 12A and 23A, plus WT controls, were grown from adventitious plantlets under greenhouse conditions for 92 days. Above-ground biomass was harvested, oven-dried and weighed. No statistically-significant difference in biomass was found between WT and any *KfALMT* RNAi line (Fig. 4.20).

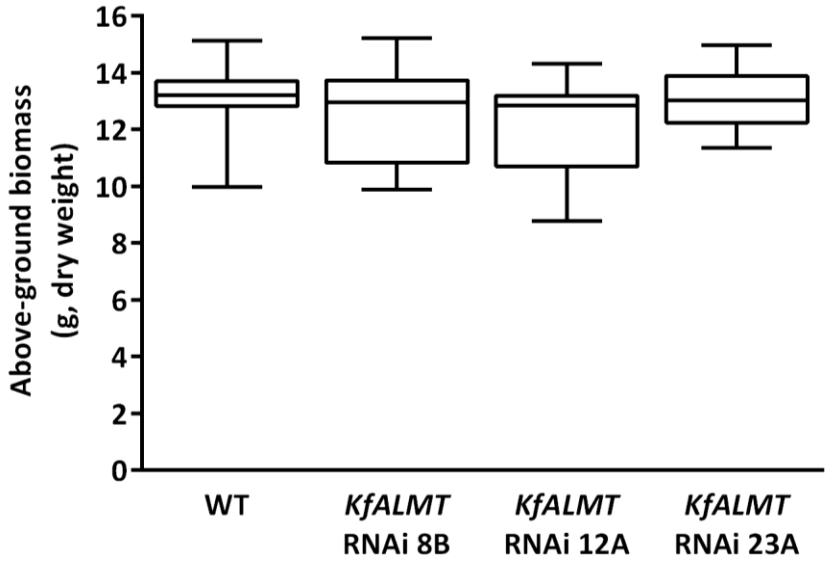


Figure 4.20 – Above-ground dry biomass accumulated during a growth experiment under greenhouse conditions. The box-and-whisker plot of dry biomass displays median, inter-quartile range and minimum-maximum range. n = 9 for *KfALMT* RNAi 8B, n = 8 for WT and Kf*ALMT* RNAi 23A, n = 7 for *KfALMT* RNAi 12A.

## 4.3. Discussion

### 4.3.1 *In vitro* assays reveal that an ALMT is the key vacuolar malate channel in *K. fedtschenkoi* CAM tissues

Prior to the beginning of this thesis project, *Agrobacterium tumefaciens* transformation and tissue culture were used to generate >20 independent *KfALMT* RNAi lines. Three independent *KfALMT* RNAi lines were selected for detailed phenotypic and biochemical characterisation. Selection of three lines controlled for any T-DNA insertion site-positional effects in individual transgenic lines and ensured that the observed phenotypes are due to the silencing of *KfALMT*s. Commonalities between the phenotypes of the three independent lines provided functional evidence for the role of KfALMTs in nocturnal vacuolar malate accumulation associated with CAM. Differences in residual *KfALMT1* steady-state transcript level between *KfALMT* RNAi lines (Fig. 4.1) had the additional benefit of allowing correlations to be drawn between this variable and each of the indices of CAM activity that were quantified in this chapter.

*KfALMT1*/KF122600/Kaladp0073s0021.1 was found to be the most abundant *KfALMT* transcript in *K. fedtschenkoi* CAM leaves using RNA-seq (Fig. 3.3). Measurement of *KfALMT1* transcript levels by RT-qPCR revealed that all three *KfALMT* RNAi lines retained less than 20% of WT transcript levels in the middle of the light period (06:00), which corresponded to the time-point when transcript levels peaked in WT (Fig. 4.1). Determining the extent of transcriptional silencing of the other genes of the *KfALMT* family using RT-qPCR with gene-specific primers is needed to determine the full effect of the hairpin dsRNA transgene in *KfALMT* RNAi lines.

Each of the *KfALMT* RNAi lines displayed reduced nocturnal $CO_2$ uptake (Figs. 4.7 and 4.11). Measurement of $CO_2$ gas exchange by detached leaves of *KfALMT* RNAi 23A and WT from 6 different positions on the stem showed that reduced dark-period $CO_2$ uptake was systemic

in *KfALMT* RNAi line 23A, and not a transient delay in developmental induction of CAM (Fig. 4.9). Dark-period malate accumulation, a second indicator of CAM activity, was also reduced in each of the *KfALMT* RNAi lines (Fig. 4.13). *KfALMT* RNAi 8B had slightly higher levels of *KfALMT1* transcript during the light period relative to lines 12A and 23A (Fig. 4.1), and this was correlated with higher diel turnover of malate and higher dark-period rates of $CO_2$ uptake in the former (Figs. 4.7, 4.11 and 4.13).

As discussed previously (Section 3.1.1), several *A. thaliana* ALMTs have been functionally characterised as anion channels (Hoekenga *et al.*, 2006; Kovermann *et al.*, 2007; Meyer *et al.*, 2010, 2011; Zhang, 2013). Arabidopsis ALMTs are expressed to differing degrees in leaf mesophyll, guard cell and root, and have different functions in each. Coupled vacuolar import of $H^+$ and anionic solutes, such as malate, to high concentration gradients with the cytosol can be effected by vacuolar ALMTs in tandem with membrane-bound $H^+$ active transporters (Kovermann *et al.*, 2007). The electrophysical properties of *A. thaliana* vacuolar ALMTs that have been identified at the molecular level were similar to those of previously unidentified *K. daigremontiana* tonoplast anion channels (Hafke *et al.*, 2003; Kovermann *et al.*, 2007). On this basis, it could be predicted that silencing of the putative vacuolar *KfALMT* gene with the highest steady-state transcript abundance in *K. fedtschenkoi* CAM leaves by RNAi (Figs. 3.3 and 4.1) would decrease the capacity of vacuoles to remove malate from the cytosol, and subject PPC to overwhelming inhibition by elevated cytosolic malate concentrations ($[mal]_{cyt}$) at night.

Tonoplast can be extracted as membrane vesicles from the bulk leaf tissue of *Kalanchoë* (Bremberger *et al.*, 1988; White and Smith, 1989). Internal acidification of tonoplast vesicles, monitored by the progressive fluorescence quenching of weakly-basic dye compounds such as quinacrine, can be used as an indicator of coupled $H^+$-anion import (Fig. 4.2; Lee and Forte,

1978; Bennett and Spanswick, 1983; White and Smith, 1989). Thus measured, the mean $H^+$ transport activity was decreased 1.8-fold and 4.8-fold in tonoplast extracts of *KfALMT* RNAi 8B and *KfALMT* RNAi 23A, respectively, relative to WT. Mean $H^+$ transport activity was significantly decreased in *KfALMT* RNAi 23A only (Fig. 4.3A).

Kinetic modelling of the quinacrine fluorescence assay has concluded that the initial rate of quenching is linearly proportional to the rate of $H^+$ transport (Bennett and Spanswick, 1983). However, Palmgren (1991) contended that anions stabilise the homo-oligomeric interactions that quench weak-base fluorophores when both are concentrated in membrane vesicles, enhance fluorescence quenching, and cause non-linearity between $H^+$-anion coupled transport and quinacrine fluorescence. Published data on this effect is only available for acridine orange with inorganic anions (Palmgren, 1991; Amado *et al.*, 2016), but, absent characterisation of any interaction between $mal^{2-}$/$Hmal^-$ and homo-oligomers of quinacrine-$H^+$, it would be unsafe to assume a linear correlation between the rates of fluorescence quenching and $H^+$ transport across the range of values of the former that were observed in this experiment (Fig. 4.3). With this caveat, the terms '$H^+$ transport activity' and 'rate of quinacrine fluorescence quenching' have been used interchangeably. The correlation between vesicle ΔpH and relative intensity of fluorescence emission should consistently be negative, and therefore the mean $H^+$ transport activity of *KfALMT* RNAi 8B can safely be regarded as intermediate between those of WT and *KfALMT* RNAi 23A (Fig. 4.3A).

Variation of $H^+$ transport activity over wide ranges was observed in replicate tonoplast extractions of WT and *KfALMT* RNAi 8B (Fig. 4.3A), and, based on the linear correlation between protein yield of tonoplast extraction and $H^+$ transport activity, inconsistent purity of the tonoplast extracts contributed to this variation (Fig. 4.3B). A weak negative correlation between

protein yield and ATPase activity further suggested that the purity of tonoplast extracts had been a confounding variable in determining tonoplast $H^+$ transport activity (Fig. 4.4B). The precision of tonoplast $H^+$ transport assays was greatly increased by normalising them to ATPase activity rather than quantity of extracted protein used (Fig. 4.6B). Mean normalised $H^+$ transport activities for *KfALMT* RNAi lines 8B and 23A were both significantly lower than that of WT. Mean $H^+$ transport activity of line 8B was significantly higher than that of line 23A (Fig. 4.6B). This is consistent with the intermediate level of *KfALMT1* transcript in line 8B with respect to WT and line 23A (Fig. 4.1), and accounts for its intermediate level of CAM activity, as measured by the key indices of dark-period $CO_2$ uptake (Fig. 4.7) and malate accumulation (Fig. 4.13).

The ATPase assay is only effective as a normalising assay if it specifically measures the activity of V-ATPase that has been co-isolated with KfALMT. $H^+$-translocating ATPases ($H^+$-ATPases) that are non-tonoplast localised may have contaminated the tonoplast extracts, and could skew normalisation for the quantity of tonoplast protein present by inflating total ATPase activity measurements. Mitochondrial and chloroplastic $F_OF_1$-type $H^+$-ATPases (Junge and Nelson, 2015) and plasma membrane P-type $H^+$-ATPase (Duby and Boutry, 2009) are potential contaminating $H^+$-ATPases. Acid phosphatase is a non-membrane-bound ATPase that could also have contaminated tonoplast extracts and inflated total ATPase measurements (Smith *et al.*, 1984*a*).

Three factors in the experimental protocol would be expected to limit the contribution of non-vacuolar and non-membrane-bound ATPases to the total activity. Firstly, initial centrifugation of the crude leaf homogenate at 13,000 *g* (Section 2.6.1) should pellet both mitochondria and chloroplasts (Cook *et al.*, 1995), and separate them from final extracts. Secondly, the buffer pH used for the enzyme assay (8.0) is optimised for V-ATPase. In

experiments on isolates of *K. daigremontiana* leaf mesophyll vacuoles, mitochondria and chloroplasts were shown to be present as contaminants, but their respective $F_OF_1$-type $H^+$-ATPases were largely inactive at pH 8.0 in a similar buffer to the one used in the current experiments (Smith *et al.*, 1984*b*). This suggests that the contribution of mitochondrial and chloroplastic $H^+$-ATPases to total ATPase activity measurements would have been minimal. Thirdly, 0.1 mM sodium orthomolybdate was included in the assay buffer as an acid phosphatase inhibitor (Smith *et al.*, 1984*a*).

The rates of inhibition of ATPase obtained in the presence of the V-ATPase inhibitor $KNO_3$ ranged between 66.8% and 80.8% (Fig. 4.5A). As an indicator of tonoplast purity, these results compare favourably with published rates of inhibition by 50 mM $KNO_3$ of *K. daigremontiana* tonoplast extracts (58%, Bremberger *et al.*, 1988; 56.3%, Mariaux *et al.*, 1997) and isolated vacuoles (45%, Jochem *et al.*, 1984). Weak negative correlations were found between the protein yield of the tonoplast extractions and the rate of $NO_3$ inhibition (Fig. 4.5B). Although the correlation coefficient ($R^2$) was lower than that between protein yield and ATPase activity (Fig. 4.4B), this did suggest that $NO_3$-insensitive ATPases were part of non-tonoplast contaminants of the tonoplast extractions. These could have included plasma membrane $H^+$-ATPase, as the *Beta vulgaris* enzyme has been found to be $NO_3$-insensitive *in vitro* (Huang and Berry, 1990). Conversely, $NO_3$ inhibition of mitochondrial $H^+$-ATPase purified from *Avena sativa* has been reported (Wang and Sze, 1985). Measurements of ATPase activity of tonoplast extracts should be made in the presence of known specific inhibitors of mitochondrial $H^+$-ATPases such as sodium azide (Wang and Sze, 1985) in order to detect the extent of contamination by mitochondrial $H^+$-ATPases in tonoplasts extracts.

In spite of the potential for non-vacuolar ATPases to confound the method for normalisation of $H^+$ transport activity used in this chapter, in principle it is no more or less arbitrary to use a sub-set of extracted protein to normalise the assay than the total extracted protein. Normalisation by ATPase activity therefore represents an improvement over the non-normalised transport assay simply by virtue of improving its precision. However, differential regulation of V-ATPase expression in WT and *KfALMT* RNAi lines as a pleiotropic effect of hairpin dsRNA-mediated *KfALMT* silencing is possible, and could invalidate normalisation by ATPase activity. No difference in *KfVHA_H* transcript abundance between CAM leaves of *KfALMT* RNAi 23A and WT was evident (Fig. 4.17). Relative abundance of transcripts encoding the other V-ATPase subunits (Kluge *et al.*, 2003) could now be measured in order to confirm that there is no transcriptional up- or down-regulation of the enzyme in response to decreased KfALMT transport activity.

Mesophyll comprises the bulk of CAM leaf tissue in *Kalanchoë* (Maxwell *et al.*, 1997). Measurements of $H^+$ transport activity in tonoplast extracts of whole CAM leaves will have been dominated by mesophyll tonoplasts, and therefore should be an accurate *in vitro* indicator of the capacity of mesophyll vacuoles to accumulate malate in CAM in *K. fedtschenkoi*. However the possibility that compromised vacuolar KfALMT function in guard cells was a contributory factor to suppressed nocturnal malate accumulation in *KfALMT* RNAi lines has not yet been addressed. Phylogenetic analysis clustered *AtALMT6*, in addition to *AtALMT4* and *AtALMT5*, with the two *KfALMT*s that were predicted to have been silenced in the *KfALMT* RNAi lines used in this study (Fig. 3.2). AtALMT6 is a vacuolar malate channel expressed in guard cells, and is thought to participate in stomatal opening (Meyer *et al.*, 2011; Palmer *et al.*, 2016). As discussed previously (Section 3.3.1), it is possible that this gene performed the same function in the most recent

common ancestral species of *A. thaliana* and *K. fedtschenkoi*, and that it was recruited to function as the CAM vacuolar malate channel during the evolution of CAM in ancestral species of *K. fedtschenkoi*, while also retaining its original stomatal function. If this was true, impaired stomatal opening in the dark period could have deprived PPC of atmospheric $CO_2$, and thus reduced nocturnal malate synthesis. Suppression of light-period $CO_2$ uptake was not apparent in *KfALMT* RNAi lines (Fig. 4.11), but their leaf stomatal resistance and intracellular $CO_2$ concentration should be measured directly throughout the diel cycle in order to determine whether impaired stomatal opening restricts diffusion of $CO_2$ to the sites of carboxylation, in addition to the CAM-specific accumulation of malate.

### 4.3.2 Reduced ALMT activity correlates with reduced nocturnal $CO_2$ uptake and organic acid synthesis

If it is accepted that nocturnal vacuolar malate import is compromised in *KfALMT* RNAi lines because of reduced tonoplast conductance of $mal^{2-}$, lower nocturnal malate accumulation in CAM leaves of these lines would be expected due to retention of malate in the cytosol and malate inhibition of PPC. Phenotypic differences between *KfALMT* RNAi lines 8B, 12A and 23A supported this hypothesis. The association of lower *KfALMT1* transcript abundance (Fig. 4.1) and greater reduction of *in vitro* tonoplast $H^+$ transport activity in *KfALMT* RNAi 23A (Fig. 4.6B) with lower dark-period $CO_2$ uptake (Figs. 4.7 and 4.11) and malate accumulation (Fig. 4.13) *in vivo* in this line, relative to *KfALMT* RNAi 8B, suggests that KfALMT1-mediated vacuolar malate import exerts a degree of control over flux in the nocturnal CAM pathway. Although tonoplast $H^+$ transport activity was not measured in *KfALMT* RNAi 12A, in this line similar *KfALMT1* transcript abundance (Fig. 4.1) and quantities of CAM leaf malate

accumulation (Fig. 4.13) and $CO_2$ uptake (Figs. 4.7 and 4.11) to those observed in *KfALMT* RNAi 23A offer additional support for a correlation between *KfALMT1* expression and CAM function.

Any trend toward increasing $[mal]_{cyt}$ due to impaired vacuolar malate import would be self-limiting due to feedback inhibition of PPC by malate. The latter would also be expected to increase the ratio of PEP concentration to $P_i$ concentration in the cytosol, which in turn would inhibit cytosolic phosphofructokinase (PFK) and reduce the supply of PEP to PPC via glycolysis (Häusler *et al.*, 1989; Plaxton, 1996). Antiport of PEP and $P_i$ by the plastidic PEP/$P_i$ translocator (PPT, Weber and Linka, 2011) would presumably mediate the inhibition of plastidic PFK also (Plaxton, 1996). PEP concentration was found to decrease sharply at the beginning of the dark period in *K. pinnata*, *K. daigremontiana* and *A. comosus* (Chen and Nose, 2004), which could indicate that regulation of the glycolytic pathway in CAM keeps PEP at a low concentration in order to maximise glycolytic flux.

Interestingly, *KfPPCK1* transcript abundance was reduced in *KfALMT* RNAi lines relative to WT at 2 h before the end of the dark period (22:00, Fig. 4.18). Given that KfPPCK1 activity is tightly controlled by its transcript abundance (Hartwell *et al.*, 1996, 1999), a decrease in KfPPCK1-catalysed PPC phosphorylation could have made the latter enzyme more sensitive to inhibition by the putative increases in $[mal]_{cyt}$ in *KfALMT* RNAi lines during the latter part of the dark period. This would help to explain observations of greater suppression of $CO_2$ uptake in CAM leaves of *KfALMT* RNAi lines, relative to WT, in the latter part of the dark period than in its earlier part (Figs. 4.7 and 4.9). However, *in vitro* measurements of PPC-malate $K_i$ (Nimmo *et al.*, 1984) should be compared between *KfALMT* RNAi lines and WT in order to show that suppression of *KfPPCK1* steady-state transcript abundance in the former actually increases PPC

sensitivity to feed-back inhibition by malate, and that this is a proximate cause of their $CO_2$ gas exchange phenotype.

The possibility that elevated $[mal]_{cyt}$ represses *PPCK* transcript abundance is supported by published observations of decreased *PPCK* translatable mRNA levels in *K. daigremontiana* that were subjected to a mid-dark period temperature increase (Borland *et al.*, 1999). The temperature increase was thought to have stimulated malate efflux from vacuoles, as previously observed in *K. daigremontiana*, and raised $[mal]_{cyt}$, resulting in suppression of *PPCK* transcript level by an as-yet uncharacterised metabolite signalling pathway (Friemert *et al.*, 1988; Borland *et al.*, 1999). This effect was eliminated when the leaves were kept in a pure $N_2$ gas atmosphere from the start of the dark period onwards, demonstrating that it depends on the prior existence of substantial vacuolar malate concentrations to drive malate export to the cytosol and suppression of *PPCK* transcript levels (Borland et al., 1999).

Nocturnal citrate accumulation was also suppressed in the *KfALMT* RNAi lines studied, although this suppression was less severe as a ratio of transgenic to WT citrate levels than suppression of malate accumulation was (Fig. 4.14). Low rates of inward-rectifying citrate transport in vacuoles isolated from *K. daigremontiana* leaf mesophyll have suggested that neither ALMT nor any other inward-rectifying channel imports citrate to the vacuolar lumen at night (Hafke *et al.*, 2003). Suppression of nocturnal citrate synthesis is, therefore, likely to be a secondary effect of the suppression of CAM in *KfALMT* RNAi lines.

Nocturnal citrate synthesis in CAM is catalysed by mitochondrial citrate synthase from OAA and acetyl-CoA (Holtum *et al.*, 2005). There are two possible pathways that can produce the pyruvate required for pyruvate dehydrogenase (PDH)-catalysed acetyl-CoA synthesis: 1. dephosphorylation of glycolysis-derived PEP, catalysed by pyruvate kinase (PK); or 2.

decarboxylation of malate, catalysed by NAD(P)-ME (Holtum *et al.*, 2005). Regardless of the source of pyruvate in CAM, consumption of newly-synthesised malate or OAA is implied by the requirement for the latter in citrate synthesis (Holtum *et al.*, 2005). If nocturnal $[mal]_{cyt}$ had increased in *KfALMT* RNAi lines, this might be expected to supply increased citrate synthesis in mitochondria.

Malate has been identified as an inhibitor of PK; purified *Ricinus communis* PK had a $K_i$ for malate of 5.7 mM at pH 7.5 (Hu and Plaxton, 1996; Plaxton, 1996). Increased $[mal]_{cyt}$ may therefore restrict flux through pathway 1. Decreased activation of NAD-ME during the dark period has been reported in extracted and solubilized mitochondria from *K. fedtschenkoi*. However, this state was reversed readily by 10 μM acetyl-CoA, and moreover could not have limited malate decarboxylation or citrate synthesis throughout the dark period because inhibition was only gradually established over its duration (Cook *et al.*, 1995).

Without an obvious enzyme regulatory mechanism that could explain suppression of pathway 2, a reduction of the nocturnal citrate synthesis rate by a lower nocturnal respiratory rate is a plausible alternative hypothesis. Respiratory activity may have been reduced by a reduced demand for ATP to drive coupled $H^+$-malate import in *KfALMT* RNAi lines (see below, Section 4.3.4; Holtum *et al.*, 2005). PDH-, mitochondrial MDH- and NAD-ME-catalysed reactions all generate NADH in the matrix, and regeneration of $NAD^+$ is coupled to ATP synthesis by the respiratory electron transport chain and mitochondrial $F_OF_1$-ATPase (Heldt and Piechulla, 2011*a*). Reduced ATP consumption could thus have decreased the rates of NADH re-oxidation, and, consequently, the $NAD^+$-reducing reactions of citrate synthesis. However, direct measurements of respiration in *KfALMT* RNAi lines and WT *K. fedtschenkoi*, by measuring

dark-period $O_2$ uptake, for example, are needed to show that respiratory rates are lower in the former.

### 4.3.3 Detached leaves were not a suitable proxy for the diel CAM rhythm of $CO_2$ assimilation in *K. fedtschenkoi*

It was not possible to observe both stable Phase II and Phase IV in a series of $CO_2$ gas exchange measurements of detached CAM leaves from WT *K. fedtschenkoi*. In two independent experiments that measured detached-leaf $CO_2$ gas exchange in leaf development gradients along the stems of WT and *KfALMT* RNAi 23A, total light-period $CO_2$ uptake showed a tendency to decline over the time-course in both genotypes (Fig. 4.10 and Appendix 3). Conversely, Phase II and Phase IV were absent in detached WT CAM leaves in a separate experiment from the onset of $CO_2$ gas exchange monitoring (Fig. 4.7). These data are inconsistent with published diel $CO_2$ gas exchange measurements of intact *Kalanchoë* specimens, which have shown significant Phase II and Phase IV $CO_2$ uptake in CAM leaves (Rascher and Lüttge, 2002; Griffiths *et al.*, 2008; von Caemmerer and Griffiths, 2009; Wild *et al.*, 2010).

Unlike detached CAM leaves, intact WT *K. fedtschenkoi* displayed substantial $CO_2$ assimilation in phases II-IV (Fig. 4.11). The WT pattern of light-period $CO_2$ gas exchange was stable over 48 h, and substantial assimilation of atmospheric $CO_2$ persisted for 12 h after the detachment of younger leaves (LP1-4; Fig. 4.11), which were at the early stages of the developmental transition from $C_3$ to CAM photosynthesis (Fig. 4.9) and would be expected to assimilate a larger proportion of their total 24 h $CO_2$ uptake during the light period (Jones, 1975). Patterns of $CO_2$ gas exchange in intact WT *K. fedtschenkoi* are consistent with previous results (Dever *et al.*, 2015), and, together with $CO_2$ gas exchange behaviour following detachment of

LP1-4, show that direct fixation of atmospheric $CO_2$ during phases II-IV makes a considerable contribution to total diel uptake (Fig. 4.11).

The loss of light-phase $CO_2$ uptake over consecutive 12:12 LD cycles in detached leaves could be explained by abolition of the source-sink relationships that pertain to CAM leaves in intact *K. fedtschenkoi*. Mayoral *et al.* (1991) demonstrated that non-invasive disruption of phloem-mediated export of fixed C from *K. pinnata* CAM leaves, by girdling of their petioles as they remained attached to the plant, led them to both accumulate starch and suppress light-period $CO_2$ uptake, while Phase I $CO_2$ uptake remained relatively unperturbed. This effect could have been replicated during $CO_2$ gas exchange measurements of detached *K. fedtschenkoi* CAM leaves. Assuming that *K. fedtschenkoi* also down-regulates light-period $CO_2$ uptake in response to blockage of phloem transport, then this response would have occurred if, as in many plant species, phloem bulk flow ceases in *K. fedtschenkoi* when leaves are detached and their cut petioles are placed in water (King and Zeevaart, 1974; Turgeon and Wolf, 2009). This is thought to occur from blockage of the sieve elements of their phloem vessels by accumulation of fibrous protein bodies and the insoluble polysaccharide callose (Mullendore *et al.*, 2010).

### 4.3.4 CAM suppression in *KfALMT* RNAi lines upsets the balance between the reciprocal turnover of malate and starch

In the three *KfALMT* RNAi lines tested and WT, the majority of the malate present in CAM leaves in the light period at 02:00 had been broken down 8 h later (10:00, Fig. 4.13), and there was concurrent accumulation of starch (Fig. 4.15). In CAM, nocturnal $CO_2$ fixation by PPC is constrained by the availability of storage carbohydrate accumulated during the previous day for conversion to PEP (Dodd *et al.*, 2002, 2003; Cushman *et al.*, 2008*a*; Borland *et al.*, 2016).

Rubisco-PPC differential $^{13}CO_2$ discrimination ($\delta^{13}C$) analysis has shown that almost all of the fixed C generated by conversion of malate to carbohydrate via the diurnal CAM pathway (Fig. 1.1B) was utilised for transitory starch accumulation in *K. daigremontiana* CAM leaves (Wild *et al.*, 2010).

Between 02:00 and 10:00, malate breakdown could have accounted for 98% and 35% of the hexose stored as starch in WT and *KfALMT* RNAi 23A, respectively, in the limiting case of regeneration of 1 mole hexose per 1.5 moles malate. Mean malate concentration in *KfALMT* RNAi 23A was significantly reduced relative to WT at 10:00 (Fig. 4.13), suggesting that increased demand for carbohydrate to supply starch synthesis drove increased consumption of malate via the diurnal CAM pathway (Fig. 1.1B). Breakdown of citrate to lower concentrations by 10:00 also occurred in each of the *KfALMT* RNAi lines relative to WT (Fig. 4.14). Although diel citrate turnover in CAM cannot function as a night-to-day shuttle of fixed C (Lüttge, 1988), *KfALMT* RNAi lines could have broken down additional citrate in order to compensate for the imbalance between the supply of nocturnally-accumulated malate and the demands of starch synthesis to sustain the next CAM cycle.

In spite of this, the quantity of CAM leaf starch accumulated during the light period in *KfALMT* RNAi 23A implies that another pool of fixed C, in addition to that derived from malate breakdown, was utilised for starch synthesis. In *K. daigremontiana* CAM leaves, carbohydrate produced during phases II and IV by direct fixation of atmospheric $CO_2$ has been found to be exported, via phloem, at double the aggregate rate for fixed C over the diel cycle (15%; Wild *et al.*, 2010). $^{14}CO_2$ labelling of *K. pinnata* CAM leaves also found that translocation of fixed $^{14}C$ to roots was more rapid when it was assimilated during Phase IV than when it was assimilated during Phase I (Mayoral and Medina, 1985). Therefore, there appears to be no absolute or

mechanistic barrier to increased partitioning to starch of fixed C derived from Rubisco-catalysed direct uptake of atmospheric $CO_2$ in *KfALMT* RNAi lines, based on partitioning data on CAM leaves of other *Kalanchoë* species. However, this would counteract previously observed patterns of differential source-to-sink translocation of Rubisco- and PPC-fixed C.

In *KfALMT* RNAi 12A and *KfALMT* RNAi 23A, lines with relatively severe suppression of CAM (Figs. 4.7 and 4.13), phases II and IV were expanded and Phase III was reduced to a relatively shallow and brief (3-4 h) dip in $J_{CO2}$ (Fig. 4.11). Similar $J_{CO2}$ traces were obtained for these lines after their younger leaves (LP1-4) were removed (Fig. 4.11), and there was a small, but significant, increase in area-normalised total $CO_2$ uptake by *KfALMT* RNAi 23A (Fig. 4.12B). This suggests that both nocturnal, PPC-catalysed $CO_2$ uptake (Fig. 4.10) and diurnal, Rubisco-mediated $CO_2$ uptake developed as leaves of this line matured beyond the LP4 stage.

Minimisation of Phase III in lines 12A and 23A (Fig. 4.11) shows that they may have increased their light-period uptake of atmospheric $CO_2$ to compensate for the aforementioned deficit between malate breakdown and starch synthesis. Although this did not produce a statistically-significant increase in total light-period $CO_2$ uptake in small populations (n = 3) of these lines, relative to WT (Fig. 4.12A), individual specimens of the former maintained near-maximal rates of $CO_2$ uptake for a longer portion of the light period (Fig. 4.11). *K. daigremontiana* CAM leaves have also been found to increase light-period $CO_2$ uptake as a response to suppression of malate accumulation during the previous dark period when this was caused by enclosure in a pure-$N_2$ gas atmosphere (Borland and Griffiths, 1997).

Whole specimens of WT and *KfALMT* RNAi 8B displayed similar patterns of $CO_2$ uptake during the light period; Phase II was brief relative to Phase IV, and the duration of Phase III was 7-8 h (Fig. 4.11). Given that suppression of CAM in line 8B is relatively mild (Figs. 4.8 and

4.13), it appears that there is a critical point on the scale of CAM activity below which the putative up-regulation of light-period $CO_2$ uptake is triggered. Phenotyping of a range of independent *KfALMT* RNAi lines, with more variety in their degrees of CAM suppression, is needed to confirm this. The quantitative contribution that expansion of phases II and IV makes to light-period starch synthesis in *KfALMT* RNAi lines cannot be determined from the present data, but could be determined by $\delta^{13}C$ analysis as performed on *K. daigremontiana* by Wild *et al.* (2010).

If it is accepted that a lower proportion, relative to WT, of light-period fixed C was available for source-to-sink translocation in *KfALMT* RNAi lines due to the demands of transitory starch synthesis in CAM leaves (Fig. 4.15), then the finding that these lines accumulated above-ground biomass at the same rate as WT (Fig. 4.20) could be explained by a compensatory increase in source-to-sink translocation of fixed C during the dark period. In the limiting case of conversion of 1 mole starch (hexose-equivalent) to 2 moles PEP via starch degradation and glycolytic pathways, only 20% of starch turnover between 14:00 and 22:00 would have been required to account for concurrent malate accumulation in *KfALMT* RNAi 23A CAM leaves, whereas the equivalent figure for WT was 67% (Figs. 4.13 and 4.15). Additionally, mitochondrial respiration is required to generate ATP for coupled vacuolar import of $H^+$ and malate (Holtum *et al.*, 2005), and import of a smaller quantity of malate would be expected to decrease the demand for respiratory substrate on the pool of soluble fixed C produced by starch breakdown. Therefore, it seems reasonable to infer that a larger quantity of starch-derived carbohydrate would have been surplus to the requirements of malate accumulation during the dark period in *KfALMT* RNAi 23A, and could have supplied an increase in translocation of fixed C to sink tissues, relative to WT, during the same period.

$\delta^{13}C$ analysis of *K. daigremontiana* CAM leaf metabolites and phloem exudate has shown that starch breakdown supplied the substrate for sucrose synthesis during the dark period, balancing phloem-mediated sucrose export during the earlier part of the dark period and increasing leaf sucrose concentration slightly during the latter part (Wild *et al.*, 2010). In source leaves of the $C_3$ species *Ricinus communis*, an increase in the supply of soluble carbohydrate from nocturnal starch breakdown, relative to the demand for respiratory substrate, has been shown to increase source-to-sink translocation of fixed C (Grimmer and Komor, 1999). If plasticity of nocturnal phloem export occurs on a similar basis in *K. fedtschenkoi*, responding to the nocturnal demand for substrate for the nocturnal CAM pathway (Fig. 1.1A) in addition to that for respiration, increased nocturnal phloem export of fixed C from CAM leaves of *KfALMT* RNAi lines could plausibly compensate for the putative decrease in its diurnal export.

Given that *K. pinnata* and *K. tubiflora* were found to suppress nocturnal starch breakdown when nocturnal malate accumulation was decreased by enclosing CAM leaves in $CO_2$-free air (Kluge, 1969), it is remarkable that, in the context of suppressed nocturnal malate accumulation, *KfALMT* RNAi lines broke down starch to the same levels as WT by 2 h before the end of the dark period (22:00, Fig. 4.15). Almost total breakdown of starch reserves during the dark period was also observed in transgenic *K. fedtschenkoi* lines with hairpin dsRNA-targeted, RNAi-mediated silencing of *KfPPDK* or *KfNAD-MEb1*, and decreased dark-period malate accumulation against a background of constitutively high CAM leaf malate concentrations (Dever *et al.*, 2015). This discrepancy could be related to a species-level difference in the regulation of starch metabolism between WT *K. fedtschenkoi* and other *Kalanchoë* species, in which case starch turnover would be unaffected in the former by suppression of nocturnal malate synthesis by enclosure in a $CO_2$-free atmosphere. Alternatively,

the regulatory mechanisms that control nocturnal starch breakdown could be unaffected by the metabolic phenotypes of *KfALMT* RNAi, *KfPPDK* RNAi and *KfNAD-MEb1* RNAi lines. Phenotyping of *K. fedtschenkoi* loss-of-function mutants in other CAM-related enzymes or transporters may reveal a phenotype with both suppressed nocturnal malate accumulation and starch breakdown. Finally, persistent starch breakdown in *KfALMT* RNAi could be a longer-term regulatory response to persistent suppression of nocturnal malate accumulation, in which case suppression of nocturnal malate synthesis by deprivation of atmospheric $CO_2$ over multiple diel cycles would be expected to replicate this effect in WT *K. fedtschenkoi*.

### 4.3.5 CAM suppression in *KfALMT* RNAi lines favours accumulation of hexoses over sucrose in leaves during the light period

Carbon is chiefly exported from CAM leaves of *Kalanchoë* species in the form of soluble sugars, particularly sucrose (Mayoral and Medina, 1985; Wild *et al.*, 2010). WT control leaves accumulated sucrose during the early light period (02:00, Fig. 4.16), a pattern that has also been observed in *K. daigremontiana* (Truesdale *et al.*, 1999; Wild *et al.*, 2010). *KfALMT* RNAi line 8B, whose light-dark turnover of malate was intermediate between WT and lines 12A and 23A (Fig. 4.13), accumulated sucrose in its CAM leaves to a similar concentration as WT at 02:00, but also accumulated glucose and fructose at this time-point. Glucose and fructose concentrations were also elevated at 02:00 in the severely CAM-suppressed lines 12A and 23A, but the sucrose peak had been eliminated. It is, therefore, apparent that *KfALMT* RNAi lines displayed preferential accumulation of glucose and fructose over sucrose (Fig. 4.16).

As previously discussed, fixed C produced by malate breakdown via the diurnal CAM pathway (Fig. 1.1B) is almost entirely utilised as substrate for starch synthesis (Wild *et al.*,

2010). Localisation of Calvin cycle, gluconeogenesis and starch synthesis pathways within plastids has the potential to altogether bypass the cytosolic enzymes that mediate synthesis of sucrose (Borland *et al.,* 2016). Sucrose accumulated during Phase II in *Kalanchoë* CAM leaves may therefore serve as a reservoir for phloem export to allow it to continue throughout Phase III.

However, suppression of phloem export and retention of soluble sugars in CAM leaves of *KfALMT* RNAi lines could provide additional substrate for starch synthesis to supplement the insufficient quantities that were available from conversion of malate to carbohydrate by the Phase III CAM pathway (Fig. 1.1), as discussed in the previous section. The mean total mass of glucose, fructose and sucrose was higher at 02:00 in the moderately CAM-suppressed *KfALMT* RNAi line 8B (2622 ± 166 μg $g^{-1}$, fresh weight) than in WT (1694 ± 61 μg $g^{-1}$, fresh weight) or the severely CAM-suppressed lines 12A and 23A (1641 ± 142 and 1451 ± 91 μg $g^{-1}$, fresh weight, respectively). Therefore, a hypothetical mechanism that down-regulates sucrose export by *K. fedtschenkoi* CAM leaves would have to be insensitive to the accumulation of hexose and sucrose, to some extent, but responsive to different levels of suppression of CAM activity in *KfALMT* RNAi lines.

Preferential accumulation of hexose over sucrose in *KfALMT* RNAi lines is consistent with suppression of phloem export of sucrose and its hydrolysis by invertase. Futile cycles of sucrose synthesis and breakdown, due to simultaneous activity of sucrose phosphate synthase and invertase, termed 'sucrose cycling', have been observed in photosynthetic tissues of a number of $C_3$ species (Huber, 1989; Kruger *et al.,* 2007; Nägele *et al.,* 2010). Some experimental evidence that reduced source-to-sink translocation of fixed C increases sucrose cycling flux was found through reduction of sink demand from the roots of $C_3$ grass *Lolium perenne* by growing it in a low-nitrate medium (Lattanzi *et al.,* 2012). This treatment did not increase gross glucose or

fructose concentrations in *L. perenne* source leaves, relative to high-nitrate growth medium (Lattanzi *et al.*, 2012). However, approximately equimolar accumulation of fructose and glucose, considered to be consistent with invertase-catalysed hydrolysis of sucrose, has been observed in source leaves of $C_3$ species from which phloem export had been partially blocked by cold-girdling, and which accumulated starch and soluble sugars as a result (Krapp *et al.*, 1993; Krapp and Stitt, 1995). Furthermore, leaves of an *Oryza sativa* vacuolar $H^+$-sucrose symporter knock-out mutant (*ossut2*) were found to accumulate glucose and fructose, in addition to sucrose, and decrease translocation of fixed C to sink tissues (Eom *et al.*, 2011). *ossut2* was thought to trap sucrose in leaf vacuoles, preventing its phloem export via the cytosol, and causing it to be hydrolysed by vacuolar invertase (Eom *et al.*, 2011).

The *ossut2* phenotype is particularly pertinent to a discussion of phenotypes of *KfALMT* RNAi lines because it relates to the likely mode of storage of soluble sugars during their putative diurnal retention in CAM leaves. Studies of transgenic *K. daigremontiana* lines that over-expressed a fructose 6-phosphate 2-kinase transgene have shown that this species has sufficient capacity for starch synthesis to abolish the accumulation of soluble sugars in CAM leaves at the beginning of the light period altogether (Truesdale *et al.*, 1999). High constitutive concentrations of the regulatory metabolite fructose 2,6-bisphosphate in these lines suppressed cytosolic gluconeogenesis, and thus sucrose synthesis, suppressed the morning sucrose peak, and increased the rate of starch synthesis during the early part of the light period (Truesdale *et al.*, 1999). Because fructose 6-phosphate is, itself, an activator of endogenous fructose 6-phosphate 2-kinase (Nielsen *et al.*, 2004), transient partitioning of soluble sugars in the vacuole may be implicit in the accumulation of glucose and fructose, rather than increased starch synthesis, as a result of the

hypothesised down-regulation of phloem export during the light period in *KfALMT* RNAi line CAM leaves.

The effects of blocking nocturnal $CO_2$ fixation by enclosing *K. daigremontiana* CAM leaves in pure $N_2$ gas on malate turnover and diurnal $CO_2$ uptake have been reported (Borland and Griffiths, 1997), and were discussed in the previous section. This method would allow relatively straightforward testing of the hypothesis that morning accumulation of fructose and glucose would, in fact, occur in WT *K. fedtschenkoi* in response to reduced $CO_2$ uptake and malate accumulation during the previous night. Cold-girdling of WT *K. fedtschenkoi* CAM leaf petioles, as described by Krapp *et al.* (1993), can also be predicted to increase morning fructose and glucose concentrations.

### 4.3.6 Feedback regulation of PPCK in response to nocturnal malate accumulation

PPCK-catalysed phosphorylation of PPC is predominately controlled at the transcript level of *PPCK* in *Kalanchoë,* and close correlation between PPC-malate $K_i$ values and *PPCK* mRNA levels has been reported under a range of experimental conditions, with few exceptions (Hartwell *et al.*, 1996, 1999; Borland *et al.*, 1999). In WT *K. fedtschenkoi* under 12:12 LD conditions, *KfPPCK1* transcript level increased throughout the 12 h dark period and decreased abruptly at the beginning of the following light period (Fig. 4.18). Rapid down-regulation of KfPPCK1 at the beginning of the light period was corroborated by the rapid disappearance of the phospho-PPC band from immunoblots (Fig. 4.19). This is consistent with previous reports of *KfPPCK1* regulation in *K. fedtschenkoi* (Dever *et al.*, 2015).

Down-regulation of *KfPPCK1* mRNA levels and PPC-malate $K_i$ in advance of the beginning of the light period under diel cycles with a long (16 h) dark period has been proposed

to result from circadian regulation (Hartwell *et al.*, 1996). Circadian control of metabolism is thought to benefit plants when it allows them initiate changes to metabolic control in advance of the rhythmic changes in environmental conditions that necessitate them (Dodd *et al.*, 2005, 2015). However, circadian feed-forward/anterograde control of *PPCK* transcription has been found to integrate with feed-back/retrograde signalling from CAM in *K. daigremontiana* (Borland *et al.*, 1999). In leaves blocked from synthesising malate during the dark period by enclosure in an atmosphere of pure $N_2$ gas, PPCK translatable mRNA levels and kinase activity remained elevated during the early part of the light period, whereas both fell rapidly in control plants that had been kept in normal air. Concurrently, PPC-malate $K_i$ remained high in the $N_2$-treated plants for the first 3 h, relative to the control. It was suggested that this feed-back signalling delayed the diurnal repression of PPC by dephosphorylation and malate inhibition, and enhanced the metabolic plasticity of CAM in *K. daigremontiana* by extending PPC activity into Phase II (Borland *et al.*, 1999).

Similarity between these observations and high levels of *KfPPCK1* transcript (Fig. 4.18) and PPC phosphorylation (Fig. 4.19) during the early part of the light period in the *KfALMT* RNAi 23A, relative to the WT control, suggests that the same signalling pathway is responsible for metabolic feed-back control of KfPPCK1 in *K. fedtschenkoi*. This putative pathway would not, therefore, discriminate between transient suppression of malate accumulation by $CO_2$ starvation, as used by Borland *et al.* (1999), and long-term impairment of nocturnal malate accumulation secondary to impaired vacuolar malate import, as in *KfALMT* RNAi 23A. No equivalent effect on *KfPPCK1* transcript level was observed in *K. fedtschenkoi* lines with transgenic RNAi-induced transcriptional silencing of *KfNAD_MEb1* or *KfPPDK*, CAM leaves of which have low nocturnal rates of malate synthesis due to constitutively high malate

concentrations (Dever *et al.*, 2015). By comparison with the *KfALMT* RNAi 23A phenotype (Figs. 4.18 and 4.19), this suggests that one or more corollary of malate synthesis acts as a signal for *KfPPCK1* transcriptional repression at the end of the dark period, rather than high malate concentration itself.

Elevated malate concentration in *KfNAD_MEb1* RNAi CAM leaves was cited as a plausible explanation for their suppressed PPC phosphorylation, acting downstream and independently of *KfPPCK1* transcriptional regulation (Dever *et al.*, 2015). In an *in vitro* study of purified *Zea mays* proteins, malate inhibition of PPC phosphorylation was found to result from the PPC-malate complex being a less active substrate for PPCK than PPC alone (Wang and Chollet, 1993). The apparent $K_i$ for malate inhibition of *K. fedtschenkoi* PPC phosphorylation was <5 mM, based on *in vitro* assays at pH 8 (Carter *et al.*, 1991). High nocturnal $[mal]_{cyt}$ in the context of impaired vacuolar malate import could, therefore, plausibly lead to direct inhibition of PPC phosphorylation in *KfALMT* RNAi lines. However, simultaneous measurements of extractable PPCK activity in *KfALMT* RNAi lines and WT would be needed to isolate the effects of transcriptional regulation of KfPPCK1 from malate inhibition of PPC phosphorylation. Phosphorylated PPC bands in *KfALMT* RNAi 23A samples taken in the dark period between 20:00 and 23:00 appeared less intense than those from WT sampled at the same time (Fig. 4.19), but it would be inappropriate to conclude relatively small inter-genotype differences in the level of PPC phosphorylation from a non-quantitative technique such as immunoblotting.

It is also tempting to attribute the prolonged Phase II in *KfALMT* RNAi 23A (Fig. 4.11) to higher PPC activity resulting from prolonged PPC phosphorylation and decreased sensitivity of PPC to feedback inhibition by malate. The same dark-period $N_2$-blocking method used by Borland *et al.* (1999) has been found to lead to net accumulation of malate during the subsequent

Phase II, contributing to its increased duration and rate of $CO_2$ assimilation (Borland and Griffiths, 1997). However, while vacuolar malate import may have functioned efficiently during Phase II in this case, increased malate accumulation in Phase II would be inconsistent with impaired vacuolar malate import in *KfALMT* RNAi lines (Fig. 4.6), and was not detected in extracted metabolites (Fig. 4.13).

## 4.4 Summary

The experiments presented in this chapter provide the first data relating to the functional characterisation of ALMTs in the context of CAM photosynthesis. In the *KfALMT* RNAi lines, CAM was impaired at the level of nocturnal $CO_2$ assimilation (Fig. 4.7) and malate synthesis (Fig. 4.11). *In vitro* $H^+$ transport activity measurements of isolated tonoplasts from *KfALMT* RNAi lines and WT provided functional evidence that vacuolar KfALMTs mediate coupled $H^+$ and malate import to vacuoles (Fig. 4.6).

The tonoplast extraction and quinacrine fluorescence assays described in this chapter required much less specialised equipment than patch-clamping techniques and were found to be a relatively straightforward method to establish a causal link between *KfALMT1* transcript abundance, tonoplast malate permeability and CAM. In order to confirm that vacuolar ALMTs are required for malate permeability in the vacuoles of *K. fedtschenkoi* CAM leaf tissue, electrophysiological characterisation by patch-clamping of intact vacuoles of *KfALMT* RNAi lines and WT should be done. Such experiments could establish the molecular identity of vacuolar KfALMTs and the CAM inward-rectifying malate channel activity (Hafke *et al.*, 2003) on firmer ground.

No negative effect on overall plant growth was evident due to the partial elimination of CAM through suppression of *KfALMT* expression (Fig. 4.20). The implication of metabolite data on *KfALMT* RNAi 23A was that reciprocal fluctuations of starch and malate over the diel CAM cycle required additional input of fixed C derived from direct uptake of atmospheric $CO_2$ during the light period in order to sustain itself. CAM leaves of *KfALMT* RNAi lines may have retained a greater proportion of photosynthate from export to sink tissues during the day, while proportionally increasing export of soluble carbohydrate derived from starch breakdown during the night, in order to maintain both growth and the diel CAM cycle. Carbon budgeting of $CO_2$ uptake and the major pools of fixed carbon (malate, starch and soluble sugars) is now needed to measure the quantity of fixed C exported from CAM leaves of *KfALMT* RNAi lines and WT *K. fedtschenkoi* to sink tissues over the diel cycle in order to show that source-to-sink translocation of fixed C is differentially regulated between them. Published examples of this technique have been cited in this chapter (Krapp *et al.*, 1993; Krapp and Stitt, 1995; Grimmer and Komor, 1999).

Altered expression and activity of KfPPCK1 was observed in the *KfALMT* RNAi lines (Figs. 4.18 and 4.19), and closely resembled the reported effects of physically blocking availability of $CO_2$ to leaves in the dark period (Borland *et al.*, 1999). Characterisation of other loss-of-function mutants of genes encoding enzymes and transporters required for nocturnal carboxylation and malate storage is ongoing at the Hartwell laboratory and others (Yang *et al.*, 2015; Hartwell *et al.*, 2016). This ongoing research effort will help to dissect the interaction between nocturnal carbon metabolism associated with CAM and the circadian regulation of PPCK expression, especially the potential for direct feedback regulation of *KfPPCK1* transcript and protein levels by cytosolic malate levels (Borland *et al.*, 1999).

## Chapter 5 - Impairment of vacuolar malate import in *KfALMT* RNAi lines leaves the CAM circadian rhythm intact, but perturbs its phase or period, or both

### 5.1 Introduction

A functional description of the CAM circadian system is a major goal of CAM research (Hartwell, 2005; Borland *et al.*, 2009). The circadian rhythm of $CO_2$ gas exchange associated with CAM is controlled by an endogenous circadian oscillator (Wilkins, 1992). A circadian rhythm is defined as a rhythm with a period of approximately 24 hours that fulfils some key criteria. Firstly, the period of the rhythm must be resistant to change due to fluctuations in ambient temperature, a property known as temperature compensation. Secondly, the phase of a circadian rhythm may be entrained by changes in the environment such as light intensity and temperature, but it persists in the absence of exogenous stimuli for several days (Wilkins, 1992; Harmer, 2009). A circadian rhythm measured in the absence of exogenous environmental inputs is sometimes referred to as a 'free-running' rhythm.

Plants possess a self-regulating network of genes known as the core circadian clock, which has been characterised most comprehensively using *A. thaliana* as a model species (Harmer, 2009). The core clock mechanism drives rhythms of transcript and protein abundance for the core circadian clock genes themselves, and also drives circadian rhythmicity in transcript abundance of a large and functionally diverse subset of the *A. thaliana* transcriptome (Harmer *et al.*, 2000; Covington *et al.*, 2008). The core circadian clock functions as an endogenous timekeeper that is set to the day-night cycle, permitting metabolic and physiological changes to pre-empt diel fluctuations in light and temperature, rather than react to them (Harmer *et al.*, 2000; Dodd *et al.*, 2005).

The results presented in this chapter focus on phenotypic characterisation of the effects of hairpin dsRNA transgene-targeted, RNAi-mediated *KfALMT* silencing on the core circadian clock and two CAM-associated circadian rhythms, of $CO_2$ gas exchange and of *KfPPCK1* transcript abundance, in one or more *KfALMT* RNAi lines.

### 5.1.1 Circadian rhythms of $CO_2$ gas exchange in CAM

Circadian rhythmicity of $CO_2$ gas exchange occurs in both $C_3$ and CAM species when they are transferred from diel to constant conditions (Wilkins, 1992; Hotta *et al.*, 2007). This section reviews the distinctive features of the CAM-associated circadian rhythm, which was originally observed in *K. fedtschenkoi* leaves that had been detached at dusk and placed in constant darkness (DD) under a $CO_2$-free atmosphere (Wilkins, 1959). The rate of respiratory $CO_2$ output from the leaves exhibited a sinusoidal rhythm, the minima of which coincided with increased re-fixation of respired $CO_2$ (Warren and Wilkins, 1961). Circadian rhythmicity of $CO_2$ gas exchange under conditions of constant illumination and temperature (LL) and normal air was later characterised in detached leaves of *K. fedtschenkoi* and other *Kalanchoë* species (Buchanan-Bollig, 1984; Wilkins, 1984). In *K. daigremontiana* and *M. crystallinum* under LL conditions, $CO_2$ uptake over the free-running rhythm of $CO_2$ gas exchange has been found to be mediated by a combination of PPC and Rubisco activity, with intervals of relatively high PPC activity that were coordinated with peaks in the rate of $CO_2$ uptake (Buchanan-Bollig *et al.*, 1984; Grams *et al.*, 1997; Wyka and Lüttge, 2003; Davies and Griffiths, 2012).

The process of light entrainment of the *K. fedtschenkoi* CAM circadian oscillator has been examined by experiments in which the phase of the circadian rhythm of $CO_2$ gas exchange by detached leaves under DD was re-entrained by periods of illumination. Exposure to white

light for 4 h was found to re-set the circadian rhythm such that the next peak of $CO_2$ output occurred following the end of the illumination period, after a predictable lag period (Harris and Wilkins, 1978*a*). The circadian rhythm was rapidly re-entrained to light-dark cycles incorporating as little as 15 mins of illumination (Harris and Wilkins, 1978*b*). "Skeleton" light periods, in which leaves were only illuminated for the first and last 15 minutes of the nominal light period, were able to "simulate" the phase-entraining effects of an uninterrupted period of illumination only when the interval of darkness was sufficiently brief (Harris and Wilkins, 1978*b*). This suggests that light signalling to the CAM circadian oscillator both entrains its phase and temporarily inhibits subsequent signalling for entrainment.

In addition to free-running rhythms of $CO_2$ gas exchange, circadian rhythmicity of PPCK activity under LL has been observed. This has been detected by measuring its steady-state transcript level (Hartwell *et al.*, 1996; Dodd *et al.*, 2003; Dever *et al.*, 2015), its phosphorylation of PPC (Dever *et al.*, 2015), and the consequent decrease in the sensitivity of PPC to inhibition by malate (Nimmo *et al.*, 1987; Kusumi *et al.*, 1994; Hartwell *et al.*, 1996; Grams *et al.*, 1997). However, circadian rhythms of $CO_2$ gas exchange have been observed that are out of phase with rhythms of PPC phosphorylation, or in the absence of the latter altogether (Nimmo *et al.*, 1987; Carter *et al.*, 1995*a*; Dever *et al.*, 2015). This suggests that circadian rhythmicity of $CO_2$ gas exchange is not strictly dependent on activation of PPC by PPCK-catalysed phosphorylation.

Moreover, circadian $CO_2$ gas exchange rhythms under LL have not been found to depend on coordinated fluctuations of leaf malate concentration. If each cycle of the free-running rhythm were a facsimile of the diel CAM cycle, leaves would be expected to initiate malate accumulation following minima in $CO_2$ uptake, continue to accumulate malate as rates of $CO_2$ uptake increased, and begin malate breakdown after $CO_2$ uptake passed its maxima (Kluge *et al.*,

1981). In the first 24-36 h under LL conditions, a transitional cycle of malate accumulation and breakdown, the latter accompanied by elevated mesophyll $CO_2$ concentration and cessation of atmospheric $CO_2$ uptake, has been observed in *K. daigremontiana* (Kluge *et al.*, 1981). A stable circadian rhythm of malate concentration was observed in *M. crystallinum* for 48 h under LL by Dodd *et al.* (2003). In longer periods under LL, rhythms of accumulation and breakdown of malate have shown a tendency to either dampen more rapidly than the circadian $CO_2$ gas exchange rhythm does (Buchanan-Bollig, 1984; Buchanan-Bollig and Smith, 1984; Nimmo *et al.*, 1987; Wyka and Lüttge, 2003; Davies and Griffiths, 2012), or move out of phase with it, or both (Ritz and Kluge, 1987; Anderson and Wilkins, 1989*a*). The reciprocal fluctuations of starch and malate levels found in *Kalanchoë* species under diel conditions were also eliminated under LL (Buchanan-Bollig, 1984).

Increased decarboxylase activity (malic enzyme or phosphoenolpyruvate carboxykinase), resulting in a futile cycle of malate synthesis and breakdown, has been suggested as the cause of the apparent decoupling of PPC activity from leaf malate concentration under LL (Davies and Griffiths, 2012). Interestingly, larger and more stable rhythmic fluctuations in malate concentration were observed in *Graptopetalum paraguyense* under constant high-intensity light than under constant low-intensity light, whereas the reverse was found for the circadian rhythm of PPC-malate $K_i$ (Kusumi *et al.*, 1994). This raises the intriguing possibility that malate accumulation and breakdown are subject to regulatory processes that are independent of those that regulate PPC phosphorylation.

The importance of stomatal control to the circadian rhythm of $CO_2$ gas exchange under LL has been shown by its abolition in pieces of *K. fedtschenkoi* leaf when their epidermis was removed (Wilkins, 1991). In *K. daigremontiana* CAM leaves, oscillations in stomatal

conductance under LL were close in phase and period to the circadian rhythm of $CO_2$ gas exchange (Wyka and Lüttge, 2003).

In $C_3$ leaves under LL, the circadian rhythm of $CO_2$ gas exchange is generated by independent modulation of stomatal conductance and leaf mesophyll photosynthetic activity (Hennessey and Field, 1991; Hennessey *et al.*, 1993; Dodd *et al.*, 2004). Similarly, spectral analysis of the effects of exposing *K. daigremontiana* CAM leaves to cycling temperature shifts of non-circadian periodicity, while maintaining constant illumination, has been used to separate the contributions to the circadian $CO_2$ gas exchange rhythm of stomatal control and of endogenous control of $CO_2$ exchange within the leaf mesophyll (Bohn *et al.*, 2003). Differential sensitivity of these two factors to the non-circadian temperature shifts indicated that control of leaf mesophyll $CO_2$ exchange operated independently of stomatal control in determining the free-running rhythm of $CO_2$ uptake (Bohn *et al.*, 2003). Circadian rhythmicity of $CO_2$ gas exchange that is independent of stomatal control has also been demonstrated by physically blocking stomatal conductance in *K. daigremontiana* and non-invasively monitoring the quantum efficiency of Photosystem II ($\Phi_{PSII}$). This measured, by proxy, internal leaf $CO_2$ concentration and the balance between $CO_2$ fixation and evolution in mesophyll (Wyka *et al.*, 2005). The rhythm of $\Phi_{PSII}$ was in reverse phase to the circadian rhythm of $CO_2$ gas exchange of control leaves, which suggested that the latter was controlled by a separate or additional regulatory mechanism to stomatal control (Wyka *et al.*, 2005).

In summary, the phenomenon of circadian rhythmicity of $CO_2$ gas exchange in CAM plants under LL appears to arise from rhythmic modulation of the rates of $CO_2$-fixation and decarboxylation at the level of the CAM mesophyll cell, and requires stomatal control of leaf gas exchange to be intact, but does not depend on underlying cycles of malate accumulation and

breakdown, such as those that occur under diel conditions. The importance of control of PPC activity to the CAM circadian rhythm of $CO_2$ gas exchange has been shown by disruption of the latter in *Kalanchoë* CAM leaves that were placed under conditions that caused constitutive suppression of PPC activity, secondary to either constitutive malate accumulation or malate breakdown (Wilkins, 1992).

Exposure to high temperatures (30-40 °C) has been found to repress PPC activity, under diel conditions, by directly increasing the affinity of the PPC-malate inhibitory interaction (Carter *et al.*, 1995*b*), by down-regulating *PPCK* transcript abundance (Hartwell *et al.*, 1996), and indirectly via increased malate inhibition of PPC due to increased vacuolar malate efflux (Friemert *et al.*, 1988; Borland *et al.*, 1999). $CO_2$ gas exchange by *Kalanchoë* CAM leaves under LL may be made arrhythmic by exposing leaves to high temperatures (Anderson and Wilkins, 1989*b*; Grams *et al.*, 1996; Rascher *et al.*, 1998), and this effect was associated with a decrease in leaf malate concentration to a low steady state (Anderson and Wilkins, 1989*b*). Reversion from arrhythmia to circadian rhythmicity following a decrease in temperature has been found to coincide with transient accumulation of malate, linking recovery of the capacity for PPC-mediated malate accumulation to reinitiation of the circadian $CO_2$ gas exchange rhythm (Grams *et al.*, 1996).

Conversely, conditions that suppress malate breakdown are thought to lead to over-accumulation of malate and enzymatic inhibition of PPC activity by malate (Anderson and Wilkins, 1989*b*; Wilkins, 1992). Low temperatures (2 °C) in *K. fedtschenkoi* under LL were found to result in rapid accumulation of malate to an elevated, near-steady state level, followed by low, arrhythmic $CO_2$ uptake (Anderson and Wilkins, 1989*b*). Reversion to 15 °C re-established the circadian rhythm (Anderson and Wilkins, 1989*b*). Circadian $CO_2$ gas exchange

rhythms under DD conditions are also thought to be subject to progressive dampening due to accumulation of malate synthesised from re-fixation of respired $CO_2$ (Wilkins and Thomas, 1993). Short periods of illumination re-initiated the stalled circadian rhythm by promoting the breakdown of accumulated malate, with the renewed rhythm phased such that a large peak of $CO_2$ output occurred at the time of illumination (Wilkins and Thomas, 1993). Red light (~660 nm) was the most active wavelength for both stimulating diurnal malate breakdown in *K. daigremontiana* under diel conditions (Barrow and Cockburn, 1982), and for entraining the phase of the circadian rhythm in *K. fedtschenkoi* under DD, although the effect on leaf malate concentration was not reported (Wilkins, 1973; Harris and Wilkins, 1978*b*).

The tonoplast itself has been hypothesised to act as circadian oscillator by switching from a malate-importing to a malate-exporting state when the vacuolar malate concentration is high, and reverting to a malate-importing state when the concentration is low. In this model of CAM circadian regulation, increased PPC activity leads to increasing $CO_2$ uptake and cytosolic malate synthesis, while malate is imported into vacuoles. Increasing vacuolar malate concentration leads to an increased probability of tonoplasts switching from a malate-importing to a malate-exporting state. When this occurs, efflux of malate from the vacuolar lumen to the cytosol inhibits PPC and causes $CO_2$ uptake to decline, but also allows malate to be broken down until PPC inhibition is relieved, the vacuole switches back to a malate-importing state, and $CO_2$ uptake begins to increase again (Lüttge and Beck, 1992; Beck *et al.*, 2001). However, in a seminal experiment, placing *K. daigremontiana* leaves intermittently in $CO_2$-free air was found to have no significant effect on the period and phase of the circadian $CO_2$ gas exchange rhythm under LL conditions, relative to control leaves in normal air (Wyka *et al.*, 2004). It was apparent that the quantity or timing of malate accumulation or breakdown in CAM leaves could not have

controlled the periodicity of the circadian rhythm of $CO_2$ gas exchange, and that additional signalling from an underlying circadian oscillator is necessary (Wyka *et al.*, 2004).

Nonetheless, malate synthesis and breakdown may entrain the phase of the circadian oscillator by retrograde signalling pathways which have yet to be characterised at the molecular level. In LL experiments where the circadian $CO_2$ gas exchange rhythm was re-initiated in *K. fedtschenkoi* leaves that had been kept at 4 °C by increasing the temperature to 15 °C, the phase of the re-established rhythm was one half-cycle removed from that of the rhythm re-established by a temperature decrease from 40 °C to 15 °C (Anderson and Wilkins, 1989*b*). Activation of malate accumulation was therefore thought to re-initiate the CAM circadian oscillator in the reverse phase to activation of malate breakdown (Anderson and Wilkins, 1989*b*). A temperature decrease from 30 °C to 22 °C in *K. daigremontiana* under LL was found to simultaneously re-initiate circadian rhythms of PPC-malate $K_i$ and $CO_2$ exchange, linking them to the same circadian oscillator (Grams *et al.*, 1997). A strong entrainment signal from a relatively abrupt change in temperature has been found to be necessary to establish a coherent circadian rhythm in *K. daigremontiana* leaves under LL. Gradual changes in temperature were thought to permit differentially-phased entrainment of the circadian oscillator in disparate parts of the leaf mesophyll, which aggregated as arrhythmia over the whole leaf (Rascher *et al.*, 1998).

Various other experimental treatments have been described that re-entrained the phase of the circadian $CO_2$ gas exchange rhythm in *K. fedtschenkoi* under LL, either by enhancing the capacity for malate accumulation (brief periods of exposure to 2 °C, high $CO_2$ concentration and darkness), or breakdown (brief exposure to 40 °C) (Anderson and Wilkins, 1989*a*,*b*,*c*). However, no significant change in leaf malate concentration was found to be necessary to produce a phase

shift, suggesting that entrainment signals operate independently of gross accumulation or breakdown of malate (Anderson and Wilkins, 1989*a*).

### 5.1.2 The model core circadian clock of *Arabidopsis thaliana*

The *Arabidopsis* core circadian clock is a cascade of transcriptional and translational feed-forward and feed-back loops that re-initiates itself with circadian periodicity. Up- and down-regulation of expression of the core circadian clock genes, most of which are transcription factors, occurs in successive waves at a controlled pace, providing a series of temporal markers throughout each cycle of the clock. Circadian regulation of the transcriptome by the core clock may occur through direct transcriptional regulation by the core clock transcription factors (Nagel *et al.*, 2015). The phase of the clock is entrained by detection of environmental signals such as light and temperature (Salomé and McClung, 2005), but the sensitivity of the clock to entrainment is regulated by its own phase, a property known as gating (Millar and Kay, 1996).

Transcript and protein levels of two *MYB*-family DNA-binding transcription factor genes, *CIRCADIAN CLOCK-ASSOCIATED1* (*CCA1*) and *LATE ELONGATED HYPOCOTYL* (*LHY*) increase from the middle of the night onwards and peak at dawn (Schaffer *et al.*, 1998; Wang and Tobin, 1998; Kim *et al.*, 2003). Transcription of *CCA1* and *LHY* is transiently up-regulated in response to light, and translation of *LHY* mRNA is also up-regulated in the light (Martínez-García *et al.*, 2000; Kim *et al.*, 2003). *CCA1* and *LHY* transcription declines during the day due to repression by two *PSEUDO-RESPONSE REGULATOR* (*PRR*)-family proteins, *PRR9* and *PRR7* (Nakamichi *et al.*, 2010). Expression of both genes increases during the morning, but transcription of *PRR9* is activated by light, and its transcript levels peak earlier than those of *PRR7* (Matsushika *et al.*, 2000; Farré *et al.*, 2005; Nakamichi *et al.*, 2010). Transcriptional

activation of *PRR7* and *PRR9* by LHY and CCA1 has been suggested (Farré *et al.*, 2005), but more recent research has shown that the direct effect of LHY on all *PRR*-family genes is transcriptional repression (Adams *et al.*, 2015).

Transcriptional repression of *CCA1* and *LHY* during the day relieves their repression of three other *PRR*-family genes: *PRR3*, *PRR5* and *TIMING OF CAB EXPRESSION1* (*TOC1*; Alabadí *et al.*, 2001; Adams *et al.*, 2015; Kamioka *et al.*, 2016). Transcript levels of the three genes peak during the evening or the early part of the night (Matsushika *et al.*, 2000), with a slight delay in peak protein levels (Fujiwara *et al.*, 2008). The *CCA1*- and *LHY*-related MYB-family transcription factor REVEILLE8 (RVE8) is thought to bind the promoters of these and other evening-expressed genes at the same sequence element as CCA1 and LHY, but mediate their transcriptional activation, rather than repression, during the day (Rawat *et al.*, 2011; Hsu *et al.*, 2013). *RVE8* is subjected to feedback transcriptional repression by *PRR5* (Rawat *et al.*, 2011).

TOC1 is a DNA-binding transcription factor that mediates transcriptional repression of *PRR7* and *PRR9*, causing their transcript levels to decline towards the end of the day (Huang *et al.*, 2012). Proteins encoded by three additional evening-phased, *CCA1*/*LHY*-repressed genes (Adams *et al.*, 2015; Kamioka *et al.*, 2016) – *EARLY FLOWERING3* (*ELF3*), *ELF4* and *LUX ARRHYTHMO* (*LUX*) – form an evening complex (EC, Nusinow *et al.*, 2011) that also represses transcription of *PRR7* and *PRR9*, in addition to *LUX* itself, by directly binding to their promoters (Nusinow *et al.*, 2011; Mizuno *et al.*, 2014). *LUX*, *ELF3* and *ELF4* are notable among core circadian clock genes in that a functional copy of each is required for circadian rhythmicity of core clock gene transcript levels (Covington *et al.*, 2001; Doyle *et al.*, 2002; Hazen *et al.*, 2005),

suggesting that transcriptional regulation by the evening complex is essential for circadian rhythmicity.

*LHY* and *CCA1* are targets of transcriptional repression by TOC1, perpetuating their repression during the early part of the night (Gendron *et al.*, 2012; Huang *et al.*, 2012). Like *TOC1*, *PRR5* is also thought to engage in mutual transcriptional repression with *CCA1* and *LHY* (Nakamichi *et al.*, 2010; Adams *et al.*, 2015; Kamioka *et al.*, 2016). Initiation of the next cycle of the circadian clock requires repression of the evening-phased *PRR*-family genes to permit reactivation of transcription of *LHY* and *CCA1* (Pokhilko *et al.*, 2012). Post-translational repression of *TOC1* during the night is mediated by proteasomal degradation, for which it is targeted by SCF E3 ubiquitin ligase-dependent ubiquitination (Más *et al.*, 2003*b*). ZEITELUPE (ZTL), a SCF subunit, interacts with TOC1 to mediate its specific ubiquitination (Más *et al.*, 2003*b*). During the day, ZTL is thought to be largely blocked from interacting with TOC1 by a competing interaction of ZTL with GIGANTEA (GI), expression of which, like *TOC1*, is evening-phased (Fowler *et al.*, 1999; Kim *et al.*, 2007). The latter interaction is stabilised by light activation of the flavin cofactor-binding LOV domain of ZTL (Kim *et al.*, 2007). At night, GI dissociates from ZTL and this permits degradation of TOC1, while PRR3 antagonises the ZTL-TOC1 interaction and moderates the rate of degradation (Fujiwara *et al.*, 2008). Nocturnal degradation of PRR5 is also thought to occur via ZTL-targeted ubiquitination (Fujiwara *et al.*, 2008).

### 5.1.3 Evidence for cross-regulation between the core circadian clock and the circadian rhythm of $CO_2$ gas exchange in CAM

Circadian regulation of transcript abundance of a large number of putatively CAM-related genes, including *PPCK*, has been demonstrated in *M. crystallinum* (Cushman *et al.*, 2008*b*). The inducible nature of CAM in this species has been used to identify patterns of gene expression that are specific to CAM. The phase and period of the circadian rhythms of transcript levels of a selection of core circadian clock genes are largely unchanged by induction of CAM (Boxall *et al.*, 2005). Phase shifts in the circadian rhythms of transcript abundance of a large set of CAM-related genes, as well as their general transcriptional up-regulation, suggested that recruitment of these genes to function in CAM involves the imposition of a distinct programme of circadian control (Cushman *et al.*, 2008*b*).

Characterisation of the interactions between the core circadian clock and CAM by reverse genetics is in its early stages. Transgenic *K. fedtschenkoi* lines that over-express *M. crystallinum TOC1* (*McTOC1*-OX lines) have been generated in the Hartwell lab (Hartwell, 2006), and their phenotypes were reported in the PhD thesis of Charles Dall'omo (Dall'omo, 2011). Overexpression of *TOC1* in *A. thaliana* causes arrhythmicity in the core clock (Makino *et al.*, 2002; Más *et al.*, 2003*a*). Loss of circadian rhythmicity of transcript abundance of *KfTOC1* and *KfCCA1* in *McTOC1*-OX lines confirmed that this phenotype was replicated. The circadian rhythm of *KfPPCK1* transcript levels was also lost in the *McTOC1-OX* lines of *K. fedtschenkoi*. Disruption of the circadian rhythm of CAM $CO_2$ gas exchange under LL in a range of *McTOC1*-OX lines showed approximate dosage dependence on *McTOC1* transcript levels. Lines in which circadian $CO_2$ gas exchange was disrupted typically displayed 2-3 cycles of diminishing amplitude and delayed phase, relative to WT controls, before becoming arrhythmic altogether.

Under 12:12 LD, Phases II and IV of the CAM cycle were increased in amplitude and duration in *McTOC1*-OX, and there was a subtle shift in the timing of the peak rate of $CO_2$ assimilation in Phase I. These results, therefore, support the necessity of a *K. fedtschenkoi* core molecular circadian clock, comprised of orthologs of *A. thaliana* core clock genes, for the circadian control of $CO_2$ uptake that is associated with CAM (Dall'omo, 2011).

As described above, circadian rhythms of $CO_2$ gas exchange in $C_3$ and CAM plants share some common features. Evidence has also been found for core clock control of the $C_3$ circadian rhythm using the *A. thaliana ztl-1* mutant. Lengthening of the period of the core clock was coordinated with longer periods in the circadian rhythms of $CO_2$ uptake and stomatal conductance in *ztl-1* (Dodd *et al.*, 2004).

Further evidence for reciprocal regulation of the core circadian clock by CAM has been provided by transgenic *K. fedtschenkoi* in which genes required for diurnal malate decarboxylation were silenced by hairpin dsRNA transgene-targeted RNAi (Dever *et al.*, 2015). Transcriptional silencing of the ß subunit of NAD-malic enzyme (*KfNAD_MEb1*) resulted in higher malate concentrations at the end of the light period and lower light-dark malate turnover relative to wild type controls under 12:12 LD, and abolished circadian rhythmicity of *KfTOC1-1* transcript under LL. By contrast, circadian rhythmicity of *KfTOC1-1* transcript was retained in the context of transcriptional silencing of *KfPPDK*, and although light-dark malate turnover was similarly reduced, malate concentrations were found to be lower at the ends of both the light and dark periods. This, therefore, suggests that the status of malate accumulation is important for regulation of the circadian clock under CAM (Dever *et al.*, 2015). Parallels may be drawn between this result and suppression of the circadian rhythm of $CO_2$ gas exchange in *K.*

*fedtschenkoi* at low temperatures, when turnover of accumulated malate was prevented (Anderson and Wilkins, 1989*b*).

## 5.2 Results

### 5.2.1 Perturbation of the circadian rhythm of $CO_2$ gas exchange in *KfALMT* RNAi lines

Detached CAM leaves (leaf pair 6, LP6) of three independent *KfALMT* RNAi lines (8B, 12A and 23A) and WT, detailed phenotypes of which have been described in Chapter 4, were switched from 12:12 LD to LL conditions at the end of the dark period. The detached leaves had been kept in the IRGA for the previous ~68 h in order to monitor $CO_2$ gas exchange under 12:12 LD conditions (Fig. 4.7). The leaf area-normalised rate of $CO_2$ uptake ($J_{CO2}$) was measured under LL for ~100 h (Fig. 5.1).

Marked differences in the patterns of $J_{CO2}$ were found between WT and each of the *KfALMT* RNAi lines at the transition between 12:12 LD and LL conditions. In WT, Phase II $CO_2$ uptake was low and decreased rapidly over the first 2 hours of LL, followed by almost complete cessation of $CO_2$ exchange for the following 6-8 h of Phase III (Fig. 5.1). Subsequently, $J_{CO2}$ increased exponentially until the first peak of the circadian rhythm at around 16:00. By contrast, in *KfALMT* RNAi lines 12A and 23A, which have been characterised as having more severe suppression of CAM than line 8B (Figs. 4.7 and 4.13), there was prolonged and rapid Phase II $CO_2$ uptake and incomplete cessation of $CO_2$ uptake during Phase III. Phase IV formed a distinct peak from the first peak of the circadian rhythm, the latter also occurring at approximately 16:00. A narrower, higher trough in $J_{CO2}$ was also observed between the first and second peaks of the circadian rhythm (Fig. 5.1). The same phenotype was observed in line 8B, to a lesser degree and without a distinct Phase IV peak.

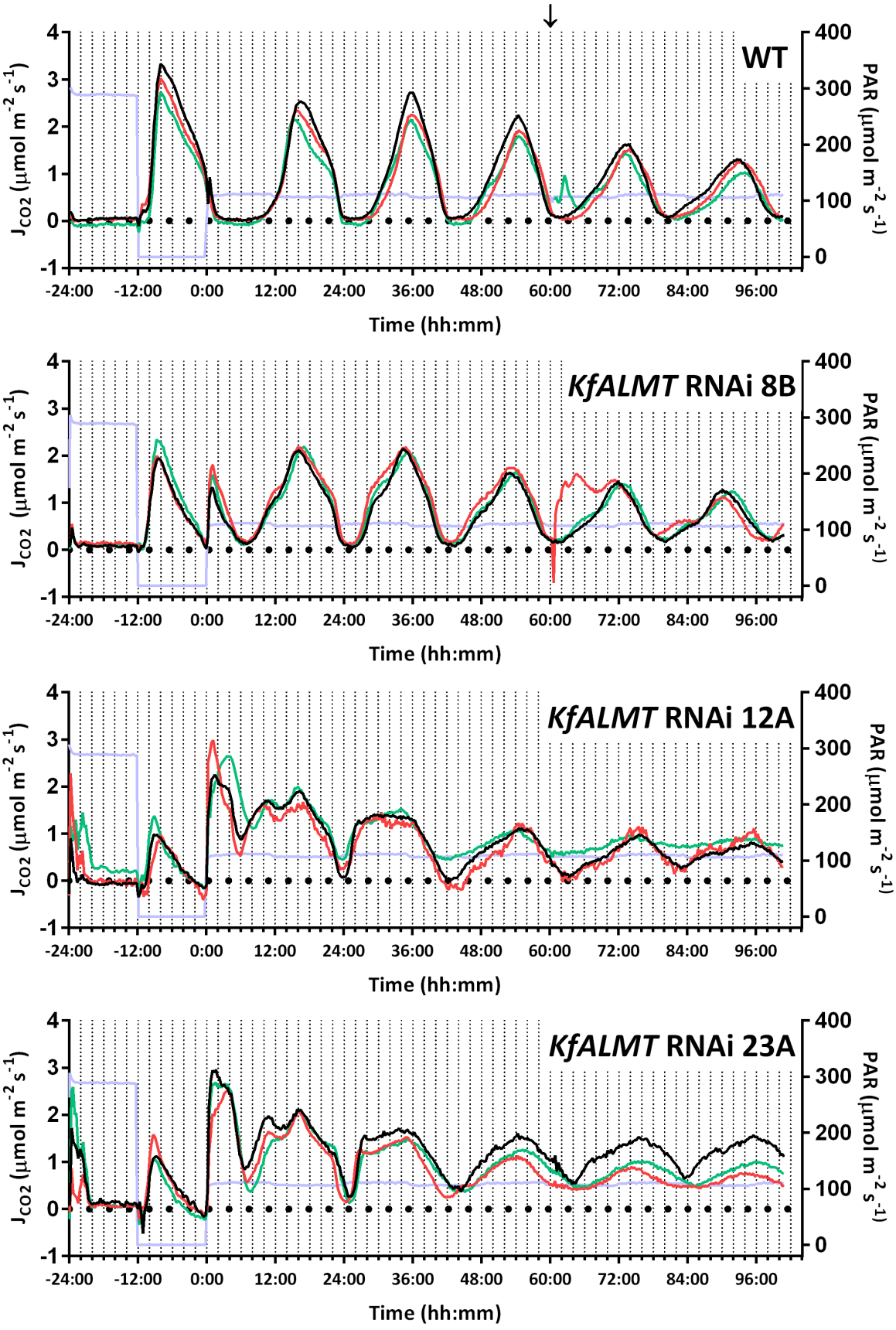
WT
KfALMT RNAi 8B
KfALMT RNAi 12A
KfALMT RNAi 23A
J_CO2 (µmol m^-2 s^-1)
PAR (µmol m^-2 s^-1)
Time (hh:mm)
-24:00
-12:00
0:00
12:00
24:00
36:00
48:00
60:00
72:00
84:00
96:00

Circadian rhythmicity of $CO_2$ gas exchange was observed for more than 72 h under LL conditions in all replicates. The period of the rhythm was lengthened slightly in *KfALMT* RNAi lines 12A and 23A relative to WT and line 8B (Figs. 5.1 and 5.2). Although $J_{CO2}$ was similar in all genotypes at the first peak of the circadian rhythm, the amplitude of the oscillation of $J_{CO2}$ in lines 12A and 23A was subsequently lower than in WT and line 8B (Fig. 5.2). Replicate leaves of WT and line 8B displayed relatively uniform dampening of their rhythms as the timecourse progressed, whereas there was considerable variation in the persistence of the circadian rhythm of $CO_2$ gas exchange within replicates of lines 12A and 23A. Notably, in one replicate of line 12A, oscillation of $J_{CO2}$ was almost eliminated after 96 h, whereas in one replicate of line 23A, the amplitude in the rhythm was much greater in the second half of the LL timecourse (Fig. 5.1). However, from this small sample size it is not possible to determine whether instability of this circadian rhythm is an authentic phenotypic feature of severely CAM-suppressed *KfALMT* RNAi lines (c.f. Figs. 4.1, 4.7 and 4.13), and one that is absent in WT *K. fedtschenkoi*.

Total $CO_2$ uptake over a 24 h interval in the $J_{CO2}$ timecourse (72:00-96:00) was measured for comparison with the final 12:12 LD cycle (24:00-48:00, Fig. 5.3). Whereas each of the

---

Figure 5.1 – Circadian rhythmicity in the rate of $CO_2$ uptake ($J_{CO2}$) by CAM leaves (leaf pair 6, LP6) under LL conditions. This figure is a continuation of the $J_{CO2}$ timecourse presented in Fig. 4.7, but the timecourses have been transposed along the x-axis so that the onset of LL conditions is at 0:00. $CO_2$ uptake is normalised to leaf area (μmol $m^{-2}$ $s^{-1}$) and net $CO_2$ uptake occurred when $J_{CO2} > 0$. The intensity of photosynthetically active radiation (PAR) is also shown (blue). Each graph presents $CO_2$ gas exchange data for three replicate LP6 of each genotype (black, red and green), with the exception of one *KfALMT* RNAi 12A single leaf 6 (red). In two timecourses (WT, green; *KfALMT* RNAi 8B, red), the chambers were briefly opened after ~60 h in LL, which transiently disturbed the circadian rhythms of $J_{CO2}$. A single measurement of $J_{CO2}$ = -2.43 μmol $m^{-2}$ $s^{-1}$ has been omitted from the WT (green) timecourse for clarity, and is indicated by an arrow above the graph.

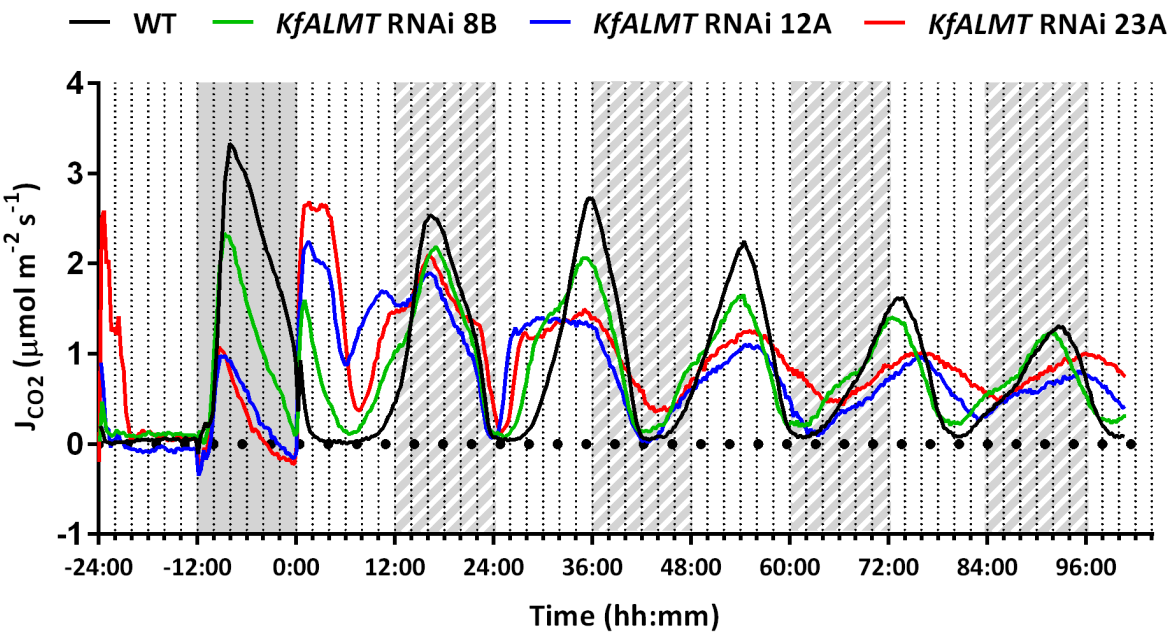


Figure 5.2 – Comparison of representative free-running rhythms of $CO_2$ gas exchange by WT and *KfALMT* RNAi lines 8B, 12A and 23A. Timecourses represented by black lines in Fig. 5.1 have been reproduced in this figure. The duration of the dark period is represented by solid shading, and the duration of subjective dark periods (i.e. the duration of the dark periods if 12:12 LD conditions had been maintained) is represented by hatched shading.

*KfALMT* RNAi lines displayed a higher mean total $CO_2$ uptake over the defined 24 h interval under LL than under 12:12 LD, the reverse was observed in WT (Fig. 5.3). Unlike lines 8B and 12A, the results of a paired t-test found that mean 24 h $CO_2$ uptake was not significantly higher under LL than 12:12 LD in line 23A, but this was likely to have been due to the fact that the LL total $CO_2$ uptake was much higher than the mean in one replicate (black line, Fig. 5.1), and to reflect the limitations of parametric statistical tests.

### 5.2.2 Perturbation of circadian rhythms of gene expression in a *KfALMT* RNAi mutant line

As described above, circadian clock function can be measured from persistent oscillations in transcript levels of core circadian clock genes under constant conditions. In order to measure the

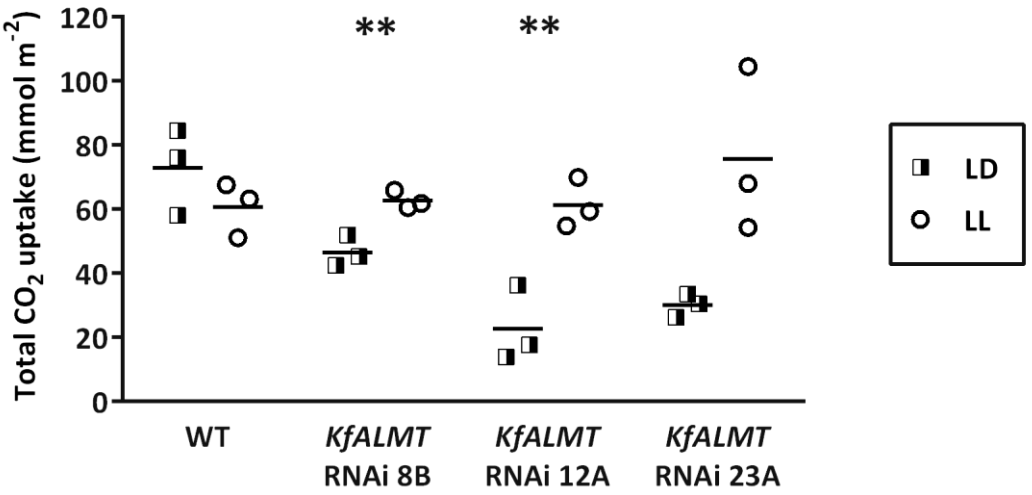


Figure 5.3 – Total $CO_2$ uptake during a 12:12 LD cycle and a 24 h section of the subsequent free-running period. LD: -24:00 to 0:00; LL: 72:00 to 96:00. Total $CO_2$ uptake was estimated from the $J_{CO2}$ timecourses presented in Figs. 4.7 and 5.1. Points represent total $CO_2$ uptake in individual IRGA chambers, normalised to leaf area. Horizontal bars represent means for each genotype. The results of a paired Welch t-test between the LD and LL means of total $CO_2$ uptake for each genotype are displayed above the bars: $P > 0.05$, not shown; $P \leq 0.01$, **.

effect of silencing of *KfALMT* on the core circadian clock, 11-week-old *KfALMT* RNAi 23A and wild type control plants were entrained to 12:12 LD conditions, and then transferred at the end of the dark period to LL. LP6 were then sampled at 4-hour intervals under LL. cDNA was synthesised from total RNA extracts of the samples and transcript levels were measured using RT-qPCR.

*K. fedtschenkoi* has two *CCA1*/*LHY* orthologs (GenBank: KM078717.1 and KM078718.1), but neither of them could be positively identified as direct orthologs of *A. thaliana CCA1* or *LHY* on the basis of sequence similarity comparisons alone. The primers that were used in this RT-qPCR timecourse are unlikely to have fully discriminated between them (Appendix 2), and therefore the transcript whose abundance has been measured is referred to as

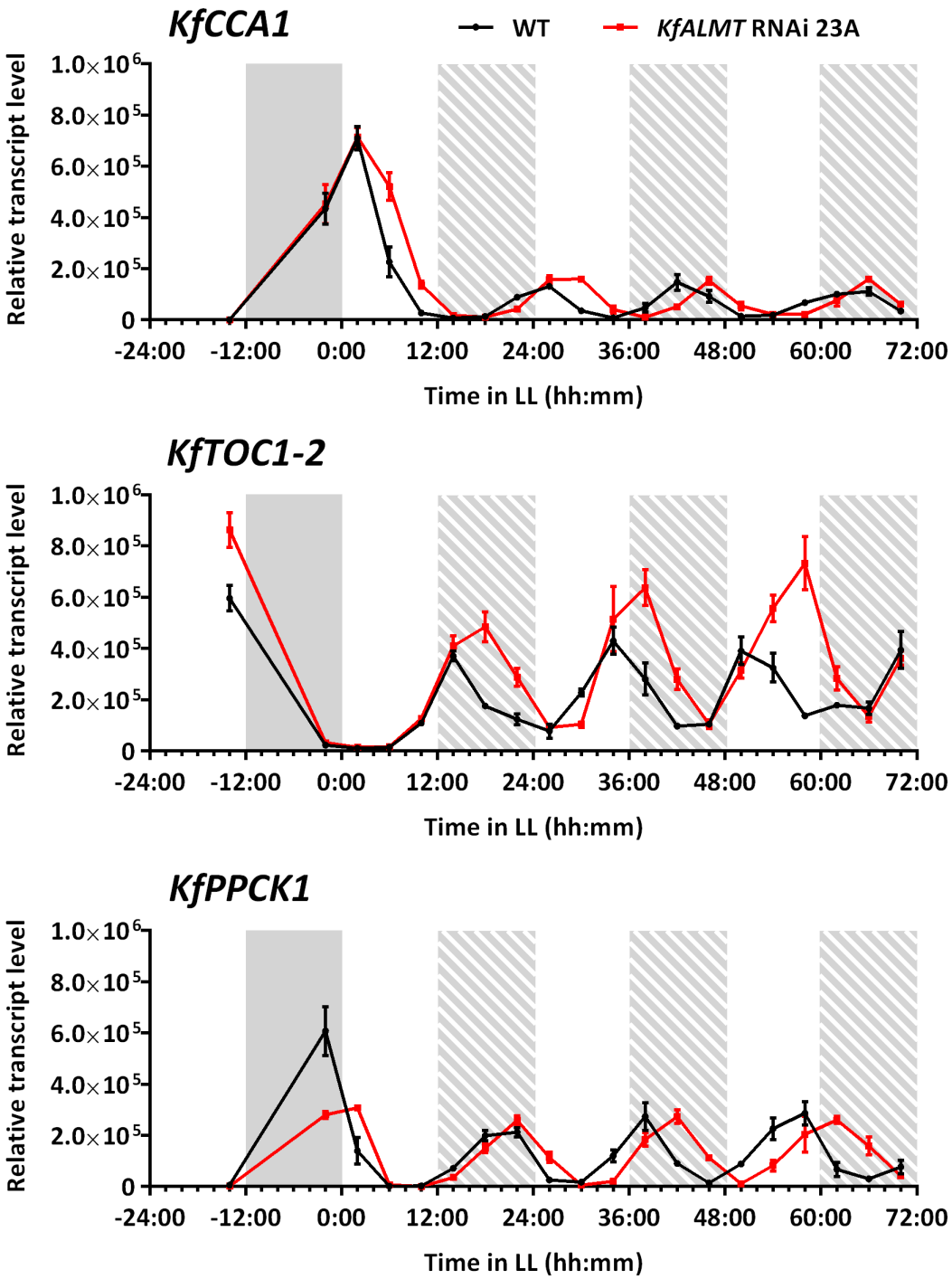


Figure 5.4 – Free-running rhythms of relative transcript abundance of core circadian clock genes and *KfPPCK1* under LL conditions. Relative transcript level was determined in cDNA samples using RT-qPCR, and normalised to a non-oscillating reference gene (*KfTFP*). Solid grey shading represents the dark period and grey cross-hatching represents subjective dark periods (i.e. the duration of dark period had 12:12 LD conditions continued). Each point represents the mean ± S.E.M. of 3 independent replicate CAM leaf samples.

*KfCCA1*. Following the transition from 12:12 LD to LL, free-running rhythms of *KfCCA1* transcript abundance persisted for the full timecourse in both WT and *KfALMT* RNAi 23A, although the amplitude of the transcript oscillations was dramatically reduced (Fig. 5.4). As expected for a dawn-phased circadian clock gene, the transcript level of *KfCCA1* was highest at 02:00 in both genotypes. The subsequent decrease in transcript level was somewhat delayed in *KfALMT* RNAi 23A relative to WT. An apparent phase delay in the circadian rhythm of *KfCCA1* persisted thereafter for the rest of the timecourse, although a statistically-robust distinction between a phase delay and a longer period would be problematic due to the low temporal resolution, the low number of replicates, and the relative brevity of this RT-qPCR timecourse.

*KfTOC1-2* (GenBank: KM078726.1) is one of two orthologs of the *A. thaliana TOC1* gene expressed in *K. fedtschenkoi*. In 12:12 LD, *KfTOC1-2* transcript level was highest in the late light period (-14:00), although slightly higher in *KfALMT* RNAi 23A than in WT, and almost completely eliminated by late in the dark period in both genotypes (-02:00, Fig. 5.4). Following the initiation of LL conditions, *KfTOC1-2* transcript levels continued to oscillate with circadian rhythmicity for the entire timecourse. As with *KfCCA1-2*, the amplitude of the circadian rhythm of *KfTOC1-2* transcript level was lower than the corresponding diel variation of transcript abundance, and, additionally, the minima of the circadian rhythm were at a higher transcript level. Transcript levels were similar in WT and *KfALMT* RNAi 23A for the first 14 h in LL before, as with *KfCCA1*, they diverged with an apparent phase delay in *KfALMT* RNAi 23A that persisted for the remainder of the timecourse. However, a distinct feature of the effect of *KfALMT* silencing on *KfTOC1-2* was an increase in the amplitude of its transcript oscillation as the timecourse progressed. There was reciprocity in the circadian fluctuations of *KfCCA1* and

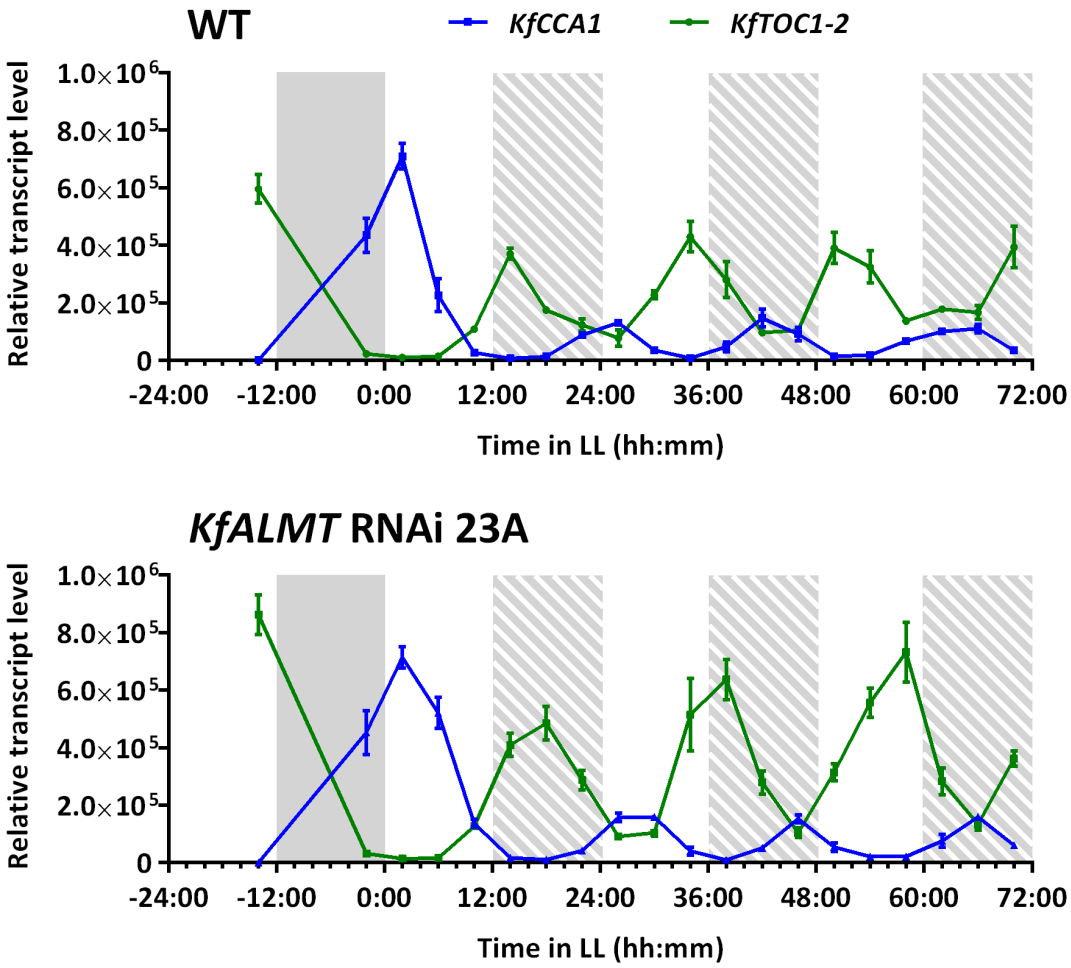


Figure 5.5 – Comparison of free-running rhythms of *KfCCA1* and *KfTOC1-2* relative transcript abundance in *KfALMT* RNAi 23A and WT. RT-qPCR relative transcript abundance measurements from Fig. 5.4 were re-plotted to compare their differential expression.

*KfTOC1-2* (Fig. 5.5), as would be predicted based on the mutual transcriptional repression that has been documented for their *A. thaliana* orthologs (Alabadí *et al.*, 2001; Gendron *et al.*, 2012).

The circadian rhythm of the transcript abundance of the clock-controlled, CAM-associated gene *KfPPCK1* was also studied under LL conditions (Fig. 5.4). As observed for the core circadian clock genes, stable free-running oscillations of *KfPPCK1* transcript levels were found in *KfALMT* RNAi 23A and the WT control. Previous observations of transcriptional

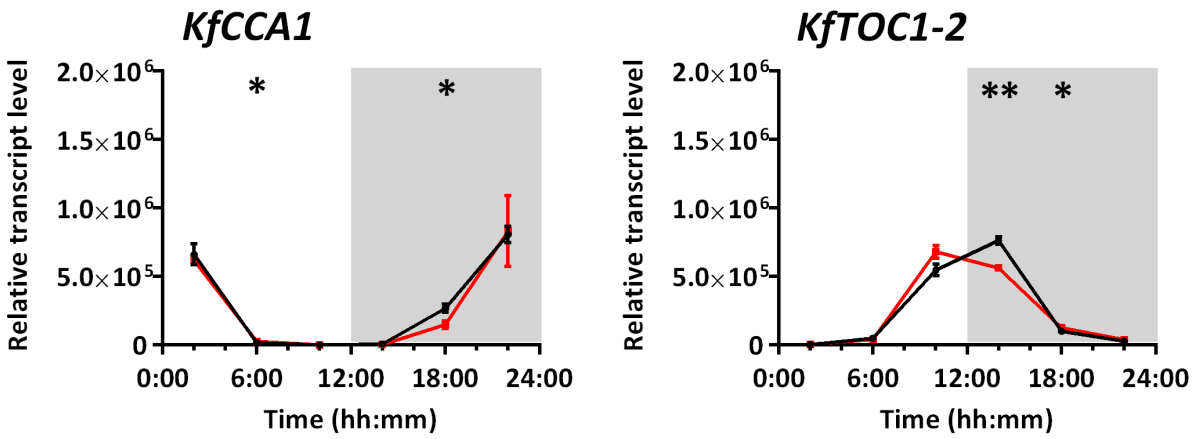


Figure 5.6 – Relative transcript level of *KfCCA1* and *KfTOC1-2* over a 12:12 LD cycle. Relative transcript abundance was determined in cDNA samples using RT-qPCR, and normalised to a non-oscillating reference gene (*KfTFP*). Points represent mean ± S.E.M, n = 3; except for *KfALMT* RNAi 23A at 10:00 and 22:00, n = 2. Shading represents the dark period. The results of a Welch t-test of the difference between mean transcript levels at each time point are displayed above that time point: $P > 0.05$, not shown; $P \leq 0.05$, *; $P \leq 0.01$, **.

repression of *KfPPCK1* at 2 h before the end of the dark period under 12:12 LD (-02:00, Fig. 4.18) in *KfALMT* RNAi 23A were replicated. The delay in down-regulation of *KfPPCK1* transcript level and activity at the beginning of the light period previously observed under 12:12 LD in *KfALMT* RNAi 23A (Figs. 4.18 and 4.19) was exaggerated at the beginning of the first subjective light period under LL (02:00) to the extent that there was a slight increase in mean transcript level from 2 h before the end of the final dark period (-02:00, Fig. 5.4). A phase delay was observed in the circadian rhythm of *KfPPCK1* transcript in *KfALMT* RNAi 23A, although, as with *KfTOC1-2* and *KfCCA1*, it is difficult to eliminate the alternative possibility of lengthening of the period (Fig. 5.4).

For comparison with their circadian rhythms, *KfTOC1-2* and *KfCCA1* transcript were measured in cDNA samples from a 12:12 LD timecourse (described above, Section 4.2.1). *KfCCA1* transcript peaked in the late dark period or the early dark period in both *KfALMT* RNAi

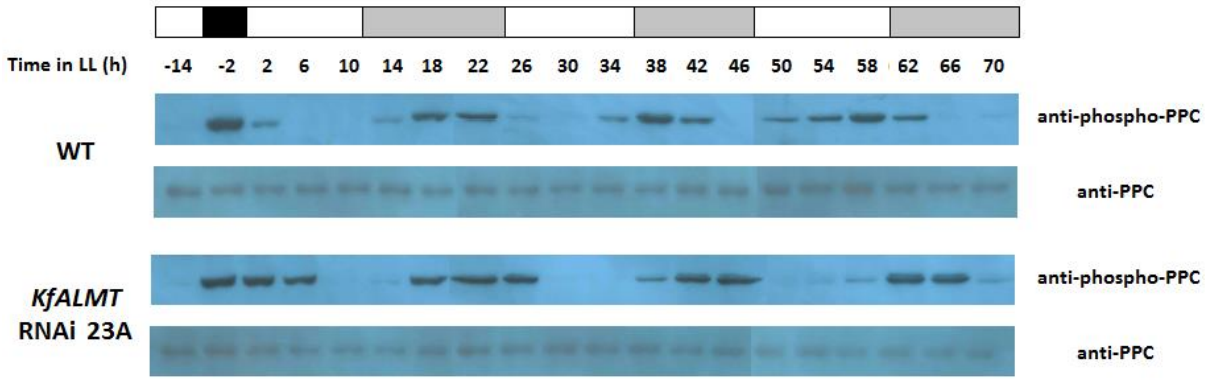


Figure 5.7 – Free-running rhythms of *in vivo* PPC phosphorylation in CAM leaves (leaf pair 6, LP6). LP6 were sampled in one cycle of 12:12 LD, followed by 70 h under LL. PPC phosphorylation was measured by immunoblotting with an anti-phospho-PPC antiserum; anti-PPC antiserum was used as a loading control. Light, darkness and subjective dark periods are indicated above the figure by white, black and grey bars respectively. Each image is a composite of three membranes covering LP6 samples taken at -14:00 to +18:00, +22:00 to +46:00, and +50:00 to +70:00. For both antisera, full timecourses of both WT and *KfALMT* RNAi 23A samples were exposed on the same chemiluminescent film at the same time.

23A and WT (Fig. 5.6). There was a minor, but statistically significant, decrease in *KfCCA1* transcript level at 18:00 in the middle of the dark period in *KfALMT* RNAi 23A relative to WT.

*KfTOC1-2* transcript level peaked early under 12:12 LD in *KfALMT* RNAi 23A (10:00) relative to WT (Fig. 5.6), in contrast to its putative phase delay in the former genotype under LL conditions (Fig. 5.4). *KfTOC1-2* transcript level was also lower in WT than *KfALMT* RNAi 23A (Welch t-test, 4 D.F., $P < 0.05$) at the equivalent time-point (-14:00) before the switch from 12:12 LD to LL conditions (Fig. 5.4).

Transcriptional regulation is known to control PPCK activity *in vivo* (Hartwell *et al.*, 1996, 1999), and therefore immunoblots of phosphorylated PPC in total protein extracted from the LL leaf samples of wild type and *KfALMT* RNAi 23A were used to investigate the target protein phosphorylation in response to the circadian rhythm of *KfPPCK1* transcript levels. Free-

running rhythms of PPC phosphorylation, persisting over the LL time-course, were detected in both *KfALMT* RNAi 23A and WT (Fig. 5.7). Phospho-PEPC abundance was closely correlated with simultaneous *KfPPCK1* transcript levels in both genotypes, other than at 06:00, when transcript level was minimal in *KfALMT* RNAi 23A, but a distinct phosphorylated PPC band was detected (cf. Fig. 5.4 and Fig. 5.7).

## 5.3 Discussion

### 5.3.1 Preliminary evidence for CAM entrainment of the core circadian clock

Suppression of CAM in a single *KfALMT* RNAi line, 23A, produced an apparent phase delay in the circadian rhythms of transcript levels of *KfTOC1-2* and *KfCCA1* (Fig. 5.4). In *A. thaliana*, *TOC1* and *CCA* play a crucial role in setting the periodicity of the core circadian oscillator by their reciprocal transcriptional repression (Alabadí *et al.*, 2001; Huang *et al.*, 2012). A phase delay was also apparent in the free-running rhythm of transcript level of *KfPPCK1* (Fig. 5.4), the CAM-specific PPC kinase (Hartwell *et al.*, 1996, 1999).

Perturbation of the phase of the circadian rhythm of *KfTOC1-2* and *KfCCA1* in *KfALMT* RNAi 23A under LL suggests an entrainment effect of CAM on the core circadian clock. As discussed in the previous chapter, the likely consequences of *KfALMT* silencing on CAM are impaired vacuolar import of malate and feedback inhibition of PPC by accumulation of malate in the cytosol, which results in less rapid nocturnal accumulation of malate by the CAM mesophyll (Sections 4.3.1 and 4.3.2). In this hypothetical model of clock entrainment, the metabolic effects of impaired vacuolar malate import would evoke a weaker signal to the core circadian clock in *KfALMT* RNAi 23A than in WT, and would thus entrain the phase of the clock with a delay relative to WT. An analogous phenotype would be that of loss-of-function mutations in

phytochrome (*phy*) and cryptochrome (*cry*) photoreceptor proteins in *A. thaliana*. The clock period is lengthened in these mutants due to impaired light entrainment (Somers *et al.*, 1998; Devlin and Kay, 2000), although it is lengthened by a weaker response to an exogenous signal rather than by deficiency in an endogenous signal, as is proposed for *KfALMT* RNAi lines.

The fact that periodicity, as opposed to phase, was unperturbed in free-running rhythms of transcript abundance of core clock genes (*KfCCA1* and *KfTOC1-2*) in *KfALMT* RNAi 23A (Fig. 5.4) could be attributed to the rapid loss of diel rhythms of malate accumulation and breakdown in CAM plants (see above, Section 5.1.1; Buchanan-Bollig, 1984; Buchanan-Bollig and Smith, 1984; Nimmo *et al.*, 1987; Ritz and Kluge, 1987; Anderson and Wilkins, 1989*a*; Wyka and Lüttge, 2003; Davies and Griffiths, 2012). By this rationale, fluctuations of malate concentration in CAM leaves of both WT and *KfALMT* RNAi 23A would have been sufficient in the first 24 h under LL to entrain the phase of the circadian clock, although with a delay in the latter. Subsequently, dampening of the diel rhythm of malate turnover would have prevented any further entrainment effect, or any effect that could have been resolved by sampling at 4 h intervals. It must be emphasised that this hypothetical model is based on published measurements of leaf malate concentrations in *K. fedtschenkoi*, closely-related *Kalanchoë* species, and other CAM plants under LL conditions, and that malate concentration has not been measured in leaf samples taken for this LL timecourse.

The potential for primary metabolism to entrain the circadian clock was recently demonstrated by entrainment of the *A. thaliana* core circadian clock by sucrose (Haydon *et al.*, 2013). High concentrations of exogenous sucrose were found to repress transcription of *PRR7*, which led to earlier transcriptional up-regulation of *LHY* and *CCA1* and shortening of the free running period of the clock. Entrainment by sucrose was gated so that the maximum decrease in

periodicity occurred early in the light period, and was proposed to be timed to coincide with the peak of sucrose concentration that follows activation of $C_3$ photosynthesis at dawn (Bläsing *et al.*, 2005; Haydon *et al.*, 2013). There are clear parallels between this mechanism of entrainment and putative entrainment of the *K. fedtschenkoi* core circadian clock by CAM. However, while a constant exogenous supply of sucrose affected the periodicity of the circadian clock in *A. thaliana*, it is important to consider that constitutively high concentrations of malate in *K. fedtschenkoi* leaves can suppress circadian rhythms of both $CO_2$ gas exchange (Anderson and Wilkins, 1989*b*) and gene expression (Dever *et al.*, 2015). As previously discussed in this chapter, entrainment of the former does not require large changes in leaf malate concentration (Anderson and Wilkins, 1989*a*).

With this considered, a possible entrainment signal could be a change in the subcellular distribution of malate, specifically its cytosolic concentration (Wilkins, 1992). Although measurement of cytosolic malate concentration is technically difficult, it has been possible to measure sub-cellular compartmentation of malate in *K. tubiflora* indirectly by determining the rate of "randomisation" by fumarase of $^{13}$C-labelled malate produced by placing CAM leaves in an atmosphere containing $^{13}CO_2$ during various intervals in the dark period (Kalt *et al.*, 1990). The authors of this study suggested that rapid removal of nocturnally-synthesised malate to the vacuole could result in lower rates of randomisation of the position of the $^{13}$C label between the 1-C and 4-C positions, catalysed by mitochondrial fumarase, and found that randomisation was most rapid early and late in the dark period, but slower during the middle of the dark period (Kalt *et al.*, 1990). If low cytosolic malate concentration in the middle of the dark period, produced as a result of high rates of malate import into the vacuole, were the signal for CAM entrainment of the circadian clock, this would explain initial phase delays in free-running rhythms of *KfCCA1*

and *KfTOC1-2* transcript levels; impaired vacuolar malate import would be expected to result in elevated cytosolic malate concentrations during the dark period, and a weaker entrainment signal.

The notion of decreased cytosolic malate concentration may appear inconsistent with high rates of malate synthesis during this section of the dark period. However, fluorometric measurements of cytosolic pH in protoplasts isolated from *K. daigremontiana* have indicated that at the end of the light period, when leaf malate concentrations were minimal, cytosolic malate concentrations remained elevated (Hafke *et al.*, 2001). This suggests that active transport of malate into the vacuole (or lack thereof) can determine cytosolic malate concentration independently of the rate of malate accumulation or gross leaf malate concentration. Furthermore, in *Kalanchoë*, PPC-malate $K_i$ remains low during the early-to-mid dark period as leaf malate concentrations begin to increase, suggesting that phosphorylation of PPC is not required to prevent inhibition due to increased cytosolic malate concentrations at this time (Nimmo *et al.*, 1984; Borland and Griffiths, 1997; Borland *et al.*, 1999).

In this hypothetical model of CAM entrainment, the onset of the dark period would initiate malate import into the vacuole (or cease its efflux from the vacuole), which would then decrease the cytosolic malate concentration and act as an entrainment signal for the circadian clock. This model could explain the advanced phase in the circadian rhythm of $CO_2$ gas exchange in *K. daigremontiana* obtained by Wyka *et al.* (2004) when dark-period $CO_2$ fixation and (presumably) malate synthesis were blocked by placing the leaves in a pure $N_2$ gas atmosphere during the three 12 h dark periods before the imposition of LL conditions, while leaves were being kept under 12:12 LD (Wyka *et al.*, 2004). Under these conditions, blocked malate synthesis would be expected to lower cytosolic malate concentrations at the beginning of

the dark period and advance the onset of the putative entraining signal. However, it should be noted that accurate system dynamics modelling of the CAM cycle in *K. daigremontiana* has given no indication of any decline in cytosolic malate concentration at the beginning of the dark period (Owen and Griffiths, 2013).

The free-running rhythms of transcript level in *KfPPCK1, KfCCA1* and *KfTOC1-2* in RT-qPCR timecourses gave little indication of the timing of any putative entrainment signal because the transcript level of each gene in *KfALMT* RNAi 23A diverged from the WT control at different points in the LL timecourse (Fig. 5.4). It is unknown whether the initial delay in down-regulation of *KfPPCK1* in *KfALMT* RNAi 23A after the onset of LL conditions resulted from circadian clock control, as this was also observed under 12:12 LD (Fig. 4.18), or if the putative phase delay is imposed by the clock later in the free-running period. Remarkably, the phase delay in the free-running rhythm of *KfCCA1* transcript abundance, which appeared shortly after the imposition of LL conditions, did not induce a detectable phase delay in the first peak of *KfTOC1-2* transcript under LL (Fig. 5.4), in spite of the known transcriptional repression of *TOC1* by CCA1 in *A. thaliana* (Alabadí *et al.*, 2001). Instead, transcript levels of *KfTOC1-2* in *KfALMT* RNAi 23A remained unperturbed from the levels observed in the WT control for at least 14 h under LL conditions, passing the first peak of their respective free-running rhythms. In spite of this, close reciprocity of *KfCCA1* and *KfTOC1-2* transcript levels was generally maintained over the LL timecourse in both WT and *KfALMT* RNAi 23A lines (Fig. 5.5).

Characterisation of the diel and circadian rhythms of transcript abundance of more *K. fedtschenkoi* core clock orthologs, under 12:12 LD and LL conditions, respectively, is needed to clarify the regulatory interactions within the core circadian clock in the *KfALMT* RNAi lines studied here. It would also particularly valuable to determine whether transcript levels of other

afternoon- and evening-phased genes, such as *GI*, *PRR5*, and *PRR3* (Fowler *et al.*, 1999; Matsushika *et al.*, 2000), remain unperturbed from their WT levels up until the same point of the LL free-run as *KfTOC1-2* did (14:00, Fig. 5.4). The increasing peak transcript levels in the circadian rhythm of *KfTOC1-2* could be explained by a loss of phased rhythmicity in *KfPRR5* transcription if this abrogated its transcriptional repression of *RVE8* (Nakamichi *et al.*, 2012), and consequently led to transcriptional up-regulation of *KfTOC1* isogenes (Hsu *et al.*, 2013). Full characterisation of the transcriptional activity of the core circadian clock genes could determine the timing of any putative entrainment signals from the CAM pathway to the circadian clock, and reveal how this putative signal is propagated to the clock as a whole under free-running conditions.

### 5.3.2 Differential entrainment of the circadian $CO_2$ gas exchange rhythm in WT and *KfALMT* RNAi lines was dependent on the degree of CAM suppression

Robust circadian rhythms of $CO_2$ gas exchange under LL were not consistently disrupted by hairpin dsRNA transgene-targeted, RNAi-mediated silencing of *KfALMT* (Figs. 5.1 and 5.2). The transition from the diel rhythm of $CO_2$ gas exchange under 12:12 LD to a free-running rhythm in the first ~36 h under LL was, however, markedly different from WT in each of the *KfALMT* RNAi lines. In the previous chapter, it was hypothesised that $CO_2$ uptake during phases II-IV was suppressed in detached leaves due to abrogation of phloem export of photosynthetically-fixed C (Section 4.3.3). This suppression was apparently reversed in the *KfALMT* RNAi lines during the first subjective light period (00:00-12:00) under the lower temperature and lower light intensity of LL conditions, but not in WT (Figs. 5.1 and 5.2). The severely CAM-suppressed *KfALMT* RNAi lines 12A and 23A were, furthermore, differentiated from the moderately

CAM-suppressed line 8B (c.f. Figs. 4.7 and 4.11), whose relatively broad and deep Phase III, and single peak in $J_{CO2}$ at ~16:00 bore more resemblance to the concurrent $CO_2$ gas exchange behaviour of WT (Figs. 5.1 and 5.2). It may be useful to consider how abrupt switching to LL conditions could have interacted with the CAM-suppressed phenotype of *KfALMT* RNAi lines to produce a dramatic increase in $CO_2$ uptake in Phase II and Phase IV early in the LL timecourse (Figs. 5.1 and 5.2).

Enhancement of $CO_2$ uptake in the first subjective light period under LL could be attributed to increased stomatal conductance. Stomatal aperture in isolated *K. daigremontiana* epidermal strips has been found to increase at 15 °C relative to 25 °C, in the absence of exogenous $CO_2$ (Jewer *et al.*, 1981). Stomatal aperture was unresponsive to illumination at ~400 μmol $m^{-2}$ (Jewer *et al.*, 1981). In itself, this previously reported stomatal regulation by temperature in *Kalanchoë* cannot explain the differences in $CO_2$ gas exchange between WT and the *KfALMT* RNAi lines. However, low temperature has also been found to prolong the lag between illumination and the onset of malate breakdown in *Kalanchoë* (Kluge *et al.*, 1991*b*), and this, in combination with lower availability of malate for decarboxylation at the end of the dark period in *KfALMT* RNAi lines (Fig. 4.13), could delay stomatal closure by delaying the build-up of leaf mesophyll $CO_2$ concentration that occurs during Phase III (Cockburn *et al.*, 1979; Kluge *et al.*, 1981).

Protracted and pronounced Phase IV $CO_2$ uptake under LL conditions in *KfALMT* RNAi lines, following its absence under 12:12 LD, is more difficult to explain from extant data. Although the period and intensity of Phase II were found to increase following suppression of malate accumulation in *K. daigremontiana* CAM leaves kept in a pure-$N_2$ atmosphere during the dark period, lower Phase IV $CO_2$ uptake was observed (Borland and Griffiths, 1997). Enhanced

Phase IV $CO_2$ uptake in *KfALMT* RNAi lines cannot, therefore, be predicted on the basis of suppression of dark-period malate accumulation. Similarly, low light intensity was found to decrease Phase IV $CO_2$ uptake in *K. blossfeldiana* performing inducible CAM (Thomas *et al.*, 1987).

Therefore, differences between the responses of the *KfALMT* RNAi lines and WT to the imposition of LL conditions after entrainment to 12:12 LD could not have been fully predicted from the results of previous experimental manipulation of CAM in *Kalanchoë.* As previously discussed, the $CO_2$ gas exchange behaviour observed in detached leaves under 12:12 LD was likely to have been an experimental artefact unrelated to CAM leaf function in intact *K. fedtschenkoi*, and was, in any case, not entirely replicable (Section 4.3.3). In future studies, it may be interesting to determine whether the light-period stomatal response to abrupt changes in light intensity and/or temperature from the entrainment conditions is different in CAM leaves of intact specimens of *KfALMT* RNAi lines and WT, but this can be treated as a separate issue to differential entrainment of the CAM circadian rhythm of $CO_2$ gas exchange.

After approximately 36 h under LL, the circadian rhythm of $CO_2$ gas exchange by each *KfALMT* RNAi line assumed a sinusoidal shape similar to WT. While peak $J_{CO2}$ declined over the LL timecourse in each genotype, total 24 h $CO_2$ uptake between 72:00 and 96:00 in each of the *KfALMT* RNAi lines was greater than it was during the final 12:12 LD cycle before switching to LL (Fig. 5.3).

As discussed in the introduction to this chapter, rhythmicity of PPC activity has been found to be required for a circadian rhythm of $CO_2$ exchange under LL, but phased turnover of malate is not. Whereas Rubisco activation and direct fixation of atmospheric $CO_2$ are largely temporally separated under diel conditions (Borland and Griffiths, 1997; Maxwell *et al.*, 1999),

under LL conditions PPC and Rubisco fix atmospheric $CO_2$ simultaneously for extended periods (Buchanan-Bollig *et al.*, 1984; Wyka and Lüttge, 2003; Davies and Griffiths, 2012). These regulatory changes appear to have allowed *KfALMT* RNAi lines to assimilate similar quantities of atmospheric $CO_2$ to WT, bypassing the inhibition of PPC by malate, secondary to impaired vacuolar malate import (see above, Section 4.3.1), that presumably persists under LL conditions.

Rhythms of *KfPPCK1* transcript and KfPPC phosphorylation persisted in WT and *KfALMT* RNAi 23A sampled over 70 h under LL and were in phase, approximately, with oscillations in $J_{CO2}$ in the $CO_2$ gas exchange timecourse of detached leaves of the same genotype (Figs. 5.4 and 5.7). This suggests that phosphorylation of KfPPC_CAM continued to facilitate its increased activity around peaks in rates of $CO_2$ uptake by decreasing its sensitivity to feedback inhibition by malate (Nimmo *et al.*, 1984; Carter *et al.*, 1991; Nimmo, 2000).

The period of the rhythm in *KfALMT* RNAi 12A and *KfALMT* RNAi 23A was longer than in WT (Fig. 5.2). The free-running period of *KfALMT* RNAi 8B was approximately equal to that of WT, showing that lengthening of the period was dependent on the degree of CAM suppression. The longer period is consistent with the hypothetical model of CAM entrainment of the circadian clock presented in the previous section, but there was no delay in phase of the circadian rhythm of $CO_2$ gas exchange like that found in the circadian rhythms of *KfCCA1*, *KfTOC1-2* or *KfPPCK1* transcript abundance in *KfALMT* RNAi 23A relative to WT (Fig. 5.4). It is possible that the lag period between detachment of the leaves and the onset of LL conditions, during which $CO_2$ gas exchange was measured under 12:12 LD (Section 4.2.3), induced regulatory changes to CAM or the circadian clock that could have produced this disparity. However, it is important to consider the possibility that these circadian $CO_2$ gas exchange data

contradict the model of entrainment of the core circadian clock that was proposed to explain the RT-qPCR data.

## 5.4 Summary

The results presented in this chapter suggest entrainment or driving of the phase of the core circadian clock by CAM. In order to explain perturbation of the circadian rhythm of transcript levels of core circadian clock genes in *KfALMT* RNAi lines with suppressed CAM function, broad assumptions have been made about related metabolic fluxes, particularly the accumulation and breakdown of malate. These assumptions were based on metabolite measurements of selected *KfALMT* RNAi lines and WT controls under 12:12 LD, and reported metabolite data of CAM species under LL (as discussed in the chapter introduction). Parallel measurements of CAM-related metabolite concentrations, especially malate, in the leaf samples taken under LL conditions used to measure transcript levels of circadian clock and clock-related genes are now needed to validate these assumptions. Measurement of transcript levels of a far more comprehensive set of core circadian clock genes is also required to complete the description of the effects of perturbation of CAM on the clock. RT-qPCR of *KfTOC1-2* and *KfCCA1* probes a single transcriptional feedback loop of the circadian clock (Alabadi *et al.* 2001, Huang *et al.* 2012), but recent models of the *A. thaliana* clock have suggested that transcriptional regulation by morning-expressed *PRR*-family genes (*PRR7* and *PRR9*) and the evening complex is required for a circadian rhythm, in addition to post-translational regulation by *ZTL* and *GI* (Pokhilko *et al.*, 2012; Fogelmark and Troein, 2014).

The concept of core clock entrainment by CAM offers testable hypotheses which could examined by future studies. For example, reversion of *K. daigremontiana* leaves to a circadian

rhythm of $CO_2$ gas exchange from arrhythmia by a negative temperature shift has been found to induce at least one cycle of malate accumulation and breakdown (Grams *et al.* 1996). If entrainment of the circadian clock by CAM were authentic, this should produce a phase delay in the re-initiated circadian rhythm of the core clock in *KfALMT* RNAi mutants, just as there was at the transition from 12:12 LD to LL conditions.

Perturbation of the circadian rhythm of $CO_2$ exchange under LL conditions by silencing of *KfALMT* was also observed, albeit as lengthening of the period of the rhythm rather than delayed phase (Figs. 5.1 and 5.2). Resolution of the discrepancy between circadian rhythms of $CO_2$ gas exchange and transcript levels could be attempted by parallel measurement of these distinct outputs of the circadian oscillator. Measurement of leaf delayed fluorescence (DF) has been suggested as a non-invasive technique to monitor circadian rhythms in photosynthetic activity in a variety of plant species, including *K. fedtschenkoi* (Gould *et al.*, 2009). Simultaneous measurement of leaf DF and sampling of leaves for metabolite analysis and RT-qPCR could be carried out on a single population of wild type and *KfALMT* RNAi plants, obviating the need to consider differences in experimental conditions when interpreting circadian data. Separately, it would be informative to measure stomatal conductance in *KfALMT* RNAi lines under LL conditions. As described above, it has been postulated that stomatal conductance and the rate of $CO_2$ fixation are governed by distinct circadian oscillators in *K. daigremontiana* (Bohn *et al.*, 2003), and it should be determined whether the phases and/or periods of both parameters are perturbed in the same way in the *KfALMT* RNAi lines.

# Chapter 6 - Preliminary phenotyping of lines with isogene-specific, transgenic hairpin dsRNA-targeted silencing of potential CAM-associated MDHs

## 6.1 Introduction

### 6.1.1 MDH isoenzymes are present in multiple intracellular compartments

MDH catalyses the reversible oxidation of malate to OAA, with the concomitant reduction of either NAD or NADP:

$$\text{malate} + \text{NAD(P)}^{+} \xleftrightarrow{\text{MDH}} \text{OAA} + \text{NAD(P)H} + \text{H}^{+}$$

Plant genomes encode both NAD-specific and NADP-specific MDHs that are targeted for localisation to plastids (Scheibe, 2004), while the cytosol, mitochondria and peroxisomes of plants each contain one or more distinct, NAD-specific isoforms (Gietl, 1992).

3D structural data on the plant MDHs is currently limited to the chloroplastic NADP-MDH (NADP-MDH) of *Flaveria bidentis* (Carr *et al.*, 1999) and *Sorghum vulgare* (Johansson *et al.*, 1999). The X-ray crystal structure of both enzymes was found to be a homodimer with two identical catalytic active sites, and the former structure was superimposed in three dimensions with mammalian and eubacterial NAD-MDH X-ray crystal structures with relatively low mean deviation between homologous residues (Carr *et al.*, 1999; Johansson *et al.*, 1999). NADP-MDH and cytoplasmic NAD-MDH (CMDH) form a separate clade to NAD-MDH isoforms that are localised to the mitochondria (MMDH), peroxisome (PxMDH) and plastid (PdMDH) in published phylogenies of the MDH family (Miller *et al.*, 1998; Schnarrenberger and Martin, 2002).

MMDH and CMDH catalyse intermediate steps in the TCA cycle and glyoxylate cycle, respectively (Nunes-Nesi *et al.*, 2005; Kaur *et al.*, 2009). Malate is accumulated in

photosynthetic tissues of many $C_3$ species (Igamberdiev and Eprintsev, 2016) and diurnally-accumulated malate has been found to be an important source of TCA cycle intermediates during the night in *A. thaliana* (Fahnenstich *et al.*, 2007; Zell *et al.*, 2010).

MDHs also mediate the transfer of reducing equivalents between various organelles and the cytosol in conjunction with membrane-bound transport proteins. In a 'malate valve' or 'malate/OAA shuttle', NAD(P)H is consumed in the reduction of OAA to malate in one intracellular compartment, and the latter is then re-oxidised to OAA by MDH in a second compartment to produce NAD(P)H. The flow of re-generated OAA in the reverse direction permits the continued movement of reducing equivalents (Heber, 1974).

The prototypical malate valve exports reducing equivalents from the chloroplastic stroma in the light using NADP-MDH (Heber, 1974). Malate and OAA are transported across the inner membrane of the plastid by the 2-oxoglutarate/malate transporter (OMT/DiT1) (Taniguchi *et al.*, 2002; Kinoshita *et al.*, 2011). The linear photosynthetic electron transport chain (PETC) synthesises ATP and NADPH concomitantly (Heldt and Piechulla, 2011*b*). When excess reducing equivalents accumulate in the stroma and the NADPH/NADP ratio rises, the NADP-MDH malate valve permits the regeneration of NADP and continued flux through the linear PETC (Scheibe, 2004). NADP-MDH is redox-regulated in order to suppress the export of stromal reducing equivalents when their redox potential is relatively high (Ashton *et al.*, 2000). The N- and C-terminal sections of the NADP-MDH polypeptide both contain a pair of cysteine residues separated by a short section of the primary structure (Ashton *et al.*, 2000). X-ray crystallography of NADP-MDH in its oxidised state has shown that disulphide bonds form between the neighbouring cysteine residues and force the C-terminus of each subunit into the active site of the same subunit, which blocks its binding of OAA or malate (Carr *et al.*, 1999;

Johansson *et al.*, 1999). The role of the N-terminus is less well understood but reduction of both disulphides is required for full activation of the enzyme (Ashton *et al.*, 2000), and deletion of the N-terminal sequence increases the rate of NADP-MDH activation (Johansson *et al.*, 1999). NADP-MDH is reduced and activated by the reduced form of one or more plastidic thioredoxins, which are in turn reduced by ferredoxin-thioredoxin reductase, thereby linking flux through the linear PETC to NADP-MDH (Scheibe, 2004). The standard redox potential of the NADP-MDH regulatory disulphide is low relative to that of thioredoxin, and reductive activation of NADP-MDH is inhibited by NADP (Rebeille and Hatch, 1986). These properties of NADP-MDH are thought to permit activation of the malate valve only when the chloroplastic pools of NADP and thioredoxin are highly reduced, and prioritise consumption of reducing equivalents in the stroma over their export (Rebeille and Hatch, 1986; Backhausen *et al.*, 1994). *In vitro* experiments demonstrated that isolated chloroplasts preferentially consumed reducing equivalents by reducing 1,3-bisphosphoglycerate (1,3BPG), via the Calvin cycle, and nitrite, catalysed by nitrite reductase, over the NADP-MDH-catalysed reduction of OAA (Backhausen *et al.*, 1994). Loss of malate valve function in an *A. thaliana nadp-mdh* knock-out mutant was found to result in no impairment of photosynthesis, but this was conditional on consumption of stromal reducing equivalents by glutamine-oxoglutarate aminotransferase (GOGAT) as part of the photorespiration pathway, and coincided with increased expression of genes and proteins associated with antioxidant system pathways (Hebbelmann *et al.*, 2012). *A. thaliana OMT* knock-out mutants (*AtpOMT1*) also showed loss of malate valve function, and displayed lower quantum efficiency of Photosystem II ($\Phi_{PSII}$) under high intensity light, indicating an excess of reducing equivalents in the linear PETC (Kinoshita *et al.*, 2011). Photorespiration was impaired in *AtpOMT1* plants due to the additional role of OMT in mediating import of 2-oxoglutarate into

the stroma as substrate for GOGAT (Kinoshita *et al.*, 2011). A comparison of the *AtpOMT1* and *nadp-mdh* phenotypes therefore suggests that there is partial redundancy between the NADP-MDH valve and photorespiration in *A. thaliana* in the consumption of reducing equivalents that are surplus to the requirements of $C_3$ photosynthesis. In the former mutant the disruption of both mechanisms apparently caused a decrease in $\Phi_{PSII}$.

In the dark and in non-photosynthetic plastids, NADP-MDH is either deactivated or not expressed, and PdMDH fulfils an identical function in the malate valve (Scheibe, 2004). ATP and NADH synthesis in darkened or non-photosynthetic plastids is catalysed by plastidic isoforms of glyceraldehyde 3-phosphate dehydrogenase (GAPDH) and phosphoglycerate kinase (PGK) as intermediate steps of the plastidic glycolysis pathway (Plaxton, 1996; Munoz-Bertomeu *et al.*, 2009):

$$\text{GAP} + \text{NAD} + \text{HPO}_4^{2-} \xleftrightarrow{\text{GAPDH}} \text{1,3BPG} + \text{NADH} + \text{H}^+$$

$$\text{1,3BPG} + \text{ADP} \xleftrightarrow{\text{PGK}} \text{3PG} + \text{ATP}$$

(key: GAP, glyceraldehyde 3-phosphate; 1,3BPG, 1,3-bisphosphoglycerate; 3PG, 3-phosphoglycerate). Regeneration of NAD and export of reducing equivalents by the PdMDH malate valve has been demonstrated *in vitro* in plastids isolated from both autotrophic and heterotrophic tissues (Backhausen *et al.*, 1998). Synthesis of 3PG from exogenous dihydroxyacetone phosphate (DHAP) was conditional on oxidation of stromal NADH, enabled by the addition of OAA to the external medium (Backhausen *et al.*, 1998). *A. thaliana* homozygous PdMDH knock-out mutants are lethal at the embryo stage and this is thought to be

due to disrupted development of plastids (Beeler *et al.*, 2014; Selinski *et al.*, 2014). Evidence for the function of the PdMDH malate valve in *A. thaliana* plants has been provided by transgenic *PdMDH* silencing, but is equivocal on whether this malate valve mediates export of reducing equivalents from plastidic glycolysis (Selinski *et al.*, 2014) or import of reducing equivalents to the stroma (Beeler *et al.*, 2014).

Transfer of reducing equivalents across the peroxisomal membrane is also thought to be mediated by a malate valve. The peroxisomal membrane contains a protein channel that mediates diffusion of OAA and malate (Reumann *et al.*, 1998) and PxMDHs can reduce the peroxisomal NAD pool by oxidising malate that has diffused into the peroxisomal matrix from the cytosol, or oxidise the NAD pool by reducing OAA that has diffused into the peroxisomal matrix via the same route. *A. thaliana* has two genes that encode peroxisomal NAD-MDHs, *PMDH1* and *PMDH2* (Pracharoenwattana *et al.*, 2007). The peroxisomal malate valve re-oxidises NADH produced by 3-hydroxyacyl-CoA dehydrogenase as part of the β-oxidation cycle that degrades fatty acids in peroxisomes. β-oxidation was strongly suppressed in the *A. thaliana* double knock-out mutant *pmdh1 pmdh2* (Pracharoenwattana *et al.*, 2007). The peroxisomal malate shuttle may also operate in the reverse direction by generating NADH in the peroxisome as a substrate for hydroxypyruvate reductase (HPR), part of the photorespiration pathway (Cousins *et al.*, 2008). Functional copies of *PMDH1* and *PMDH2* were not essential in *A. thaliana* for survival in air (Cousins *et al.*, 2008), as are many genes encoding photorespiration pathway enzymes (Bauwe *et al.*, 2010). However, the rate of $CO_2$ loss from photorespiration was increased in *pmdh1 pmdh2* plants, and it was suggested that the mutant compensated for loss of the supply of NADH to peroxisomal HPR with alternative pathways that are less efficient at recovering 3PG from 2-phosphoglycolate (Cousins *et al.*, 2008).

Antiport of OAA and malate across the inner mitochondrial membrane in plants can be mediated by both the dicarboxylate-tricarboxylate transporter (DTC) and dicarboxylate carrier (DIC) family proteins (Picault *et al.*, 2002; Palmieri *et al.*, 2008). Mitochondria isolated from *Spinacia oleracia* were found to divert a portion of their reducing equivalents, generated by respiration of glycine and malate, from oxidative phosphorylation to malate export when they were supplied with physiological concentrations of exogenous OAA (Hanning and Heldt, 1993). It was suggested that during photorespiration one or more malate valves mediate transfer of a portion of the reducing equivalents generated by the glycine decarboxylase complex (GDC) to the peroxisome to supply HPR-catalysed hydroxypyruvate reduction (Hanning and Heldt, 1993). MMDH activity has also been suggested to be important for maintaining high rates of photorespiration because re-oxidation of NADH produced by glycine decarboxylation in the matrix is needed to prevent feedback inhibition of the GDC by NADH (Bykova *et al.*, 2014). *A. thaliana* has two *MMDH* isogenes, *mMDH1* and *mMDH2*, and the double knock-out *mmdh1/mmdh2* mutants displayed impaired photorespiration (Tomaz *et al.*, 2010). More detailed metabolic characterisation of a *mmdh1* knock-out mutant showed that glycine accumulation coincided with reduced reabsorption of $NH_3$ by chloroplastic glutamine synthase, which indicated suppression of GDC activity (Lindén *et al.*, 2016). These results are indicative of a role for MMDH in maintaining a low NADH:NAD ratio during photorespiration, although without direct evidence of mitochondrial OAA-malate exchange (Tomaz *et al.*, 2010; Lindén *et al.*, 2016).

### 6.1.2 Potential models for OAA reduction in nocturnal malate accumulation

The simplest model for converting OAA to malate in CAM would be reduction catalysed by CMDH at the location of OAA synthesis by PPC (Cushman and Bohnert, 1997). Glycolysis in the cytosol produces 1 mol NADH for every mole of PEP via the intermediate, GAPDH-catalysed reaction (Plaxton, 1996). This could supply the substrate *in situ* for reduction of OAA to malate by CMDH, and the equilibrium constant of this reaction strongly favours oxidation of NADH ($[NADH][OAA]/[NAD^+][malate] = 2.8 \times 10^{-5}$ at equilibrium; Igamberdiev and Eprintsev, 2016). Moreover, continuous re-oxidation of NADH would be required to maintain a sufficiently high redox potential in the cytosolic NADH/NAD pool for GAP oxidation. Conversion of OAA to malate for vacuolar storage and regeneration of cytosolic NAD to permit glycolytic conversion of storage carbohydrates to PEP may thus be coupled to CMDH. A large majority of NAD-MDH activity in *M. crystallinum* following the induction of CAM by salt stress was found to be associated with the cytosol when it was isolated from the organelles by density gradient ultracentrifugation, suggesting that CMDH is the major OAA reductase in this CAM species (Winter *et al.*, 1982*a*). Light-dependent over-expression of a *CMDH* transgene has been found to increase leaf and root malate concentration, and root malate exudation in *Nicotiana tabacum*, showing that CMDH can exert control over the rate of malate synthesis in a $C_3$ photosynthesis context (Wang *et al.*, 2010).

The reduction of OAA by organellar MDHs in CAM would adapt malate valve mechanisms found in $C_3$ plants from a closed OAA-malate cycle to a linear pathway that consumes OAA supplied by PEP carboxylation and produces malate for vacuolar import. Such a metabolic pathway has been proposed in the light in mesophyll cells of $C_4$ species of the NADP-malic enzyme subtype. Cytosolic PPC synthesises OAA, which is imported into

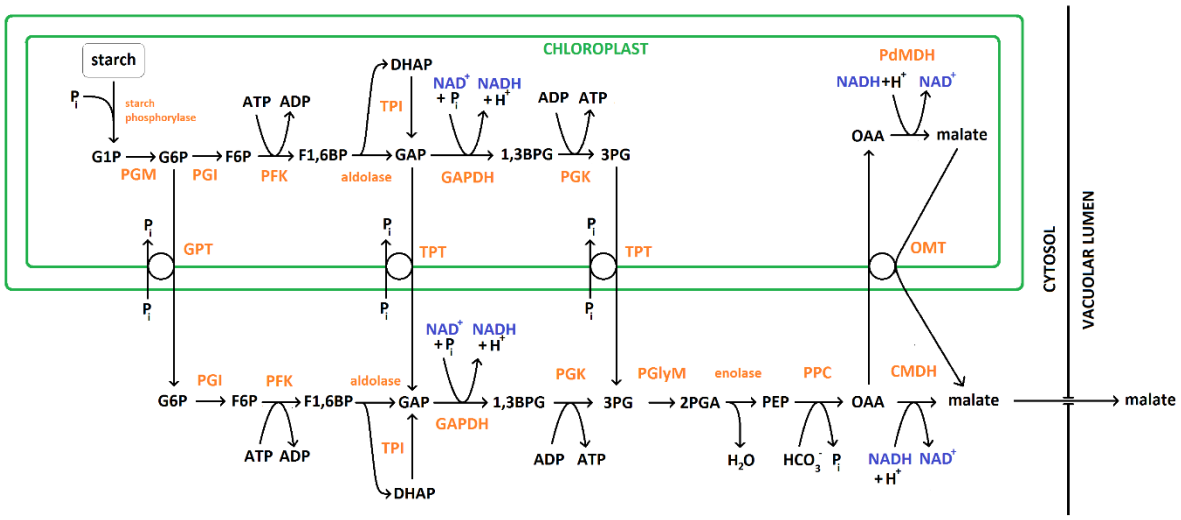


Figure 6.1 – Models for alternative subcellular compartmentation of fluxes from starch breakdown to PEP synthesis, via glycolysis, and reduction of OAA to malate in CAM at night. This figure is based on information from Neuhaus and Schulte (1996) and Weber and Linka (2011).
*Additional abbreviations – Intermediates: G1P, glucose 1-phosphate; G6P, glucose 6-phosphate; F6P, fructose 6-phosphate; F1,6BP, fructose 1,6-bisphosphate; DHAP, dihydroxyacetone phosphate; 1,3BPG, 1,3-bisphosphoglycerate; 2PG, 2-phosphoglycerate. Enzymes and transporters: GPT, glucose/phosphate translocator; PGM, phosphoglucomutase; PGI, phosphoglucoisomerase; PFK, phosphoglucokinase; TPI, triose phosphate isomerase; PGK, phosphoglycerate kinase; PGlyM, phosphoglycerate mutase.*

chloroplasts, reduced to malate by NADP-MDH, and then exported to the cytosol and subsequently to the bundle-sheath cells (Weber and von Caemmerer, 2010). Redox-regulation of NADP-MDH would presumably preclude a role in converting OAA to malate in the dark in CAM, as the redox potential of the chloroplastic thioredoxin pool would not be low enough to activate the enzyme in the absence of PETC activity (Scheibe, 2004).

*In vitro* manipulation of isolated chloroplasts of CAM-induced *M. crystallinum* has indicated that a portion of the malate accumulated in Phase I is produced by reduction of OAA in the stroma (Neuhaus and Schulte, 1996; Fig. 6.1). ATP was found to increase the rate of starch breakdown when supplied to chloroplasts isolated at the beginning of the dark period from *M.*

*crystallinum* in either its constitutive $C_3$ or induced CAM modes. This effect was replicated by the addition of OAA, and led to export of 3PG and malate from the chloroplasts of *M. crystallinum* in CAM mode. Reduction of exogenous OAA to malate, catalysed by PdMDH, therefore provided a sink for reducing equivalents generated by GAPDH, in the form of NADH, and permitted glycolytic conversion of starch-derived glucose to 3PG in the stroma to act as an endogenous source of ATP. Like the cytosolic pathway, this pathway would permit PEP synthesis to be coupled to OAA reduction in CAM (Neuhaus and Schulte, 1996; Fig. 6.1). Some *in vivo* evidence for PdMDH-catalysed malate accumulation in a $C_3$ species was provided by its overexpression in *Medicago sativa*, whereupon root malate concentration and malate exudation were increased (Imsande *et al.*, 2001; note that the so-called nodule-enhanced MDH was only later identified as a plastid-localised NAD-MDH isoform by Tesfaye *et al.* (2001)).

Mitochondria could conceivably contribute to nocturnal malate accumulation in CAM via reduction of OAA to malate by MMDH and DTC/DIC-mediated antiport of malate in the matrix for OAA from the cytosol. Mitochondrial malate synthesis would imply an incomplete TCA cycle and competition by MMDH with the respiratory electron transport chain for NADH produced by the mitochondrial decarboxylases, pyruvate dehydrogenase (PDH), isocitrate dehydrogenase (ICDH) and oxoglutarate dehydrogenase (OGDH) (Heldt and Piechulla, 2011*a*). However, a requirement for OAA to act as a redox sink for NAD(P)H produced by glycolysis, via the cytosol or the plastidic stroma, in a 1:1 stoichiometric ratio with PEP would restrict mitochondrial reduction of OAA synthesised in the cytosol. Flux balance analysis of simulated plant metabolism, which has largely reconstructed the diel cycle of CAM from a $C_3$ model with a small number of additional constraints that replicated observed features of CAM stomatal control and carbohydrate metabolism, has indicated that MMDH contributes to cyclical flux in the full

TCA cycle in the dark, rather than OAA reduction (Cheung *et al.*, 2014). Mitochondrial respiration is thought to be required in CAM in order to synthesise ATP required for active transport of $H^+$ into the vacuole and citrate for nocturnal accumulation (Kalt *et al.*, 1990; Holtum *et al.*, 2005).

Potentially, a portion of the OAA synthesised by PPC could be imported into peroxisomes, reduced to malate by PxMDH and re-exported to the cytosol, with NADH provided by the β-oxidation cycle from fatty acid degradation, hormone synthesis or branched amino acid degradation (Kaur *et al.*, 2009). However, unlike the plastidic pathway, there is no known obvious way for flux between carbohydrate and PEP during Phase I to be diverted through a peroxisomal, NAD-reducing pathway. Therefore, a role for peroxisomes in OAA reduction would be contingent on the activity of non-CAM metabolic pathways to supply reducing equivalents and is likely to be peripheral to other pathways.

## 6.2 Results

### 6.2.1 Genomic and transcriptomic analysis of the *K. fedtschenkoi* MDH gene family

*K. fedtschenkoi* genomic and transcriptomic datasets (described above, Section 2.9.1) were mined for data to assemble a phylogeny of the *K. fedtschenkoi* MDH gene family and to determine the differential regulation of the steady-state transcript abundance of each gene in $C_3$ and CAM leaves sampled over a 12:12 LD cycle. Although *K. laxiflora* was used as the CAM model species for phenotyping MDH isogene silencing, genomic and transcriptomic profiling of *K. fedtschenkoi* is currently more comprehensive and provides more information on CAM MDH function. The *A. thaliana* MDH gene family is comprised of 9 genes in total, although the function of the CMDHs has not been characterised in this species (Maurino and Engqvist, 2015; Table 6.1). A BLASTP search of a database of *K. fedtschenkoi* predicted proteins was performed with the peptide sequence of each *A. thaliana* MDH. 12 sequences were retrieved that aligned with at least one query sequence with $E < 1 \times 10^{-20}$. Three of these putative genes (KF18985, KF47385 and KF97860) lacked one or more of a quintet of conserved amino acid residues that formed the active site in reported MDH crystal structures (Goward and Nicholls, 1994; Carr *et al.*, 1999). These sequences (197, 88 and 109 a.a. respectively) were shorter than the other nine (≥257 a.a.). These curtailed MDH peptide predictions could be an artefact of genome sequencing, assembly or annotation, but their inclusion in the phylogenetic analysis considerably restricted its power by severely decreasing the length of the ungapped multiple sequence alignment yielded by TCoffee and GBlocks. KF18985, KF47385 and KF97860 were therefore omitted from the phylogenetic analysis, but have been analysed separately below.

Table 6.1 – *A. thaliana* genes used in phylogenetic analysis

| Description | Gene | *A. thaliana* genomic locus | UniProtKB Accession |
|---|---|---|---|
| Cytosolic NAD-MDH | *AtCMDH1* | AT1G04410 | P93819 |
| | *AtCMDH2* | AT5G43330 | P57106 |
| | *AtCMDH3* | AT5G56720 | Q9FJU0 |
| Mitochondrial NAD-MDH | *AtMMDH1* | AT1G53240 | Q9ZP06 |
| | *AtMMDH2* | AT3G15020 | Q9LKA3 |
| Plastidic NAD-MDH | *AtPdMDH* | AT3G47520 | Q9SN86 |
| Chloroplastic NADP-MDH | *AtNADP-MDH* | AT5G58330 | Q8H1E2 |
| Peroxisomal NAD-MDH | *AtPxMDH1* | AT2G22780 | O82399 |
| | *AtPxMDH2* | AT5G09660 | B3H560 |
| Lactate dehydrogenase (outgroup) | *AtLDH* | AT4G17260 | O23569 |

The data for this table was obtained from Maurino & Engqvist (2015).

Table 6.2 – Predicted *K. fedtschenkoi* MDH genes

| Description | *K. fedtschenkoi* sequence | Abbreviation | Method |
|---|---|---|---|
| Cytosolic NAD-MDH | KF122385 | *KfCMDH1* | MSA |
| | KF18985 | *KfCMDH2* | PWA |
| | KF97860 | *KfCMDH3* | |
| Mitochondrial NAD-MDH | KF129900 | *KfMMDH1* | MSA |
| | KF133040 | *KfMMDH2* | |
| | KF47385 | *KfMMDH3* | PWA |
| Plastidic NAD-MDH | KF74595 | *KfPdMDH1* | MSA |
| | KF17940 | *KfPdMDH2* | |
| | KF132500 | *KfPdMDH3* | |
| Chloroplast NADP-MDH | KF14750 | *KfNADP-MDH* | |
| Peroxisomal NAD-MDH | KF124800 | *KfPxMDH1* | |
| | KF05650 | *KfPxMDH2* | |

Key: MSA, multiple sequence alignment; PWA, pair-wise alignment.

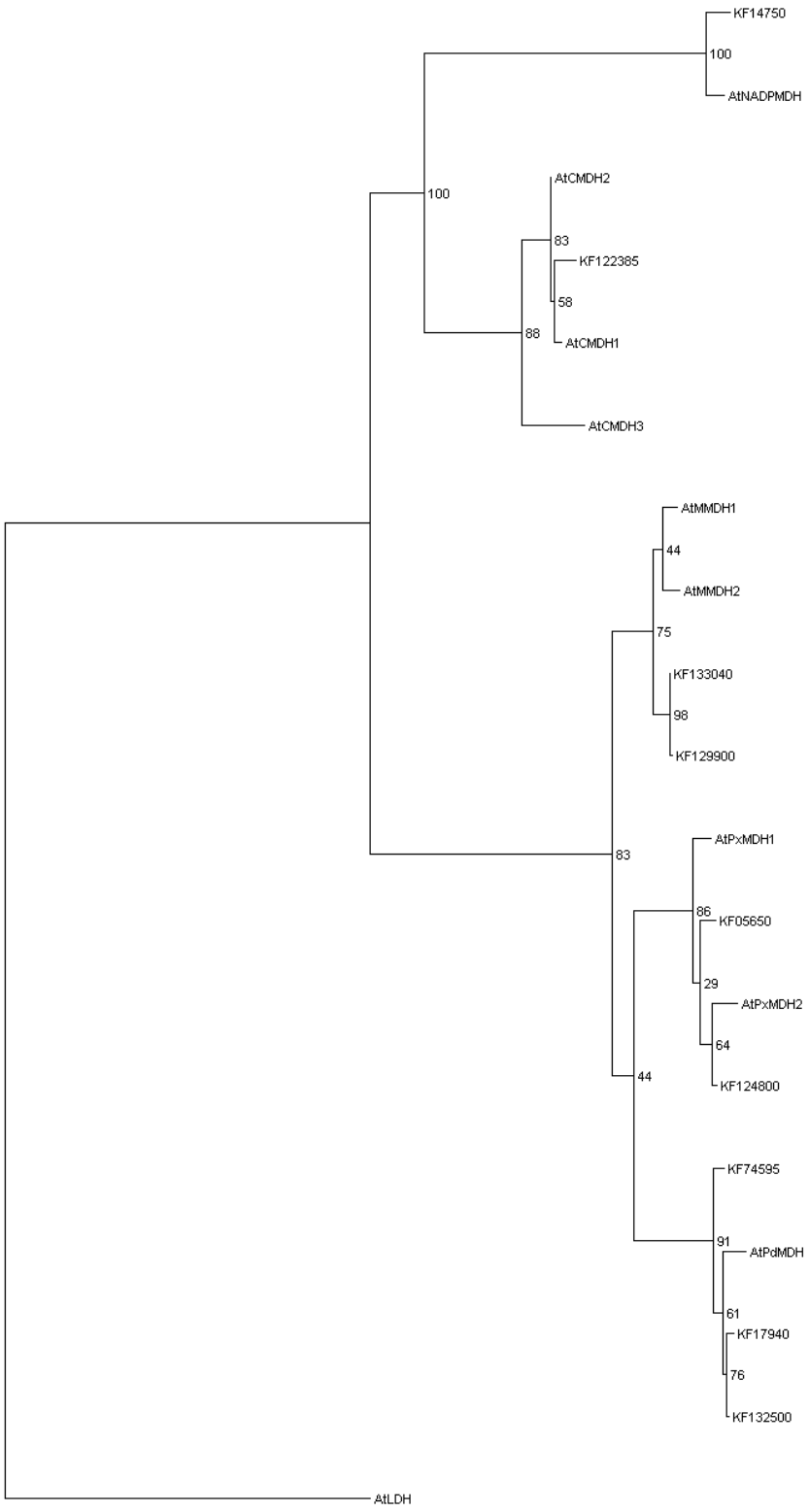


Figure 6.2 – Molecular phylogeny of predicted and functionally-characterised MDH genes. The topology of the phylogenetic tree was calculated using RaxML (Stamatakis, 2006). The results of bootstrap analysis (1000 iterations) are shown at the nodes.

The topology of the resulting phylogenetic tree (Fig. 6.2) was similar to published phylogenies, with *AtNADP-MDH* and *AtCMDH* comprising a distinct clade to *AtPdMDH*, *AtMMDH* and *AtPxMDH* (Schnarrenberger and Martin, 2002; Cavalcanti *et al.*, 2014). Each of the *K. fedtschenkoi* sequences analysed was closely grouped with one compartment- and cofactor-specific *A. thaliana* MDH isogene with high bootstrap support (78-100%), and this allowed each sequence to be provisionally designated as a *CMDH*, *PxMDH*, *NADP-MDH*, *MMDH* or *PdMDH* (Table 6.2). The phylogeny of the *PdMDH – PxMDH – MMDH* clade could not be resolved due to a low bootstrap score at one node (44%). *AtNADP-MDH,* two *AtPxMDH* isogenes and two *AtMMDH1* isogenes each clustered with an equal number of predicted *K. fedtschenkoi* isogenes. Conversely, the single *AtPdMDH* isogene clustered with three predicted *KfPdMDH* isogenes, while three *AtCMDH* isogenes clustered with a single predicted *KfCMDH* (Fig. 6.2).

The three sequences that were excluded from the phylogenetic analysis were analysed by pairwise alignment with the *K. fedtschenkoi* predicted protein database and an *A. thaliana* predicted protein database (TAIR10; http://www.arabidopsis.org) using BLASTP. The alignments with highest sequence identity for KF18985 were KF122385 and *AtCMDH2*, with 93% and 86% identity respectively. The alignments with the highest sequence identity for KF47385 were KF133040 and *AtMMDH1*, with 93% and 85% identity respectively. The alignments with the highest sequence identity for KF97860 were KF122385 and *AtCMDH1*, with 97% and 91% identity respectively. Accordingly, these sequences were assigned to the intracellular compartment of their closest *A. thaliana* BLAST match, as listed in Table 6.2, although this is not to suggest that these predicted peptide sequences are actually expressed as functional MDHs in *K. fedtschenkoi*.

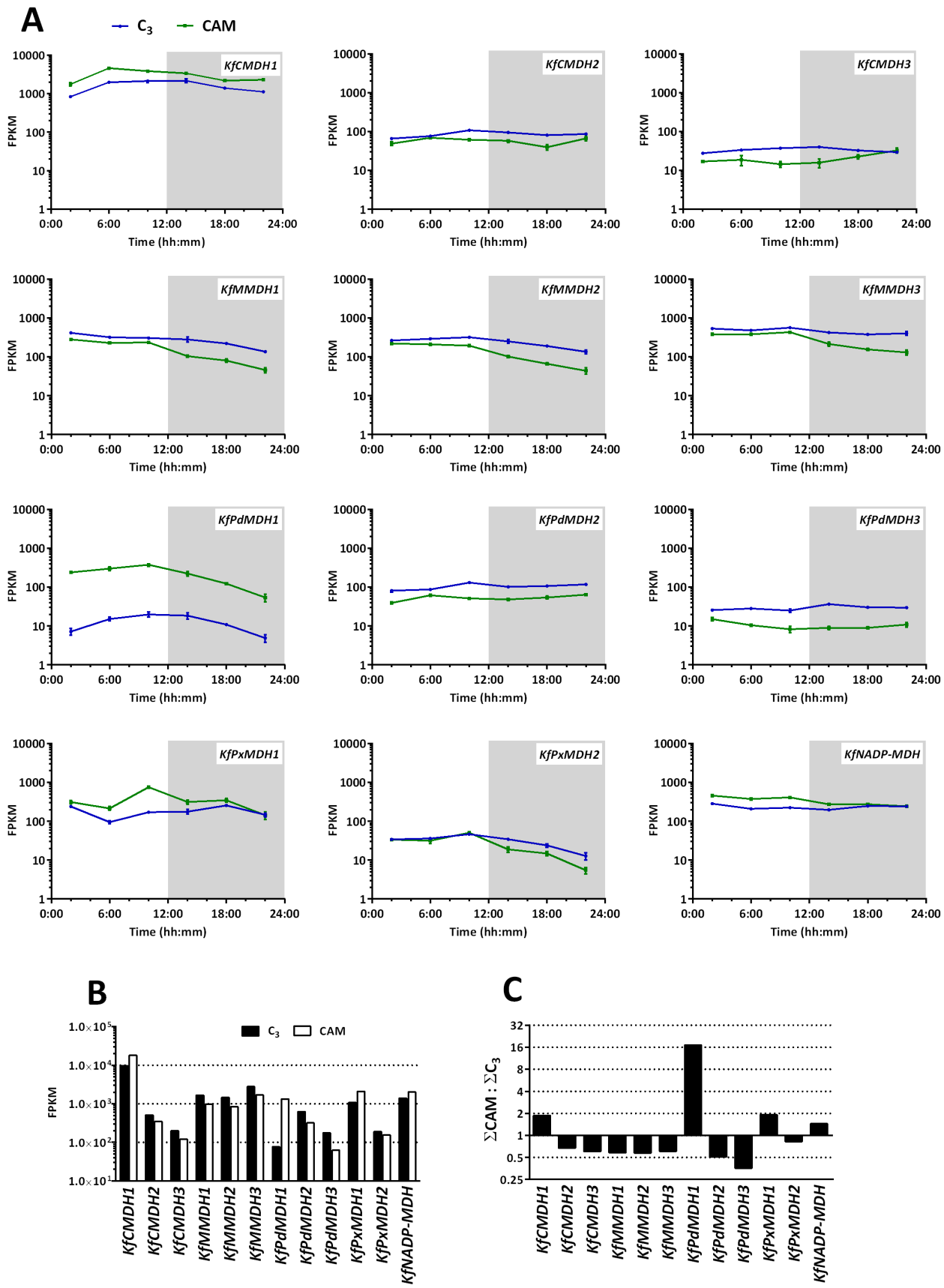
A
C3
CAM
KfCMDH1
KfCMDH2
KfCMDH3
KfMMDH1
KfMMDH2
KfMMDH3
KfPdMDH1
KfPdMDH2
KfPdMDH3
KfPxMDH1
KfPxMDH2
KfNADP-MDH
FPKM
Time (hh:mm)
0:00
6:00
12:00
18:00
24:00
B
C3
CAM
FPKM
C
ΣCAM : ΣC3

SOLiD RNA-seq data showed that the majority of *K. fedtschenkoi* predicted MDH genes were down-regulated at the level of transcript in CAM leaves relative to $C_3$ leaves. *KfNADP-MDH* and one gene each in the *KfCMDH*, *KfPxMDH* and *KfPdMDH* clades were up-regulated (*KfCMDH1*, *KfPxMDH1* and *KfPdMDH1*, respectively). *KfPdMDH1* relative transcript abundance was increased >17-fold following developmental induction of CAM, whereas the other three genes were much less dramatically up-regulated (<2-fold, Fig. 6.3C).

There was a degree of temporal coordination of transcript level in *KfCMDH1*, *KfPxMDH1*, *KfPdMDH1* and *KfNADP-MDH*. Each of the four genes attained their peak transcript level during the light period, and maintained a higher transcript level at 2 h before the end of the light period (10:00) than at any time-point in the dark period (Fig. 6.3A). *KfPxMDH1*, *KfPdMDH1* and *KfCMDH1* were the most abundant transcript in their respective clades. All three orthologous sequences to *AtMMDH1/2* identified were down-regulated at the level of transcript in CAM leaves relative to $C_3$ leaves (Fig. 6.3B).

---

Figure 6.3 – Evidence from quantitative RNA-seq datasets of differential regulation of MDH isogenes between *K. fedtschenkoi* $C_3$ and CAM leaves.
A – Relative transcript abundance of *K. fedtschenkoi* putative MDH genes over a 12:12 LD cycle in $C_3$ (leaf pair 1; blue) and CAM (leaf pair 6; green) tissue. Transcript levels are expressed as the number of RNA-seq fragments aligned to genes per kilobase CDS per million total reads (FPKM). Each point represents the mean ± S.E.M. of 3 independent samples. Grey shading represents the duration of the dark period.
B – Sum of FPKM over 12:12 LD cycle in $C_3$ and CAM leaves.
C – Ratio of total FPKM over 12:12 LD cycle in CAM leaves to $C_3$ leaves.

### 6.2.2 Transgenic RNAi of MDH isogenes in *K. laxiflora*

Isogene-specific transcriptional silencing of *K. laxiflora* orthologs of *KfCMDH1*, *KfPxMDH1*, *KfPdMDH1* and *KfNADP-MDH* was pursued using a transgenic RNAi approach. Hairpin RNAi vector binary constructs were designed to target these genes. The stable transgenic lines that were generated using these constructs will be referred to as *KlCMDH* RNAi, *KlPxMDH* RNAi, *KlPdMDH* RNAi and *KlNADP-MDH* RNAi lines, respectively. *K. laxiflora* was selected as a model species for MDH function in CAM, rather than *K. fedtschenkoi*, because the capacity of the former to set seed may enable crossing of MDH isogene-specific RNAi lines in future studies, allowing more than one isogene to be simultaneously silenced (Hartwell *et al.*, 2016).

Hairpin dsRNA sequences were designed from predicted *K. laxiflora* cDNA sequences of their respective transcripts to target those transcripts for RNAi-mediated silencing (see above, Section 2.2.1). A fragment of the cDNA of each gene was amplified by PCR from a *K. laxiflora* cDNA pool and cloned into the Gateway entry vector pENTR/D. Entry vectors were sequenced, and alignment by BLAST2 of the entry vector with predicted *K. laxiflora* cDNA sequences showed nucleotide identity of 99-100%. The cloned cDNA fragment was subcloned into p7GWIWG2(I) hairpin RNAi binary constructs (Karimi *et al.*, 2002). *K. laxiflora* explants were transformed with the RNAi constructs by *Agrobacterium*-mediated transformation. Stable transgenic lines were regenerated by tissue culture. Regrettably, individual transformation calluses were not tracked or segregated during tissue culture of *KlPxMDH* RNAi, *KlCMDH* RNAi and *KlNADP-MDH* RNAi lines, and therefore it is not possible to state with certainty that different lines have arisen from independent transformation events. This error was corrected during tissue culture of *KlPdMDH* RNAi transformants.

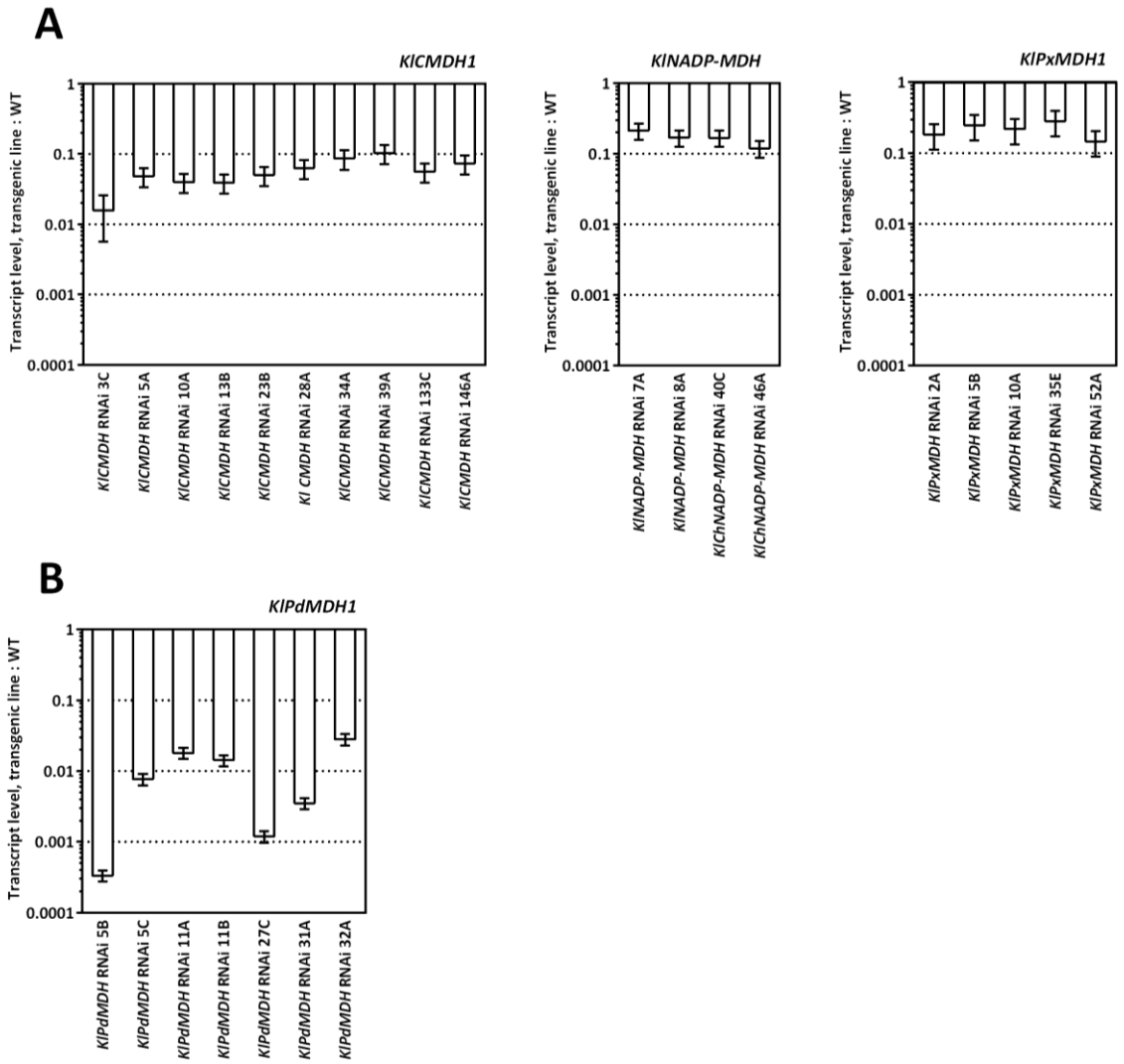


Figure 6.4 - Screening of *MDH* RNAi transgenic lines. Relative transcript level was measured using RT-qPCR of cDNA samples. cDNA was synthesised using total RNA extracts of CAM leaves (leaf pair 6) that had been sampled at 2 h before the end of the light period under 12:12 LD (10:00). Transcript level relative to WT controls was calculated using the $2^{-\Delta\Delta Ct}$ method. A single sample was taken for each of the transgenic lines. Bars represent the mean ± S.E.M. of $2^{-\Delta\Delta Ct}$ values that were calculated from ΔCt of n replicate WT controls.
A – *KlCMDH* RNAi, *KlPxMDH* RNAi and *KlNADP-MDH* RNAi lines (n = 5). *KlUBQ10* was used as the reference gene for calculating $2^{-\Delta\Delta Ct}$.
B – *KlPdMDH* RNAi lines (n = 3). *KlTFP* was used as the reference gene for calculating $2^{-\Delta\Delta Ct}$.

### 6.2.3 Screening *MDH* RNAi lines for target transcript reduction

Stable transgenic RNAi lines were screened for silencing of the targeted MDH genes. In the first screening experiment, a selection of *KlCMDH* RNAi, *KlPxMDH* RNAi and *KlNADP-MDH* RNAi lines were entrained with five WT control plants in 12:12 LD, and CAM leaves (LP6) were sampled at 2 h before the end of the light period (10:00). Relative transcript levels of the targeted genes were determined using RT-qPCR with the $2^{-\Delta\Delta Ct}$ method of calculating transcript level fold change. The same experimental procedure was repeated for a second screen of a selection of *KlPdMDH* RNAi lines with another set of three WT controls.

Silencing of the RNAi-targeted gene was consistently detected in transgenic lines (Fig. 6.4). $2^{-\Delta\Delta Ct}$ calculations suggested that the level of transcript of the targeted gene was reduced by 3.5- to 9-fold in the selected *KlPxMDH* RNAi and *KlNADP-MDH* RNAi lines, and 10- to 60-fold in the selected *KlCMDH* RNAi lines (Fig. 6.4A). Severe suppression of transcript was also found in all of the *KlPdMDH* RNAi lines selected, but with a much broader range of $2^{-\Delta\Delta Ct}$ values (30- to 3000-fold; Fig. 6.4B).

### 6.2.4 Determination of MDH isogene-specific silencing in selected RNAi lines

Two lines each of *KlCMDH* RNAi, *KlPxMDH* RNAi and *KlPdMDH* RNAi that had been screened by RT-qPCR were grown side-by-side with WT controls under greenhouse conditions for 11 weeks. The plants were then entrained to 12:12 LD conditions in a Snijders growth cabinet and LP6 were sampled at 1 h before the end of the light period (11:00) and 1 h before the end of the dark period (23:00). RT-qPCR was used to determine the transcript abundance at 11:00 of *KlPxMDH1*, *KlCMDH1*, *KlPdMDH1* and *KlNADP-MDH* relative to a reference gene (*KfTFP*, Fig. 6.5A). Relative transcript levels of the more abundant *KlMMDH* isogene,

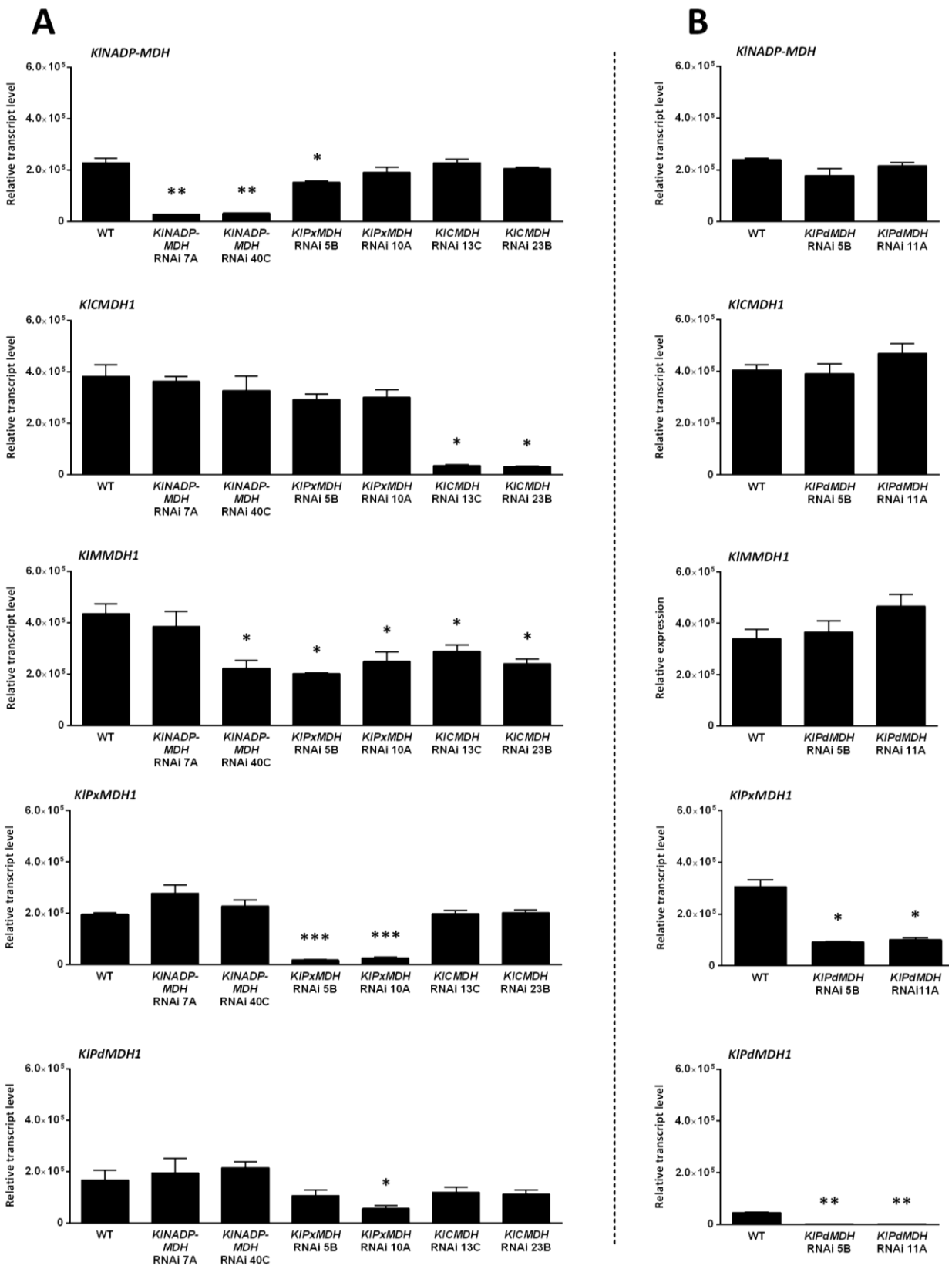
A
B
KlNADP-MDH
KlCMDH1
KlMMDH1
KlPxMDH1
KlPdMDH1
Relative transcript level
Relative expression
6.0×10⁵
4.0×10⁵
2.0×10⁵
0
WT
KlNADP-MDH RNAi 7A
KlNADP-MDH RNAi 40C
KlPxMDH RNAi 5B
KlPxMDH RNAi 10A
KlCMDH RNAi 13C
KlCMDH RNAi 23B
KlPdMDH RNAi 5B
KlPdMDH RNAi 11A
KlPdMDH RNAi11A

*KlMMDH1* (Fig. 6.3B), were also measured, although the primers used are also likely to amplify the *KMMDH2* transcript to some extent (see below, Appendix 2). The same procedure was used to sample a separate cohort of multiple *KlPdMDH* RNAi lines and WT controls that had been grown side-by-side under greenhouse conditions for 13 weeks, and to measure the transcript level of the same set of genes (Fig. 6.5B).

A statistically-significant reduction of mean transcript level of the targeted MDH isogene was found in all of the lines tested, relative to WT (Fig. 6.5). The fold-changes in transcript levels of *KlPxMDH1*, *KlCMDH1* and *KlNADP-MDH* in their corresponding transgenic RNAi lines were in the same ranges as in the screening experiment (Fig. 6.5A c.f. Fig. 6.4A). *KlPdMDH1* transcript was much less severely reduced in *KlPdMDH* RNAi 5A in this experiment (~50-fold) than in the screening experiment (~3000-fold), while it was reduced to approximately the same extent in *KlPdMDH* RNAi 11A (Fig. 6.5B c.f. Fig. 6.4B).

Silencing of MDH isogenes other than the intended target of the hairpin dsRNA construct was found in some lines, although always with a smaller fold-change than the targeted gene. *KlPxMDH1* relative transcript level was reduced by ~3-fold relative to WT in *KlPdMDH* RNAi lines 5B and 11A (Fig. 6.5B). Conversely, *KlPdMDH1* transcript abundance was reduced in both of the *KlPxMDH* RNAi lines tested, although only the difference between line 10A and WT was

---

Figure 6.5 – Relative abundance of MDH isogene transcripts in selected transgenic lines. Relative transcript level was measured by RT-qPCR in CAM leaves (leaf pair 6) that had been sampled at 1 h before the end of the light period under 12:12 LD (11:00), and calculated using *KlTFP* as a reference gene. Bars represent mean ± S.E.M. of 3-4 independent replicate samples. The results of Welch t-tests between mean transcript levels in each line and the WT control are displayed above the bar representing that line: $P > 0.05$, not shown; $P \leq 0.05$, *; $P \leq 0.01$, **; $P \leq 0.001$, ***.
A - *KlCMDH* RNAi, *KlPxMDH* RNAi, and *KlNADP-MDH* RNAi lines; n = 3.
B - *KlPdMDH* RNAi lines; n = 4.

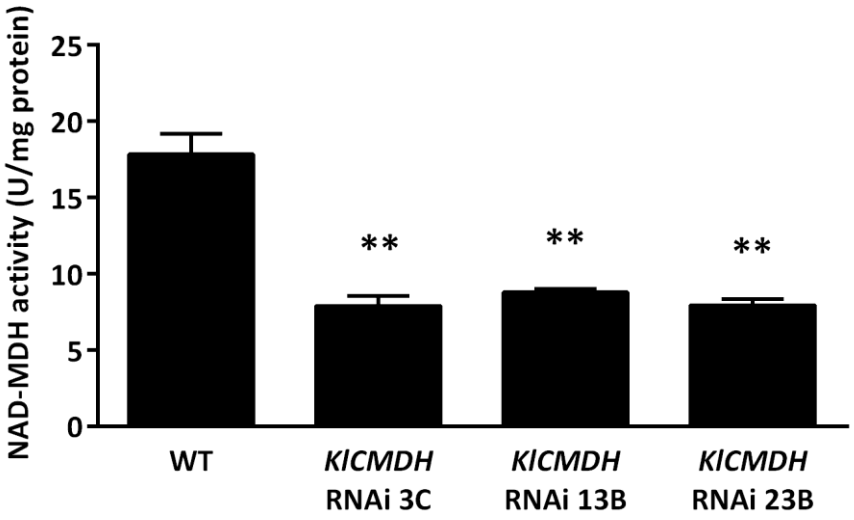


Figure 6.6 – Extractable NAD-MDH activity from CAM leaves (LP6) of *KlCMDH* RNAi lines and WT *K. laxiflora*. LP6 were sampled at 1 h before the end of the light period under 12:12 LD (11:00). Bars represent mean activity ± S.E.M of n independent LP6 samples; n = 3 for *KlCMDH* RNAi 13B; n = 4 for WT, *KlCMDH* RNAi 3C and *KlCMDH* RNAi 23B. The results of Welch t-tests between the mean WT activity and the mean activity of each line are shown above the bar representing that line (**, $P \leq 0.01$).

statistically significant (Fig. 6.5A). *KlNADP-MDH* transcript level was significantly reduced relative to WT in *KlPxMDH* RNAi 5B, but not in *KlPxMDH* RNAi 10A (Fig. 6.5A). *KlMMDH* transcript level was reduced by ~2-fold relative to WT in both *KlCMDH* RNAi lines, both *KlPxMDH* RNAi lines and one *KlNADP-MDH* RNAi line, 40C, but was apparently unaffected in *KlNADP-MDH* RNAi line 7A and both *KlPdMDH* RNAi lines tested (Fig. 6.5A).

### 6.2.5 Suppression of NAD-MDH activity in *KlCMDH* RNAi lines

In order to confirm the effect of *KlCMDH1* silencing on gene expression at the level of enzyme activity, the NAD-MDH activities of protein extracts of *KlCMDH* RNAi lines 3C, 13B and 23B were determined using a spectrophotometric assay of OAA-NADH redox.

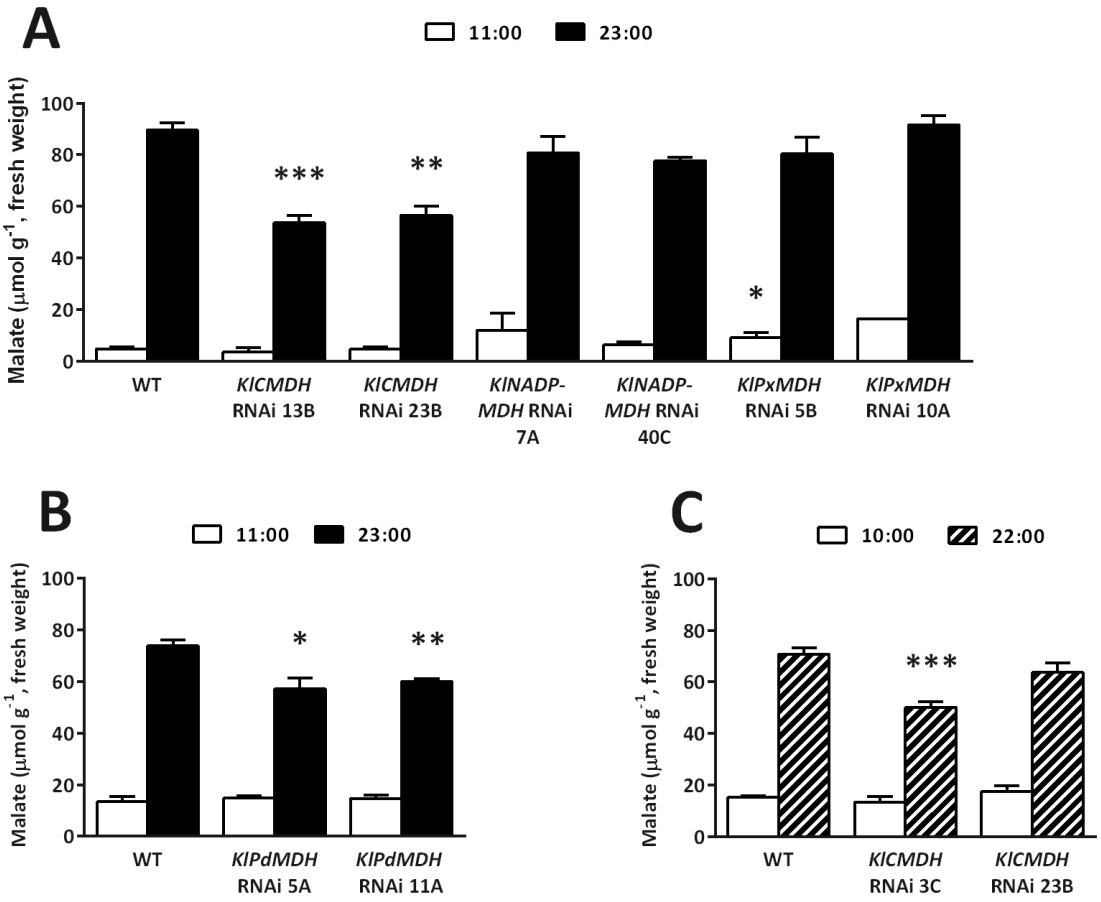


Figure 6.7 – Detection of suppressed diel malate turnover in *MDH* RNAi lines. Malate concentration was measured in soluble metabolite extracts of CAM leaves (LP6) collected over a 12:12 LD cycle at time-points indicated by figure legends. Bars represent mean ± S.E.M of n replicate LP6 samples. The results of Welch t-tests between mean malate concentrations in each line and the WT control at the same time-point are displayed over the bar representing that line/time-point: $P > 0.05$, not shown; $P \leq 0.05$, *; $P \leq 0.01$, **; $P \leq 0.001$, ***.
A: n = 3; except for the 11:00 sample of *KlPxMDH* RNAi 10A, n = 1.
B: n = 4; except for the 11:00 sample of *KlPdMDH* RNAi 5B, n = 3.
C: n = 4

*KlCMDH* RNAi lines and WT controls were entrained under 12:12 LD conditions and LP6 were collected at 4 h intervals from 2:00 to 22:00 over a single 12:12 LD cycle. Leaves sampled at 14:00, 2 h into the dark period, were used to assay NAD-MDH activity. Protein was extracted from frozen, ground tissue by homogenisation in extraction buffer. Mean NAD-MDH

activity in extracts from each of the *KlCMDH* RNAi lines tested was reduced by >50% relative to the WT control (Fig. 6.6).

### 6.2.6 The effects of MDH isoform silencing on diel malate turnover

In order to determine the effect of silencing of each MDH isogene on CAM photosynthesis, malate accumulation during the dark period in selected *MDH* RNAi lines was compared with a WT control. Soluble metabolites were extracted from the LP6 samples that had been collected at 11:00 and 23:00, as described in Section 6.2.4, and malate concentrations were determined by enzyme-linked spectrophotometric assay (Fig. 6.7A, B).

Diel malate turnover was found in all of the genotypes tested. Mean malate concentrations at 1 h before the end of the dark period (23:00) in both *KlCMDH* RNAi 13B and *KlCMDH* RNAi 23B were both significantly reduced by ~40% relative to the WT control. There was no significant difference between malate accumulation by 23:00 in *KlNADP-MDH* RNAi or *KlPxMDH* RNAi lines and WT controls (Fig. 6.7A). Conversely, at 1 h before the end of the light period (11:00), there was a statistically-significant increase in malate concentration relative to WT controls in one line only, *KlPxMDH* RNAi 5B (Fig. 6.7A). There was a small, but statistically significant, decrease (~20%) in mean malate concentration at 23:00 in both of the *KlPdMDH* RNAi lines sampled, relative to WT controls (Fig. 6.7B).

Malate concentration was also determined in *KlCMDH* RNAi 3C and *KlCMDH* RNAi 23B LP6 samples collected at 10:00 and 22:00 as part of the sampling timecourse described in the previous section (Fig. 6.7C). Although the sampling time-points were close to those used in the previous determination of diel malate turnover in this line, there was, by contrast with the previous result (Fig. 6.7A), no significant difference between malate concentration in WT and

*KlCMDH* RNAi 23B at 22:00 (Fig. 6.7C). The difference between the mean malate concentrations in the two genotypes was smaller than in the previous experiment (7.1 ± 1.6 μmol $g^{-1}$, compared with 33.0 ± 1.5 μmol $g^{-1}$ previously), due to both a decrease in the WT mean and an increase in the *KlCMDH* RNAi 23B mean. Conversely, a significantly lower mean malate concentration was found in *KlCMDH* RNAi 3C relative to the WT control at 22:00 (Fig. 6.7C).

### 6.2.7 Diel $CO_2$ gas exchange patterns were similar in detached CAM leaves of *KlCMDH* RNAi lines and WT

In order to determine whether impaired malate accumulation was associated with decreased $CO_2$ uptake during the dark period when *KlCMDH1* was transcriptionally silenced, the rates of $CO_2$ uptake ($J_{CO2}$) by detached CAM leaves (LP6) of *KlCMDH* RNAi lines 3C, 13B and 23B, and WT controls were measured concurrently for 48 h under 12:12 LD using the 12-channel IRGA (Fig. 6.8A). Cuttings of *KlCMDH* RNAi lines and WT were grown for 7 weeks under greenhouse conditions and entrained to 12:12 LD conditions before detachment of LP6 for $CO_2$ gas exchange measurements. WT and *KlCMDH* RNAi lines 13B and 23B were monitored in triplicate, but only a single LP6 from *KlCMDH* RNAi 3C was available for this experiment.

$J_{CO2}$ increased rapidly from the beginning of the dark period, described a single major peak, and declined to 40-60% of the maximum $J_{CO2}$ by the end of the dark period. The time that LP6 took to reach maximum $J_{CO2}$ varied between 4 and 8 h after the beginning of the dark period, but there was no apparent association between genotype and the distribution of $J_{CO2}$ over the dark period (Fig. 6.8A). Phase II and Phase IV patterns of $J_{CO2}$ were inconsistent between replicate LP6 of the same genotype, and between the consecutive light periods in most LP6 specimens (Fig. 6.8A). These inconsistencies have also been found in $CO_2$ gas exchange

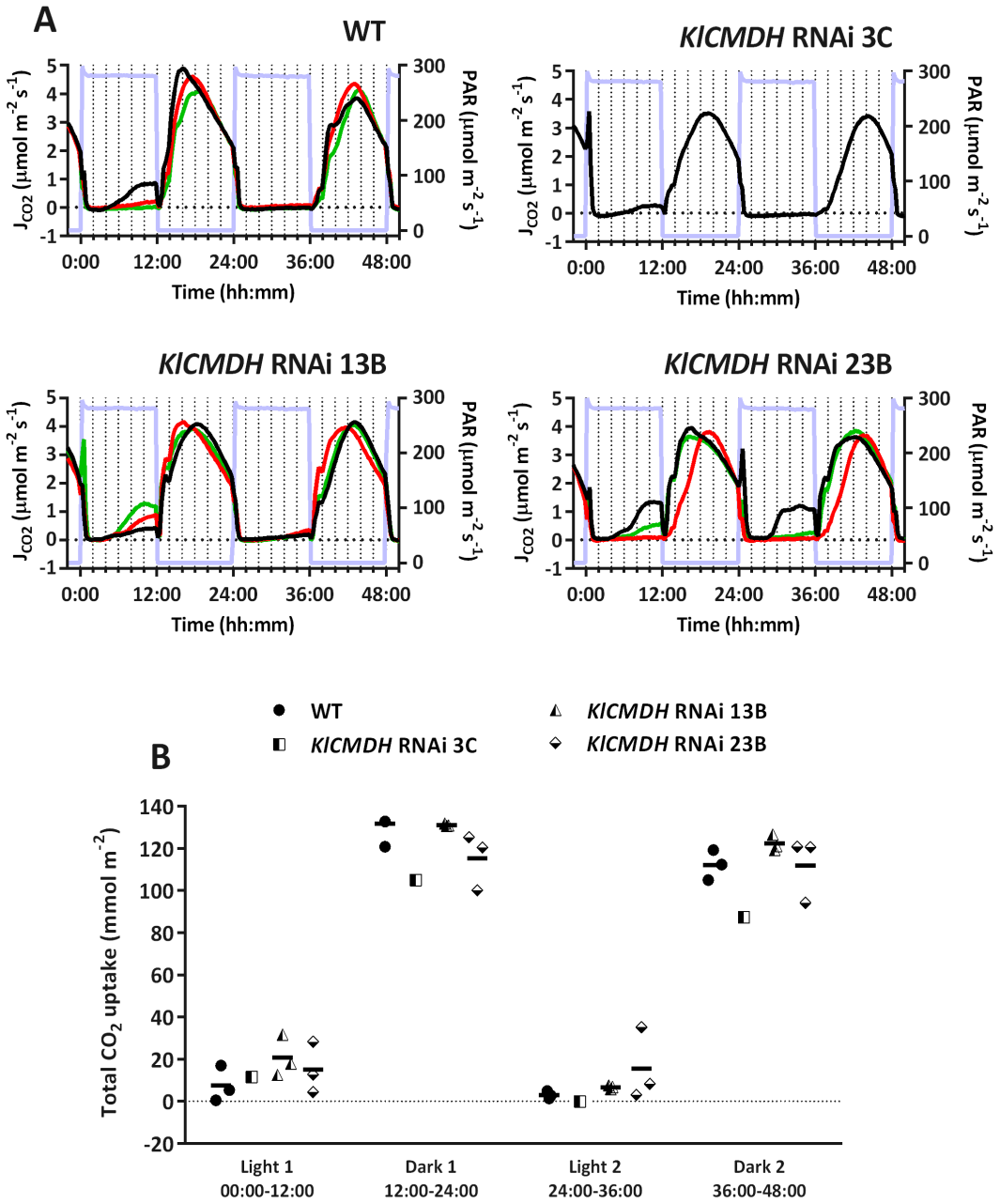


Figure 6.8 – Timecourse of the rate of $CO_2$ gas uptake ($J_{CO2}$) by detached CAM leaves of *KfCMDH* RNAi lines and WT *K. laxiflora* under 12:12 LD.
A – CAM leaf pairs (LP6) were detached from the stem and placed in the IRGA chamber at ~-12:00. Replicate LP6 were taken from three cuttings each of *KlCMDH* RNAi 13B, *KlCMDH* RNAi 23B and WT; a single *KlCMDH* RNAi 3C was measured. Photosynthetically active radiation (PAR) is shown (blue line).
B – Total $CO_2$ uptake over 12 h light/dark periods. Points represent the 12 h total $CO_2$ uptake of a single LP6 sample. Horizontal bars display the mean total $CO_2$ uptake for the genotype.

measurements of *K. fedtschenkoi* (Figs. 4.7 and 4.9) detached leaves, and have been discussed previously in this thesis (Section 4.3.3).

Total $CO_2$ uptake during entire 12 h light/dark periods was estimated by measuring the area between the $J_{CO2}$-time plot and the x-axis (Fig. 6.8B). No significant difference in total $CO_2$ uptake between WT, *KlCMDH* RNAi 13B or *KlCMDH* RNAi 23B was found during either dark period using one-way ANOVA ($P > 0.05$, 2 and 6 D.F.).

## 6.3 Discussion

A set of transgenic lines was generated to individually target four MDH isogenes for RNAi-mediated silencing but functional characterisation of these lines only progressed as far as initial phenotypic screening before the end of this PhD project. *KlPdMDH* RNAi, *KlCMDH* RNAi, *KlPxMDH* RNAi and *KlNADP-MDH* RNAi lines each showed transcriptional silencing of the gene targeted by their respective RNAi constructs (Fig. 6.5). Reduction in total extractable NAD-MDH activity in *KlCMDH* RNAi lines by >2-fold relative to wild type was observed, suggesting that *KlCMDH1* expression was suppressed at the protein level (Fig. 6.6).

Transcript levels of *KfMMDH1*, a gene that was not selected for functional characterisation due to down-regulation of its transcript abundance in *K. fedtschenkoi* CAM leaves relative to $C_3$ leaves, were decreased by ~2-fold in both of the *KlCMDH* RNAi and *KlPxMDH* RNAi lines tested, and in one *KlNADP-MDH* RNAi line only (Fig. 6.5A). The possibility that a decrease in KlMMDH1 activity contributed to the phenotypes of these lines, either independently of, or synergistically with, silencing of the targeted gene, cannot be ruled out at this stage. Similar pleiotropic effects were detected for the independent *KlPdMDH* RNAi lines, which displayed a consistent reduction in transcript levels of *KlPxMDH1* (Fig. 6.5).

The most straightforward explanation for this non-isogene specific silencing is that, in these lines, processing of the transgenic hairpin dsRNA by Dicer-like enzymes (DCLs) produced siRNAs that targeted the RNA-induced silencing complex (RISC) to the transcript of these non-specific isogenes. Silencing by RNAi of transcripts that share as few as seven complimentary nucleotides with the siRNA sequence has been reported (Small, 2007). However, it is also possible that reduced expression of the specific target of the hairpin RNAi construct led to the activation of endogenous regulatory mechanisms that suppressed transcription of additional, non-specific MDH isogenes. In order to discriminate between these possibilities it would be useful to compare these results using an alternative technique that would allow isogene-specific loss-of-function to be conclusively established, e.g. CRISPR-Cas9 (Tang and Tang, 2017). This would also allow any CAM-associated phenotype(s) to be definitely linked to the expression of a specific gene. However, very dissimilar phenotypes have been reported for transcriptional silencing and homozygous knock-out mutations of *MMDH* in $C_3$ species *Solanum lycopersicum* and *A. thaliana*, respectively, which suggests that the two techniques for inducing loss of function in MDH genes do not always produce easily comparable phenotypes (Nunes-Nesi *et al.*, 2005; Tomaz *et al.*, 2010). Moreover, homozygous knock-out mutations in the *A. thaliana PdMDH* ortholog caused embryo lethality (Beeler *et al.*, 2014; Selinski *et al.*, 2014). Therefore, gene knock-out mutagenesis of *K. laxiflora* MDH isogenes would, ideally, be a complementary technique to transgenic RNAi, as the latter allows residual levels of transcript to persist in transgenic lines to support relatively low-flux 'housekeeping' metabolism but has the potential to disrupt the large metabolic fluxes associated with CAM.

*KlCMDH* RNAi and *KlPdMDH* RNAi lines both exhibited a reduction in malate concentration relative to WT controls at 1 h before the end of the dark period, while retaining

malate breakdown during the light period (Fig. 6.7). Decreased malate accumulation in the dark period in these lines is indicative that KlCMDH1 and KlPMDH1 function in CAM. No difference in malate concentration was observed between either *KlNADP-MDH* RNAi or *KlPxMDH* RNAi and WT controls, and therefore no evidence to support a function for *KlNADP-MDH* and *KlPxMDH1* in CAM has been found so far (Fig. 6.7A).

There was inconsistency in the observation of decreased dark-period malate accumulation in *KlCMDH* RNAi lines, as line 23B displayed both significant and non-significant decreases in mean malate concentration, relative to WT, under standard, climate-controlled 12:12 LD conditions at time-points that were only 1 h apart (Fig. 6.7A and C). However, *KlCMDH* RNAi 3C, which displayed a similar reduction in NAD-MDH activity to *KlCMDH* RNAi 23B in enzyme activity assays (Fig. 6.6), was found in the same experiment to have a significantly reduced malate concentration relative to wild type (Fig. 6.7C). The concurrent malate concentration measurement of *KlCMDH* RNAi 23B could be an aberrant result arising from imprecision in metabolite extraction and malate concentration assays, and this difficulty could potentially be resolved by using larger samples of replicates than four plants.

There is also an apparent discrepancy between lower malate concentrations 1-2 h before the end of the dark period in *KlCMDH* RNAi lines and the fact that the dark-period $CO_2$ uptake relative to the WT experimental control was not significantly reduced in *KlCMDH* RNAi lines 13B and 23B (Fig. 6.8B). The simplest explanation for this discrepancy is that the method used to measure this CAM-metabolic variable (12-channel IRGA) was insufficiently precise to resolve the relatively small reduction in dark-period $CO_2$ assimilation implied by the reduction of malate accumulation during the dark period. This could be resolved by measuring a larger sample of *KfCMDH* RNAi and WT *K. laxiflora* CAM leaves.

The aforementioned silencing of *KlPxMDH1* transcript in the two independent *KlPdMDH* RNAi lines studied raises the possibility that loss of PxMDH activity is implicated in their lower malate accumulation, but given that *KlPxMDH* RNAi lines, which had a more drastic reduction in *KlPxMDH1* transcript, accumulated malate at similar concentrations to the WT control during the dark period (Fig. 6.7A), this appears unlikely. However, phenotypic characterisation of mutants with highly selective suppression of *KlPdMDH1* transcript abundance would be needed to determine whether or not the CAM-related phenotype was caused by a synergistic effect of decreased KlPdMDH1 and KlPxMDH1 activity.

Loss of PdMDH function in *KlPdMDH* RNAi lines also needs to be established by chloroplast isolation and comparison of extracted NAD-MDH activity with a WT control. The plastidic pathway of CAM OAA reduction (Fig. 6.1) proposed by Neuhaus and Schulte (1996) would explain the decreased malate accumulation in *KlPdMDH* RNAi lines (Fig. 6.7B). If it were possible to replicate the exchange of exogenous OAA for malate and 3PG that was observed in isolated chloroplasts of CAM-induced *M. crystallinum* undergoing starch breakdown (Neuhaus and Schulte, 1996) using WT *K. laxiflora* chloroplasts, the same phenomenon should be suppressed in chloroplasts of *KlPdMDH* RNAi lines.

The ratio of *KfPdMDH1* transcript level in CAM leaves to $C_3$ leaves of *K. fedtschenkoi* (17.2) is comparable to those of key CAM genes such as *KfPPC1_CAM* (18.8) and *KfPPCK1* (32.9) (J. Hartwell *et al.*, unpublished results). Dramatic up-regulation of *KfPdMDH1* coinciding with developmental induction of CAM is consistent with its recruitment to the nocturnal malate accumulation pathway. PdMDH was found to comprise a small proportion of total NAD-MDH activity in leaves of *S. oleracea* (Backhausen *et al.*, 1998). Assuming that this is typical of $C_3$ photosynthesis, it is possible that developmental transcriptional up-regulation of *PdMDH1* only

allows the activity of this enzyme to approach a significant proportion of CMDH1 activity, transcript of which is much more abundant in both $C_3$ and CAM leaves (Fig. 6.3B), rather than to function as the principal CAM MDH in *Kalanchoë*.

It appears likely that reduction of OAA is simultaneously catalysed by KlCMDH1 and KlPdMDH1 during Phase I in *K. laxiflora*. Redundancy may exist between the two MDHs to a degree, so that chloroplast-compartmentalised NADH-generating glycolytic flux and OAA reduction in WT *K. laxiflora* was re-distributed to the cytosol in *KlPdMDH* RNAi lines, with the reverse having occurred in *KlCMDH* RNAi lines. This hypothesis could be tested using crosses of *KlPdMDH* RNAi and *KlCMDH* RNAi lines to generate *K. laxiflora* with silencing of both *KlPdMDH1* and *KlCMDH1* (i.e. *KlPdMDH KlCMDH* RNAi lines). Redundancy would be demonstrated if the decrease in nocturnal malate accumulation caused by the combined RNAi-mediated silencing of *KlPdMDH1* and *KlCMDH1* together were greater than the combined effects of silencing them individually, or:

$$\Delta\text{mal}(\textit{KlPdMDH KlCMDH}\ \text{RNAi}) < \Delta\text{mal}(\text{WT}) - [\Delta\text{mal}(\text{WT}) - \Delta\text{mal}(\textit{KlPdMDH}\ \text{RNAi})] - [\Delta\text{mal}(\text{WT}) - \Delta\text{mal}(\textit{KlCMDH}\ \text{RNAi})]$$

where Δmal(genotype) is the quantity of malate accumulated during the dark period in a given genotype.

## 6.4 Summary

The results presented in this chapter point towards a role for isoforms of both PdMDH and CMDH in catalysing the conversion of OAA to malate downstream of nocturnal $CO_2$ fixation in CAM. Far more comprehensive phenotypic characterisation of *KlPMDH1* and *KlCMDH1* loss-of-function mutants is needed to confirm that suppression of transcript relates to loss of NAD-MDH activity in a specific compartment and associated impairment of CAM photosynthesis. The *KlPxMDH* RNAi and *KlNADP-MDH* RNAi lines generated and characterised in a preliminary fashion here were not found to have a CAM-impaired phenotype, as would be predicted based upon the subcellular localisation of the former and the post-translational regulation of the latter (see above, Section 6.1.2). However, loss of function of their targeted genes must also be established at the level of subcellular NAD-MDH activity before they can be completely ruled out as CAM OAA reductases. Transgenic *Kalanchoë* with loss-of-function in multiple MDH genes, particularly *KlPdMDH1* in combination with *KlCMDH1*, should be generated in order to establish a comprehensive set of CAM MDHs, as the ability of metabolic fluxes to shift dynamically between compartments may prevent severe impairment of CAM from loss-of-function of single MDH isoforms.

## Chapter 7 - General discussion

### 7.1 Functional genomics of CAM

The study of CAM molecular genetics has been given a new imperative in recent years by the prospect of CAM engineering in $C_3$ agricultural or biomass crops in order to enhance their drought resistance (Borland *et al.*, 2014; Yang *et al.*, 2015). As part of this process, minimal sets of genes encoding enzymes and transporters required to mediate the nocturnal and diurnal CAM pathways (Fig. 1.1) in leaf mesophyll cells of $C_3$ host species, referred to as the "nocturnal carboxylation module" and "diurnal decarboxylation module" respectively, are to be delineated from the whole genomes of model CAM species. Coding sequences of these genes, interspersed with regulatory sequences that program gene expression with the correct phase and amplitude to drive the large diel metabolite fluxes of CAM, are then to be introduced transgenically into target $C_3$ host species, in addition to modules designed to program reversed-phase stomatal control (stomatal opening at night and stomatal closure during the day) and development of leaf succulence (Borland *et al.*, 2014; Yang *et al.*, 2015).

Genomics and transcriptomics of the model CAM species *K. laxiflora* and *K. fedtschenkoi* have identified candidate enzyme and membrane transporter genes for inclusion in the nocturnal carboxylation module or the diurnal decarboxylation module. Systematic evaluation of the CAM-related function of this set of genes is in progress. Individual genes have been targeted for RNAi-mediated transcriptional silencing in transgenic *K. fedtschenkoi* or *K. laxiflora* so that the phenotypic effect of their loss-of-function on CAM can be determined (Dever *et al.*, 2015; Yang *et al.*, 2015; Hartwell *et al.*, 2016).

The results presented in Chapters 3 and 4 support the inclusion of one or more vacuolar ALMTs in the nocturnal carboxylation module. *KfALMT* RNAi lines expressed a hairpin dsRNA

transgene that targeted the transcript of two predicted vacuolar *KfALMT*s for RNAi-mediated silencing (Figs. 3.2 and 3.5), and steady-state transcript abundance of the more abundant of these genes, *KfALMT1*, was severely reduced in three independent *KfALMT* RNAi lines (Fig 4.1). In these three lines, two key indices of CAM, nocturnal $CO_2$ uptake and nocturnal malate accumulation, were reduced relative to WT controls (Figs. 4.8 and 4.13). Decreased $H^+$ transport activity by isolated tonoplast vesicles of two independent *KfALMT* RNAi lines, relative to WT controls (Fig. 4.6), corroborated a long-standing model for CAM vacuolar malate import, by which import of $H^+$ and malate is mediated by the simultaneous activity of $H^+$ active transporters and a passive anion channel, such as an ALMT, and is coupled through the trans-tonoplast $H^+$ electrochemical gradient (Fig. 3.1; Smith et al., 1996; Hafke et al., 2003; Holtum et al., 2005).

Integration of a vacuolar ALMT into a multi-gene nocturnal carboxylation module, and optimisation of the four proposed functional gene modules to engineer CAM photosynthesis in a $C_3$ host species will likely involve multiple cycles of transformant evaluation and vector re-design (Yang *et al.*, 2015). A simpler proof-of-concept demonstration of the utility of a vacuolar ALMT as a nocturnal malate importer for CAM engineering could be furnished by generating transgenic *KfALMT1* overexpressor lines in a $C_3$ model species and screening for increased accumulation of malate during the day. Increased activity of another candidate nocturnal carboxylation module enzyme, CMDH, has already been shown to increase leaf malate accumulation in transgenic *N. tabacum* (Wang *et al.*, 2010). By contrast, enhancement of leaf malate accumulation by overexpression of *PPC* in transgenic *Solanum tuberosum* depended on the usage of a modified gene encoding an enzyme with low sensitivity to malate inhibition (i.e. high PPC-malate $K_i$), whereas equivalent overexpression of a form of PPC with relatively low $K_i$ did not cause a significant increase in leaf malate concentrations (Rademacher *et al.*, 2002).

Therefore, feedback inhibition of PPC by malate appeared to limit malate accumulation in *S. tuberosum PPC* overexpressors (Rademacher *et al.*, 2002). If dual overexpression of a low-$K_i$ *PPC* and *KfALMT1* could be shown to enhance diurnal malate accumulation, relative to overexpression of *PPC* alone, in *S. tuberosum*, this would show that a CAM-related vacuolar ALMT can mediate vacuolar malate import in a transgenic $C_3$ species, and thus maintain PPC in a relatively uninhibited state.

Further research is also needed to determine whether vacuolar ALMTs are constitutively active in CAM leaves, or whether they are down-regulated during the day to prevent futile re-import of malate as it is exported from vacuoles for breakdown by the CAM decarboxylases. Given that *KfALMT1* steady-state transcript levels peaked in the light period (Figs. 3.3 and 4.1), transcriptional control of the activity of CAM-related ALMTs appears unlikely in *K. fedtschenkoi*. Post-translational regulation of vacuolar ALMTs may, instead, exert control over CAM-related vacuolar malate import. Patch-clamping of vacuolar ALMTs of $C_3$ species in a *Xenopus* oocyte heterologous expression system has proven to be a useful method for characterising their regulation by protein kinases (Ligaba *et al.*, 2009; Imes *et al.*, 2013), and could be applied to CAM-related vacuolar ALMTs.

Chapter 6 describes preliminary attempts to define which of the plant MDH isoforms are necessary for nocturnal malate synthesis in *K. laxiflora*, and thus which MDH genes would be candidates for inclusion in the nocturnal carboxylation module. Hairpin dsRNA constructs were designed to individually target each of four *K. laxiflora* MDH isogenes - *KlCMDH1*, *KlPdMDH1*, *KlPxMDH1* and *KlNADP-MDH* - for RNAi-mediated silencing. WT *K. laxiflora* were transformed with these constructs using *Agrobacterium*. Quantification of steady-state transcript abundance of MDH isogenes in *KlCMDH* RNAi, *KlPxMDH* RNAi, *KlPdMDH* RNAi

and *KlNADP-MDH* RNAi lines showed more-or-less specific silencing of the intended MDH isogene (Fig. 6.5). No suppression of diel malate turnover, relative to WT controls, was found in *KlPxMDH* RNAi or *KlNADP-MDH* RNAi lines (Fig. 6.7). On this basis, *KlPxMDH1* and *KlNADP-MDH* can be excluded from the nocturnal carboxylation module, although loss of function of these genes at the level of enzyme activity in their respective RNAi lines would need to be confirmed for this determination to be made with confidence. Mild suppression of CAM, as measured by diel malate turnover, was found in *KlCMDH* RNAi and *KlPdMDH* RNAi lines (Fig. 6.7), suggesting that both CMDH1 and PdMDH1 act as nocturnal OAA reductases for CAM in *Kalanchoë*. The fact that these lines retained much of their capacity for CAM (Figs. 6.7 and 6.8) suggests that a parsimonious nocturnal carboxylation module could exclude one of them. However, it is possible that CMDHs and PdMDHs act synergistically in mediating flux in the nocturnal CAM pathway (see above, Section 6.3), and this should be tested using double *CMDH1 PdMDH1* loss-of-function mutants in *Kalanchoë*, which could be generated through performing genetic crosses between the two strongest RNAi lines recovered in this work for *CMDH1* and *PdMDH1*.

## 7.2 The ongoing search for a CAM vacuolar malate exporter

Preliminary characterisation of a single *KfTDT* RNAi line did not eliminate the possibility that KfTDT is the CAM vacuolar malate exporter, which has been sought to explain rapid and sustained co-transport of malate and $H^+$ from the vacuolar lumen to the cytosol during the day (Hafke *et al.*, 2001; Holtum *et al.*, 2005; Borland *et al.*, 2009). However, no evidence was found that KfTDT performs this function, and KfTDT was proposed to be a vacuolar citrate exporter instead (see above, Section 3.3.3). Further phenotypic characterisation of two or more

independent *KfTDT* RNAi lines and functional characterisation of the substrate-specificity of KfTDT-mediated membrane transport are required to confirm that TDT does not play any role in the diurnal CAM pathway (Fig. 1.1B). If this can be confirmed, an ongoing search for a CAM vacuolar malate exporter may require new leads.

Current techniques in proteomics may offer an alternative approach to identification of a CAM vacuolar malate exporter, or, possibly, an alternative model of diurnal vacuolar malate export. Tonoplast proteomics of $C_3$ species including *A. thaliana* and *Brassica oleracea* has been performed by variations on a basic protocol: subcellular fractionation of membranes, SDS-PAGE of the tonoplast protein fraction, protease digestion of gel bands, and mass spectroscopy to determine the molecular identity of proteins (Trentmann and Haferkamp, 2013). Comparative proteomics of tonoplasts of *M. crystallinum* in its constitutive $C_3$ and inducible CAM states has already been used to determine the extent of up-regulation of expression of V-ATPase subunits in the latter state (Cosentino *et al.*, 2013).

Re-investigation of past insights into CAM tonoplast function using current proteomic techniques could prove useful in characterising the CAM system of diurnal malate export. For instance, decreased tonoplast fluidity as an adaptive response to high growth temperatures has been reported in *K. daigremontiana*, with underlying changes in tonoplast lipid and protein composition (Kliemchen *et al.*, 1993; Behzadipour *et al.*, 1998). Unadapted control plants broke down malate rapidly during the light period at the higher temperature, reaching baseline CAM leaf malate concentration prematurely with respect to the pattern of malate breakdown under the control temperature. By contrast, high temperature-adapted plants broke down malate more gradually and retained higher concentrations of malate at the end of the light period under both conditions (Kliemchen *et al.*, 1993). These results were adduced in support of a model of diel

CAM regulation in which export of malate$^{2-}$ and $H^+$ from the vacuole proceeds by diffusion of undissociated malic acid ($H_2$mal) through the tonoplast lipid bilayer. In this model, rising temperature at dawn would initiate malate breakdown by making the tonoplast more fluid and permeable to diffusion of $H_2$mal from the vacuolar lumen to the cytosol, where or whence it is decarboxylated (Lüttge and Smith, 1984; Kluge *et al.*, 1991*b*; Kliemchen *et al.*, 1993). Decreased basal tonoplast fluidity in high temperature-adapted plants would thus suppress vacuolar malate export relative to control plants by decreasing the permeability of its lipid bilayer to diffusion of $H_2$mal (Kliemchen *et al.*, 1993; Behzadipour *et al.*, 1998).

Empirical evidence has been found that the rate of vacuolar malate efflux is positively correlated with temperature (Friemert *et al.*, 1988). However, a more recent assessment of diurnal vacuolar malate export has held that unmediated trans-tonoplast diffusion would be insufficient to account for observed rates of diurnal malate breakdown in CAM species, and that at least one tonoplast integral membrane protein transporter would be required (Holtum *et al.*, 2005). If vacuolar malate export were, nonetheless, down-regulated in high temperature-adapted *Kalanchoë*, then this could be exploited to identify a vacuolar malate exporter if its peptide abundance were reduced relative to tonoplasts of control plants. Conversely, Behzadipour *et al.* (1998) identified a 35 kDa peptide, using SDS-PAGE, that was up-regulated in tonoplasts of high temperature-adapted *K. daigremontiana* and could be a negative regulator of vacuolar malate efflux.

Molecular identification of the putative CAM vacuolar malate exporter would significantly broaden the scope of the study of CAM regulation. Comparison of two independent *KfALMT* RNAi lines with WT showed that different levels of *in vitro* $H^+$ transport activity correlated with quantities of dark-period $CO_2$ uptake and malate accumulation (Figs. 4.6, 4.7 and

4.13), and that vacuolar ALMT activity was likely to exert control on the rate of flux in the Phase I CAM pathway (see above, Section 4.3.2). Likewise, generation of a set of transgenic lines with different transcript levels of a vacuolar malate exporter gene, due to incomplete hairpin dsRNA transgene-targeted, RNAi-mediated silencing, and/or from a full-length ORF overexpression construct, could determine the level of control that this transporter exerts over the rate of diurnal malate breakdown. Isolation of protoplasts from *K. daigremontiana* CAM leaves and non-invasive measurement of pH has been used to estimate cytosolic malate concentration during the day, and found it to have increased by 11 mM between dawn and the middle of the day (Hafke *et al.*, 2001). The fact that this figure was below the bulk cell sap concentration (>100 mM; Hafke *et al.*, 2001) suggests that malate concentration does not equalise between the vacuolar lumen and cytosol during Phase III, and that the rate of vacuolar malate efflux continues to exert control over flux through the diurnal CAM pathway (Fig. 1.1B) when the latter is at its maximum rate.

Furthermore, heterologous expression of the putative CAM vacuolar exporter, e.g. in *Xenopus* oocytes, in combination with site-directed mutagenesis could identify any post-translational modifications that may control its activity *in vivo*. Pajor and Sun (1999) used this approach to characterise post-translational regulation by phosphorylation of NaDC-1, the mammalian TDT ortholog. Although phosphorylation of NaDC-1 was catalysed by endogenous *Xenopus* kinases and modulated by incubation of oocytes with kinase small-molecule inhibitors and activators in this study (Pajor and Sun, 1999), interactions between the putative vacuolar malate exporter and specific plant regulatory proteins could be determined by their co-expression in the *Xenopus* oocytes. This approach has been used to demonstrate a regulatory interaction between *A. thaliana* ALMT12/QUAC1 and the kinase Open Stomata 1 (OST1), through which the latter probably activates the former by phosphorylating it (Imes *et al.*, 2013)

However, if molecular identification of the CAM vacuolar malate exporter proves to be a 'roadblock' on the 'roadmap' to CAM engineering (Yang *et al.*, 2015), the *A. thaliana* TDT ortholog (AtTDT) could potentially be adopted as a vacuolar malate exporter for engineered CAM. AtTDT is a tonoplast-localised membrane-bound transporter with selectivity for malate over citrate (Emmerlich *et al.*, 2003; Hurth *et al.*, 2005). Although some ambiguity remains over its transport mechanism (see above, Section 3.1.2), it may be possible to show that AtTDT has the capacity to mediate $H^+$-malate symport from the vacuolar lumen to the cytosol by generating transgenic *Kalanchoë* in which a copy of *AtTDT* is positioned downstream of a constitutive promoter. If AtTDT possessed the desired $2H^+$: malate symport activity, and were constitutively active when over-expressed, this would be expected to cause futile cycling between the vacuolar lumen and the cytosol during the night, and reduce malate accumulation. An analogous result was obtained when the $H^+$-sucrose symporter *AtSUC4* was overexpressed in *A. thaliana*, resulting in decreased accumulation of sucrose in aerial tissues (Schneider *et al.*, 2012). If AtTDT proved to be suitable candidate for the diurnal vacuolar malate exporter in engineered CAM, cis-regulatory sequences would then need to be selected to code for its phased expression during the day in the $C_3$ host species. Genetic modification of its sensitivity to endogenous protein degradation pathways might also be required to prevent residual expression of *AtTDT* during the night, which could prevent malate and $H^+$ from being trapped in the vacuole during Phase I (DePaoli *et al.*, 2014).

## 7.3 Prospects for characterisation of bi-directional signalling between the core circadian clock and CAM

Evidence of core circadian clock entrainment by CAM in *K. fedtschenkoi* was garnered from the phenotypes of *KfALMT* RNAi lines (Chapter 5). Differential entrainment of the free-running rhythms of transcript level of *KfTOC1-2* and *KfCCA1* was observed between *KfALMT* RNAi line 23A and the WT control (Fig. 5.4). Entrainment of the free-running rhythm of PPC phosphorylation and the underlying transcript abundance of *KfPPCK1* was also perturbed in *KfALMT* RNAi 23A (Figs. 5.4 and 5.7), and this is consistent with the transcriptional control of *KfPPCK1* by the core circadian clock. In addition, differences between the period of the CAM-related free-running rhythm of $CO_2$ gas exchange were observed between the WT control and two severely CAM-suppressed *KfALMT* RNAi lines, 12A and 23A (Fig. 5.2, cf. Fig. 4.7).

As discussed in Section 5.1.3, disruption of the free-running rhythms of $CO_2$ gas exchange and *KfPPCK1* transcript abundance have been reported in *K. fedtschenkoi* transgenic lines that over-expressed *McTOC1* (Hartwell, 2006; Dall'omo, 2011). These lines replicated the arrhythmic core circadian clock phenotype of *A. thaliana TOC1* overexpressing lines (Makino *et al.*, 2002; Más *et al.*, 2003*a*), suggesting that the core circadian clock regulates CAM in *Kalanchoë* (Hartwell, 2006; Dall'omo, 2011). In future research, phenotyping of a more comprehensive set of *Kalanchoë* core circadian clock mutants could define a subset of genetic components of the diel CAM cycle that are subject to control by the core circadian clock. For example, the core circadian clock has been shown to regulate carbohydrate metabolism in *A. thaliana* by controlling both the rate of nocturnal starch breakdown and diurnal partitioning of fixed C (Graf *et al.*, 2010; Kölling *et al.*, 2015). Carbohydrate metabolism is an important aspect of CAM (Borland *et al.*, 2016). Determining the extent to which circadian control of

carbohydrate metabolism is conserved between the $C_3$ model species *A. thaliana* and CAM model species in *Kalanchoë* could provide insights into the latter. Other elements of CAM are insensitive to certain environmental or metabolic signals during certain periods of the diel cycle, and therefore may be subject to circadian control. Examples include light-insensitivity of malate accumulation in *Kalanchoë* species during the subjective night (Winter, 1980; Kluge *et al.*, 1981; Ritz and Kluge, 1987), and $CO_2$ partial pressure-insensitivity of *K. daigremontiana* stomatal aperture during Phase III (von Caemmerer and Griffiths, 2009). Phenotyping of arrhythmic core circadian clock mutants to determine whether these phenomena are absent or present could be used to confirm or exclude, respectively, underlying control by the core clock.

Furthermore, *Kalanchoë* core circadian clock mutants could be used to identify specific elements of the core clock as originators of signals to CAM, or effectors of feedback signalling from CAM to the core clock. Haydon *et al.* (2013) showed that entrainment of the phase of the *AtCCA1* free-running rhythm by exogenous sucrose was lost in an *A. thaliana prr7* knock-out line, and that sucrose entrainment was therefore dependent on *AtPRR7*. *AtPRR7* was proposed to be an essential component in a signalling pathway that entrains the core circadian clock in response to activation of $C_3$ photosynthesis and accumulation of sucrose following dawn (Haydon *et al.*, 2013).

Specific components of the core circadian clock could be designated as mediators of entrainment by CAM if loss-of-function mutations of their genes were epistatic to loss-of-function of CAM-related genes. For instance, assume that a transgenic *K. fedtschenkoi* line in which *KfPRR7* were silenced or knocked out has the same core circadian clock phenotype as the *prr7* mutant of Arabidopsis; i.e. no change to the period of the *KfCCA1* free-running rhythm under LL conditions (Nakamichi *et al.*, 2005). If transgenic *K. fedtschenkoi* lines in which both

*KfALMT* and *KfPRR7* were knocked out or silenced were found to have the same core circadian clock phenotype as the *KfPRR7* loss-of-function line, this would show that feed-back signalling between CAM and the core clock is dependent on the latter gene. Conversely, if the double loss-of-function line had a core circadian clock phase delay relative to the *KfPRR7* loss-of-function line that was similar to the apparent phase delay of the free-running rhythms of transcript abundance of core clock genes in *KfALMT* RNAi 23A, relative to WT (Fig. 5.4), this would show that *KfPRR7* was not necessary for CAM entrainment of the core clock.

## Appendix 1 - Standard curves to determine amplification efficiencies of primers used in RT-qPCR

Standard curves show the cycle number ($C_t$) required for fluorescence to exceed an arbitrary threshold (10 x the standard deviation of baseline fluorescence) plotted against the base-10 logarithm of the relative transcript concentration ($\log_{10}(Q)$), based on the rate of dilution of a stock cDNA pool.

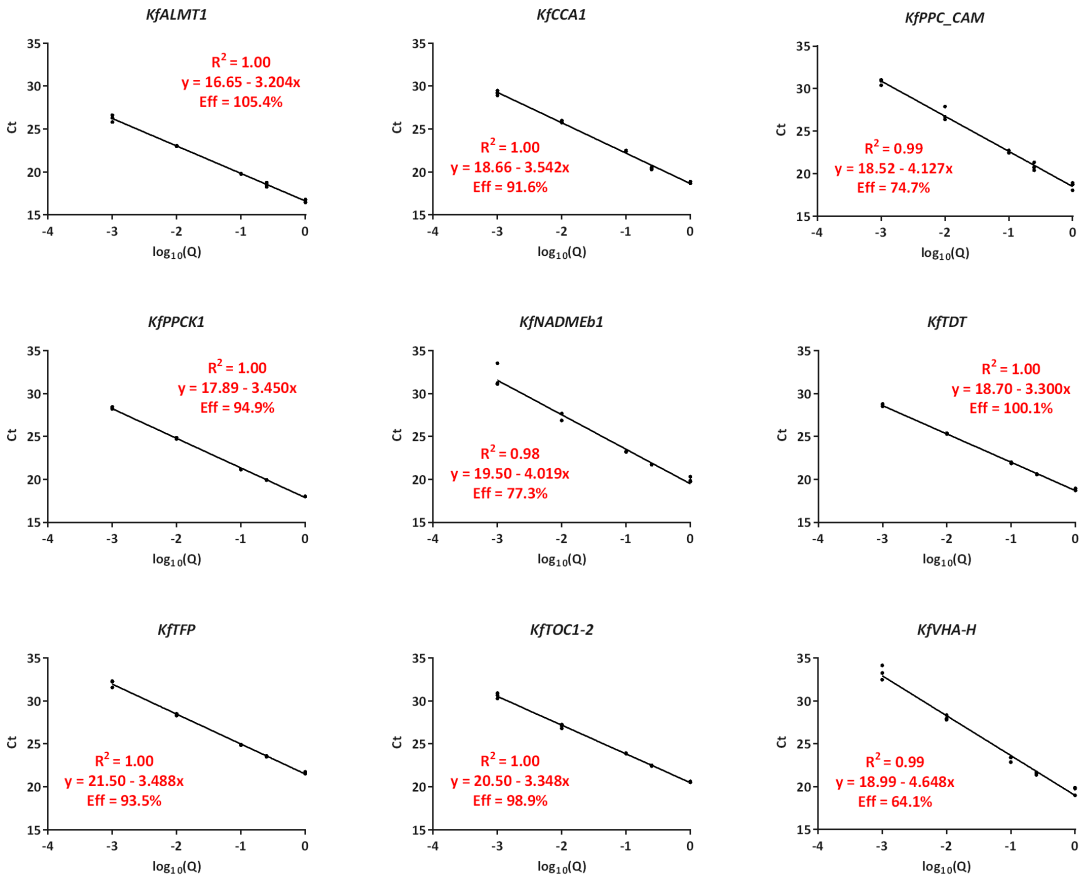

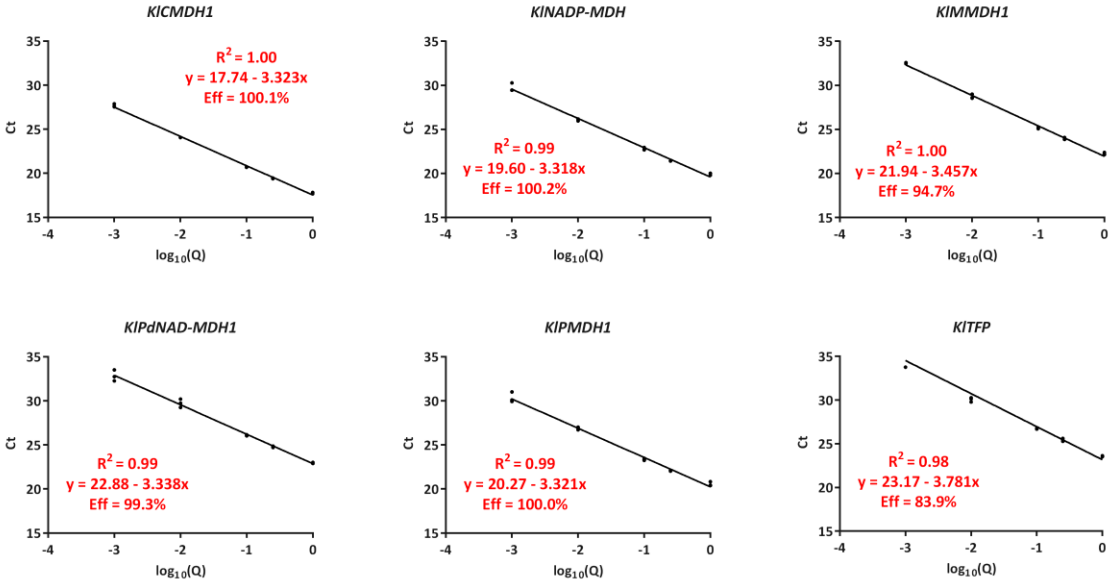
KlCMDH1
R2 = 1.00
y = 17.74 - 3.323x
Eff = 100.1%
KlNADP-MDH
R2 = 0.99
y = 19.60 - 3.318x
Eff = 100.2%
KlMMDH1
R2 = 1.00
y = 21.94 - 3.457x
Eff = 94.7%
KlPdNAD-MDH1
R2 = 0.99
y = 22.88 - 3.338x
Eff = 99.3%
KlPMDH1
R2 = 0.99
y = 20.27 - 3.321x
Eff = 100.0%
KlTFP
R2 = 0.98
y = 23.17 - 3.781x
Eff = 83.9%
Ct
log10(Q)

**Appendix 2 - Validation of the gene specificity of the primers used in RT-qPCR**

cDNA sequences were retrieved from the annotated *K. fedtschenkoi* (http://www.cgr.liv.ac.uk/gview/kalanchoe) and *K. laxiflora* (https://phytozome.jgi.doe.gov) genomes. For each gene of interest, the cDNA sequence of its predicted transcript was aligned with those of its homologs using Clustal Omega. Sections of the alignment containing the targeted RT-qPCR amplicon have been included below. Possible primer binding sites were identified using BLASTN with low-selectivity parameters. The low-complexity filter was disabled, and the minimum 'word' size and mismatch penalty were set at their lowest and highest possible values, i.e.:

```
blastall.exe -p blastn -i [cDNA sequence] -j [primer sequence] -
                              W 4 -F F
```

cDNA-primer nucleotide matches are highlighted in black and mismatches in red. Methionine start and stop codons are indicated by blue and green lettering, respectively. Pink lettering demarcates sequences that were excluded from predicted transcript sequences, but were retrieved from genomic sequences.

***KfALMT1***

| Gene Abbreviation | *K. fedtschenkoi* genome annotation (v. 1.1, Phytozome) | *K. fedtschenkoi* draft genome annotation |
|---|---|---|
| - | Kaladp0024s0194.1 | KF112315 |
| *KfALMT1* | Kaladp0073s0021.1 | KF122600 |
| - | Kaladp0091s0013.1 | KF116735 |
| - | Kaladp0048s0850.1 | KF85525 |
| - | Kaladp0062s0038.1 | KF111435 |

```
KfALMT1           CTTACCAGGAGCTCAGCGAGGTTGCCAAATTCAAGGAGCCCGTAGCTGAAATGCCCGAAC 1780
Kaladp0024s0194.1 CCTACCAGGAGCTCAGTGAGGTTGCCAAATTCAAGGAACCCGTTGCCGCCCGACCAGAGC 2092
Kaladp0091s0013.1 AGGTTGAGGAATTGGGAAGCTGTGGGAGGTTTAAGGAGTACACTGCATGTGATGAAGTGG 1601
Kaladp0048s0850.1 CATTTGAAGAGTTAAGTATAAAAGCTGCATTTAAGGACCCAGCGCAGCATTCGGCAGAAG 1843
Kaladp0062s0038.1 CGTACCAGGAGCTCTGCACGGTAGCCGGCTTCAAAGAGCCTGCGGCGGAGCCTGCAGCGG 1920
                        * **  *  *       *     ** ** **                  *

KfALMT1           TGCCTAAAGACAA---------------GGAACCCTCAGGCCTCTGTTGCGGACTTCTT- 1824
Kaladp0024s0194.1 AGCCAACAGATAA---------------GGAACCCACAGGCCTTTGCTGCGGATTACTG- 2136
Kaladp0091s0013.1 TTGTGAATTGTGAGCAAAACAAAATGGAGAGGGCACTGGGAAATCATCAAGGCTCCAATG 1661
Kaladp0048s0850.1 CTGAAGCGA--CA---------------GGGTGCTGGAGCAGGTTAAAAAGGTCTCTGA- 1885
Kaladp0062s0038.1 ACTCTAAAGGTCC---------------GGCTGCTGTTTGAACTGGCCTGGTTCTGTTCA 1965
                                             *    *              *

KfALMT1           AGGCTCCTGCACTTGAGTAACTAAGAGACGCCTGTTTGC-CCTTCATCGTGTCCGCATGA 1883
Kaladp0024s0194.1 AGGCTCCTGCACTTGACTAACTGAAACACCCTATTTGAT--CTTCATCTTCTCTACAAAC 2194
Kaladp0091s0013.1 GGGCTGAGTAGATTGAGATATT-TCCAACACAATGTGAATTTTT---------TAGTGAC 1711
Kaladp0048s0850.1 ---AAGTTTGGAGTTAGATTATGGACGACACCAGTTTCATATCTTATAATCTATCCGAAA 1942
Kaladp0062s0038.1 AGACAGTTGCGATCATCTATGTGAATGTTGCCAGGGTGACTGAGCAACTGCAATTCATCG 2025
                                  *        *
```

***KfCCA1***

| Gene Abbreviation | GenBank | *K. fedtschenkoi* genome locus |
|---|---|---|
| *KfCCA1-1* | KM078717.1 | KF02345 |
| *KfCCA1-2* | KM078718.1 | KF106970 |

```
KfCCA1-1  ATGGAAGACAGTTGTTTTATATGGTCTTTGTCCTAGAAGATTTGAAGTGGCAGCAGGTTG   765
KfCCA1-2  ATGGAAGAGGGTTGTTTTATATGCTGTTTATCCAAGAGGATTTGAAACGGCGGGAGGTTC   1366
          ********  ************* * *** *** *** ********  *** * *****

KfCCA1-1  TGCGAGTTGAGTTatgGATATGTGTTCATCTGGGGAGGAGATGGTTATCAAGCCAAGAAA   825
KfCCA1-2  AGCGATTTGAGTTatgGATCTGTGTTCATCTGGGGAAGAGCTGGTTATCAAGTCAAGAAA   1426
           **** ************* *************** *** *********** *******

KfCCA1-1  ACCTTATACAATATCCAAACAGAGGGAGAGGTGGACTGAGGAGGAGCATGGTAGATTTCT   885
KfCCA1-2  ACCTTATACAATTTCCAAACAGAGAGAGAGGTGGACAGAGGAGGAACATGGTAGATTTCT   1486
          ************ *********** *********** ******** **************
```

***KfTOC1-2***

| Gene Abbreviation | GenBank | *K. fedtschenkoi* genome locus |
|---|---|---|
| *KfTOC1-1* | KM078716.1 | KF107670 |
| *KfTOC1-2* | KM078726.1 | KF72690 |

```
KfTOC1-1  ACAATTCGTGTCGCCCTAAGGAGATCTCCACCGCTGTCGTCGTCGCCGTCGCCGTCTCCG  162
KfTOC1-2  GACTCGCCTGTCACACTTTGGCT---GCTCCGGCTTTCAAACTCACGGATTGTGTCTGAA  417
               * **** * **  **      *  * *** **    ** * *     ****

KfTOC1-1  TCA----ACAACCCTTGACTCCGACATCGCC------------------------CGACG  194
KfTOC1-2  TCAGGTATTGAGTTTTATCTTAGAGGATGCTCAGGTCTTGATTTGTGGGGATTGGCCGCG  477
          ***       *   **  **  **    **                         *  **

KfTOC1-1  ATCCG-------ACTCACCTGCAGCTCTCTCCGCTTAATATAAGTGAAAGGAGGAATTGA  247
KfTOC1-2  TTGCGATTGTGGTGTTATGAGGAGTTATTTCGGATCTGTTTTGTAGAGATGGCAGCGTTA  537
           * **         * *   * ** * * ** * *   * *    ** * *      * *

KfTOC1-1  AATTGAGGAGTTATGGAAAGTGAGATGAAGGTGAATAAAGCTGGTTCAAGCAGATATGGT  307
KfTOC1-2  TAGTGGTGAGTCGT-----CGGTGATGGCGAGGAACGAGTTTGCCGGATTGGGGAGGGAT  592
           * **  ****  *       * ****  *  ***  *   **    *    *    * *
```

***KfPPC_CAM***

| Gene Abbreviation | GenBank | *K. fedtschenkoi* genome annotation (v. 1.1, Phytozome) | *K. fedtschenkoi* draft genome annotation |
|---|---|---|---|
| *KfPPC_CAM* | KM078709.1 | Kaladp0095s0055.1 | KF133030 |
| - | - | Kaladp0062s0055.1 | KF41615 |
| - | - | Kaladp0048s0578.1 | KF95865 |
| - | - | Kaladp0011s1355.1 | KF136880 |
| - | - | Kaladp0011s0355.1 | KF150550 |

```
KfPPC_CAM          TGCTGCTGGCCTGCAGAACACTGGTTAAACACAGCAGCTCCTTCCTCGCCCGCCCTCCCT 2982
Kaladp0062s0055.1 TGCGGCTGGCATGAGGAACACAGGCTGACAGATTTCCGCGTTCTAACTGTCGCCCATCCA 3472
Kaladp0048s0578.1 TGCAGCCGGCATGCAGAACACCGGTTAAACTCCGTCAAGTACTTAATTTACTTGGCAAAT 3069
Kaladp0011s0355.1 TGCTGCCGGCATGCAGAACACAGGCTGAACTCCTCCTACTGTTTTTATTTACTTCTGTAT 3191
Kaladp0011s1355.1 CGCCGCCGGGCTTCAGAACACCGGCTAAGCTCAGCTCCTCGGTCGCCTGGTTCGCAGATT 3335
                   ** ** **  *   ****** ** * *

KfPPC_CAM          ---------------------------------------------CCCTGCACTTCCCCCA 2998
Kaladp0062s0055.1 TCTGCGACAAGTATATCTAGCTGTTTACCCATTCCATACTTAGTGTTTTAGGTTCAGAAT 3532
Kaladp0048s0578.1 ---------------------------------------------AATGCAGTCACCGTGT 3085
Kaladp0011s0355.1 ---------------------------------------------T-------GACCGCGT 3200
Kaladp0011s1355.1 ---------------------------------------------GCATATCGCCAAGGTC 3351

KfPPC_CAM          GCAATTTCCTCCGCATA-------ATAAAGCATCCCTTTTTT--------CTGAGTGTCG 3043
Kaladp0062s0055.1 CATCTGAAATGATTCTAGGCGCTGTTCAGCTACCATTCATGCTTGAAGGGCTCTTGTTAG 3592
Kaladp0048s0578.1 AATATAT--TTCCGCCCCCGCCCTTTGCTTCCGAACATTAAG------CTCTCA------ 3131
Kaladp0011s0355.1 AATACGT--TTAAGCTGTCAGTTTTTAATCTATGTTTCTCAC------GTCGCATCCTAG 3252
Kaladp0011s1355.1 AA-ATTTTGTCAACCTTGTGACTGATGATGCACCCTAACTAT------CTCTATGTATTG 3404
                            *               *                    *
```

***KfPPCK1***

| Gene abbreviation | GenBank | *K. fedtschenkoi* genome annotation (v. 1.1, Phytozome) | *K. fedtschenkoi* draft genome annotation |
|---|---|---|---|
| KfPPCK1 | AF162662.1 | Kaladp0037s0517.1 | KF135105 |
| - | - | Kaladp0082s0192.1 | KF31450 |
| - | - | Kaladp0050s0014.1 | KF41300 |
| - | KM078720.1 | Kaladp0604s0001.1 | KF107975 |

```
KfPPCK1           TTCCCATTTCGAGCTTTTAGGAACGTCTCGGCTGGGGCCAAGGATTTGCTTAGGAGAATG  828
Kaladp0050s0014.1 TTTCCGACCAGGGTTTTCAGAGGGGTGTCGCCTGCGGCCAAGGATCTGCTGAGGAAGATG  780
Kaladp0082s0192.1 TTTCCTACTCGGCTTTTTCACTCTGTGTCACCTGGGGCCAAGGATCTGCTGAGGAAGATG  750
Kaladp0604s0001.1 TTTCCTACCCGGTCTTTTCACTCCGTGTCGCCGGCCGCTAAGGATCTGCTGAGGAAGATG  751
                  ** **     *   ***       ** **  * *  ** ****** **** ****  ***

KfPPCK1           CTCTGCAGAGATGTGTCCAGGAGATTTTCTGCAGAACAAGTCTTAAGGCATTCATGGATC  888
Kaladp0050s0014.1 TTGTGCAGGGATGTTTCCAGAAGATTCTCAGCAGAACAAGTCTTGAGACATCCATGGATT  840
Kaladp0082s0192.1 TTGTGTAAAGACGTTTCCAGAAGACTCTCTGCTGAGCAAGTACTGAGACATCCATGGATG  810
Kaladp0604s0001.1 CTGTGTAAAGACGTTTCCAGAAGACTCTCCGCTGACCAAGTTCTGAGACATCCATGGATG  811
                   * ** *  ** ** ***** *** * ** ** ** *****  * ** *** *******

KfPPCK1           CTCAGCGCAGGAGACGACACTAATTTCTGATCCCATCACCCAATCCAGCAAGAAACTTG-  947
Kaladp0050s0014.1 GTGAATGGGGGTGTGAGAGAGGATTCACGCTAGATTGTCTCAGGCGTGTTTCAGAGAAGA  900
Kaladp0082s0192.1 ATGAGTGGAGGAGACTTGAGAGATGACTAAATACTCTTGGA-AGG--ACCAGAGCAGAGT  867
Kaladp0604s0001.1 ATGAGTGGAGGAGAGTTGAGACCAATGACGAAGTAAATAGTGGAG--GAATGACCACAGT  869
                   * *  *  ** *                                        *     *
```

***KfNAD_MEb1***

| Gene abbreviation | GenBank | *K. fedtschenkoi* genome annotation (v. 1.1, Phytozome) | *K. fedtschenkoi* genome annotation |
|---|---|---|---|
| *KfNAD_MEb1* | KM078712.1 | Kaladp0472s0027.1 | KF109035 |
| - | - | Kaladp0037s0467.1 | KF37390 |
| - | - | Kaladp0033s0124.1 | KF99860 |
| - | - | Kaladp0015s0134.1 | KF133175 |
| - | - | Kaladp0063s0037.1 | KF107260 |

```
KfNAD_MEb1          CTGTGTATCATCCTCTGGTGCATGAAAAATAGAACCAACCCCCTTCCTCAGCCTGCTGTG 1925
Kaladp0037s0467.1   CTGAATACCCTACACTGGTTTATAAGAAAGATTAACTCCATCCATCAACAACTCAACTCA 2094
Kaladp0033s0124.1   CCGAATACCCTACGCTGGTTTACAAGGAGGATTAACGGCCATCAGTCAACAACTAG---T 2066
Kaladp0015s0134.1   CTATTTACAGTCCTGTCGTTCATGAAAAGTGAAGGCTTCCAACGCACAAAAAAAAGAAGA 2189
Kaladp0063s0037.1   CTGTGTATCATCCTCTTGTGCATGAAAAGTAGAACCACCTTCCCCGGGCCTGCT---ATG 1909
                    *    **   * *  * **  *  *  *       *  *   *

KfNAD_MEb1          TAATTGAATCTTTTGATTTGTTTGA-------GGGAGGAGG---ATCTCTTCACCAAGCA 1975
Kaladp0037s0467.1   TAATCTATCATCTACCATAATACCTAGTGTAATGAAGTGTCTCCTTGCTATCAAACAACA 2154
Kaladp0033s0124.1   CCATCTTTCATGTACCATAAATCTTAGTATATTGAAGTGAGCTGTTGGATATCAACAGCA 2126
Kaladp0015s0134.1   AAAAAGCATGTTTAGAGTTTGTACC-------TCATAAAAT----GCAGAACAAAGGAAA 2238
Kaladp0063s0037.1   TAAATTGTATCTTTTC--------T-------TGATGGATC---TCCTCACCAACAATTA 1951
                      *         *                                          *

KfNAD_MEb1          CACCTCAAAAGGAACAAATATTATTCAAGGAACAAACTTGGAAACCCTCCCTGCTTTTGC 2035
Kaladp0037s0467.1   GGCCTGCTTCAG---CACT--TATCCA--ATTTGCACTTTGCAGCGATGGTTGCCCTGTC 2207
Kaladp0033s0124.1   GGCCTGCTTCTTCAGCACA--TATCCG--ATCCCCGCTGCG-----ACCGTTATCTAGTA 2177
Kaladp0015s0134.1   CTCCTGGTTGGAGCAAACATCTATGTC------ATTCTTAGCAAACCACA-----TTGTA 2287
Kaladp0063s0037.1   GAGCTCAAAAAAGGTGAAGAATATATAAGGCACAAACATGCCCACCTGGCTGATTTCCTC 2011
                       **           *    ***           *

KfNAD_MEb1          CTGATTA----------------------AAAGCACACTTCACTTGGTATTCCCCAAAAT 2073
Kaladp0037s0467.1   TGCATAAAT-TACCACTGCTTCCTTAGCTTTACATAAATTTTTGTTGTAATGTGTAACAT 2266
Kaladp0033s0124.1   GAACTCACCTCACTGTTCGCTCTGCATTTAAAAAAAAAGTTTTGTTGTAATGTGTAACGT 2237
Kaladp0015s0134.1   CTGATGC----------------------AAGTCCCAATAACCATTACAATCAATAAAAT 2325
Kaladp0063s0037.1   CC------------------------------------------------------------ 2013
```

***KfVHA-H***

| Gene abbreviation | *K. fedtschenkoi* genome annotation (v. 1.1, Phytozome) | *K. fedtschenkoi* genome annotation |
|---|---|---|
| *KfVHA-H* | KF107970 | Kaladp0032s0079.1 |
| - | KF27345 | Kaladp0058s0368.1 |

```
KfVHA-H           ATCCAGAGGCTTTTCCTCGGAGCCAAGTATGCAAGTTTCTTGCAGGCGTAAAGCCGCTAT 1320
Kaladp0058s0368.1 ATCCAGAGGCTGTTCCTCGGAGCCAAGTATGCCAGTTTCCTGCAAGTTtaaATCAGCAAC 1030
                  *********** ****************** ****** **** *  **** * ** *

KfVHA-H           CGAGCTGCACCCCTCGGCGAAAGGCTTT----GCCGAGAGTTTGTGAAGGTGTATGTAAT 1376
Kaladp0058s0368.1 TTAAAAAGCAAATGAGTATGAAGAGAATAAGTGTAAGAAGGTTATGGGGGAGTCTGGCAG 1090
                    *           *    ***    *    *     ** ** **  ** ** **  *
```

***KfTDT***

| **Gene abbreviation** | ***K. fedtschenkoi* genome annotation (v. 1.1, Phytozome)** | ***K. fedtschenkoi* draft genome annotation** |
|---|---|---|
| *KfTDT* | Kaladp0042s0251.1 | KF148075 |

```
KfTDT      TTGCTGGAACGGCTGCATTGTCACTTCTCATGCCCACACTCGGCGTTTATGTATTCGGGA  1660

KfTDT      CAAACGGGCCAGCTATATGATTGGACGAAGTCTCAAGATGAAGATGGGGTGGCCATGCAT  1720
```

***KlMMDH***

| Gene abbreviation | *K. laxiflora* transcript number |
|---|---|
| *KlMMDH1.1* | Kalax.0092s0056.1 |
| *KlMMDH1.2* | Kalax.0610s0029.1 |
| *KlMMDH2.1* | Kalax.0018s0053.1 |
| *KlMMDH2.2* | Kalax.0021s0058.1 |

```
KlMMDH1.1       TCAATTTCGCCAACCAGAGCTAATTGGATGCGTTTGCCA----------AACATGATGGA  1093
KlMMDH1.2       TCAATTTCGCCAACCAGAGCTAATTGGACGCGAATGCCA----------AACATGATGGA  1109
KlMMDH2.1       TCAATTTCGCCAACCAGAGCTAATTGGATGCTCATGCCATAATATGCCAAACATGATGAA  1140
KlMMDH2.2       TCAATTTCGCCAACCAGAGCTAATTGGATGCTCATGCCATAATATGCCAAACATGATGAA  1133
                ***************************** **   *****          ********* *

KlMMDH1.1       TTCTTCTCCTTTCTCACTGAACTACATAAATTTTTGAACTCTGCACTCCGTGCGTGGCTT  1153
KlMMDH1.2       TTCTTCTCCTTTCTCACTTAACTATATAAATTTTTGAACTCTGCACTCTGTGCATGGCTT  1169
KlMMDH2.1       TTCTTCTCCTTTCTCAATGAACTACCAAAATTTTTTGAACTATGCATAAGGC--GATAGA  1198
KlMMDH2.2       TTCTTCTCCTTTCTCAATGAACTACCAAAATTTTTTGAACTATGCGTAAGGC--GATAGA  1191
                **************** * *****   ********  *        *  *

KlMMDH1.1       TATATTTCCCAAGGTTTCTTGAGACAGAAAAGGGCATCTAGATGAGGTCCATTAGTTTGT  1213
KlMMDH1.2       TATATTTCCCAAGGTTTCTTGAGACAGATAAGGGCATCTGGATGAGGTCCATTAGTTTGT  1229
KlMMDH2.1       AACAAGTCACGAGGTTTATCGAGACCGGAAAGGACCTCTAGATGAGGTCCTTGAGCTTGC  1258
KlMMDH2.2       AACAAGTCACGAGGTTTATCGAGACCGGAAAGGACCTCTAGATGAGGTCCTTGAGCTTGC  1251
                 * *  ** * ****** * ***** *  **** * *** ********** * ** ***

KlMMDH1.1       TGATGAGTTGTTTACTTGTCTGCCCG-AAATTTCATTCGACCAATAAGTGGAATTCACTC  1272
KlMMDH1.2       TGATGAGTTGTTTACTTGTCTGCACCGAAGTTTCATTCGACTAATAAGTGGAATTCACTC  1289
KlMMDH2.1       TGATTAGTTTGTTACTTGCCTG-ACTAAGTTTCCTTTAGCT-AATAAGTTGGATTCACCC  1316
KlMMDH2.2       TGATTAGTTTGTTACTTGCCTGCACTAAGTTTCCTTTAGCT-AATAAGTTGGATTCACCC  1310
                **** ****  ******* ***  *  *  ** * ** *   ******* * ****** *
```

***KlPxMDH1***

| Gene abbreviation | *K. laxiflora* transcript number |
|---|---|
| *KlPxMDH1.1* | Kalax.0405s0018.1 |
| *KlPxMDH1.2* | Kalax.0061s0014.1 |
| *KlPxMDH2.1* | Kalax.0035s0134.1 |
| *KlPxMDH2.2* | Kalax.0377s0059.1 |

```
KlPxMDH1.1       TCCTTCATCAGGAAGTAAGACAGCGGAGGAGAAG----CTAACCG-TACTGTATGAATCT  1251
KlPxMDH1.2       TCCTTCATCAGGAAGTAAGACGGCGGAGGAGAAGCTAGCTAACCG-TACTGTATGAATCT  1180
KlPxMDH2.1       GCCTTCGTCAGGAAATGAAAAGGCCAACGCCGCGGGGCTAAGGGCGAACTCTAGACATGT  1252
KlPxMDH2.2       GCCTTCGTCAGGAAATGAAAAGGCCAACGCCGCGGGGCTACGGCCGAACTCTAGACATGT  1250
                  ***** ******* * * *  **  * *    *            *** **   ** *

KlPxMDH1.1       ACAAGTTCCA----AA-----TTCAGGTCCGGAAGGGAAGTTGTTGCTTATGTAAATTTG  1302
KlPxMDH1.2       ACAAGTTTGA----AA-----TTCAGGTCCGGAAGGGAAGTTGTTGCTTATGTAAATTTG  1231
KlPxMDH2.1       TTCTGCATCGGGTAATAATACCTCTTTTCCGGAAACTAAAAG----ATAATAGGGTT---  1305
KlPxMDH2.2       TTCTGCATCGGGTAATAATCCCTCTTTTCCGGAAACTAAAAG----ATAATAGGGTT---  1303
                     *         *       **   *******   **        * **     *

KlPxMDH1.1       CGCCACAAGATTCTGCATAAACACTGTCT------CCAACTCTTGTACTGGTTGTATGTC  1356
KlPxMDH1.2       GGCCACAAGATTCTGCATAAACACTGTCT------CCAACTCTTAAAAAAAAATTTATATT  1285
KlPxMDH2.1       ---GTATCGACTCTCAAACAAAACTCACTTTGCTTTCAATTAGGGACATGCA-CATGATC  1361
KlPxMDH2.2       ---GTATCGACTCCCAAACAAAACTCACTTTGCTTTCAATTAGGGACATGCA-CATGATC  1359
                        ** **   *  ** ***  **       **  *                 *
```

***KlPdMDH1***

| Gene abbreviation | *K. laxiflora* transcript number |
|---|---|
| *KlPdMDH1.1* | Kalax.0520s0005.1 |
| *KlPdMDH1.2* | Kalax.0326s0011.1 |
| *KlPdMDH2.1* | Kalax.1025s0012.1 |
| *KlPdMDH2.2* | Kalax.0017s0107.1 |
| *KlPdMDH3.1* | Kalax.0085s0063.1 |
| *KlPdMDH3.2* | Kalax.0047s0017.1 |

```
KlPdMDH1.1  CGTCCA---------CCACCAGTTGCAGAGATCGCAGTCGCTCAGAGTTCAAGATGTTGG  112
KlPdMDH1.2  CGTCCA---------CCACCAGTTGCAGAGATCGCAGTCGCTCAGAGTTCAAGATGTTGG  84
KlPdMDH2.1  TTTCATCTCAC-------TTTCCATTCATTTGCGCGAGCATTTTCTGTTCATGATGGCTG  142
KlPdMDH2.2  TTTCATCGCGC-------TTTCCGTTCATTTGCGCGAGCAGTTTCTGTTCATGATGGCTG  227
KlPdMDH3.1  TTTCATCGCGCTTTCCGCTTCGTAGTCGATTCTCGAGAGCATTTCTGTCTAAGATGGCAG  122
KlPdMDH3.2  TTTCATCGCGCTTTCCGCTTCGTAGGCGATTCTCGAGAGCATTTCTGTCTAAGATGGCAG  128
              **                                    *    **  * ****   *

KlPdMDH1.1  CGACCACAGCAGCTACATTCTCGGTTGGATCAAATGCCTTCCTTGGCACCAAAGCGAGCT  172
KlPdMDH1.2  CGACCACAGCAGCTACATTCTCGGTTGGATCAAATGCCTTCCTTGGCACCAAAGCGAACT  144
KlPdMDH2.1  CTGCAGTTGGAACCACTCTCTCGGTTGGATCAGCCATTTCTGCTGGTTGCAAGCCAGGCC  202
KlPdMDH2.2  CTGCAGTTGGAACCACTCTCTCGGTTGGATCAGCCATTTCTGCTGGTTGCAAGCCAGGCC  287
KlPdMDH3.1  CAGCAGTTGGAAAAACTCTCTCGGTTGGATCGACCATTTCTGCTGGTTCCAAGTCAGGCC  182
KlPdMDH3.2  CAGCAGTTGGAAAAACTCTCTCGGTTGGATCGACCATTTCTGCGGGTTCCAAGTCAGGCC  188
            *  *    * *   **  *************       *     **   ***  *   *

KlPdMDH1.1  CATCTACGCAGCCCAAGTCCGTGGGAAGAGCATCTTACTCACCTCCACGTCTCAGCAGTT  232
KlPdMDH1.2  CATCTACGCAGCCCAAGTCCGTGGGAAGAGTATCTTACTCACCTCCGCGTCTCAGCAGTT  204
KlPdMDH2.1  CAGTTACGCCGCAAAAGACAATGGGAGTGAAGCTTAACTCTGTGTCACGTCTTAGCTGTT  262
KlPdMDH2.2  CAGTTACGCCGCAAAAGACAATGGGAGTGAAGCTTAACTCTGTGTCACGCCTTAGCTGTT  347
KlPdMDH3.1  CAGCTACGCATCACAAGACGATGGGAGTGAAGCTCAACTCTGTGGCGCGATTTAGCAGTT  242
KlPdMDH3.2  CAGCTACGCATCACAAGACGATGGGAGTGAAGCTCAACTCTGTGGCGCGATTTAGCAGTT  248
            **  *****  *  *** *  *****          ****       **  * *** ***
```

### *KlNADP-MDH*

| Gene abbreviation | *K. laxiflora* transcript number |
|---|---|
| *KlNADP-MDH.1* | Kalax.0100s0048.1 |
| *KlNADP-MDH.2* | Kalax.0131s0010.1 |

```
KlNADP-MDH.1    ATTTGATGACTTCCTTCGTCAGAGAATTGCTAAGAGTGAGGCAGAGTTGCTGGCTGAGAA  1376
KlNADP-MDH.2    ATTTGATGACTTCCTTCGTCAGAGAATTGCTAAGAGTGAGGCAGAGTTGCTGGCTGAGAA  1547
                ************************************************************

KlNADP-MDH.1    GAGATGTGTGGCTCATCTGACAGGAGAGGGAATTGCTGTCTGCGATCTGCCCGAGGACAC  1436
KlNADP-MDH.2    GAGATGTGTTGCTCATCTGACAGGAGAGGGAATTGCTGTCTGCGATCTACCCGAGGACAC  1607
                ********* ************************************* ***********

KlNADP-MDH.1    TATGCTCCCAGGAGAAATGTAACTAACACAAGCACCATCCTCGTACTCCATTCCTTCCAG  1496
KlNADP-MDH.2    TATGCTCCCAGGAGAAATGTAACTAACACAAGCACCATCCTTGTACTCCATTCCTCCCAG  1667
                ****************************************** ************ ****
```

### *KlCMDH1*

| Gene abbreviation | *K. laxiflora* transcript number |
|---|---|
| *KlCMDH1.1* | Kalax.0075s0049.1 |
| *KlCMDH1.2* | Kalax.0094s0014.1 |
| *KlCMDH2.1* | Kalax.0023s0164.1 |
| *KlCMDH2.2* | Kalax.0074s0014.1 |

```
KlCMDH1.1       CTGAAGAGCTCAGTGAGGAGAAGGCTCTAGCCTACTCATGCCTCACATAGATACCCCCAC  1092
KlCMDH1.2       CTGAAGAGCTCAGTGAGGAGAAGGCTCTAGCCTACTCATGCCTCACATAGATACC-CCAC  1081
KlCMDH2.1       CTGAGGAGCTCAGTGATGAGAAGGCTCTGGCCTACTCATGCCTCTCGTAGATGCCCCATT  1081
KlCMDH2.2       CTGAGGAGCTCAGTGATGAGAAGGCTCTGGCCTACTCATGCCTCTCGTAGATGCCCCATT  1307
                **** *********** *********** *************** * ***** ** *

KlCMDH1.1       TGGTGATGCTGAAGTGAGTGTTGCAGTACTTGCAGTTTTGA--ATAAGCCATTGTTATGA  1150
KlCMDH1.2       TGGTGATGCTGAAGTGAGTGTTGCAGTACTTGCAGTTTTGA--ATAAGCCATTGTTATGA  1139
KlCMDH2.1       TATGGTGTTGAA-----------GAGTACTTGCAGTTCTGAATAAAGCCAATATTTACAA  1130
KlCMDH2.2       TATGGTGTTGAA-----------GAGTACTTGCAGTTCTGAATAAAGCCAATATTTACAA  1356
                *   *      *            ************* ***  * *  * **  ***  *

KlCMDH1.1       TTTGGTGGAATTGTCCATGTAAGAGAAGTAGCTTCTCTGTGGCTCTTTTTTTTTCGTG-C  1209
KlCMDH1.2       TTTGGTGGAATTGTCCATGTAAGAGAAGTAGCTTCTCTGTGGCTCGTTTTTTTTCGTG-C  1198
KlCMDH2.1       TTTGGTGGAAGTGGCCATATAAGAGAAGTAGCTTCTTTTTGGCTCATATTTTCAGTGCAT  1190
KlCMDH2.2       TTTGGTGGAAGTGGCCATATAAGAGAAGTAGCTTCTTTTTGGCTCATATTTTCAGTGCAT  1416
                ********** ** **** ***************** * ****** * ****
```

***KlUBQ10***

| Gene abbreviation | GenBank | *K. laxiflora* transcript number |
|---|---|---|
| *KlUBQ1* | - | Kalax.0069s0095.1 |

```
KlUBQ10          CCAGCAGAGGCTGATCTTTGCAGGCAAGCAGTTGGAAGATGGGAGGACTCTGGCCGACTAC  1500
KlUBQ10          AACATCCAGAAAGAGTCTACCCTGCACTTGGTCCTGCGTCTGCGTGGCGGAAACTAAGGGT  1560
KlUBQ10          GGATTTGTCTTATGATGCTGGTTGTTGTGTCTTGGGTGTGAATCTGGTCTGTCATCTTTGT  1620
```

***TFP***

| Gene abbreviation | *K. fedtschenkoi* draft genome annotation | *K. laxiflora* transcript |
|---|---|---|
| *KfTFP* | Kaladp0068s0118.1 | N/A |
| *KlTFP.1* | N/A | Kalax.1110s0007.1 |
| *KlTFP.2* | N/A | Kalax.0134s0055.1 |

```
KfTFP           CCGCAATGTTGTTCCTGCCACAGAAGAAGAGGCACGACGTGTGCTTGAGCGCATCGATGC  1670
KlTFP.1         CCGCAATGTTGTTCCTGCCACAGAAGAAGAGGCACGGCGTGTGCTTGAGCGCATTGATGC  3120
KlTFP.2         CCGCAATGTTGTTCCTGCCACAGAAGAAGAGGCACGACGTGTGCTTGAGCGCATCGATGC  1463
                ********************************** ***************** *****

KfTFP           TGAAAACTCCCTGCTGGCAAGGTCATAGTGTGATTGATATGTTTAATAGCGTGATCACTA  1730
KlTFP.1         TGAAAACTCCCTGGTGGCAAAGTCAA--------------------TAGCGTGATCACTA  3160
KlTFP.2         TGAAAACTCCCTGCTGGCAAAGTCAA--------------------TAGCGTGATCACTA  1497
                ************ ****** ****                     ********

KfTFP           TCACTGTTCTGGGACCTTCACCCTCTAAAATAGTTCTCCGGATCACATATCAAAAAAACT  1790
KlTFP.1         TCACTATTCTGGGACCGTCACCCTCTAAATAGTACTCAGGACCACATATAAAAAAAAAAA  3220
KlTFP.2         TCACTATTCTGGGACCTTCACCCTCTAAATAGTTCTCAGGACCACATATCAAAAAAAAAA  1557
                ***** ********** ************          *           *******
```

**Appendix 3 – Replicate developmental series of WT *K. fedtschenkoi* and *KfALMT* RNAi line 23A**

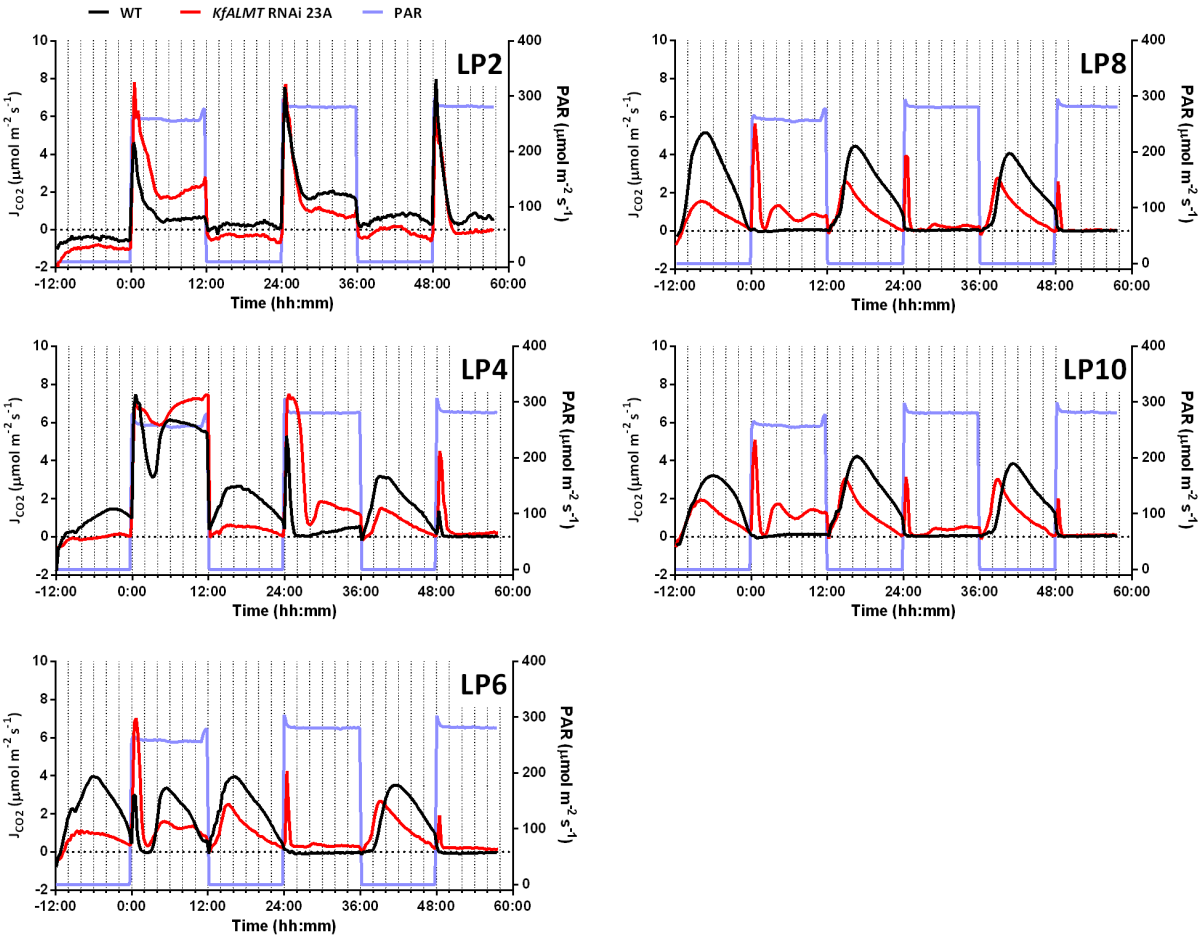


An additional developmental series of IRGA $CO_2$ gas exchange measurements of *KfALMT* RNAi line 23A and WT leaves under 12:12 LD. Cuttings were grown under glasshouse conditions for 9 weeks until July 2016, before entrainment to 12:12 LD. Even numbered leaf pairs from leaf pair 2 (LP2) to leaf pair 10 (LP10) were removed from cuttings and placed in the IRGA at ~12 h before the beginning of the first light period (00:00). $CO_2$ gas exchange rates ($J_{CO2}$) were normalised to leaf area (µmol m$^{-2}$ s$^{-1}$). Net $CO_2$ uptake occurred when $J_{CO2} > 0$.

**References to literature cited**


**Abraham PE, Yin H, Borland AM, *et al.*** 2016. Transcript, protein and metabolite temporal dynamics in the CAM plant *Agave*. Nature Plants **2**, 16178.

**Adams S, Manfield I, Stockley P, Carré IA**. 2015. Revised Morning Loops of the *Arabidopsis* Circadian Clock Based on Analyses of Direct Regulatory Interactions. PLoS ONE **10**, 1–11.

**Alabadí D, Oyama T, Yanovsky MJ, Harmon FG, Más P, Kay SA**. 2001. Reciprocal Regulation Between *TOC1* and *LHY/CCA1* Within the Arabidopsis Circadian Clock. Science **293**, 880–883.

**Altschul SF, Madden TL, Schaffer AA, Zang J, Zhang Z, Miller W, Lipman DJ**. 1997. Gapped BLAST and PSI-BLAST: a new generation of protein database search programs. Nucleic Acids Research **25**, 3389–3402.

**Amado AM, Ramos AP, Silva ER, Borissevitch IE**. 2016. Quenching of acridine orange fluorescence by salts in aqueous solutions: Effects of aggregation and charge transfer. Journal of Luminescence **178**, 288–294.

**Anderson CM, Wilkins MB**. 1989*a*. Phase resetting of the circadian rhythm of carbon dioxide assimilation in *Bryophyllum* leaves in relation to their malate content following brief exposure to high and low temperatures, darkness and 5% carbon dioxide. Planta **180**, 61–73.

**Anderson CM, Wilkins MB**. 1989*b*. Period and phase control by temperature in the circadian rhythm of carbon dioxide fixation in illuminated leaves of *Bryophyllum fedtschenkoi*. Planta **177**, 456–469.

**Anderson CM, Wilkins MB**. 1989*c*. Control of the circadian rhythm of carbon dioxide assimilation in *Bryophyllum* leaves by exposure to darkness and high carbon dioxide concentrations. Planta **177**, 401–408.

**De Angeli A, Baetz U, Francisco R, Zhang J, Chaves MM, Regalado A**. 2013*a*. The vacuolar channel VvALMT9 mediates malate and tartrate accumulation in berries of *Vitis vinifera*. Planta **238**, 283–291.

**De Angeli A, Zhang J, Meyer S, Martinoia E**. 2013*b*. AtALMT9 is a malate-activated vacuolar chloride channel required for stomatal opening in *Arabidopsis*. Nature Communications **4**, 1804.

**Arata H, Iwasaki I, Kusumi K, Nishimura M**. 1992. Thermodynamics of Malate Transport across the Tonoplast of Leaf-Cells of CAM Plants. Plant and Cell Physiology **33**, 873–880.

**Ashton AR, Trevanion SJ, Carr PD, Verger D, Ollis DL**. 2000. Structural basis for the light regulation of chloroplast NADP malate dehydrogenase. Physiologia Plantarum **110**, 314–321.

**Backhausen JE, Kitzmann C, Scheibe R**. 1994. Competition between electron acceptors in photosynthesis: Regulation of the malate valve during $CO_2$ fixation and nitrite reduction. Photosynthesis Research **42**, 75–86.

**Backhausen JE, Vetter S, Baalmann E, Kitzmann C, Scheibe R**. 1998. NAD-dependent malate dehydrogenase and glyceraldehyde 3-phosphate dehydrogenase isoenzymes play an important role in dark metabolism of various plastid types. Planta **205**, 359–366.

**Barrow SR, Cockburn W**. 1982. Effects of Light Quantity and Quality on the Decarboxylation of Malic Acid in Crassulacean Acid Metabolism Photosynthesis. Plant Physiology **69**, 568–571.

**Bauwe H, Hagemann M, Fernie AR**. 2010. Photorespiration: players, partners and origin. Trends in Plant Science **15**, 330–336.

**Beck F, Blasius B, Lüttge U, Neff R, Rascher U**. 2001. Stochastic noise interferes coherently with a model biological clock and produces specific dynamic behaviour. Proceedings of the Royal Society of London **268**, 1307–1313.

**Beeler S, Liu H-C, Stadler M, Schreier T, Eicke S, Lue W-L, Truernit E, Zeeman SC, Chen J, Kötting O**. 2014. Plastidial NAD-dependent malate dehydrogenase is critical for embryo development and heterotrophic metabolism in Arabidopsis. Plant Physiology **164**, 1175–90.

**Behzadipour M, Ratajczak R, Faist K, Pawlitschek P, Trémolières A, Kluge M**. 1998. Phenotypic Adaptation of Tonoplast Fluidity to Growth Temperature in the CAM Plant *Kalanchoë daigremontiana* Ham. et Per. is Accompanied by Changes in the Membrane Phospholipid and Protein Composition. The Journal of Membrane Biology **166**, 61–70.

**Bennett AB, Spanswick RM**. 1983. Membrane Biology Optical Measurements of $\Delta$pH and $\Delta\Psi$ in Corn Root Membrane Vesicles: Kinetic Analysis of $Cl^-$ Effects on a Proton-Translocating ATPase. Journal of Membrane Biology **71**, 95–107.

**Bertl A, Blumwald E, Coronado R, *et al.*** 1992. Electrical measurements on endomembranes. Science **258**, 873–874.

**Bettey M, Smith JAC**. 1993. Dicarboxylate transport at the vacuolar membrane of the CAM plant *Kalanchoë daigremontiana*: sensitivity to protein-modifying and sulphydryl reagents. Biochimica et Biophysica Acta - Biomembranes **1152**, 270–279.

**Black CC**. 1973. Photosynthetic carbon fixation in relation to net $CO_2$ uptake. Annual Review of Plant Physiology **24**, 253–286.

**Bläsing OE, Gibon Y, Günter M, Höhne M, Morcuende R, Osuna D, Thimm O, Usadel B, Scheible W-R, Stitt M**. 2005. Sugars and Circadian Regulation Make Major Contributions to the Global Regulation of Diurnal Gene Expression in Arabidopsis. The Plant Cell **17**, 3257–3281.

**Bohn A, Hinderlich S, Hütt M-T, Kaiser F, Lüttge U**. 2003. Identification of Rhythmic Subsystems in the Circadian Cycle of Crassulacean Acid Metabolism under Thermoperiodic Perturbations. Biological Chemistry **384**, 721–728.

**Borland AM, Barrera Zambrano VA, Ceusters J, Shorrock K**. 2011. The photosynthetic plasticity of crassulacean acid metabolism: An evolutionary innovation for sustainable productivity in a changing world. New Phytologist **191**, 619–633.

**Borland AM, Grffiths H, Maxwell C, Broadmeadow MSJ, Griffiths NM, Barnes JD**. 1992. On the ecophysiology of the Clusiaceae in Trinidad: expression of CAM in *Clusia minor* L. during the transition from wet to dry season and characterization of three endemic species. New Phytologist **122**, 349–357.

**Borland AM, Griffiths H**. 1997. A comparative study on the regulation of $C_3$ and $C_4$ carboxylation processes in the constitutive crassulacean acid metabolism (CAM) plant *Kalanchoë daigremontiana* and the $C_3$-CAM intermediate *Clusia minor*. Planta **201**, 368–378.

**Borland AM, Griffiths H, Hartwell J, Smith JAC**. 2009. Exploiting the potential of plants with crassulacean acid metabolism for bioenergy production on marginal lands. Journal of Experimental Botany **60**, 2879–2896.

**Borland AM, Guo HB, Yang X, Cushman JC**. 2016. Orchestration of carbohydrate processing for crassulacean acid metabolism. Current Opinion in Plant Biology **31**, 118–124.

**Borland AM, Hartwell J, Jenkins GI, Wilkins MB, Nimmo HG**. 1999. Metabolite Control Overrides Circadian Regulation of Phospho*enol*pyruvate Carboxylase Kinase and $CO_2$ Fixation in Crassulacean Acid Metabolism. Plant Physiology **121**, 889–896.

**Borland AM, Hartwell J, Weston DJ, Schlauch KA, Tschaplinski TJ, Tuskan GA, Yang X, Cushman JC**. 2014. Engineering crassulacean acid metabolism to improve water-use efficiency. Trends in Plant Science **19**, 327–338.

**Boxall SF, Foster JM, Bohnert HJ, Cushman JC, Nimmo HG, Hartwell J**. 2005. Conservation and divergence of circadian clock operation in a stress-inducible Crassulacean acid metabolism species reveals clock compensation against stress. Plant Physiology **137**, 969–82.

**Bremberger C, Haschke HP, Lüttge U**. 1988. Separation and purification of the tonoplast ATPase and pyrophosphatase from plants with constitutive and inducible Crassulacean acid metabolism. Planta **175**, 465–470.

**Bremberger C, Lüttge U**. 1992. Dynamics of tonoplast proton pumps and other tonoplast proteins of *Mesembryanthemum crystallinum* L. during the induction of Crassulacean acid metabolism. Planta **188**, 575–580.

**Brilhaus D, Bräutigam A, Mettler-Altmann T, Winter K, Weber APM**. 2016. Reversible Burst of Transcriptional Changes during Induction of Crassulacean Acid Metabolism in *Talinum triangulare*. Plant Physiology **170**, 102–122.

**Buchanan-Bollig IC**. 1984. Circadian rhythms in *Kalanchoë*: effects of irradiance and temperature on gas exchange and carbon metabolism. Planta **160**, 264–271.

**Buchanan-Bollig IC, Fischer A, Kluge M**. 1984. Circadian rhythms in *Kalanchoë*: the pathway of $^{14}CO_2$ Fixation during Prolonged Light. Planta **161**, 71–80.

**Buchanan-Bollig IC, Smith JAC**. 1984. Circadian rhythms in crassulacean acid metabolism: phase relationships between gas exchange, leaf water relations and malate metabolism in *Kalanchoë daigremontiana*. Planta **161**, 314–319.

**Bykova N V., Møller IM, Gardeström P, Igamberdiev AU**. 2014. The function of glycine decarboxylase complex is optimized to maintain high photorespiratory flux via buffering of its reaction products. Mitochondrion **19**, 357–364.

**von Caemmerer S, Furbank RT**. 2003. The $C_4$ pathway: an efficient $CO_2$ pump. Photosynthesis Research **77**, 191–207.

**von Caemmerer S, Griffiths H**. 2009. Stomatal responses to $CO_2$ during a diel Crassulacean acid metabolism cycle in *Kalanchoë daigremontiana* and *Kalanchoë pinnata*. Plant, Cell and Environment **32**, 567–576.

**Cariani L, Thomas L, Brito J, del Castillo J.** 2004. Bismuth citrate in the quantification of inorganic phosphate and its utility in the determination of membrane-bound phosphatases. Analytical Biochemistry **324**, 79–83.

**Carr PD, Verger D, Ashton AR, Ollis DL**. 1999. Chloroplast NADP-malate dehydrogenase: Structural basis of light- dependent regulation of activity by thiol oxidation and reduction. Structure **7**, 461–475.

**Carter PJ, Nimmo HG, Fewson CA, Wilkins MB**. 1991. Circadian rhythms in the activity of a plant protein kinase. The EMBO Journal **10**, 2063–2068.

**Carter PJ, Wilkins MB, Nimmo HG, Fewson CA**. 1995*a*. The role of temperature in the regulation of the circadian rhythm of $CO_2$ fixation in *Bryophyllum fedtschenkoi*. Planta **196**, 381–386.

**Carter PJ, Wilkins MB, Nimmo HG, Fewson CA**. 1995*b*. Effects of temperature on the activity of phosphoenolpyruvate carboxylase and on the control of $CO_2$ fixation in *Bryophyllum fedtschenkoi*. Planta **196**, 375–380.

**Castresana J**. 2000. Selection of Conserved Blocks from Multiple Alignments for Their Use in Phylogenetic Analysis. Molecular Biology and Evolution **17**, 540–552.

**Cavalcanti JHF, Esteves-Ferreira AA, Quinhones CGS, Pereira-Lima IA, Nunes-Nesi A, Fernie AR, Araujo WL**. 2014. Evolution and functional implications of the tricarboxylic acid cycle as revealed by phylogenetic analysis. Genome Biology and Evolution **6**, 2830–2848.

**Chase MW, Christenhusz MJM, Fay MF, *et al.*** 2016. An update of the Angiosperm Phylogeny Group classification for the orders and families of flowering plants: APG IV. Botanical Journal of the Linnean Society **181**, 1–20.

**Cheffings CM, Pantoja O, Ashcroft FM, Smith JAC**. 1997. Malate transport and vacuolar ion channels in CAM plants. Journal of Experimental Botany **48**, 623–631.

**Chen L-S, Nose A**. 2000. Characteristics of Adenosinetriphosphatase and Inorganic Pyrophosphatase in Tonoplasts Isolated from Three CAM Species, *Ananas comosus*, *Kalanchoë pinnata* and *K. daigremontiana*. Plant Production Science **3**, 24–31.

**Chen L-S, Nose A**. 2004. Day-Night Changes of Energy-rich Compounds in Crassulacean Acid Metabolism (CAM) Species Utilizing Hexose and Starch. Annals of Botany **94**, 449–455.

**Cheung CYM, Poolman MG, Fell DA, Ratcliffe RG, Sweetlove LJ**. 2014. A Diel Flux Balance Model Captures Interactions between Light and Dark Metabolism during Day-Night Cycles in $C_3$ and Crassulacean Acid Metabolism Leaves. Plant Physiology **165**, 917–929.

**Christopher JT, Holtum J**. 1996. Patterns of Carbon Partitioning in Leaves of Crassulacean Acid Metabolism Species during Deacidification. Plant Physiology **112**, 393–399.

**Cipriano DJ, Wang Y, Bond S, Hinton A, Jefferies KC, Qi J, Forgac M**. 2008. Structure and regulation of the vacuolar ATPases. Biochimica et Biophysica Acta (BBA) - Bioenergetics **1777**, 599–604.

**Cockburn W, Ting IP, Sternberg LO**. 1979. Relationships between Stomatal Behavior and Internal Carbon Dioxide Concentration in Crassulacean Acid Metabolism Plants. Plant Physiology **63**, 1029–1032.

**Cook RM, Lindsay JG, Wilkins B, Nimmo HG**. 1995. Decarboxylation of Malate in the Crassulacean Acid Metabolism Plant *Bryophyllum* (*Kalanchoë*) *fedtschenkoi*. Plant Physiology **109**, 1301–1307.

**Cook BI, Smerdon JE, Seager R, Coats S**. 2014. Global warming and 21st century drying. Climate Dynamics **43**, 2607–2627.

**Cosentino C, Di Silvestre D, Fischer-Schliebs E, Homann U, De Palma A, Comunian C, Mauri PL, Thiel G**. 2013. Proteomic analysis of *Mesembryanthemum crystallinum* leaf microsomal fractions finds an imbalance in V-ATPase stoichiometry during the salt-induced transition from C3 to CAM. Biochemical Journal **450**, 407–415.

**Cote FX, Andre M, Folliot M, Massimino D, Daguenet A**. 1989. $CO_2$ and $O_2$ Exchanges in the CAM Plant *Ananas comosus* (L.) Merr.: Determination of Total Malate-decorboxylation-dependent $CO_2$-assimilation rates: Study of Light $O_2$-Uptake. Plant Physiology **89**, 61–68.

**Cousins AB, Pracharoenwattana I, Zhou W, Smith SM, Badger MR**. 2008. Peroxisomal Malate Dehydrogenase Is Not Essential for Photorespiration in Arabidopsis But Its Absence Causes an Increase in the Stoichiometry of Photorespiratory $CO_2$ Release. Plant Physiology **148**, 786–795.

**Covington MF, Maloof JN, Straume M, Kay SA, Harmer SL**. 2008. Global transcriptome analysis reveals circadian regulation of key pathways in plant growth and development. Genome Biology **9**, R130.

**Covington MF, Panda S, Liu XL, Strayer CA, Wagner DR, Kay SA**. 2001. ELF3 modulates resetting of the circadian clock in Arabidopsis. The Plant Cell **13**, 1305–1315.

**Crayn DM, Winter K, Smith JAC**. 2004. Multiple origins of crassulacean acid metabolism and the epiphytic habit in the Neotropical family Bromeliaceae. Proceedings of the National Academy of Sciences **101**, 3703–3708.

**Cushman JC, Agarie S, Albion RL, Elliot SM, Taybi T, Borland AM**. 2008*a*. Isolation and characterization of mutants of common ice plant deficient in crassulacean acid metabolism. Plant Physiology **147**, 228–238.

**Cushman JC, Bohnert HJ**. 1997. Molecular genetics of Crassulacean acid metabolism. Plant Physiology **113**, 667–676.

**Cushman JC, Borland AM**. 2002. Induction of Crassulacean acid metabolism by water limitation. Plant, Cell and Environment **25**, 295–310.

**Cushman JC, Tillett RL, Wood JA, Branco JM, Schlauch KA**. 2008*b*. Large-scale mRNA expression profiling in the common ice plant, *Mesembryanthemum crystallinum*, performing $C_3$ photosynthesis and Crassulacean acid metabolism (CAM). Journal of Experimental Botany **59**, 1875–1894.

**Dall'omo C**. 2011. Timing is everything: The molecular basis for the interaction between the circadian clock and primary metabolism in $C_3$ and Crassulacean acid metabolism plant species. PhD thesis. University of Liverpool.

**Davies BN, Griffiths HG**. 2012. Competing carboxylases: circadian and metabolic regulation of Rubisco in $C_3$ and CAM *Mesembryanthemum crystallinum* L. Plant, Cell & Environment **35**, 1211–1220.

**DePaoli HC, Borland AM, Tuskan GA, Cushman JC, Yang X**. 2014. Synthetic biology as it relates to CAM photosynthesis: challenges and opportunities. Journal of Experimental Botany **65**, 3381–3393.

**Dever L V, Boxall SF, Kneřová J, Hartwell J**. 2015. Transgenic perturbation of the decarboxylation phase of Crassulacean acid metabolism alters physiology and metabolism but has only a small effect on growth. Plant Physiology **167**, 44–59.

**Devlin PF, Kay SA**. 2000. Cryptochromes Are Required for Phytochrome Signaling to the Circadian Clock but Not for Rhythmicity. The Plant Cell **12**, 2499–2509.

**Dodd AN, Belbin FE, Frank A, Webb AAR**. 2015. Interactions between circadian clocks and photosynthesis for the temporal and spatial coordination of metabolism. Frontiers in Plant Science **6**, Article 245.

**Dodd AN, Borland AM, Haslam RP, Griffiths H, Maxwell K**. 2002. Crassulacean acid metabolism: plastic, fantastic. Journal of Experimental Botany **53**, 569–580.

**Dodd AN, Griffiths H, Taybi T, Cushman JC, Borland AM**. 2003. Integrating diel starch metabolism with the circadian and environmental regulation of Crassulacean acid metabolism in *Mesembryanthemum crystallinum*. Planta **216**, 789–97.

**Dodd AN, Parkinson K, Webb AAR**. 2004. Independent circadian regulation of assimilation and stomatal conductance in the *ztl-1* mutant of *Arabidopsis*. New Phytologist **162**, 63–70.

**Dodd AN, Salathia N, Hall A, Kévei E, Tóth R, Nagy F, Hibberd JM, Millar AJ, Webb AAR**. 2005. Plant circadian clocks increase photosynthesis, growth, survival, and competitive advantage. Science **309**, 630–633.

**Doyle MR, Davis SJ, Bastow RM, McWatters HG, Kozma-Bognár L, Nagy F, Millar AJ, Amasino RM**. 2002. The *ELF4* gene controls circadian rhythms and flowering time in *Arabidopsis thaliana*. Nature **419**, 74–77.

**Duby G, Boutry M**. 2009. The plant plasma membrane proton pump ATPase: a highly regulated P-type ATPase with multiple physiological roles. Pflügers Archiv - European Journal of Physiology **457**, 645–655.

**Emmerlich V, Linka N, Reinhold T, Hurth MA, Traub M, Martinoia E, Neuhaus HE**. 2003. The plant homolog to the human sodium/dicarboxylic cotransporter is the vacuolar malate carrier. Proceedings of the National Academy of Sciences **100**, 11122–11126.

**Eom J-S, Cho J-I, Reinders A, *et al.*** 2011. Impaired Function of the Tonoplast-Localized Sucrose Transporter in Rice, *OsSUT2* , Limits the Transport of Vacuolar Reserve Sucrose and Affects Plant Growth. Plant Physiology **157**, 109–119.

**Etxeberria E, Pozueta-Romero J, Gonzalez P**. 2012. In and out of the plant storage vacuole. Plant Science **190**, 52–61.

**Fahnenstich H, Saigo M, Niessen M, Zanor MI, Andreo CS, Fernie AR, Drincovich MF, Flügge U-I, Maurino VG**. 2007. Alteration of organic acid metabolism in Arabidopsis overexpressing the maize $C_4$ NADP-malic enzyme causes accelerated senescence during extended darkness. Plant Physiology **145**, 640–652.

**Farré EM, Harmer SL, Harmon FG, Yanovsky MJ, Kay SA**. 2005. Overlapping and Distinct Roles of *PRR7* and *PRR9* in the *Arabidopsis* Circadian clock. Current Biology **15**, 47–54.

**Feria A-B, Alvarez R, Cochereau L, Vidal J, García-Mauriño S, Echevarría C**. 2008. Regulation of Phosphoenolpyruvate Carboxylase Phosphorylation by Metabolites and Abscisic Acid during the Development and Germination of Barley Seeds. Plant Physiology **148**, 761–774.

**Fogelmark K, Troein C**. 2014. Rethinking Transcriptional Activation in the *Arabidopsis* Circadian Clock. PLOS Computational Biology **10**, e1003705.

**Fowler S, Lee K, Onouchi H, Samach A, Richardson K, Morris B, Coupland G, Putterill J**. 1999. GIGANTEA: a circadian clock-controlled gene that regulates photoperiodic flowering in Arabidopsis and encodes a protein with several possible membrane-spanning domains. The EMBO Journal **18**, 4679–4688.

**Friemert V, Heininger D, Kluge M, Ziegler H**. 1988. Temperature effects on malic-acid efflux from the vacuoles and on the carboxylation pathways in Crassulacean-acid-metabolism plants. Planta **174**, 453–461.

**Fujiwara S, Wang L, Han L, Suh SS, Salomé PA, McClung CR, Somers DE**. 2008. Post-translational regulation of the *Arabidopsis* circadian clock through selective proteolysis and phosphorylation of pseudo-response regulator proteins. Journal of Biological Chemistry **283**, 23073–23083.

**Fusaro AF, Matthew L, Smith NA, *et al.*** 2006. RNA interference-inducing hairpin RNAs in plants act through the viral defence pathway. EMBO Reports **7**, 1168–1175.

**Gehrig H, Gaußmann O, Marx H, Schwarzott D, Kluge M**. 2001. Molecular phylogeny of the genus *Kalanchoe* (Crassulaceae) inferred from nucleotide sequences of the ITS-1 and ITS-2 regions. Plant Science **160**, 827–835.

**Gendron JM, Pruneda-Paz JL, Doherty CJ, Gross AM, Kang SE, Kay SA**. 2012. *Arabidopsis* circadian clock protein, TOC1, is a DNA-binding transcription factor. Proceedings of the National Academy of Sciences **109**, 3167–3172.

**Gietl C**. 1992. Malate dehydrogenase isoenzymes: Cellular locations and role in the flow of metabolites between the cytoplasm and cell organelles. Biochimica et Biophysica Acta - Bioenergetics **1100**, 217–234.

**Gould PD, Diaz P, Hogben C, Kusakina J, Salem R, Hartwell J, Hall A**. 2009. Delayed fluorescence as a universal tool for the measurement of circadian rhythms in higher plants. The Plant Journal **58**, 893–901.

**Goward CR, Nicholls DJ**. 1994. Malate dehydrogenase: A model for structure, evolution, and catalysis. Protein Science **3**, 1883–1888.

**Graf A, Schlereth A, Stitt M, Smith AM**. 2010. Circadian control of carbohydrate availability for growth in *Arabidopsis* plants at night. Proceedings of the National Academy of Sciences **107**, 9458–9463.

**Grams TEE, Beck F, Lüttge U**. 1996. Generation of rhythmic and arrhythmic behaviour of Crassulacean acid metabolism in *Kalanchoë daigremontiana* under continuous light by varying the irradiance or temperature: Measurements in vivo and model simulations. Planta **198**, 110–117.

**Grams TEE, Borland AM, Roberts A, Griffiths H, Beck F, Lüttge U**. 1997. On the Mechanism of Reinitiation of Endogenous Crassulacean Acid Metabolism Rhythm by Temperature Changes. Plant Physiology **113**, 1309–1317.

**Griffiths H, Broadmeadow MSJ, Borland AM, Hetherington CS**. 1990. Short-term changes in carbon-isotope discrimination identify transitions between $C_3$ and $C_4$ carboxylation during Crassulacean acid metabolism. Planta **181**, 604–610.

**Griffiths H, Ong BL, Avadhani PN, Goh CJ**. 1989. Recycling of respiratory $CO_2$ during Crassulacean acid metabolism: alleviation of photoinhibition in *Pyrrosia piloselloides*. Planta **179**, 115–122.

**Griffiths H, Robe WE, Girnus J, Maxwell K**. 2008. Leaf succulence determines the interplay between carboxylase systems and light use during Crassulacean acid metabolism in *Kalanchoë* species. Journal of Experimental Botany **59**, 1851–1861.

**Griffiths H, Smith JAC**. 1983. Photosynthetic Pathways in the Bromeliaceae of Trinidad: Relations between Life-Forms, Habitat Preference and the Occurrence of CAM. Oecologia **60**, 176–184.

**Grimmer C, Komor E**. 1999. Assimilate export by leaves of *Ricinus communis* L. growing under normal and elevated carbon dioxide concentrations: The same rate during the day, a different rate at night. Planta **209**, 275–281.

**Hafke JB, Hafke Y, Smith JAC, Lüttge U, Thiel G**. 2003. Vacuolar malate uptake is mediated by an anion-selective inward rectifier. The Plant Journal **35**, 116–128.

**Hafke JB, Neff R, Hütt MT, Lüttge U, Thiel G**. 2001. Day-to-night variations of cytoplasmic pH in a crassulacean acid metabolism plant. Protoplasma **216**, 164–70.

**Hanning I, Heldt HW**. 1993. On the Function of Mitochondrial Metabolism during Photosynthesis in Spinach (*Spinacia oleracea* L.) Leaves: Partitioning between Respiration and Export of Redox Equivalents and Precursors for Nitrate Assimilation Products. Plant Physiology **103**, 1147–1154.

**Harmer SL**. 2009. The Circadian System in Higher Plants. Annual Review of Plant Biology **60**, 357–377.

**Harmer SL, Hogenesch JB, Straume M, Chang HS, Han B, Zhu T, Wang X, Kreps JA, Kay SA**. 2000. Orchestrated transcription of key pathways in *Arabidopsis* by the circadian clock. Science **290**, 2110–2113.

**Harris PJC, Wilkins MB**. 1978*a*. The Circadian Rhythm in *Bryophyllum* Leaves: Phase Control by Radiant Energy. Planta **143**, 323–328.

**Harris PJC, Wilkins MB**. 1978*b*. Evidence of phytochrome involvement in the entrainment of the circadian rhythm of carbon dioxide metabolism in *Bryophyllum*. Planta **138**, 271–278.

**Hartwell J**. 2005. The co-ordination of central plant metabolism by the circadian clock. Biochem Soc Trans **33**, 945–948.

**Hartwell J**. 2006. The circadian clock in CAM plants. In: Hall AJW, McWatters HG, eds. Endogenous Plant Rhythms. Oxford: Blackwell Publishing Ltd, 211–236.

**Hartwell J, Dever L V., Boxall SF**. 2016. Emerging model systems for functional genomics analysis of Crassulacean acid metabolism. Current Opinion in Plant Biology **31**, 100–108.

**Hartwell J, Gill A, Nimmo GA, Wilkins MB, Jenkins GI, Nimmo HG**. 1999. Phosphoenolpyruvate carboxylase kinase is a novel protein kinase regulated at the level of expression. The Plant Journal **20**, 333–342.

**Hartwell J, Smith LH, Wilkins MB, Jenkins GI, Nimmo HG**. 1996. Higher plant phosphoenolpyruvate carboxylase kinase is regulated at the level of translatable mRNA in response to light or a circadian rhythm. The Plant Journal **10**, 1071–1078.

**Häusler RE, Holtum JAM, Latzko E**. 1989. Cytosolic Phosphofructokinase from Spinach Leaves. I. Purification, Characteristics, and Regulation. Plant Physiology **90**, 1498–1505.

**Haydon MJ, Mielczarek O, Robertson FC, Hubbard KE, Webb AAR**. 2013. Photosynthetic entrainment of the *Arabidopsis thaliana* circadian clock. Nature **502**, 689–692.

**Hazen SP, Schultz TF, Pruneda-Paz JL, Borevitz JO, Ecker JR, Kay SA**. 2005. *LUX ARRHYTHMO* encodes a Myb domain protein essential for circadian rhythms. Proceedings of the National Academy of Sciences of the United States of America **102**, 10387–10392.

**Hebbelmann I, Selinski J, Wehmeyer C, *et al.*** 2012. Multiple strategies to prevent oxidative stress in *Arabidopsis* plants lacking the malate valve enzyme NADP-malate dehydrogenase. Journal of Experimental Botany **63**, 1445–1459.

**Heber U**. 1974. Metabolite Exchange Between Chloroplasts and Cytoplasm. Annual Review of Plant Physiology **25**, 393–421.

**Heldt H-W, Piechulla B**. 2011*a*. Mitochondria are the power station of the cell. In: Heldt H-W, Piechulla B, eds. Plant Biochemistry. Academic Press, 133–161.

**Heldt H-W, Piechulla B**. 2011*b*. ATP is generated by photosynthesis. In: Heldt H-W, Piechulla B, eds. Plant Biochemistry. Academic Press, 113–131.

**Hennessey TL, Field CB**. 1991. Circadian Rhythms in Photosynthesis: Oscillations in Carbon Assimilation and Stomatal Conductance under Constant Conditions. Plant Physiology **96**, 831–836.

**Hennessey TL, Freeden AL, Field CB**. 1993. Environmental effects on circadian rhythms in photosynthesis and stomatal opening. Planta **189**, 369–376.

**Herrera A**. 2009. Crassulacean acid metabolism and fitness under water deficit stress: If not for carbon gain, what is facultative CAM good for? Annals of Botany **103**, 645–653.

**Hoekenga OA, Maron LG, Pineros MA, *et al.*** 2006. *AtALMT1*, which encodes a malate transporter, is identified as one of several genes critical for aluminum tolerance in *Arabidopsis*. Proceedings of the National Academy of Sciences **103**, 9738–9743.

**Holtum JAM, Osmond CB**. 1981. The Gluconeogenic Metabolism of Pyruvate During Deacidification in Plants With Crassulacean Acid Metabolism. Australian Journal of Plant Physiology **8**, 31–44.

**Holtum JAM, Smith JAC, Neuhaus HE**. 2005. Intracellular transport and pathways of carbon flow in plants with crassulacean acid metabolism. Functional Plant Biology **32**, 429–449.

**Holtum JAM, Summons R, Roeske CA, Comins HN, O'Leary MH**. 1984. Oxygen-18 incorporation into malic acid during nocturnal carbon dioxide fixation in crassulacean acid metabolism plants. A new approach to estimating in vivo carbonic anhydrase activity. Journal of Biological Chemistry **259**, 6870–6881.

**Horn JW, Xi Z, Riina R, Peirson JA, Yang Y, Dorsey BL, Berry PE, Davis CC, Wurdack KJ**. 2014. Evolutionary bursts in *Euphorbia* (Euphorbiaceae) are linked with photosynthetic pathway. Evolution **68**, 3485–3504.

**Hotta CT, Gardner MJ, Hubbard KE, Baek SJ, Dalchau N, Suhita D, Dodd AN, Webb AAR**. 2007. Modulation of environmental responses of plants by circadian clocks. Plant, Cell and Environment **30**, 333–349.

**Le Houérou HN**. 1996. The role of cacti (*Opuntia* spp.) in erosion control, land reclamation, rehabilitation and agricultural development in the Mediterranean Basin. Journal of Arid Environments **33**, 135–159.

**Hsu PY, Devisetty UK, Harmer SL**. 2013. Accurate timekeeping is controlled by a cycling activator in *Arabidopsis*. eLife **2013**, 1–20.

**Huang L, Berry EA**. 1990. Purification and characterization of the proton translocating plasma membrane ATPase of red beet storage tissue. Biochimica et Biophysica Acta - Protein Structure and Molecular Enzymology **1039**, 241–252.

**Huang W, Pérez-Garcia P, Pokhilko A, Millar AJ, Antoshechkin I, Riechmann JL, Mas P**. 2012. Mapping the Core of the *Arabidopsis* Circadian Clock Defines the Network Structure of the Oscillator. Science **336**, 75–79.

**Hu Z, Plaxton WC**. 1996. Purification and characterization of cytosolic pyruvate kinase from leaves of the castor oil plant. Archives of Biochemistry and Biophysics **333**, 298–307.

**Huber SC**. 1989. Biochemical Mechanism for Regulation of Sucrose Accumulation in Leaves during Photosynthesis. Plant Physiology **91**, 656–662.

**Hurth MA, Suh SJ, Kretzschmar T, Geis T, Bregante M, Gambale F**. 2005. Impaired pH Homeostasis in Arabidopsis Lacking the Vacuolar Dicarboxylate Transporter and Analysis of Carboxylic Acid Transport across the Tonoplast. Plant Physiology **137**, 901–910.

**Igamberdiev AU, Eprintsev AT**. 2016. Organic Acids: The Pools of Fixed Carbon Involved in Redox Regulation and Energy Balance in Higher Plants. Frontiers in Plant Science **7**, Article 1042.

**Imes D, Mumm P, Böhm J, Al-Rasheid KAS, Marten I, Geiger D, Hedrich R**. 2013. Open stomata 1 (OST1) kinase controls R-type anion channel QUAC1 in Arabidopsis guard cells. The Plant Journal **74**, 372–382.

**Imsande J, Berkemeyer M, Scheibe R, Schumann U, Gietl C, Palmer RG**. 2001. A Soybean Plastid-Targeted NADH-Malate Dehydrogenase : Cloning and Expression Analyses. American Journal of Botany **88**, 2136–2142.

**Iwasaki I, Arata H, Kijima H, Nishimura M**. 1992. Two Types of Channels Involved in the Malate Ion Transport across the Tonoplast of a Crassulacean Acid Metabolism Plant. Plant Physiology **98**, 1494–1497.

**Iwasaki I, Arata H, Nishimura M**. 1988. Ionic Balance during Malic Acid Accumulation in Vacuoles of a CAM Plant, *Graptopetalum paraguayense*. Plant and Cell Physiology **29**, 643–647.

**Jenner HL, Winning BM, Millar AH, Tomlinson KL, Leaver CJ, Hill SA**. 2001. NAD malic enzyme and the control of carbohydrate metabolism in potato tubers. Plant Physiology **126**, 1139–1149.

**Jewer PC, Incoll LD, Howarth GL**. 1981. Stomatal responses in isolated epidermis of the crassulacean acid metabolism plant *Kalanchoe daigremontiana* Hamet et Perr. Planta **153**, 238–245.

**Jochem P, Rona J-P, Smith JAC, Lüttge U**. 1984. Anion-sensitive ATPase activity and proton transport in isolated vacuoles of species of the CAM genus *Kalanchoë*. Physiologia Plantarum **62**, 410–415.

**Johansson K, Ramaswamy S, Saarinen M, Lemaire-Chamley M, Issakidis-Bourguet E, Miginiac-Maslow M, Eklund H**. 1999. Structural Basis for Light Activation of a Chloroplast Enzyme: The Structure of Sorghum NADP-Malate Dehydrogenase in Its Oxidized Form. **38**, 4319–4326.

**Jones MB**. 1975. The effect of leaf age on leaf resistance and $CO_2$ exchange of the CAM plant *Bryophyllum fedtschenkoi*. Planta **123**, 91–96.

**Junge W, Nelson N**. 2015. ATP Synthase. Annual Review of Biochemistry **84**, 631–657.

**Kalt W, Osmond CB, Siedow JN**. 1990. Malate Metabolism in the Dark after $^{13}CO_2$ Fixation in the Crassulacean Plant *Kalanchoë tubiflora*. Plant Physiology **94**, 826–832.

**Kamioka M, Takao S, Suzuki T, Taki K, Higashiyama T, Kinoshita T, Nakamichi N**. 2016. Direct repression of evening genes by CIRCADIAN CLOCK-ASSOCIATED 1 in Arabidopsis circadian clock. Plant Cell **28**, 696–711.

**Karimi M, Inzé D, Depicker A**. 2002. GATEWAY$^{TM}$ vectors for Agrobacterium-mediated plant transformation. Trends in Plant Science **7**, 193–195.

**Kaur N, Reumann S, Hu J**. 2009. Peroxisome Biogenesis and Function. The Arabidopsis Book **7**, e0123.

**Kim W-Y, Fujiwara S, Suh S-S, Kim J, Kim Y, Han L, David K, Putterill J, Nam HG, Somers DE**. 2007. ZEITLUPE is a circadian photoreceptor stabilized by GIGANTEA in blue light. Nature **449**, 356–60.

**Kim JY, Song HR, Taylor BL, Carré IA**. 2003. Light-regulated translation mediates gated induction of the *Arabidopsis* clock protein LHY. EMBO Journal **22**, 935–944.

**King ARW, Zeevaart JAD**. 1974. Enhancement of Phloem Exudation from Cut Petioles by Chelating Agents. Plant Physiology **53**, 96–103.

**Kinoshita H, Nagasaki J, Yoshikawa N, Yamamoto A, Takito S, Kawasaki M, Sugiyama T, Miyake H, Weber APM, Taniguchi M**. 2011. The chloroplastic 2-oxoglutarate/malate transporter has dual function as the malate valve and in carbon/nitrogen metabolism. The Plant Journal **65**, 15–26.

**Klavsen SK, Madsen T V., Maberly SC**. 2011. Crassulacean acid metabolism in the context of other carbon-concentrating mechanisms in freshwater plants: A review. Photosynthesis Research **109**, 269–279.

**Kliemchen A, Schomburg M, Galla H-J, Lüttge U, Kluge M**. 1993. Phenotypic changes in the fluidity of the tonoplast membrane of crassulacean-acid-metabolism plants in response to temperature and salinity stress. Planta **189**, 403–409.

**Kluge M**. 1969. Zur Analyse des $CO_2$-Austausches von *Bryophyllum* II. Hemmung des nächtlichen Stärkeabbaus in $CO_2$ verarmter Atmosphäre. Planta **86**, 142–150.

**Kluge M, Böhlke C, Queiroz O**. 1981. Crassulacean acid metabolism (CAM) in *Kalanchoë*: Changes in intercellular $CO_2$ concentration during a normal CAM cycle and during cycles in continuous light or darkness. Planta **152**, 87–92.

**Kluge M, Brulfert J, Ravelomanana D, Lipp J, Ziegler H**. 1991*a*. Crassulacean acid metabolism in *Kalanchoë* in various climatic zones of Madagascar: a survey by $\delta^{13}C$ analysis. Oecologia **88**, 407–414.

**Kluge C, Lahr J, Hanitzsch M, Bolte S, Golldack D, Dietz K-J**. 2003. New insight into the structure and regulation of the plant vacuolar H+-ATPase. Journal of Bioenergetics and Biomembranes **35**, 377–388.

**Kluge M, Wolf H, Fischer A**. 1991*b*. Crassulacean acid metabolism: Temperature effects on the lag-phase in the photosynthetic oxygen evolution ocurring at the onset of the light period. Plant Physiology and Biochemistry **29**, 83–90.

**Kölling K, Thalmann M, Müller A, Jenny C, Zeeman SC**. 2015. Carbon partitioning in *Arabidopsis thaliana* is a dynamic process controlled by the plants metabolic status and its circadian clock. Plant, Cell & Environment **38**, 1965–1979.

**Kovermann P, Meyer S, Hörtensteiner S, Picco C, Scholz-Starke J, Ravera S, Lee Y, Martinoia E**. 2007. The Arabidopsis vacuolar malate channel is a member of the ALMT family. The Plant Journal **52**, 1169–1180.

**Krapp A, Hofmann B, Schäfer C, Stitt M**. 1993. Regulation of the expression of rbcS and other photosynthetic genes by carbohydrates: a mechanism for the 'sink regulation' of photosynthesis? The Plant Journal **3**, 817–828.

**Krapp A, Stitt M**. 1995. An evaluation of direct and indirect mechanisms for the 'sink-regulation' of photosynthesis in spinach: Changes in gas exchange, carbohydrates, metabolites, enzyme activities and steady-state transcript levels after cold-girdling source leaves. Planta **195**, 313–323.

**Kruger NJ, Le Lay P, Ratcliffe RG**. 2007. Vacuolar compartmentation complicates the steady-state analysis of glucose metabolism and forces reappraisal of sucrose cycling in plants. Phytochemistry **68**, 2189–2196.

**Kusumi K, Arata H, Iwasaki I, Nishimura M**. 1994. Regulation of PEP-Carboxylase by Biological Clock in a CAM Plant. Plant Cell Physiol. **35**, 233–242.

**Lattanzi FA, Ostler U, Wild M, Morvan-Bertrand A, Decau M-L, Lehmeier CA, Meuriot F, Prud'homme M-P, Schäufele R, Schnyder H**. 2012. Fluxes in central carbohydrate metabolism of source leaves in a fructan-storing $C_3$ grass: rapid turnover and futile cycling of sucrose in continuous light under contrasted nitrogen nutrition status. Journal of Experimental Botany **63**, 2363–2375.

**Lee HC, Forte JG**. 1978. A study of $H^+$ transport in gastric microsomal vesicles using fluorescent probes. Biochimica et Biophysica Acta - Biomembranes **508**, 339–356.

**Li W, Cowley A, Uludag M, Gur T, McWilliam H, Squizzato S, Park YM, Buso N, Lopez R**. 2015. The EMBL-EBI bioinformatics web and programmatic tools framework. Nucleic Acids Research **43**, W580–W584.

**Ligaba A, Kochian L, Piñeros M**. 2009. Phosphorylation at S384 regulates the activity of the TaALMT1 malate transporter that underlies aluminum resistance in wheat. The Plant Journal **60**, 411–423.

**Lindén P, Keech O, Stenlund H, Gardeström P, Moritz T**. 2016. Reduced mitochondrial malate dehydrogenase activity has a strong effect on photorespiratory metabolism as revealed by $^{13}C$ labelling. Journal of Experimental Botany **67**, 3123–3135.

**Livak KJ, Schmittgen TD**. 2001. Analysis of Relative Gene Expression Data Using Real-Time Quantitative PCR and the $2^{-\Delta\Delta CT}$ Method. Methods **25**, 402–408.

**Lüttge U**. 1986. Nocturnal water storage in plants having Crassulacean acid metabolism. Planta **168**, 287–289.

**Lüttge U**. 1987. Carbon Dioxide and Water Demand: Crassulacean Acid Metabolism (CAM), a Versatile Ecological Adaptation Exemplifying the Need for Integration in Ecophysiological Work. New Phytologist **106**, 593–629.

**Lüttge U**. 1988. Day-night changes of citric acid levels in crassulacean acid metabolism: phenomenon and ecophysiological significance. Plant, Cell and Environment **11**, 445–451.

**Lüttge U**. 2004. Ecophysiology of Crassulacean Acid Metabolism (CAM). Annals of Botany **93**, 629–652.

**Lüttge U**. 2010. Photorespiration in Phase III of Crassulacean Acid Metabolism: Evolutionary and Ecophysiological Implications. Progress in Botany **72**. 371–384.

**Lüttge U, Ball E**. 1979. Electrochemical investigation of active malic acid transport at the tonoplast into the vacuoles of the CAM plant *Kalanchoë daigremontiana*. The Journal of Membrane Biology **47**, 401–422.

**Lüttge U, Ball E**. 1980. $2H^+$:1 $malate^{2-}$ stoichiometry during Crassulacean Acid Metabolism is unaffected by lipophilic cations. Plant, Cell & Environment **3**, 195–200.

**Lüttge U, Beck F**. 1992. Endogenous rhythms and chaos in crassulacean acid metabolism. Planta **188**, 28–38.

**Lüttge U, Smith JAC**. 1984. Mechanism of passive malic-acid efflux from vacuoles of the CAM plant *Kalanchoë daigremontiana*. The Journal of Membrane Biology **81**, 149–158.

**Maeshima M**. 2000. Vacuolar $H^+$-pyrophosphatase. Biochimica et Biophysica Acta **1465**, 37–51.

**Makino S, Matsushika A, Kojima M, Yamashino T, Mizuno T**. 2002. The APRR1/TOC1 Quintet Implicated in Circadian Rhythms of *Arabidopsis thaliana* : I . Characterization with APRR1-Overexpressing Plants. **43**, 58–69.

**Mariaux JB, Fischer-Schliebs E, Lüttge U, Ratajczak R**. 1997. Dynamics of activity and structure of the tonoplast vacuolar-type $H^+$-ATPase in plants with differing CAM expression and in a $C_3$ plant under salt stress. Protoplasma **196**, 181–189.

**Martínez-García JF, Huq E, Quail PH**. 2000. Direct targeting of light signals to a promoter element-bound transcription factor. Science **288**, 859–863.

**Martinoia E, Maeshima M, Neuhaus HE**. 2007. Vacuolar transporters and their essential role in plant metabolism. Journal of Experimental Botany **58**, 83–102.

**Más P, Alabadí D, Yanovsky MJ, Oyama T, Kay SA**. 2003*a*. Dual role of TOC1 in the control of circadian and photomorphogenic responses in Arabidopsis. The Plant Cell **15**, 223–36.

**Más P, Kim WY, Somers DE, Kay SA**. 2003*b*. Targeted degradation of TOC1 by ZTL modulates circadian function in *Arabidopsis thaliana*. Nature **426**, 567–570.

**Matsushika A, Makino S, Kojima M, Mizuno T**. 2000. Circadian waves of expression of the APRR1/TOC1 family of pseudo-response regulators in *Arabidopsis thaliana*: Insight into the plant circadian clock. Plant and Cell Physiology **41**, 1002–1012.

**Maurino VG, Engqvist MKM**. 2015. 2-Hydroxy Acids in Plant Metabolism. The Arabidopsis Book **13**, e0182.

**Maxwell K, Borland A, Haslam R, Helliker B, Roberts A, Griffiths H**. 1999. Modulation of Rubisco Activity during the Diurnal Phases of the Crassulacean Acid Metabolism Plant *Kalanchoë daigremontiana*. Plant Physiology **121**, 849–856.

**Maxwell K, von Caemmerer S, Evans JR**. 1997. Is a Low Internal Conductance to $CO_2$ Diffusion a Consequence of Succulence in Plants with Crassulacean Acid Metabolism? Australian Journal of Plant Physiology **24**, 777–786.

**Mayoral ML, Medina E**. 1985. $^{14}$C-translocation in *Kalanchoe pinnata* at two different stages of development. Journal of Experimental Botany **36**, 1405–1413.

**Mayoral ML, Medina E, Garcia V**. 1991. Effect of source-sink manipulations on the Crassulacean acid metabolism of *Kalanchoë pinnata*. Journal of Experimental Botany **42**, 1123–1129.

**McRae SR, Christopher JT, Smith JAC, Holtum JAM**. 2002. Sucrose transport across the vacuolar membrane of *Ananas comosus*. Functional Plant Biology **29**, 717–724.

**Meyer S, Mumm P, Imes D, Endler A, Weder B, Al-Rasheid KAS, Geiger D, Marten I, Martinoia E, Hedrich R**. 2010. *At*ALMT12 represents an R-type anion channel required for stomatal movement in Arabidopsis guard cells. The Plant Journal **63**, 1054–1062.

**Meyer S, Scholz-Starke J, De Angeli A, Kovermann P, Burla B, Gambale F, Martinoia E**. 2011. Malate transport by the vacuolar AtALMT6 channel in guard cells is subject to multiple regulation. The Plant Journal **67**, 247–257.

**Millar AJ, Kay SA**. 1996. Integration of circadian and phototransduction pathways in the network controlling *CAB* gene transcription in *Arabidopsis*. Proceedings of the National Academy of Sciences of the United States of America **93**, 15491–15496.

**Miller SS, Driscoll BT, Gregerson RG, Gantt JS, Vance CP**. 1998. Alfalfa malate dehydrogenase (MDH): molecular cloning and characterization of five different forms reveals a unique nodule-enhanced MDH. Plant Journal **15**, 173–184.

**Ming R, VanBuren R, Wai CM, *et al.*** 2015. The pineapple genome and the evolution of CAM photosynthesis. Nature Genetics **47**, 1435–1442.

**Mizuno T, Nomoto Y, Oka H, Kitayama M, Takeuchi A, Tsubouchi M, Yamashino T**. 2014. Ambient temperature signal feeds into the circadian clock transcriptional circuitry through the EC night-time repressor in *Arabidopsis thaliana*. Plant and Cell Physiology **55**, 958–976.

**Möllering H**. 1974. L-Malate: determination with malate dehydrogenase and glutamate-oxaloacetate transaminase. In: Bergmeyer HU, ed. Methods in enzymatic analysis. Weinheim: Verlag Chemie, 1589–1593.

**Möllering H**. 1985. Citrate. In: Bergmeyer HU, ed. Methods of enzymatic analysis. Weinheim: Verlag Chemie, 2–13.

**Mullendore DL, Windt CW, Van As H, Knoblauch M**. 2010. Sieve tube geometry in relation to phloem flow. The Plant Cell **22**, 579–93.

**Munoz-Bertomeu J, Cascales-Minana B, Mulet JM, Baroja-Fernandez E, Pozueta-Romero J, Kuhn JM, Segura J, Ros R**. 2009. Plastidial Glyceraldehyde-3-Phosphate Dehydrogenase Deficiency Leads to Altered Root Development and Affects the Sugar and Amino Acid Balance in Arabidopsis. Plant Physiology **151**, 541–558.

**Mustilli A-C, Merlot S, Vavasseur A, Fenzi F, Giraudat J**. 2002. Arabidopsis OST1 Protein Kinase Mediates the Regulation of Stomatal Aperture by Abscisic Acid and Acts Upstream of Reactive Oxygen Species Production. The Plant Cell **14**, 3089–3099.

**Nagel DH, Doherty CJ, Pruneda-Paz JL, Schmitz RJ, Ecker JR, Kay SA**. 2015. Genome-wide identification of CCA1 targets uncovers an expanded clock network in *Arabidopsis*. Proceedings of the National Academy of Sciences of the United States of America **112**, E4802-10.

**Nägele T, Henkel S, Hörmiller I, Sauter T, Sawodny O, Ederer M, Heyer AG**. 2010. Mathematical Modeling of the Central Carbohydrate Metabolism in Arabidopsis Reveals a Substantial Regulatory Influence of Vacuolar Invertase on Whole Plant Carbon Metabolism. Plant Physiology **153**, 260–272.

**Nakamichi N, Kiba T, Henriques R, Mizuno T, Chua N-H, Sakakibara H**. 2010. PSEUDO-RESPONSE REGULATORS 9, 7, and 5 are transcriptional repressors in the *Arabidopsis* circadian clock. The Plant Cell **22**, 594–605.

**Nakamichi N, Kiba T, Kamioka M, Suzuki T, Yamashino T, Higashiyama T, Sakakibara H, Mizuno T**. 2012. Transcriptional repressor PRR5 directly regulates clock-output pathways. Proceedings of the National Academy of Sciences **109**, 17123–17128.

**Nakamichi N, Kita M, Ito S, Yamashino T, Mizuno T**. 2005. PSEUDO-RESPONSE REGULATORS, PRR9, PRR7 and PRR5, Together Play Essential Roles Close to the Circadian Clock of *Arabidopsis thaliana*. Plant and Cell Physiology **46**, 686–698.

**Neff R, Blasius B, Beck F, Lüttge U**. 1998. Thermodynamics and energetics of the tonoplast membrane operating as a hysteresis switch in an oscillatory model of Crassulacean acid metabolism. Journal of Membrane Biology **165**, 37–43.

**Nelson EA, Sage RF**. 2008. Functional constraints of CAM leaf anatomy: Tight cell packing is associated with increased CAM function across a gradient of CAM expression. Journal of Experimental Botany **59**, 1841–1850.

**Neuhaus HE, Schulte N**. 1996. Starch degradation in chloroplasts isolated from $C_3$ or CAM (crassulacean acid metabolism)-induced *Mesembryanthemum crystallinum* L. The Biochemical Journal **318**, 945–953.

**Nielsen T, Rung J, Villadsen D**. 2004. Fructose-2,6-bisphosphate: a traffic signal in plant metabolism. Trends in Plant Science **9**, 556–563.

**Nimmo HG**. 2000. The regulation of phosphoenolpyruvate carboxylase in CAM plants. Trends in Plant Science **5**, 75–80.

**Nimmo GA, Nimmo HG, Fewson CA, Wilkins MB**. 1984. Diurnal changes in the properties of phosphoenolpyruvate carboxylase in *Bryophyllum* leaves: a possible covalent modification. FEBS Letters **178**, 199–203.

**Nimmo GA, Nimmo HG, Hamilton ID, Fewson CA, Wilkins MB**. 1986. Purification of the phosphorylated night form and dephosphorylated day form of phosphoenolpyruvate carboxylase from *Bryophyllum fedtschenkoi*. Biochemical Journal **239**, 213–220.

**Nimmo GA, Wilkins MB, Fewson CA, Nimmo HG**. 1987. Persistent circadian rhythms in the phosphorylation state of phosphoenolpyruvate carboxylase from *Bryophyllum fedtschenkoi* leaves and in its sensitivity to inhibition by malate. Planta **170**, 408–415.

**Nishida K, Tominaga O**. 1987. Energy-dependent Uptake of Malate into Vacuoles Isolated from CAM Plant, *Kalanchoë daigremontiana*. Journal of Plant Physiology **127**, 385–393.

**Notredame C, Higgins DG, Heringa J**. 2000. T-coffee: a novel method for fast and accurate multiple sequence alignment. Journal of Molecular Biology **302**, 205–217.

**Nunes-Nesi A, Carrari F, Lytovchenko A, Smith AMO, Loureiro ME, Ratcliffe RG, Sweetlove LJ, Fernie AR**. 2005. Enhanced photosynthetic performance and growth as a consequence of decreasing mitochondrial malate dehydrogenase activity in transgenic tomato plants. Plant Physiology **137**, 611–22.

**Nusinow DA, Helfer A, Hamilton EE, King JJ, Imaizumi T, Schultz TF, Farré EM, Kay SA**. 2011. The ELF4-ELF3-LUX complex links the circadian clock to diurnal control of hypocotyl growth. Nature **475**, 398–402.

**Osmond CB**. 1978. Crassulacean Acid Metabolism: A curiosity in context. Annual Review of Plant Physiology **29**, 379–414.

**Owen NA, Griffiths H**. 2013. A system dynamics model integrating physiology and biochemical regulation predicts extent of crassulacean acid metabolism (CAM) phases. New Phytologist **200**, 1116–1131.

**Pajor AM**. 2014. Sodium-coupled dicarboxylate and citrate transporters from the SLC13 family. Pflügers Archiv - European Journal of Physiology **466**, 119–130.

**Pajor AM, Sun N**. 1999. Protein kinase C-mediated regulation of the renal $Na^+$/dicarboxylate cotransporter, NaDC-1. Biochimica et Biophysica Acta - Biomembranes **1420**, 223–230.

**Palmer AJ, Baker A, Muench SP**. 2016. The varied functions of aluminium-activated malate transporters-much more than aluminium resistance. Biochemical Society Transactions **44**, 856–862.

**Palmgren MG**. 1991. Acridine orange as a probe for measuring pH gradients across membranes: Mechanism and limitations. Analytical Biochemistry **192**, 316–321.

**Palmieri L, Picault N, Arrigoni R, Besin E, Palmieri F, Hodges M**. 2008. Molecular identification of three *Arabidopsis thaliana* mitochondrial dicarboxylate carrier isoforms: organ distribution, bacterial expression, reconstitution into liposomes and functional characterization. Biochemical Journal **410**, 621–629.

**Pantoja O, Smith JAC**. 2002. Sensitivity of the plant vacuolar malate channel to pH, $Ca^{2+}$ and anion-channel blockers. Journal of Membrane Biology **186**, 31–42.

**Pedersen O, Rich SM, Pulido C, Cawthray GR, Colmer TD**. 2011. Crassulacean acid metabolism enhances underwater photosynthesis and diminishes photorespiration in the aquatic plant *Isoetes australis*. New Phytologist **190**, 332–339.

**Picault N, Palmieri L, Pisano I, Hodges M, Palmieri F**. 2002. Identification of a novel transporter for dicarboxylates and tricarboxylates in plant mitochondria: Bacterial expression, reconstitution, functional characterization, and tissue distribution. Journal of Biological Chemistry **277**, 24204–24211.

**Plaxton WC**. 1996. The organization and regulation of plant glycolysis. Annual Review of Plant Physiology and Plant Molecular Biology **47**, 185–214.

**Pokhilko A, Fernández AP, Edwards KD, Southern MM, Halliday KJ, Millar AJ**. 2012. The clock gene circuit in *Arabidopsis* includes a repressilator with additional feedback loops. Molecular Systems Biology **8**, 574.

**Pracharoenwattana I, Cornah JE, Smith SM**. 2007. Arabidopsis peroxisomal malate dehydrogenase functions in β-oxidation but not in the glyoxylate cycle. The Plant Journal **50**, 381–390.

**Rademacher T, Häusler RE, Hirsch H-J, Zhang L, Lipka V, Weier D, Kreuzaler F, Peterhänsel C**. 2002. An engineered phosphoenolpyruvate carboxylase redirects carbon and nitrogen flow in transgenic potato plants. The Plant Journal **32**, 25–39.

**Rascher U, Blasius B, Beck F, Lüttge U**. 1998. Temperature profiles for the expression of endogenous rhythmicity and arrhythmicity of $CO_2$ exchange in the CAM plant *Kalanchoë daigremontiana* can be shifted by slow temperature changes. Planta **207**, 76–82.

**Rascher U, Lüttge U**. 2002. High-Resolution Chlorophyll Fluorescence Imaging Serves as a Non-Invasive Indicator to Montitor the Spatio-Temporal Variations of Metabolism during the Day-Night Cycle and during the Endogenous Rhythm in Continuous Light in the CAM Plant *Kalanchoë daigremontiana*. Plant Biology **4**, 671–681.

**Ratajczak R**. 2000. Structure, function and regulation of the plant vacuolar $H^+$-translocating ATPase. Biochimica et Biophysica Acta (BBA) - Biomembranes **1465**, 17–36.

**Ratajczak R, Kemna I, Lüttge U**. 1994. Characteristics, partial purification and reconstitution of the vacuolar malate transporter of the CAM plant *Kalanchoë daigremontiana* Hamet et Perrier de la Bâthie. Planta **195**, 226–236.

**Rawat R, Takahashi N, Hsu PY, Jones MA, Schwartz J, Salemi MR, Phinney BS, Harmer SL**. 2011. REVEILLE8 and PSEUDO-REPONSE REGULATOR5 form a negative feedback loop within the Arabidopsis circadian clock. PLoS Genetics **7**, e1001350.

**Rebeille F, Hatch MD**. 1986. Regulation of NADP-Malate Dehydrogenase in $C_4$ Plants: Effect of Varying NADPH to NADP Ratios and Thioredoxin Redox State on Enzyme Activity in Reconstituted Systems. Archives of Biochemistry and Biophysics **249**, 164–170.

**Reumann S, Maier E, Heldt HW, Benz R**. 1998. Permeability properties of the porin of spinach leaf peroxisomes. European Journal of Biochemistry **251**, 359–366.

**Ritz D, Kluge M**. 1987. Circadian rhythmicity of CAM in continuous light: Coincidences between gas exchange parameters, $^{14}CO_2$ fixation patterns and PEP-carboxylase properties. Journal of Plant Physiology **131**, 285–296.

**Roberts A, Borland AM, Griffiths H**. 1997. Discrimination Processes and Shifts in Carboxylation during the Phases of Crassulacean Acid Metabolism. Plant Physiology **113**, 1283–1292.

**Rodríguez A, Rodríguez M, Córdoba JJ, Andrade MJ.** Design of Primers and Probes for Quantitative Real-Time PCR Methods. In: Basu C (ed.) PCR Primer Design, New York: Springer, 31-56.

**Rona JP, Pitman MG, Lüttge U, Ball E**. 1980. Electrochemical data on compartmentation into cell wall, cytoplasm, and vacuole of leaf cells in the CAM genus *Kalanchoë*. The Journal of Membrane Biology **57**, 25–35.

**Rygol J, Winter K, Zimmermann U**. 1987. The relationship between turgor pressure and titratable acidity in mesophyll cells of intact leaves of a Crassulacean-acid-metabolism plant, *Kalanchoë daigremontiana* Hamet et Perr. Planta **172**, 487–493.

**Salomé PA, McClung CR**. 2005. What makes the Arabidopsis clock tick on time? A review on entrainment. Plant, Cell and Environment **28**, 21–38.

**Sasaki T, Yamamoto Y, Ezaki B, Katsuhara M, Ahn SJ, Ryan PR, Delhaize E, Matsumoto H**. 2004. A wheat gene encoding an aluminum-activated malate transporter. Plant Journal **37**, 645–653.

**Schaffer R, Ramsay N, Samach A, Corden S, Putterill J, Carré IA, Coupland G**. 1998. The *late elongated hypocotyl* mutation of *Arabidopsis* disrupts circadian rhythms and the photoperiodic control of flowering. Cell **93**, 1219–1229.

**Scheibe R**. 2004. Malate valves to balance cellular energy supply. Physiologia Plantarum **120**, 21–26.

**Schnarrenberger C, Martin W**. 2002. Evolution of the enzymes of the citric acid cycle and the glyoxylate cycle of higher plants: A case study of endosymbiotic gene transfer. European Journal of Biochemistry **269**, 868–883.

**Schneider S, Beyhl D, Hedrich R, Sauer N**. 2008. Functional and physiological characterization of Arabidopsis INOSITOL TRANSPORTER1, a novel tonoplast-localized transporter for myo-inositol. The Plant Cell **20**, 1073–1087.

**Schneider S, Hulpke S, Schulz A, *et al.*** 2012. Vacuoles release sucrose via tonoplast-localised SUC4-type transporters. Plant Biology **14**, 325–336.

**Selinski J, König N, Wellmeyer B, Hanke GT, Linke V, Neuhaus HE, Scheibe R**. 2014. The Plastid-Localized NAD-Dependent Malate Dehydrogenase Is Crucial for Energy Homeostasis in Developing *Arabidopsis thaliana* Seeds. Molecular Plant **7**, 170–186.

**Shimada T, Nakano R, Shulaev V, Sadka A, Blumwald E**. 2006. Vacuolar citrate/$H^+$ symporter of citrus juice cells. Planta **224**, 472–480.

**Sievers F, Wilm A, Dineen D, *et al.*** 2011. Fast, scalable generation of high-quality protein multiple sequence alignments using Clustal Omega. Molecular Systems Biology **7**, 539.

**Silvera K, Neubig KM, Whitten WM, Williams NH, Winter K, Cushman JC**. 2010. Evolution along the crassulacean acid metabolism continuum. Functional Plant Biology **37**, 995–1010.

**Silvera K, Santiago LS, Cushman JC, Winter K**. 2009. Crassulacean acid metabolism and epiphytism linked to adaptive radiations in the Orchidaceae. Plant Physiology **149**, 1838–47.

**Silvera K, Santiago LS, Winter K**. 2005. Distribution of crassulacean acid metabolism in orchids of Panama: Evidence of selection for weak and strong modes. Functional Plant Biology **32**, 397–407.

**Silvera K, Winter K, Leticia Rodriguez B, Albion RL, Cushman JC**. 2014. Multiple isoforms of phosphoenolpyruvate carboxylase in the Orchidaceae (subtribe Oncidiinae): implications for the evolution of crassulacean acid metabolism. Journal of Experimental Botany **65**, 3623–3636.

**Sipes DL, Ting IP**. 1985. Crassulacean Acid Metabolism and Crassulacean Acid Metabolism Modifications in *Peperomia camptotricha*. Plant Physiology **77**, 59–63.

**Small I**. 2007. RNAi for revealing and engineering plant gene functions. Current Opinion in Biotechnology **18**, 148–153.

**Smith JAC, Ingram J, Tsiantis MS, Barkla DM, Bettey M, Pantoja O, Pennington AJ**. 1996. Transport across the vacuolar membrane in CAM plants. In: Winter K, Smith JAC, eds. Ecological Studies. Crassulacean Acid Metabolism: Biochemistry, ecophysiology and evolution. Berlin, Heidelberg: Springer Berlin Heidelberg, 53–71.

**Smith JAC, Lüttge U**. 1985. Day-night changes in leaf water relations associated with the rhythm of crassulacean acid metabolism in *Kalanchoë daigremontiana*. Planta **163**, 272–282.

**Smith JAC, Marigo G, Lüttge U, Ball E**. 1982. Adenine-dinucletoide levels during Crassulacean acid metabolism and the energetics of malate accumulation in *Kalanchoë tubiflora*. Plant Science Letters **26**, 13–21.

**Smith FA, Raven JA**. 1979. Intracellular pH and Its Regulation. Annual Review of Plant Physiology **30**, 289–311.

**Smith JAC, Uribe EG, Ball E, Heuer S, Lüttge U**. 1984*a*. Characterization of the vacuolar ATPase activity of the crassulacean-acid-metabolism plant *Kalanchoë daigremontiana* Receptor modulating. European Journal of Biochemistry **141**, 415–420.

**Smith JAC, Uribe EG, Ball E, Lüttge U**. 1984*b*. ATPase activity associated with isolated vacuoles of the crassulacean acid metabolism plant *Kalanchoë daigremontiana*. Planta **162**, 299–304.

**Smith AM, Zeeman SC**. 2006. Quantification of starch in plant tissues. Nature protocols **1**, 1342–1345.

**Somers DE, Devlin PF, Kay SA**. 1998. Phytochromes and Cryptochromes in the Entrainment of the *Arabidopsis* Circadian Clock. Science **282**, 1488–1490.

**Stamatakis A**. 2006. RAxML-VI-HPC: maximum likelihood-based phylogenetic analyses with thousands of taxa and mixed models. Bioinformatics **22**, 2688–2690.

**Struve I, Lüttge U**. 1987. Characteristics of $MgATP^{2-}$-dependent electrogenic proton transport in tonoplast vesicles of the facultative crassulacean-acid-metabolism plant *Mesembryanthemum crystallinum* L. Planta **170**, 111–120.

**Tang W, Tang AY**. 2017. Applications and roles of the CRISPR system in genome editing of plants. Journal of Forestry Research **28**, 15–28.

**Taniguchi M, Taniguchi Y, Kawasaki M, Takeda S, Kato T, Sato S, Tahata S, Miyake H, Sugiyama T**. 2002. Identifying and characterizing plastidic 2-oxoglutarate/malate and dicarboxylate transporters in *Arabidopsis thaliana*. Plant and Cell Physiology **43**, 706–717.

**Tesfaye M, Temple SJ, Allan DL, Vance CP, Samac DA**. 2001. Overexpression of Malate Dehydrogenase in Transgenic Alfalfa Enhances Organic Acid Synthesis and Confers Tolerance to Aluminum. Plant Physiology **127**, 1836–1844.

**Thomas DA, André M, Ganzin A-M**. 1987. Oxygen and carbon dioxide exchanges in crassulacean acid metabolism plants: II. Effects of $CO_2$ concentration and irradiance. Plant Physiology and Biochemistry **25**, 95–103.

**Tomaz T, Bagard M, Pracharoenwattana I, Lindén P, Lee CP, Carroll AJ, Ströher E, Smith SM, Gardeström P, Millar AH**. 2010. Mitochondrial Malate Dehydrogenase Lowers Leaf Respiration and Alters Photorespiration and Plant Growth in Arabidopsis. Plant Physiology **154**, 1143–1157.

**Trentmann O, Haferkamp I**. 2013. Current Progress in Tonoplast Proteomics Reveals Insights into the Function of the Large Central Vacuole. Frontiers in Plant Science **4**.

**Truesdale MR, Toldi O, Scott P**. 1999. The Effect of Elevated Concentrations of Fructose 2,6-Bisphosphate on Carbon Metabolism during Deacidification in the Crassulacean Acid Metabolism Plant *Kalanchoë daigremontiana*. Plant Physiology **121**, 957–964.

**Turgeon R, Wolf S**. 2009. Phloem transport: cellular pathways and molecular trafficking. Annual Review of Plant Biology **60**, 207–221.

**Untergasser A, Nijveen H, Rao X, Bisseling T, Geurts R, Leunissen JAM**. 2007. Primer3Plus, an enhanced web interface to Primer3. Nucleic Acids Research **35**, W71–W74.

**Wang Y-H, Chollet R**. 1993. Partial Purification and Characterization of Phospho*enol*pyruvate Carboxylase Protein-Serine Kinase From Illuminated Maize Leaves. Arch Biochem Biophys **304**, 496–502.

**Wang Y, Sze H**. 1985. Similarities and differences between the tonoplast-type and the mitochondrial $H^+$-ATPases of oat roots. Journal of Biological Chemistry **260**, 10434–10443.

**Wang ZY, Tobin EM**. 1998. Constitutive expression of the *CIRCADIAN CLOCK ASSOCIATED 1* (*CCA1*) gene disrupts circadian rhythms and suppresses its own expression. Cell **93**, 1207–1217.

**Wang Q-F, Zhao Y, Yi Q, Li K-Z, Yu Y-X, Chen L-M**. 2010. Overexpression of malate dehydrogenase in transgenic tobacco leaves: enhanced malate synthesis and augmented Al-resistance. Acta Physiologiae Plantarum **32**, 1209–1220.

**Warren M, Smith JAC, Apps DK**. 1992. Rapid purification and reconstitution of a plant vacuolar ATPase using Triton X-114 fractionation: Subunit composition and substrate kinetics of the $H^+$-ATPase from the tonoplast of *Kalanchoë daigremontiana*. Biochimica et Biophysica Acta - Biomembranes **1106**, 117–125.

**Warren DM, Wilkins MB**. 1961. An endogenous rhythm in the rate of dark-fixation of carbon dioxide in leaves of *Bryophyllum fedtschenkoi*. Nature **191**, 686–688.

**Weber AP, von Caemmerer S**. 2010. Plastid transport and metabolism of $C_3$ and $C_4$ plants—comparative analysis and possible biotechnological exploitation. Current Opinion in Plant Biology **13**, 256–264.

**Weber APM, Linka N**. 2011. Connecting the Plastid: Transporters of the Plastid Envelope and Their Role in Linking Plastidial with Cytosolic Metabolism. Annual Review of Plant Biology **62**, 53–77.

**Whelan S, Goldman N**. 2001. A General Empirical Model of Protein Evolution Derived from Multiple Protein Families Using a Maximum-Likelihood Approach. Molecular Biology and Evolution **18**, 691–699.

**White PJ, Marshall J, Smith JAC**. 1990. Substrate Kinetics of the Tonoplast $H^+$-Translocating Inorganic Pyrophosphatase and Its Activation by Free $Mg^{2+}$. Plant Physiology **93**, 1063–1070.

**White PJ, Smith JAC**. 1989. Proton and anion transport at the tonoplast in crassulacean-acid-metabolism plants: specificity of the malate-influx system in *Kalanchoë daigremontiana*. Planta **179**, 265–274.

**White PJ, Smith JAC**. 1992. Malate-Dependent Proton Transport in Tonoplast Vesicles Isolated from Orchid Leaves Correlates with the Expression of Crassulacean Acid Metabolism. Journal of Plant Physiology **139**, 533–538.

**Wild B, Wanek W, Postl W, Richter A**. 2010. Contribution of carbon fixed by Rubisco and PEPC to phloem export in the Crassulacean acid metabolism plant *Kalanchoë daigremontiana*. Journal of Experimental Botany **61**, 1375–1383.

**Wilkins MB**. 1959. An endogenous rhythm in the rate of carbon dioxide output in Bryophyllum. I. Some preliminary experiments. Journal of Experimental Botany **10**, 377–390.

**Wilkins MB**. 1973. An Endogenous Circadian Rhythm in the Rate of Carbon Dioxide Output of *Bryophyllum*. VI. Action spectrum for the induction of phase shifts by visible radiation. Journal of Experimental Botany **24**, 488–896.

**Wilkins MB**. 1984. A rapid circadian rhythm of carbon-dioxide metabolism in *Bryophyllum fedtschenkoi*. Planta **161**, 381–384.

**Wilkins MB**. 1991. The role of the epidermis in the generation of the circadian rhythm of carbon dioxide fixation in leaves of *Bryophyllum fedtschenkoi*. Planta **185**, 425–431.

**Wilkins MB**. 1992. Circadian rhythms: their origin and control. New Phytologist **121**, 347–375.

**Wilkins MB, Thomas SL**. 1993. The Damping and Reinitiation of the Circadian Rhythm of $CO_2$ Output in *Bryophyllum* Leaves in Relation to their Malate Content. Journal of Experimental Botany **44**, 901–906.

**Winter K**. 1980. Carbon Dioxide and Water Vapor Exchange in the Crassulacean Acid Metabolism Plant *Kalanchoë pinnáta* during a Prolonged Light Period: Metabolic and Stomatal Control of Carbon Metabolism. Plant Physiology **66**, 917–921.

**Winter K, Foster JG, Edwards GE, Holtum JA**. 1982*a*. Intracellular Localization of Enzymes of Carbon Metabolism in *Mesembryanthemum crystallinum* Exhibiting $C_3$ Photosynthetic Characteristics or Performing Crassulacean Acid Metabolism. Plant Physiology **69**, 300–307.

**Winter K, Garcia M, Holtum JAM**. 2008. On the nature of facultative and constitutive CAM: Environmental and developmental control of CAM expression during early growth of *Clusia*, *Kalanchoë*, and *Opuntia*. Journal of Experimental Botany **59**, 1829–1840.

**Winter K, Holtum JAM**. 2014. Facultative crassulacean acid metabolism (CAM) plants: Powerful tools for unravelling the functional elements of CAM photosynthesis. Journal of Experimental Botany **65**, 3425–3441.

**Winter K, Smith JAC**. 1996. Crassulacean acid metabolism: current status and perspectives. In: Winter K, Smith JAC, eds. Ecological Studies. Crassulacean Acid Metabolism: Biochemistry, Ecophysiology and Evolution. Berlin, Heidelberg: Springer Berlin Heidelberg, 389–426.

**Winter K, Tenhunen JD**. 1982. Light-Stimulated Burst of Carbon Dioxide Uptake following Nocturnal Acidification in the Crassulacean Acid Metabolism Plant *Kalanchoë daigremontiana*. Plant Physiology **70**, 1718–1722.

**Winter K, Wallace BJ, Stocker GC, Roksandic Z**. 1983. Crassulacean acid metabolism in australian vascular epiphytes and some related species. Oecologia **57**, 129–141.

**Wyka TP, Bohn A, Duarte HM, Kaiser F, Lüttge UE**. 2004. Perturbations of malate accumulation and the endogenous rhythms of gas exchange in the Crassulacean acid metabolism plant *Kalanchoë daigremontiana*: testing the tonoplast-as-oscillator model. Planta **219**, 705–713.

**Wyka TP, Duarte HM, Lüttge UE**. 2005. Redundancy of Stomatal Control for the Circadian Photosynthetic Rhythm in *Kalanchoë daigremontiana* Hamet et Perrier. Plant Biology **7**, 176–181.

**Wyka TP, Lüttge U**. 2003. Contribution of $C_3$ carboxylation to the circadian rhythm of carbon dioxide uptake in a Crassulacean acid metabolism plant *Kalanchoë daigremontiana*. Journal of Experimental Botany **54**, 1471–1479.

**Yamaguchi M**. 2005. Evidence for the Plasma Membrane Localization of Al-activated Malate Transporter (ALMT1). Plant and Cell Physiology **46**, 812–816.

**Yang X, Cushman JC, Borland AM, *et al.*** 2015. A roadmap for research on crassulacean acid metabolism (CAM) to enhance sustainable food and bioenergy production in a hotter, drier world. New Phytologist **207**, 491–504.

**Zell MB, Fahnenstich H, Maier A, *et al.*** 2010. Analysis of Arabidopsis with highly reduced levels of malate and fumarate sheds light on the role of these organic acids as storage carbon molecules. Plant Physiology **152**, 1251–1262.

**Zhang J**. 2013. Functional and structural characterization of the vacuolar anion channels *At*ALMT9 and *At*ALMT4 in *Arabidopsis thaliana*. PhD Thesis. Der Universität Zürich.

**Zhang J, Baetz U, Krugel U, Martinoia E, De Angeli A**. 2013. Identification of a Probable Pore-Forming Domain in the Multimeric Vacuolar Anion Channel AtALMT9. Plant Physiology **163**, 830–843.